

SHEET	i	4-087051-20			
TOTAL	v				
CODE		1500-9-1			
ISSUE DATE		10/09/03			
REVISION					
No.	PAGE	DATE	No.	PAGE	DATE
A	thru	01/30/04	E	Chpts 1,3,4,6-9	12/22/04
B	Chpts 1,3,4, 9	3/26/04			
C	Chpts 1,2,9	6/30/04			
D	Chpts 1,6,7,9	10/08/04			


ENGINEERING REPORT

FAA CONTRACT NO. DTFA03-02-C-00044
PHASE 3, CLIN 0003c(3)

Q9 Data Analysis

Distribution

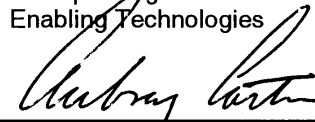
General Manager, Enabling Technologies, Dept. 572
Liston Broughton, Technical Sales and Marketing - 4 copies
(Contract Deliverables to be forwarded to:
- Phyliss Schlegel
- John Bakuckas
- Robert Eastin
- Greg Schneider)



Venkat Raghuraman
Senior Engineer
Enabling Technologies



David Steadman
Principal Engineer
Enabling Technologies



Aubrey Carter
General Manager
Enabling Technologies

Revision E: Revised to update as Q9 Data Analysis Report. Chapter 1 adds a summary of progress during Q9 to the existing progress summaries. Chapters 3 and 4 (FEA Analysis), 7 (Crack Growth), 8 (Initiation), and 9 (Analysis Supporting Testing) revised to reflect the current level of progress.

PROPRIETARY DATA - RESTRICTED DISTRIBUTION - CONTROLLED BY TERMS OF FAA AGREEMENT

SHEET	ii	NO.	4-087051-20
TOTAL	v		
ISSUE DATE		06/30/04	

TABLE OF CONTENTS

LIST OF COMMON ACRONYMS

EXECUTIVE SUMMARY

CHAPTER 1. INTRODUCTION AND SUMMARY

Introduction.....	1-1
Q4 Progress Summary.....	1-2
Q5 Progress Summary.....	1-4
Q6 Progress Summary.....	1-6
Q7 Progress Summary.....	1-7
Q8 Progress Summary.....	1-9
Q9 Progress Summary.....	1-11
Figures	1-13

CHAPTER 2: TEST SPECTRUM

Baseline Spectrum	2-2
Test Spectrum Profile.....	2-8
Crack Growth Equivalence	2-9
FASTER Test Spectra.....	2-11
References.....	2-13
Figures	2-14

CHAPTER 3: FT2 FINITE ELEMENT ANALYSIS

CHAPTER 4: FT1, FT3, AND FT4 FINITE ELEMENT ANALYSIS

CHAPTER 5: HALF BAY SHELL MODEL

Fastener Compliance	5-1
Boundary Conditions and Applied Loads	5-2
Results.....	5-2
Figures	5-3

CHAPTER 6: STRESS STATE AT THE FASTENER HOLE

2-D Rivet Installation Simulation.....	6-1
3-D Joint Analysis.....	6-4

SHEET	iii	NO.	4-087051-20
TOTAL	v		
ISSUE DATE	06/30/04		

CHAPTER 7: CRACK GROWTH ANALYSIS

Local Crack Growth Analysis	7-1
MSD Propagation Simulation.....	7-3
Stress Intensity Calculation	7-4
Growth Rate Calculation.....	7-7
Pre-Test Predictions	7-8
Validation.....	7-9
Equivelent Initial Flaw Distribution.....	7-10
Monte Carlo Simulation.....	7-11
References	7-13
Figures.....	7-14

CHAPTER 8: INITIATION

Introduction.....	8-1
Neural Network Algorithms	8-2
Application to Teardown Data	8-5
Concept Evaluation.....	8-6
References.....	8-10
Figures	8-11

CHAPTER 9: ANALYSIS SUPPORTING PANEL TESTING

Introduction.....	9-1
FT2 Strain Surveys	9-1
FT2 Load Transducer Survey	9-6
FT2 Stringer Clip Analysis	9-8
FT2 Skin Cracking Analysis	9-16
Preventative Modifications to FT1	9-17
References.....	9-18
Figures	9-19

APPENDIX A: INITIATION MODELS LITERATURE REVIEW

APPENDIX B: STRESS INTENSITY FACTOR LITERATURE REVIEW

SHEET	iv	NO.	4-087051-20
TOTAL	v		
ISSUE DATE		06/30/04	

LIST OF COMMON ACRONYMS

DVI	Detailed Visual Inspection
FASTER	Full-Scale Aircraft Structural Test Evaluation and Research Facility
FEA	Finite Element Analysis
FS	Fuselage Station (Aircraft Coordinate System)
FT1-FT4	Panels modified for FASTER testing
GRBN	Gaussian Radial Basis Network
GVI	General Visual Inspection
HFEC	High-Frequency Eddy Current
LFEC	Low Frequency Eddy Current
MOI	Magneto-Optical Imaging
MLG	Main Landing Gear
MS	Microsoft application
MSD	Multiple Site Damage
NDI	Non-Destructive Inspection
NFOV	Narrow Field of View Camera, Remote Control Crack Monitoring System
NLG	Nose Landing Gear
PNN	Probabilistic Neural Network
SB	Service Bulletin
SEM	Scanning Electron Microscopy
SIF	Stress Intensity Factor
TOPP	Delta's FAA-approved Technical Operations Policy and Procedures manual
WFD	Widespread Fatigue Damage
WL	Water Line (Aircraft Coordinate System)
WS	Wing Station (Aircraft Coordinate System)

SHEET	v	NO.	4-087051-20
TOTAL	v		
ISSUE DATE		06/30/04	

EXECUTIVE SUMMARY

This report supports Task 10 of FAA Contract DTFA03-02-C-00044, Data Analysis. The Statement of Work requires that the contractor analyze the crack data (patterns, distributions, sizes and shapes) calculated during the Damage Characterization (Task 9) and demonstrate how to use this data to characterize MSD crack initiation, crack detection, crack link-up, residual strength and the WFD average behavior in the structures removed. Analysis methods will be developed to correlate the state of MSD at any point in time.

This Task in the Statement of Work requires quarterly updates reporting the procedures, data, and results obtained in the previous quarter. This report is the Ninth Quarter Update, and satisfies the third deliverable requirement of CLIN 0003c.

SHEET	1-1	NO.	4-087051-20
TOTAL	1-13		
ISSUE DATE		12/22/04	

CHAPTER 1. INTRODUCTION AND SUMMARY

Introduction

This report supports Task 10 of FAA Contract DTFA03-02-C-00044, Data Analysis. The Statement of Work requires that the contractor analyze the crack data (patterns, distributions, sizes and shapes) calculated during the Damage Characterization (Task 9) and demonstrate how to use this data to characterize MSD crack initiation, crack detection, crack link-up, residual strength and the WFD average behavior in the structures removed. Analysis methods will be developed to correlate the state of MSD at any point in time.

Analytical work within this task includes:

- Generate Stress Spectra
- Determine and document how to estimate number of cycles to crack initiation and estimate the size, extent and distribution of cracks characterizing MSD initiation. Select one or more approaches and determine the applicability and feasibility in conducting WFD assessments.
- Determine and document the size, extent and distribution of MSD causing a reduction of residual strength below predefined levels. Select one or more approaches and determine the applicability and feasibility in conducting WFD assessments.
- Conduct fatigue crack growth analysis for each structure removed. Select one or more approaches and determine the applicability and feasibility in conducting WFD assessments.
- Predict the fatigue crack growth and residual strength of the FASTER panels test. Comment on the ability of the models to accurately analyze and predict crack growth and residual strength.

The Data Analysis Task requires quarterly updates reporting the procedures, data, and results obtained in the previous quarter. This revision is the Ninth Quarter Update, and satisfies the third deliverable requirement of CLIN 0003c.

SHEET	1-2	NO.	4-087051-20
TOTAL	1-13		
ISSUE DATE	12/22/04		

Q4 Progress Summary

1) Generate Stress Spectra

- The load spectra for each test phase of FT1 and FT2 have been developed using finite element analysis (FEA) and crack growth simulation. A hierarchy of finite element analyses (see Figure 1-1) was accomplished to develop FASTER loads for the FT2 and FT1 test panels. Results presented at the Q3 review were preliminary and applied to FT2 only. Results completed this quarter are final for both FT1 and FT2.
 - The Global Stiffness Model of the forward fuselage was completed. This model determined the overall load transfer pattern within the forward fuselage structural elements. During Q4 the model was extended forward to encompass FT1 (see Chapters 3 and 4).
 - The FT2 and FT1 Intermediate Stiffness Models were completed. These models determined the stress state in the primary test area along the lap joint under several flight conditions (see Chapters 3 and 4).
 - The FT2 and FT1 Test Panel Models were completed. These models have geometry and boundary conditions consistent with the modified test panels and the FASTER fixture. Actuator loads for the test plan were determined by iterating applied loads on this model until the stress state in the primary test area matched that of the Intermediate Stiffness Models (see Chapters 3 and 4).
 - The Half Bay Shell Model of a section of 0.040" lap joint and surrounding structure was completed. This model determined the detailed stress and fastener load distributions within a lap joint frame bay used in the pre-test predictions (see Chapter 5).
- A comparative analysis was completed to determine a constant amplitude test spectrum that produces crack growth equivalent to that seen in service. Results presented at Q3 review were preliminary and applied to FT2 only. Those results are now considered final and are applicable to both FT1 and FT2 (see Chapter 2).

SHEET	1-3	NO.	4-087051-20
TOTAL	1-13		
ISSUE DATE	12/22/04		

- 2) Determine and document how to estimate number of cycles to crack initiation and estimate the size, extent and distribution of cracks characterizing MSD initiation.
 - Finite element analysis was accomplished to identify requirements for accurate simulation of residual stresses due to rivet installation in a typical B727 lap joint. These fastener rivet models are used to investigate the residual stresses and displacements in the skin, towards identifying the relationships between the installation process and crack initiation. Nonlinear axisymmetric and 3D models were developed and preliminary results for residual hoop stresses were obtained (see Chapter 6).
- 3) Determine and document the size, extent and distribution of MSD causing a reduction of residual strength below predefined levels.
 - An engineering approach to residual strength analysis based on an empirically tuned criteria was incorporated into an MSD propagation simulation. This approach allows prediction of the residual strength of any simulated MSD state (see Chapter 7).
- 4) Conduct fatigue crack growth analysis for each structure removed.
 - An MSD propagation simulation was developed to model the growth of independent cracks from each hole in a fastened joint. Although used during Q4 for pre-test prediction, the simulation was designed for broader applications, including the propagation of random initial MSD states as part of a Monte-Carlo simulation (see Chapter 7).
- 5) Predict the fatigue and residual strength of the FASTER panels test.
 - The MSD propagation simulation was used to make pre-test predictions for the FT2 and FT1 FASTER tests. The predictions for Phases 1 and 2 required simulation of MSD crack growth under service conditions. In addition, the prediction for Phase 3 required simulation of residual strength degradation and subsequent MSD link-up (see Chapter 7).

SHEET	1-4	NO.	4-087051-20
TOTAL	1-13		
ISSUE DATE	12/22/04		

Q5 Progress Summary

1) Generate Stress Spectra

- The load spectra for each test phase of all four panels have been completed using finite element analysis (FEA) and crack growth simulation. The FEA hierarchy developed in Q4 was extended to develop final FASTER loads for the FT1, FT2, and FT3 test panels. A simplified hierarchy was used to develop FASTER loads for FT4.
 - The Global Stiffness Model of the forward fuselage was extended to encompass FT3. This model determined the overall load transfer pattern within the forward fuselage structural elements.(see Chapters 3 and 4).
 - The FT3 and FT4 Intermediate Stiffness Models were completed. These models determined the stress state in the primary test area along the lap joint under several flight conditions (see Chapters 3 and 4).
 - The FT3 and FT4 Test Panel Models were completed. These models have geometry and boundary conditions consistent with the modified test panels and the FASTER fixture. (see Chapters 3 and 4).
- A comparative analysis was completed to determine a constant amplitude test spectrum that produces crack growth equivalent to that seen in service for each of the four panels. Previous results for FT1 and FT2 included only cabin pressure and vertical bend loads. Results developed this quarter also included nose landing yaw loads (FT3) and vertical fin gust loads (FT4) within the baseline spectra (see Chapter 2). In addition, the analysis was re-accomplished for FT1 and FT2 to reflect an increase in testing pressure.

2) Determine and document how to estimate number of cycles to crack initiation and estimate the size, extent and distribution of cracks characterizing MSD initiation.

- Preliminary equivalent flaw size distributions based on non-parametric integration of striation count data were developed to evaluate this methodology for modeling MSD initiation and growth (see Chapter 8).

SHEET	1-5	NO.	4-087051-20
TOTAL	1-13		
ISSUE DATE	12/22/04		

3) Determine and document the size, extent and distribution of MSD causing a reduction of residual strength below predefined levels.

- The residual strength analysis capability of the MSD propagation simulation was improved to allow for shear and bending loads (see Chapter 7).

4) Conduct fatigue crack growth analysis for each structure removed.

- The crack growth analysis capability of the MSD propagation simulation was improved to allow for shear and bending loads (see Chapter 7).

5) Predict the fatigue and residual strength of the FASTER panels test.

- The MSD propagation simulation was used to make pre-test predictions applicable to all four test panels (see Chapter 7).

SHEET	1-6	NO.	4-087051-20
TOTAL	1-13		
ISSUE DATE		12/22/04	

Q6 Progress Summary

1) Generate Stress Spectra

- The panel FEA model of FT2 was modified to better model the boundary conditions of the FASTER fixture. Complex displacement restraints were incorporated to model the frame radial and loader links and the fulcrum geometry of the skin loaders (see Chapter 3)
- Predicted strain data at the FT2 strain gage locations were collected from the FT2 test panel model. FEA predictions were compared to strain measurements on the FASTER panels for several conditions of 5 psi internal pressure (see Chapter 9).

2) Determine and document how to estimate number of cycles to crack initiation and estimate the size, extent and distribution of cracks characterizing MSD initiation.

3) Determine and document the size, extent and distribution of MSD causing a reduction of residual strength below predefined levels.

- The residual strength analysis capability within the MSD propagation simulation for FASTER panels is complete, waiting for test results for validation (see Chapter 7).

4) Conduct fatigue crack growth analysis for each structure removed.

- MSD propagation simulation for FASTER panels is complete, waiting for test results for validation (see Chapter 7).

5) Predict the fatigue and residual strength of the FASTER panels test.

- Pre-test predictions for FT2 are complete.

SHEET	1-7	NO.	4-087051-20
TOTAL	1-13		
ISSUE DATE	12/22/04		

Q7 Progress Summary

1) Generate Stress Spectra

- The FASTER circular buffer data was parsed to create time histories of the FASTER force transducers. Time histories for frame and skin force transducers were compared to each other and to the FT2 Test Plan loads (see Chapter 9)
- The panel FEA model of FT2 and new local models were used to determine the stress state in the stringer clips after cracking was discovered during testing. FEA clip analysis was conducted for the nominal test plan loads and for loads taken from FASTER force transducers (see Chapter 9).
- Options to address clip cracking for the remainder of FT2 testing were considered, with final recommendations listed (see Chapter 9).

2) Determine and document how to estimate number of cycles to crack initiation and estimate the size, extent and distribution of cracks characterizing MSD initiation.

- The non-deterministic approach was refined as a solution to a crack initiation classification problem. Examples demonstrating the conceptual basis for non-deterministic classification were developed using crack length data from the damage characterization. (see Chapter 8)

3) Determine and document the size, extent and distribution of MSD causing a reduction of residual strength below predefined levels.

- The residual strength analysis capability within the MSD propagation simulation for FASTER panels is complete, waiting for test results for validation (see Chapter 7).

4) Conduct fatigue crack growth analysis for each structure removed.

- MSD propagation simulation for FASTER panels is complete, waiting for damage characterization and test results for validation (see Chapter 7).

SHEET	1-8	NO.	4-087051-20
TOTAL	1-13		
ISSUE DATE		12/22/04	

5) Predict the fatigue and residual strength of the FASTER panels test.

- Pre-test predictions for all four panels are complete. The methodology and assumptions within those analyses may be updated following completion of the FT2 test (see Chapter 7).

SHEET	1-9	NO.	4-087051-20
TOTAL	1-13		
ISSUE DATE	12/22/04		

Q8 Progress Summary

1) Generate Stress Spectra

- A 3D FEA model of one strip (3 fasteners) in the lap joint was created (see Chapter 6). This model is an evolution of previous models in that it is curved circumferentially and loaded by internal pressure, rather than flat and loaded in tension. This change allows the model to accurately capture the effects of skin bending and the resulting inflection points.
- Finite Element Analysis of the FT2 test panel was used to evaluate circumferential skin cracking occurring outside of the test area (see Chapter 9). Proactive pre-test modifications to FT1 were designed to prevent the reoccurrence of this cracking in future tests.

2) Determine and document how to estimate number of cycles to crack initiation and estimate the size, extent and distribution of cracks characterizing MSD initiation.

- Analytical crack growth models were used to backtrack to a distribution of equivalent initial flaw sizes (EIFS) for the frame bay FS 540- 560 4R (see Chapter 7). While the EIFS distribution is closely tied to its backtrack methodology, a future analysis at another frame station will test if this distribution can be propagated forward to the current damage state.

3) Determine and document the size, extent and distribution of MSD causing a reduction of residual strength below predefined levels.

- Starting from the crack array at DSG, the damage in frame bay FS 540- 560 4R was propagated forward using the MSD propagation simulation. The crack array vs flight cycles was evaluated against failure criteria at the regulatory residual strength requirements of JAR 25.571 (see Chapter 7).

4) Conduct fatigue crack growth analysis for each structure removed.

- FADD2D models of starburst cracking were accomplished to determine the effects of pin loading and finite edge widths on crack propagation characteristics (see Chapter 7).

SHEET	1-10	NO.	4-087051-20
TOTAL	1-13		
ISSUE DATE	12/22/04		

- The MSD propagation simulation was validated against striation count data for every lower row hole in frame bay FS 540- 560 4R (see Chapter 7). The MSD simulation was shown to be a good model of MSD average behavior in this area.
- 5) Predict the fatigue and residual strength of the FASTER panels test.
- Pre-test predictions for all four panels are complete. The methodology and assumptions within those analyses may be updated following completion of the FT2 test (see Chapter 7).

SHEET	1-11	NO.	4-087051-20
TOTAL	1-13		
ISSUE DATE	12/22/04		

Q9 Progress Summary

1) Generate Stress Spectra

- FEA stress results from a 2D axisymmetric rivet model (Ga. Tech) were successfully mapped onto the 3D strip model of the 3-row lap joint (see Chapter 6). This mapping was a methodology demonstration to ensure that local stress concentrations related to hole quality, rivet installation, and surface sealant can be incorporated into a 3D strip model capturing second order bending and load transfer effects. Future work will map local stresses from 3D local rivet models onto the 3D strip model.
- Finite Element Analysis to determine FT1 test loads was reaccomplished, based on lessons learned from FT2 testing.
- Finite Element Analysis of the FT1 test panel was used to refine pre-test modifications designed to prevent the reoccurrence of the longitudinal edge cracking seen in FT2.(see Chapter 9).

2) Determine and document how to estimate number of cycles to crack initiation and estimate the size, extent and distribution of cracks characterizing MSD initiation.

- A prototype Probabilistic Neural Network (PNN) was evaluated using single parameter data as part of a building block approach to crack initiation modeling. Evaluation data was representative of a Probability of Detection classification problems, and comparisons were made to a standard industry approach. This evaluation successfully demonstrated the PNN's ability to model data of the volume and distribution expected from the Damage Characterization Task. Future work will expand the PNN to model the effects of the multiple parameters affecting crack initiation.
- A Weibull distribution was fit to the backtracked equivalent initial flaw sizes (EIFS) for one frame bay developed during Q8 (see Chapter 7). This distribution was the basis for a Monte Carlo simulation of MSD propagation to find distributions of crack lengths at 60,000 cycles. Future work will use results from the PNN initiation model as a basis for the Monte Carlo MSD simulation.

SHEET	1-12	NO.	4-087051-20
TOTAL	1-13		
ISSUE DATE	12/22/04		

- 3) Determine and document the size, extent and distribution of MSD causing a reduction of residual strength below predefined levels.
 - The predicted crack arrays from the Monte Carlo MSD simulation were evaluated against failure criteria at the regulatory residual strength requirements of JAR 25.571 (see Chapter 7).
- 4) Conduct fatigue crack growth analysis for each structure removed.
 - The predicted crack arrays from the Monte Carlo MSD simulation were compared against crack length measurements from the lower row hole in frame bay FS 540- 560 4R (see Chapter 7).
The MSD simulation was shown to be a good model of MSD average behavior for this airplane.
Further work would be needed to apply these results to other airplanes in the fleet.
- 5) Predict the fatigue and residual strength of the FASTER panels test.
 - Pre-test predictions for all four panels are complete. The methodology and assumptions within those analyses may be updated following completion of the FT1 test (see Chapter 7).

SHEET	1-13	NO. 4-087051-20
TOTAL	1-13	
ISSUE DATE		12/22/04

Figures

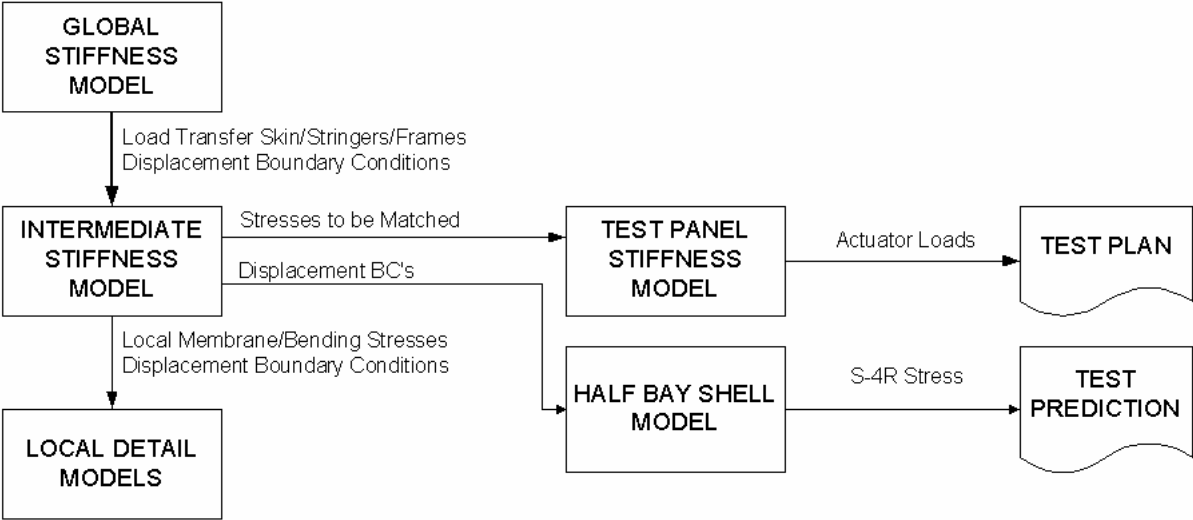


Figure 1-1: Finite Element Analysis Hierarchy for Test Plans

SHEET	2-1	NO.	4-087051-20
TOTAL	2-20		
ISSUE DATE	01/30/04		

CHAPTER 2: TEST SPECTRUM

The test spectrum during Phases 1 and 2 is designed as a compromise between two requirements: that the crack growth in the test specimen represent the crack growth in a service airplane, and that the spectrum be reasonably simple to program and accomplish at the FASTER facility.

The discussion in this section is focused on the Phase 1 and 2 test spectrum. The Phase 3 test spectrum is a Constant Amplitude application of the critical residual strength requirement of 14 CFR 25.571 and JAR 25.571 (see Chapters 3 and 4).

The steps to develop the FASTER spectrum that produces equivalent MSD propagation to that seen in service are:

- 1) Develop a Baseline Spectrum for each panel that represents the variety of loads seen during service.
 - a) Cabin pressurization is 8.6 psi every flight.
 - b) Flight and ground load exceedance data is taken from published data for B727 and similar transport aircraft.
 - c) FT1 and FT2 representative spectra include pressure and vertical bending loads
 - d) FT3 representative spectrum includes pressure, vertical bending, and NLG yaw loads
 - e) FT4 representative spectrum includes pressure, vertical bending, and vertical fin loads
- 2) Conduct iterative Crack Growth Equivalency Analysis to determine the constant amplitude test spectrum that produces similar crack growth to the Representative Spectrum.

It is important to note that these spectra are not intended to be conservative, and it is acknowledged that crack growth in service could be faster or slower than during this testing. Therefore, the baseline spectrum is not intended for repair assessment, analysis of STC's, or any other certification damage tolerance analysis, and the test spectrum is not intended for certification fatigue testing

SHEET	2-2	NO.	4-087051-20
TOTAL	2-20		
ISSUE DATE		01/30/04	

Baseline Spectrum

The hoop and shear skin stresses at the S-4 lap joint are due predominantly to two loads - cabin pressurization and fuselage bending. The cabin pressurization varies little from flight to flight, and a once-per-flight fatigue stress based on the cabin pressure differential (ΔP) is an accurate model.

Fuselage bending is a function of maneuver, gust, and other varying loads whose frequency of occurrence has been the subject of much industry research. In addition to frequency, the grouping and sequence of the fuselage bending loads are important to crack growth and retardation.

FT1 and FT2 are in the forward fuselage, where vertical bending loads due to positive load factors are sufficient for the baseline spectrum. FT3 is forward of the wing, where shear stresses due to nose landing gear yaw are potentially significant. FT4 is aft of the wing, where torsion and shear stresses due to vertical fin gusts are potentially significant. Occurrences of these load conditions based on published service data were included in the respective baseline spectra for FT3 and FT4.

Vertical Bending

One established experimental spectrum for flight loads is the Transport Wing Structures or TWIST.

The truncated version mini-TWIST outlined in Ref [2-1] is a collection of 4,000 flights as shown in Table 2-1. Within the 4,000 flights, there is a range between the single severe “A” flight and the 2,211 mild “J” flights. Each “J” flight has a single excursion from 1-g cruise with a cycle from 1.222 g’s to 0.778 g’s. The “A” flight contains 1,100 load cycles, including 500 0.222 g “J” excursions and a single 1.6 g excursion up to 2.6 g’s.

The TWIST spectrum was based on a survey of transport aircraft, but in some ways it is more aggressive than necessary for this testing. For example, the Mini-TWIST spectrum has four flights excursions at or above 2.5 g’s every 4,000 flights. This level corresponds to a limit load condition for the B727, an event which is unlikely to occur in an aircraft’s entire service career.

Exceedance data for the B727-232 has been published by NASA in Ref [2-2]. In addition, extensive operational and exceedance data has been published for the 737-400 in Ref [2-3]. As shown in Table 2-2, the transport missions of the 727-232 and 737-400 are similar, so it is reasonable to take the 737-400 data as representative of the test airplane’s service.

ENGINEERING DEPARTMENT

SHEET	2-3	NO.	4-087051-20
TOTAL	2-20		
ISSUE DATE	01/30/04		

Flight		1.6	1.5	1.3	1.15	0.995	0.84	0.685	0.53	0.375	0.222	Cycles in Flight
A	1	1	1	1	4	8	18	64	112	391	500	1100
B	1		1	1	2	5	11	39	76	366	449	950
C	3			1	1	2	7	22	61	277	379	750
D	9				1	1	2	14	44	208	270	540
E	24					1	1	6	24	165	213	410
F	60						1	3	19	115	157	295
G	181							1	7	70	97	175
H	420								1	16	25	42
I	1090									1	2	3
J	2211										1	1
Total Cycles at Amplitude		1	2	5	18	52	152	800	4170	34800	51496	Total Cycles 91496

Table 2-1: Frequency Table of Cycle Amplitudes for Mini-Twist

	Typical B727 per Aircraft Information Report	727 per Ref [2-2]	B737-400 per Ref [2-3]
Stage Length	600 nm	734 nm	550 nm (Median, Fig A-11)
Cruise Altitude	33,000 ft	34,000 ft	31,100 ft (Average, Fig. A-7)
Flight Length	1.4 hrs	1.8 hrs	1.42 hrs (Average, A-59 60)
Time in Climb	19%	18%	18% (Average, Fig. A-58)
Time in Descent	25%	18%	25% (Average, Fig. A-58)

Table 2-2: 727 to 737-400 Mission Comparison

Figure 2-1 shows an exceedance comparison between Mini-TWIST factored by 50%, the NASA reported 727, and the 737-400 data. The lines in Figure 2-1 are taken from a plot of cumulative occurrences for combined maneuver and gust vertical loads (Ref [2-3], Figure A-59), normalized by the average 1.42 hr flight time. This comparison shows good agreement between the TWIST-based model and the two service data sources. Therefore, the vertical bending component of the baseline spectra use the 50% Mini-TWIST spectrum with amplitudes shown in Table 2-3.

ENGINEERING DEPARTMENT

SHEET	2-4	NO.	4-087051-20
TOTAL	2-20		
ISSUE DATE	01/30/04		

Flight		0.8	0.75	0.65	0.575	0.4975	0.42	0.3425	0.265	0.1875	0.111	Cycles in Flight
A	1	1	1	1	4	8	18	64	112	391	500	1100
B	1		1	1	2	5	11	39	76	366	449	950
C	3			1	1	2	7	22	61	277	379	750
D	9				1	1	2	14	44	208	270	540
E	24					1	1	6	24	165	213	410
F	60						1	3	19	115	157	295
G	181							1	7	70	97	175
H	420								1	16	25	42
I	1090									1	2	3
J	2211										1	1
Total Cycles at Amplitude		1	2	5	18	52	152	800	4170	34800	51496	Total Cycles 91496

Table 2-3: Frequency Table for 50% Mini-TWIST

During Q4, the pressurized fuselage gust and maneuver spectrum discussed in Ref [2-4] was evaluated as a potential representative spectrum. Other spectra discussed in Ref [2-4] are a lateral gust loading spectrum, ground loading spectrum, fighter aircraft maneuver spectrum, and a wing gust and maneuver spectrum. Based on correspondence with the paper's author, the pressurized fuselage spectrum was generated by superimposing the wing gust and maneuver loads spectrum onto cabin pressure loads. The gusts were calculated using the equations and parameters included in Appendix G of FAR-25, and the maneuvers were calculated using MIL-A-8866B (Maneuvers for transport aircraft). Like Mini-TWIST, this spectrum is used for coupon testing and has not been validated as representative of a specific large transport aircraft.

Comparison of the total excursion exceedance from 1-g shows the Ref [2-4] spectrum to be very similar to Mini-TWIST (see Figure 2-2). The Ref [2-4] spectrum was developed for the Gulfstream G200 business jet, which has a MTOW of 35,450 lbs. This weight leads to a limit maneuver load factor of 2.63g (14 CFR 25.337), higher than the 727's 2.5g limit. This higher limit load is evident in the Ref [2-4] spectrum. Like Mini-TWIST, the Ref [2-4] fuselage spectrum is too severe to represent B727 service without factoring of the excursion amplitudes.

The conclusions from this Q4 evaluation are a) it is reasonable to create a fuselage gust and maneuver spectrum through superposition of wing load factors and pressure loads, and b) once factored, use of the Ref [2-4] fuselage spectrum would produce similar results to those gained with $\Delta P+50\%$ Mini-TWIST. Therefore, $\Delta P+50\%$ Mini-TWIST is retained as the representative spectrum for pressurization plus vertical bending loads.

SHEET	2-5	NO.	4-087051-20
TOTAL	2-20		
ISSUE DATE	01/30/04		

Nose Landing Gear Yaw

This condition is defined by the requirements of CAR 4b.235(e) “Ground Handling Conditions – Nose Gear Yawing”. NLG yaw was included in the baseline spectrum for FT3 because it produces shear within the S-4 lap joint. However, the CAR 4b.235(e) condition is in static equilibrium application of loads; a prescribed lateral load at the NLG is balanced by braking at one MLG (see Figure 2- 3). This type of load application is not a common service event, so a conservative estimate of NLG yaw occurrence was developed for the baseline spectrum.

NLG side loads typically occur during normal turns, so the conservative estimate of NLG yaw load frequency and amplitude is based on published data for side loads [2-5]. The Side Load condition is defined by the requirements of CAR 4b.235(c) “Ground Handling Conditions – Turning”, which is a static 0.5 g side load on all three gear sets. The exceedance diagram for lateral load factor during turns is shown in Figure 2- 4, as well as the conservative estimate used within the FT3 baseline spectrum: 4 worst case (left) NLG yaws per flight at 50% limit.

Cycle-by-cycle analysis were conducted including and excluding this conservative condition, with no appreciable difference between the analysis outcome. One conclusion from this analysis is that the NLG yaw has no appreciable effect to lap joint MSD growth.

Vertical Fin Gust

This condition is defined by the requirements of CAR 4b-215 “Yawing Conditions – Lateral Gust” (see Figure 2- 5). Since rudder maneuver fatigue loads from service are not widely available, an engineering model for combined gust/maneuver fin loads was developed using 727 derived gust velocities in Ref [2-2].

An engineering model based on the mini-TWIST frequency table is ideal for two reasons:

- Factored mini-TWIST was shown to be effective model for vertical gust and maneuver loads
- Using mini-TWIST for lateral loads simplifies incorporation of those loads into a TWIST-based cycle-by-cycle analysis.

ENGINEERING DEPARTMENT

SHEET	2-6	NO.	4-087051-20
TOTAL	2-20		
ISSUE DATE	01/30/04		

For this model, a Limit Mini-TWIST table was created by transforming the load factor data in Table 2-1 to a limit factor table by factoring all amplitudes by 1/1.5 (see Table 4). This transformation is founded on the 2.5 g limit load definition in 14 CFR 25.337, which is equal to a 1.5g excursion from 1g in Table 2-1. As with vertical load factor, the factor applied to the limit mini-TWIST amplitudes was tuned to match the service data as shown in Figure 2- 6. Based on this analysis, the FT4 baseline spectrum includes a 60% Limit mini-TWIST fin gust.

Table 4: Mini-TWIST Frequency Table as Percent of Limit Load

Flight		107%	100%	87%	77%	66%	56%	46%	35%	25%	15%	Cycles in Flight
A	1	1	1	1	4	8	18	64	112	391	500	1100
B	1		1	1	2	5	11	39	76	366	449	950
C	3			1	1	2	7	22	61	277	379	750
D	9				1	1	2	14	44	208	270	540
E	24					1	1	6	24	165	213	410
F	60						1	3	19	115	157	295
G	181							1	7	70	97	175
H	420								1	16	25	42
I	1090									1	2	3
J	2211										1	1
Total Cycles at Amplitude		1	2	5	18	52	152	800	4170	34800	51496	Total Cycles 91496

SHEET	2-7	NO.	4-087051-20
TOTAL	2-20		
ISSUE DATE		01/30/04	

Baseline Spectra Summary

In summary, the baseline spectra for the test panels contain the following components:

1) FT1 and FT2

- a) Cabin pressurization
- b) 50% Mini-TWIST vertical load factor

2) FT3

- a) Cabin pressurization
- b) 50% Mini-TWIST vertical load factor
- c) 4 per flight conservative NLG yaw at 50% limit

3) FT4

- a) Cabin pressurization
- b) 50% Mini-TWIST vertical load factor
- c) 60% Limit Mini-TWIST fin load factor

SHEET	2-8	NO.	4-087051-20
TOTAL	2-20		
ISSUE DATE	01/30/04		

Test Spectrum Profile

Potential FASTER load spectra were developed for evaluation from three potential load profiles:

- 1) The Constant Amplitude is the simplest, which has advantages when programming the test controller, performing the crack growth analysis, and conducting the subsequent fractography. A schematic Constant Amplitude Spectrum is shown in Figure 2-7.
- 2) The 250-step Composite Spectrum has been validated by one OEM in Ref [2-6] as producing accurate damage propagation and retardation behavior in structures where flight loads are dominant. Note that FASTER panels FT1 and FT2 are cut from the forward fuselage where loads due to cabin pressurization are more influential than flight loads. FASTER panels FT3 and FT4 are adjacent to the wing and have stronger flight load effects. A schematic 250-step Composite Spectrum is shown in Figure 2-8.
- 3) The 10-Step Composite Spectrum is a compromise between the two previous options. A schematic 10-Step Composite Spectrum is shown in Figure 2-9.

Following significant evaluation during Q4 and Q5, a constant amplitude test spectrum will be used for all phases of all tests:

- This spectrum provides the best test logistics, with an estimated 80 flt cyc/hr (at 45 second per cycle)
- Use of this spectrum simplifies any future use of the test data, such as validating WFD assessment methods. For example, a constant amplitude analysis allows closed-form integration of crack growth rate during a crack growth analysis, while other options would require a cycle-by-cycle analysis.
- Only minor effects of the variable amplitude service loads were found during examination of fracture surfaces (see Q4 and Q5 Damage Characterization reports).

SHEET	2-9	NO.	4-087051-20
TOTAL	2-20		
ISSUE DATE	01/30/04		

Crack Growth Equivalence

A series of crack growth analyses were run to determine load factors to use for each spectrum to produce crack growth rates equivalent to the baseline spectrum. All analysis had the following characteristics in common:

- Stresses at each flight condition at S-4 and the center of each test panel.
- Separate analyses conducted in the hoop (longitudinal cracking) and axial (circumferential cracking) directions.
- Normal and shear stresses combined using formula similar to the maximum principal stress:

$$\sigma = \frac{\sigma_x}{2} + \sqrt{\left(\frac{\sigma_x}{2}\right)^2 + \tau_x^2}$$

- Stress intensity function for infinite series of 5/32 fastened holes with equal length diametric cracks, 39% load transfer.
- Cycle-by-cycle crack growth using the modified Forman equation, with empirical constants from reference [2-7].

The objective of this analysis is to determine the equivalence factors that should be applied to each load case. Since this equivalence factor must be valid for all damage propagation in the test panel, it cannot be highly sensitive to the assumed crack geometry or the nominal stress.

The analysis results for longitudinal and hoop loads are shown in Figure 2-10 through Figure 2-14. Up to six crack growth results are plotted:

- The baseline spectrum
- The test spectrum with tuned equivalence factors
- A conservative constant amplitude spectrum of $1.5\Delta P + 1.5g$ recommended for crack growth analysis of a generic aircraft repair by the Los Angeles ACO [2-8]

ENGINEERING DEPARTMENT

SHEET	2-10	NO.	4-087051-20
TOTAL	2-20		
ISSUE DATE		01/30/04	

- A conservative constant amplitude spectrum of ($\Delta P + 0.5$ psi) +1.3g recommended for crack growth analysis of a generic antenna installation by the FAA Chief Scientific Advisor - Fracture Mechanics [2-9].
- A Constant Amplitude spectrum of $\Delta P + 1.25g$, with stress ratio at 0.1
- A Constant Amplitude spectrum of $\Delta P + 1.25g$, with stress ratio at 0.0.

SHEET	2-11	NO.	4-087051-20
TOTAL	2-20		
ISSUE DATE		01/30/04	

FASTER Test Spectra

Fatigue Summary (Phases 1 and 2)

Based on the crack growth equivalence, the conditions corresponding to the fatigue test spectrum are as follows:

FT1 and FT2

- Internal pressure, hoop, and axial loads
- 8.9 psi internal pressure (normal operating + 0.3 psi)
- 1.25g vertical load factor

FT3

- Internal pressure, hoop, axial, and shear loads
- 8.9 psi internal pressure
- 1.25g vertical load factor

FT4

- Internal pressure, hoop, axial, and shear loads
- 8.9 psi internal pressure
- 1.25g vertical load factor
- 10% limit lateral fin gust

See Finite Element Analysis (Chapters 3 and 4) for the development of FASTER actuator loads corresponding to these conditions.

SHEET	2-12	NO.	4-087051-20
TOTAL	2-20		
ISSUE DATE	01/30/04		

Residual Strength (Phase 3)

Assuming lap splice MSD is the dominant damage at the end of Phase 2, the residual strength spectrum during Phase 3 will be driven by the pressurized cabin conditions of JAR 25.571 (b)(5)(ii) which define a condition where “the maximum value of normal operating differential pressure (including the expected external aerodynamic pressures during 1 g level flight) multiplied by a factor of 1.15 omitting other loads.” Note that this condition is more aggressive than the similar section of 14 CFR 25.571, which does not multiply the aerodynamic pressure by the 1.15 factor. Applying this condition leads to Phase 3 Constant Amplitude spectra as follows, with a 0.1 stress ratio:

FT1, FT2, and FT3

- 10.24 psi internal pressure ($1.15 * [8.6 \text{ psi cabin} + 0.3 \text{ ext. aero}]$) + 1.0 g vertical

FT4

- 10.24 psi internal pressure ($1.15 * [8.6 \text{ psi cabin} + 0.3 \text{ ext. aero}]$) + 1.0 g vertical

See Finite Element Analysis (Chapters 3 and 4) for the development of FASTER actuator loads corresponding to these conditions.

SHEET	2-13	NO.	4-087051-20
TOTAL	2-20		
ISSUE DATE	01/30/04		

References

- [2-1] H. Lowak, J. B. DeJonge, J. Franz, and D. Schuetz, "MINITWIST: A Shortened version of TWIST", LBF-TB-146, Laboratorium fur Betriebsfestigkeit, 1979.
- [2-2] Crabill, N.L., "The NASA Digital VGH Program - Exploration of Methods and Final Results, Vol. III - B 727 Data 1978-1980: 1765 Hours", Eagle Engineering, Inc., Hampton, VA, DOT-RAA-CT-89/36-I, December 1989.
- [2-3] Report DOT/FAA/AR-98/28, "Statistical Loads Data for Boeing 737-400 Aircraft in Commercial Operations", August 1998.
- [2-4] A. Brot and C. Matias, "An Evaluation Of Several Retardation Models For Crack Growth Prediction Under Spectrum Loading", Presented to the 2002 USAF Aircraft Structural Integrity Program Conference, Savannah, Georgia, 10 December 2002.
- [2-5] D.O. Tipps, J. Rustenburg, D. Skinn, and T. DeFiore, Side Load Factor Statistics From Commercial Aircraft Ground Operations, Final Report DOT/FAA/AR-02/129, January 2003.
- [2-6] H.J. Schmidt, "Evaluation Methodologies Applied for Pressurized Fuselages of Airbus Aircraft", Structural Integrity of Aging Airplanes, Atluri, Sampath, Tong (Eds) , Springer Verlag Berlin Heidelberg 1991.
- [2-7] JSC-22267A, "Fatigue Crack Growth Computer Program 'NASA FLAGRO' Version 2.0, Revision A, 1994.
- [2-8] Memorandum, "ANM-120L Damage Tolerance Philosophy", Los Angeles Aircraft Certification Office, 1995.
- [2-9] R. G. Eastin, "Damage Tolerance Evaluation of Antenna Installations", presented at the Chicago ACO DER Recurrent Seminar, 2000.

SHEET	2-14	NO.	4-087051-20
TOTAL	2-20		
ISSUE DATE	01/30/04		

Figures

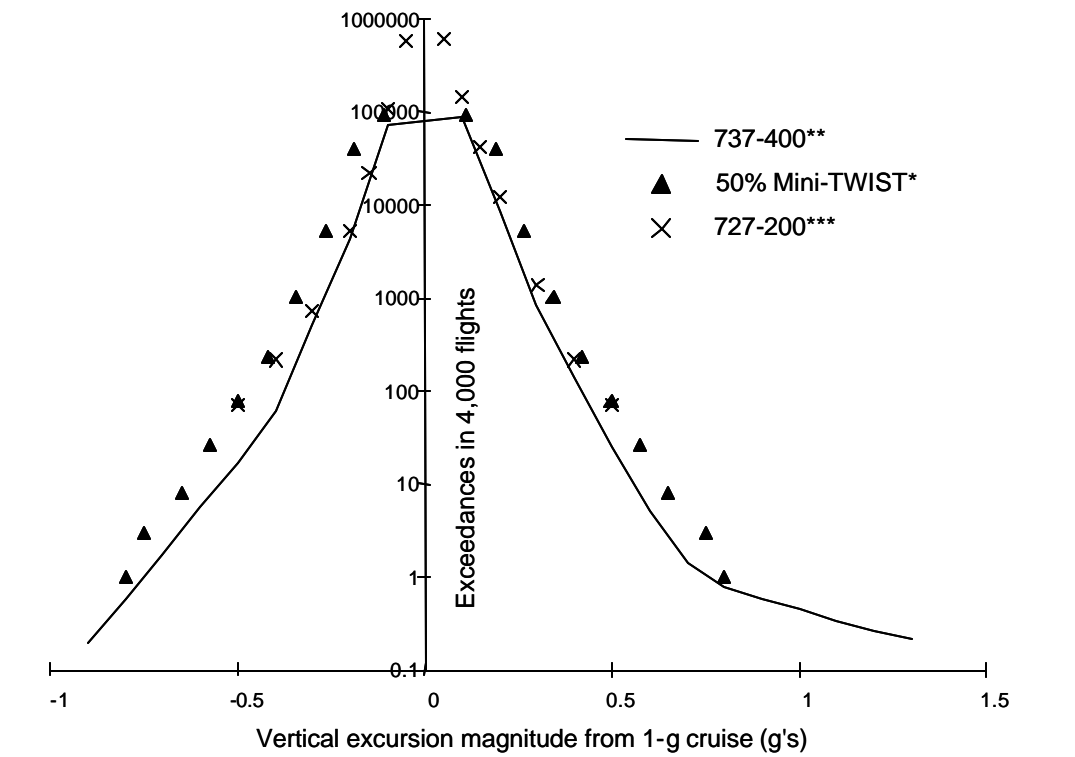


Figure 2-1: Comparison Exceedance Diagram for 50% Mini-TWIST vs 727 and 737-400

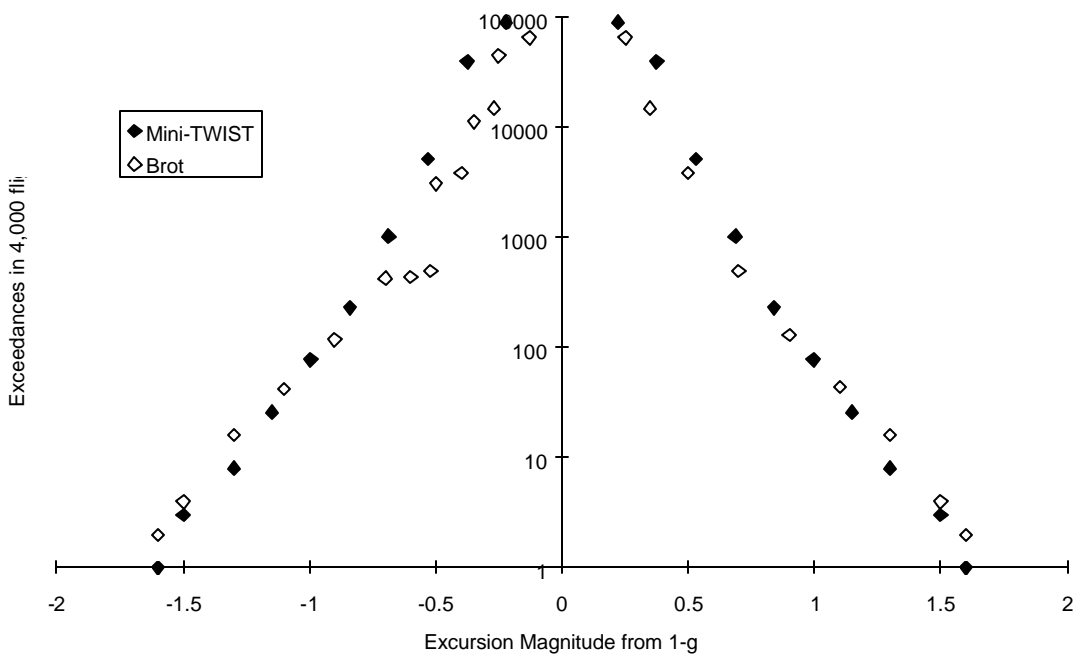


Figure 2-2 Comparison Exceedance Diagram for Mini-TWIST vs Ref [2-4]

SHEET	2-15	NO.	4-087051-20
TOTAL	2-20		
ISSUE DATE	01/30/04		

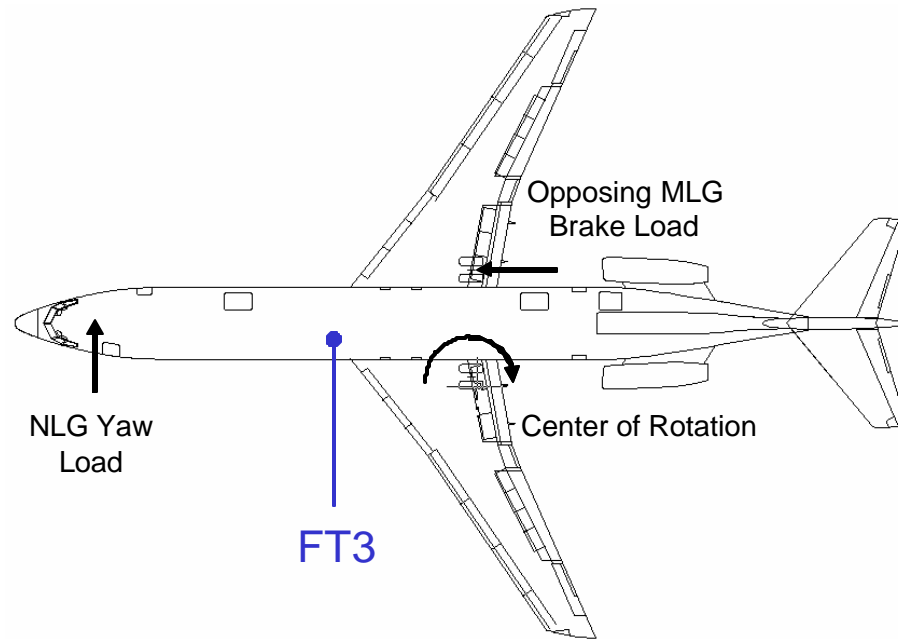


Figure 2- 3: Nose Landing Gear Yaw

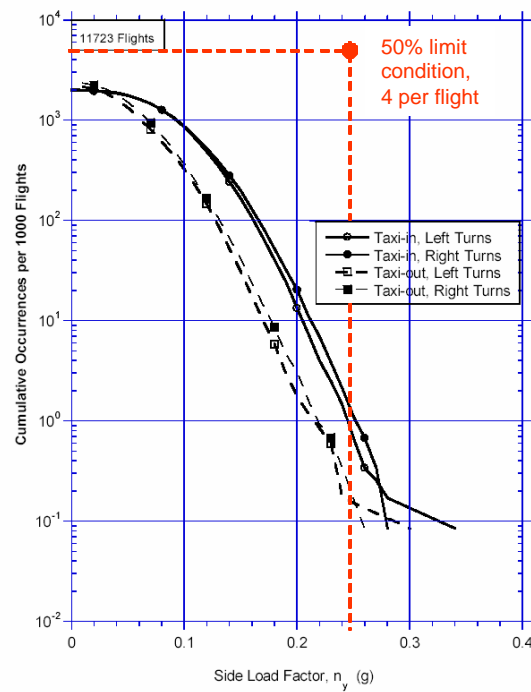
CUMULATIVE FREQUENCY OF LATERAL LOAD FACTOR
DURING GROUND TURNING, B-737-400

Figure 2- 4: Side Load Exceedance and Conservative Model

SHEET	2-16	NO.	4-087051-20
TOTAL	2-20		
ISSUE DATE	01/30/04		

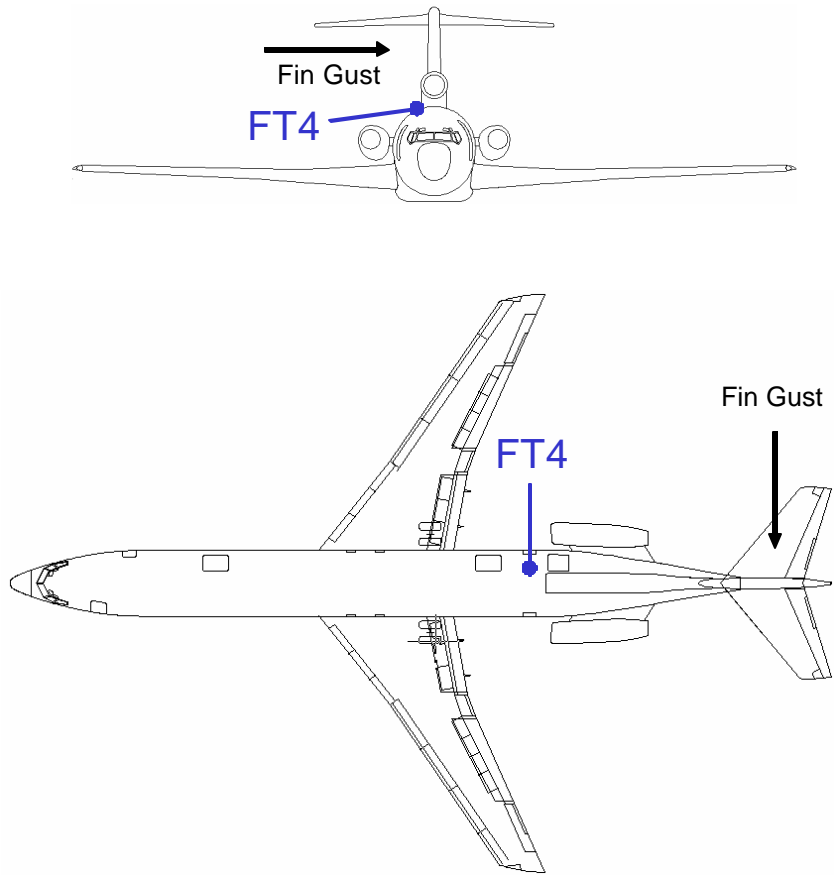


Figure 2- 5: Vertical Fin Gust

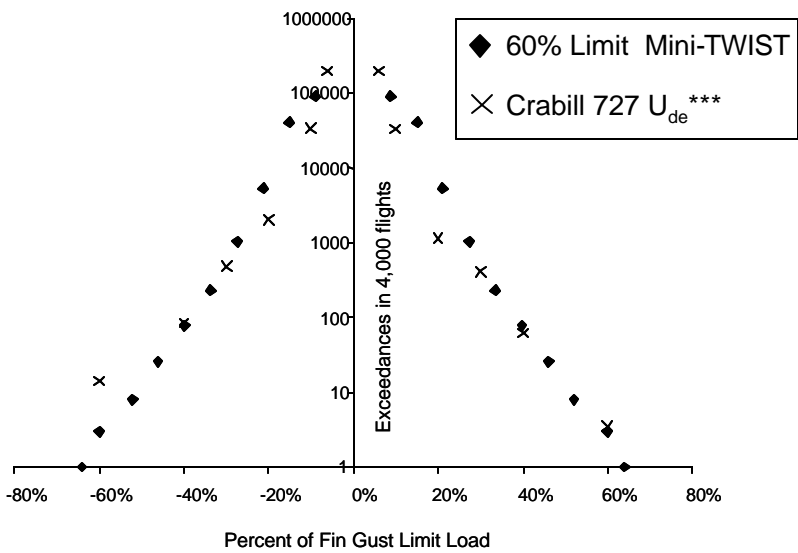


Figure 2- 6: Derived Gust Velocities

SHEET	2-17	NO.	4-087051-20
TOTAL	2-20		
ISSUE DATE	01/30/04		

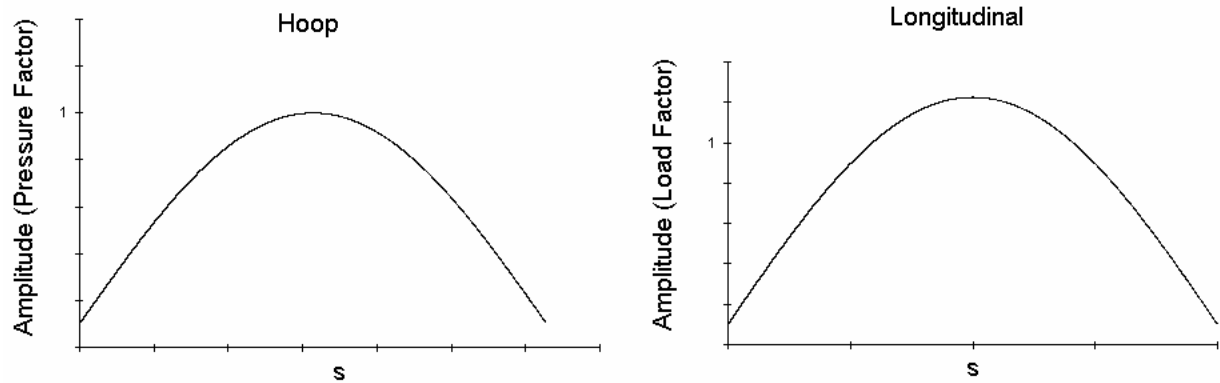


Figure 2-7: Constant Amplitude Spectrum (schematic only – actual profile need not be symmetric)

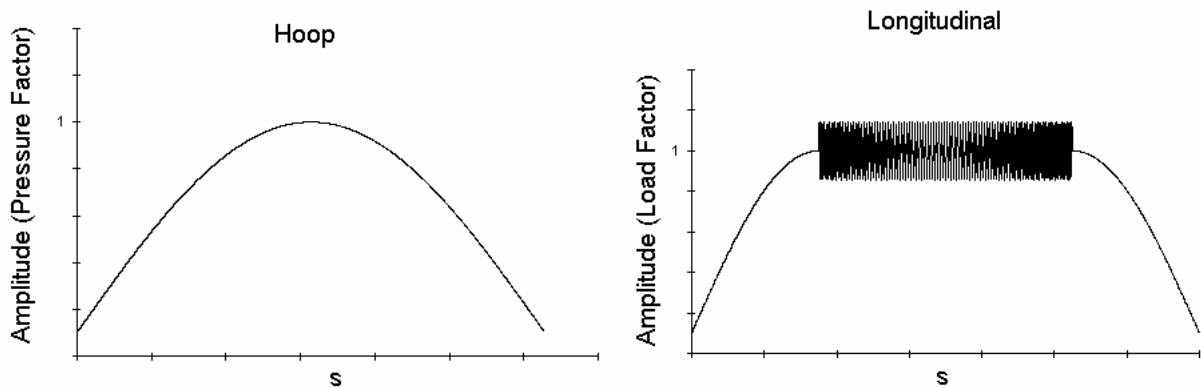


Figure 2-8: 250-Peak Composite Spectrum

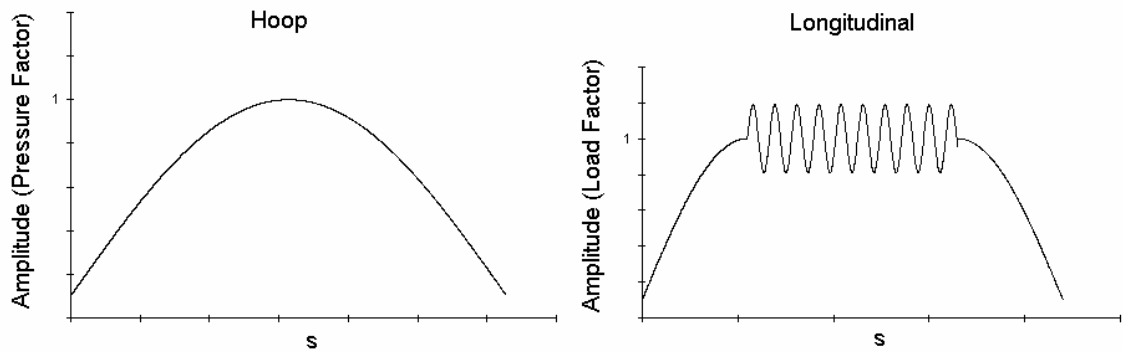


Figure 2-9: 10-Peak Composite Spectrum

SHEET	2-18	NO.	4-087051-20
TOTAL	2-20		
ISSUE DATE	01/30/04		

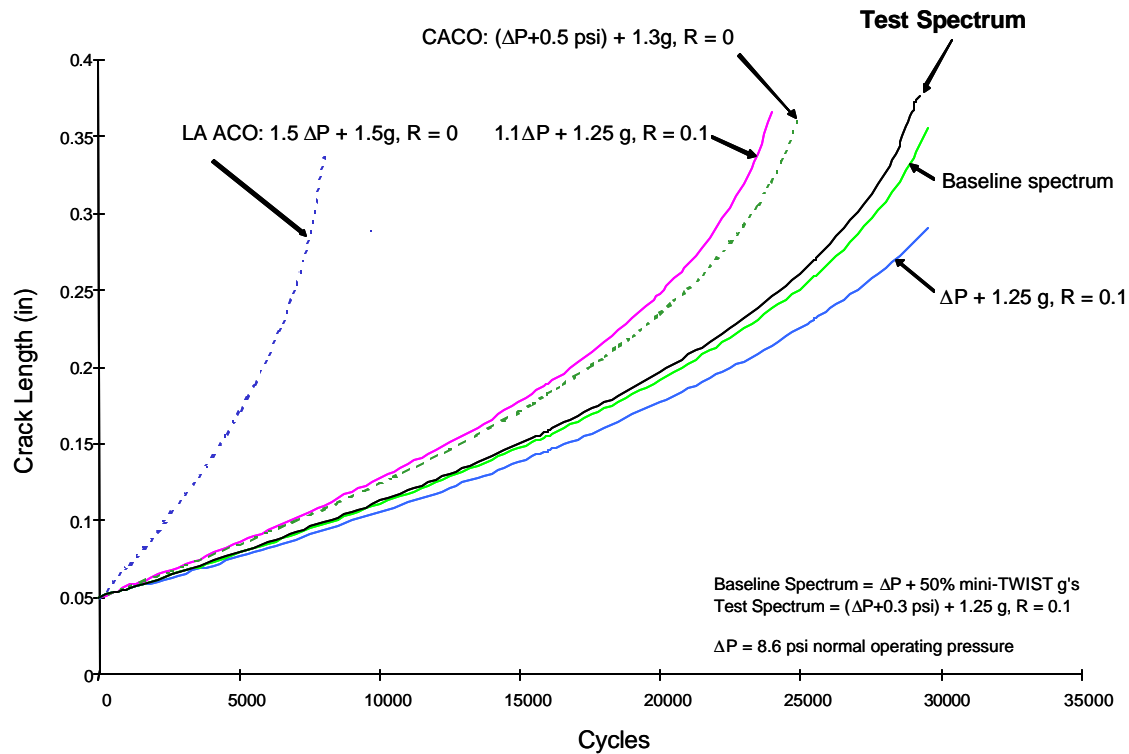


Figure 2-10: FT2 Crack Growth Analysis for Hoop Loads

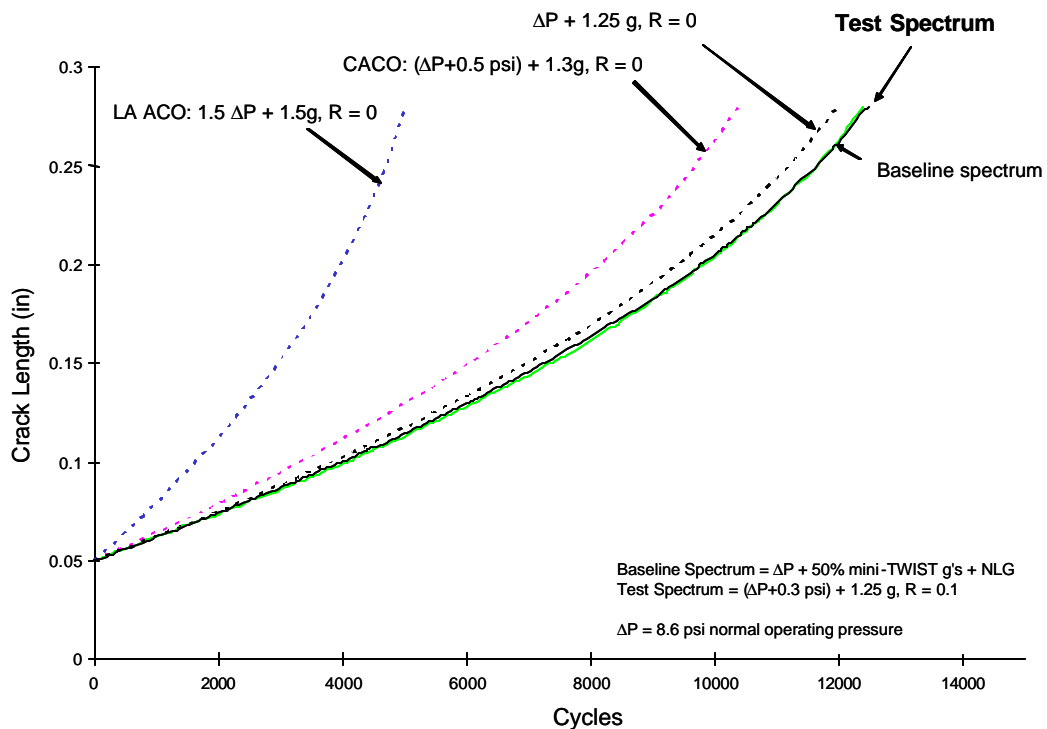


Figure 2-11: FT3 Axial Loads (Circumferential Cracking)

SHEET	2-19	NO.	4-087051-20
TOTAL	2-20		
ISSUE DATE	01/30/04		

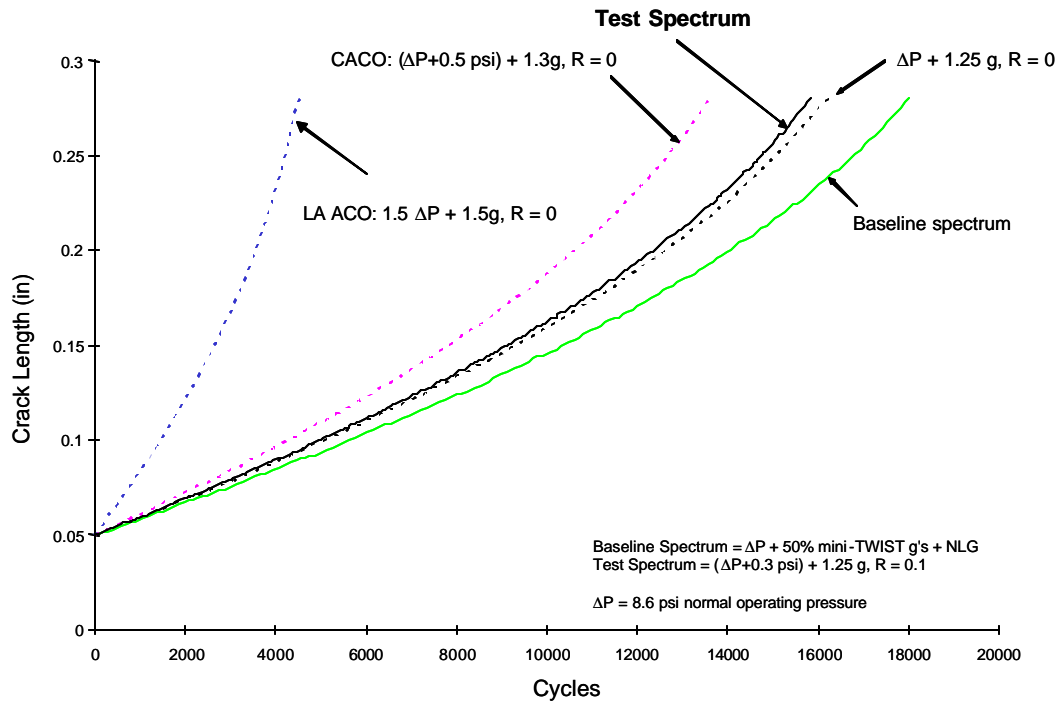


Figure 2- 12: FT3 Hoop Loads (Longitudinal Cracking)

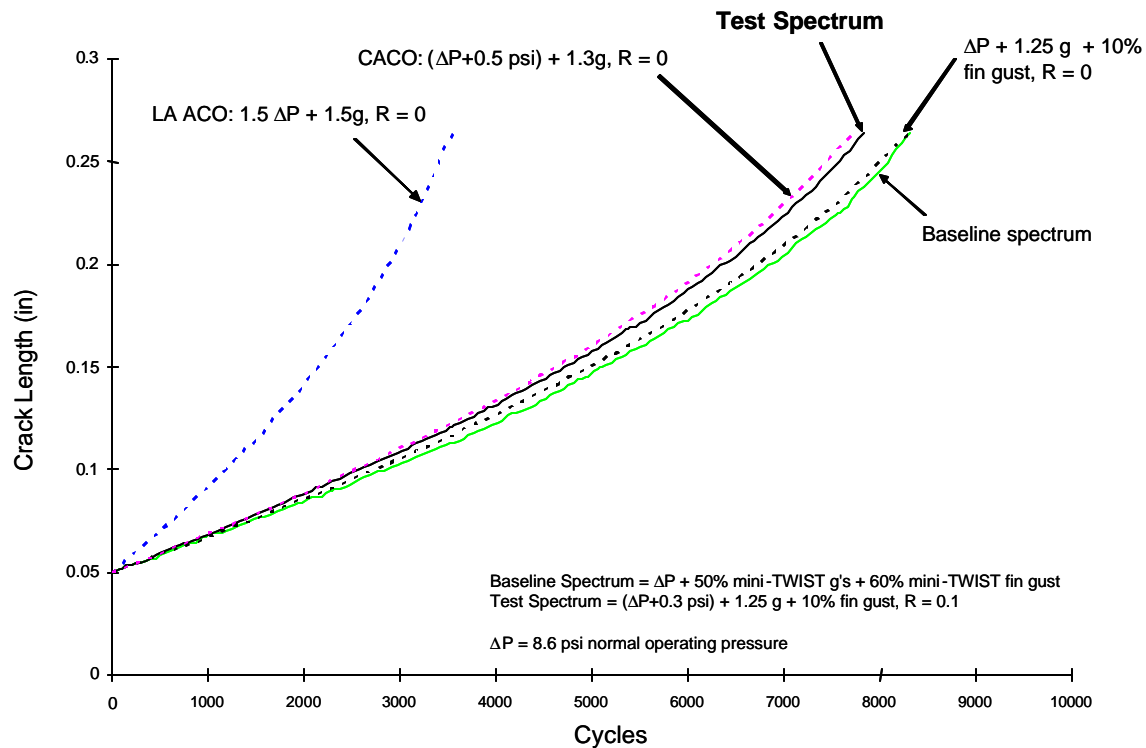


Figure 2- 13: FT4 Axial Loads (Circumferential Cracking)

SHEET	2-20	NO.	4-087051-20
TOTAL	2-20		
ISSUE DATE	01/30/04		

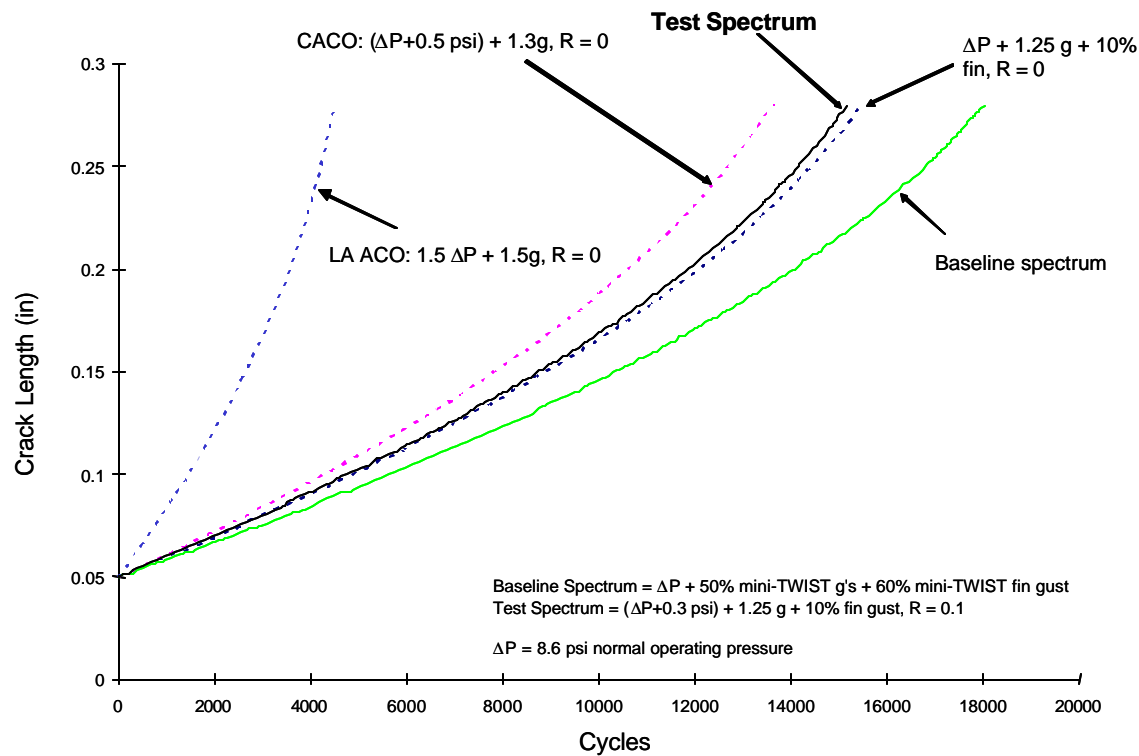


Figure 2- 14: FT4 Hoop Loads (Longitudinal Cracking)

SHEET	3-1	NO.	4-087051-20
TOTAL	3-38		
ISSUE DATE	12/21/04		

CHAPTER 3: FT2 FINITE ELEMENT ANALYSIS

Note: The actuator loads for the revised loading conditions are listed in Table 3-5.

Geometrically nonlinear finite element analysis was accomplished in order to assess stresses in the fuselage subjected to pressure and flight loads, and predict FASTER loads for the FT2 test panel. Geometrically nonlinear modeling was required to account for significant bending stiffening associated with membrane tension in the pressurized fuselage skin [3-1]. The skin bending stiffening affects the load distribution among the skin, stringers, and frames. Multi-level stiffness models were developed in IDEAS finite element code.

A global model of the B727-200 fuselage Section 43 was developed. Figures 3-1 and 3-2 show the shaded and the wireframe views of the finite element mesh. The fuselage has a constant 74" radius in the upper lobe above stringer 10 and variable radius in the lower lobe. The model is 380" long. Its forward end corresponds to the frame station 480, and the aft end is aligned with the frame station 740. The fuselage right side is symmetric to the left side except at the cargo door. Shell elements of variable thickness simulate the fuselage skin. Offset beam elements represent frames, stringers, intercoastals, and cargo door sills. Beam elements are also used to simulate the skin splices and the floating frame attachments in the fuselage upper lobe area. The total number of degrees of freedom is 50,000. The aft end of the model is fixed. The edge effects due to the constraints are not significant at the FT2 structure location. The unmodified FT2 test panel structure is located between the frame stations 620 and 720, and stringers 2 and 7. The test critical area is located between the frame stations 640 and 700, and stringers 4 and 5. The loads include skin internal pressure, axial loads due to the pressure and bending applied at the frame station 480, and shear loads due to the weight of the aircraft, passengers and cargo, applied at the frame station 480 and distributed throughout the model [3-2]. The applied loads are shown in the table below:

SHEET	3-2	NO.	4-087051-20
TOTAL	3-38		
ISSUE DATE	12/21/04		

Load	Location	Magnitude
Passenger (Positive gust condition)	Locations on Floor beams at 45" and 25" from center	70% of 6 abreast passenger seating- All seats full with 120 passengers
Cargo	Frames between 27R and 27L lower lobe (applied as force/frame/unit length)	Average checked bag weight for 120 passengers
Gravity (1g)	Entire Model	32.17 ft/sec ²
Front End Axial and Shear loads (Positive Maneuver)	STA 480 (Front End)	Varies with stringer locations
Pressure	Entire model	8.6 psi

Table 3-1: Global fuselage section 43 loads

The investigated loading scenarios included 8.6 psi pressure, and combined 8.6 psi pressure and 1g flight, 8.6 psi and 2.5g flight, and 9.89 psi and 1g flight conditions. An existing beam-type solution supported by test evidence was used to estimate the loads at the frame station 480 in accordance with the positive maneuver condition.

Figure 3-3 shows a contour plot of the skin hoop stress predicted by the global model for the 8.6 psi pressure loading case. Figure 4 isolates the hoop stress in the FT2 panel area. The skin axial and shear stress contour plots are shown in Figures 3-5 through 3-8. The global model predicts a 13 ksi hoop stress and a 7 ksi axial stress in the FT2 panel area. The shear stress is negligible. Symmetric distribution of all stress components in the fuselage upper lobe shows that the cargo door effect is not significant in this area. The axial stress level is higher than a 5.85 ksi stress determined based on an assumption of equal stresses in the skin and stringers. This effect requires further investigation.

In order to determine a more accurate stress distribution, an intermediate stiffness model of the unmodified FT2 panel structure was developed. The model consists of linear shell elements with approximately 63,000 degrees of freedom. A model with parabolic shell elements, developed to ensure

SHEET	3-3	NO.	4-087051-20
TOTAL	3-38		
ISSUE DATE	12/21/04		

the computational accuracy, predicted the same stress and deformation states. Geometrically nonlinear analysis results for models with linear elements are presented in this report.

Figures 3-9 and 3-10 show the hoop and the axial stress contour plots predicted by the intermediate model for the 8.6 psi pressure loading case. Symmetry displacement constraints are imposed at the model edges. The axial load is applied at the forward and aft edges per the existing beam-type solution. The intermediate model predicts a 13.7 ksi hoop membrane stress and a 14.3 ksi hoop surface stress in the 0.04" skin. The nominal $s_h = pR/t$ hoop stress level is 15.9 ksi. An average frame load is 12% of the total hoop load. The predicted axial stress is 7.53 ksi that is higher than the assumed 5.85 ksi axial stress. Such stress increase is associated with the skin axial stiffening from the pressure load.

To investigate this effect, consider a curved 0.04" thick skin panel that panel has a 74" radius and is 80" long. The panel is reinforced with 6 stringers symmetrically spaced at 9.6". The stringers are 0.032" thick. The skin and the stringers are made of 2024-T3 Aluminum. The Young modulus and the Poisson ratio of 2024-T3 Aluminum are $E = 10.5 \cdot 10^3$ ksi and $\nu = 0.33$ [3-3]. Symmetry constraints are applied at the panel edges. A uniform 0.0185" axial displacement applied at the panel forward edge simulates a $e_a = 0.0185/80 = 231 \mu\epsilon$ axial strain. The resulting axial stress in the skin and the stringers is $s_a = Ee_a = 2.43$ ksi as shown in Figure 3-11. A combination of this uniform axial strain with 8.6 psi pressure load results in a stress increase in the skin. The skin stress becomes

$s_a = Ee_a + \nu s_h = 2.43 + 0.33 \cdot 15.9 = 2.43 + 5.25 = 7.68$ ksi as shown in Figure 3-12. The stress redistribution is less straightforward if the axial load is applied instead of the uniform axial displacement to simulate a uniform stress state for panel in the absence of pressure load. A 234 lb/in axial load to the skin and a 187 lb/in axial load to the stringers applied at the panel forward and aft edges result in a 5.85 ksi uniform axial stress. The corresponding finite element contour plot is shown in Figure 3-13. If 8.6 psi pressure only is applied, the skin axial stress becomes 2.12 ksi as shown in Figure 3-14. A linear superposition of the tension and the pressure loading cases results in a 7.97 ksi axial stress in the skin.

SHEET	3-4	NO.	4-087051-20
TOTAL	3-38		
ISSUE DATE	12/21/04		

The finite element analysis predicts a 7.98 ksi axial stress in the skin for the combined loading as shown in Figure 3-15. As the applied axial load is increased, the linear superposition becomes less accurate. For example, if the axial load is increased to a 11.7 ksi, the finite element analysis predicts a 14.8 ksi axial stress in the skin instead of the expected $11.7 + 2.12 = 13.8$ ksi as shown in Figure 3-16.

A linear superposition of the stiffened axial stress due to pressure loading and the axial stress due to bending predicts a lower bound, and the stress stiffening for the pressure loading assumed for any additional axial loading predicts an upper bound to the skin axial stress due to the combined loading. In the example considered above, the lower and the upper bounds to the combined axial stress are $7.97 + 5.85 = 13.8$ ksi and $7.97/5.85 \cdot 11.7 = 15.7$ ksi.

The intermediate finite element model of the unmodified FT2 panel structure predicts a 7.53 ksi skin axial stress for the 8.6 psi pressure loading combined with the axial loading due to pressure per the existing beam-type solution, as well as for the 8.6 psi pressure loading combined with an equivalent 0.0185" edge axial displacement, as shown in Figures 3-9, 3-10, 3-17 and 3-18. An average value for the unstiffened axial stress at stringers 2-7 is 5.83 ksi per the existing beam-type solution. Therefore, the axial stress stiffening coefficient is $7.53 / 5.83 = 1.29$. The intermediate model predicts a 8.43 ksi axial stress due to a $1.15 \cdot 8.6 = 9.89$ psi pressure loading. The corresponding stress stiffening coefficient is 1.26. The estimated lower and the upper bounds to the skin axial stress due to the combined 8.6 psi pressure and 1g flight, 8.6 psi and 2.5g flight, and 9.89 psi and 1g flight conditions are shown in Tables 3-2 and 3-3. Hoop membrane stresses of 13.7 ksi and 14.3 ksi, and hoop surface stresses of 15.7 ksi and 16.5 ksi are predicted for 8.6 psi and 9.89 psi pressure conditions, respectively.

Loading Condition	Skin Axial Stress Lower Bound, ksi
-------------------	------------------------------------

SHEET	3-5	NO. 4-087051-20
TOTAL	3-38	
ISSUE DATE		12/21/04

	STA 640	STA 700	Average
8.6 psi and 1g	13.7	15.3	14.5
8.6 psi and 2.5g	22.8	27.0	24.9
9.89 psi and 1g	14.6	16.2	15.4

Table 3-2: Estimated lower bounds to the skin axial stress

Loading Condition	Skin Axial Stress Upper Bound, ksi		
	STA 640	STA 700	Average
8.6 psi and 1g	15.5	17.7	16.8
8.6 psi and 2.5g	27.6	33.1	30.4
9.89 psi and 1g	16.2	18.4	17.3

Table 3-3: Estimated upper bounds to the skin axial stress

The global model average axial stress results for the FT2 panel area are 13 ksi for the combined 8.6 psi pressure and 1g flight loading, 22 ksi for the combined 8.6 psi pressure and 2.5g flight loading, and 14 ksi for the combined 9.89 psi pressure and 1g flight loading cases. The average shear stress level in the FT2 panel area is 10% of the axial stress. The stress contour plots are shown in Figures 3-19 through 3-36. The global model predictions for the axial stresses are approximately 10% below the estimated lower bound values. An FT2 panel area model created on the same geometry as the fuselage global model, with a refined mesh of the same type elements as in the global model, and with the edge displacement boundary conditions mapped from the global model, predicts similar membrane stress values. A 25% weight correction factor is applied to the loads in the global model to match the estimated lower bound axial stress values. The corrected stress contour plots for the combined 8.6 psi and 1g flight loading are shown in Figures 3-37 through 3-42.

A stiffness model of the FT2 test panel was developed in order to predict FASTER loads. The model consists of linear shell elements with approximately 102,000 degrees of freedom. Uniform axial and hoop loads are applied to the skin through rigid links simulating the FASTER skin loading mechanisms [3-4]. The FASTER facility provides 6 frame, 7 skin hoop and 4 skin axial load actuators. The loader

SHEET	3-6	NO.	4-087051-20
TOTAL	3-38		
ISSUE DATE	12/21/04		

configurations are shown in Figures 3-43 through 3-45. There are 4 load attachment points per skin actuator resulting in 28 points at each longitudinal edge, and 16 points at each circumferential edge of the panel. In the finite element model, the load attachment points are constrained through independent links as shown in Figure 3-46. For each link, the rotational DOF are free at the end that represents the fulcrum point to allow for the skin displacements. Uniform hoop loads are applied to the frame ends. The frames are constrained through steel radial links represented by beam elements with a 0.5" by 1" rectangular cross section shown in Figure 3-47. One rotational DOF is unconstrained at both ends of each radial link.

The skin hoop load, frame load, and skin axial load resulting in the skin 13.7 ksi hoop membrane stress and 14.3 ksi hoop surface stress for 8.6 psi pressure, and the skin 15.7 ksi hoop membrane stress and 16.5 ksi hoop surface stress for 9.89 psi pressure conditions, and the estimated lower bound axial stresses in the critical test area are listed in Table 3-4.

Loading Condition	Load per Frame, lbs	Skin Total Hoop Load, lbs	Skin Total Axial Load, lbs
8.6 psi	1,465	64,368	21,384
8.6 psi and 1g	1,465	64,368	55,000
8.6 psi and 2.5g	1,465	64,368	105,424
9.89 psi and 1g	1,685	74,023	58,208

Table 3-4: Estimated lower bound axial stresses in the critical test area

The contour plots for the axial and hoop stresses due to 8.6 psi pressure, and combined 8.6 psi pressure and 1g flight, 8.6 psi pressure and 2.5g flight, and 9.89 psi pressure and 1g flight loading conditions are shown in Figures 3-48 through 3-55. It is worth noting that although the axial stress due to fatigue loading exceeds the hoop stress level, an estimated 40% local skin bending stress concentration at the stringer 4 lap joint will result in earlier longitudinal crack initiation.

The actuator loads for the fatigue and limit load test conditions are listed in Table 3-5.

SHEET	3-7	NO.	4-087051-20
TOTAL	3-38		
ISSUE DATE	12/21/04		

Loading Condition	Load per Frame Actuator, lbs	Load per Skin Hoop Actuator, lbs	Load per Skin Axial Actuator, lbs
8.6 psi and 1.25g	1,470	9,200	15,850
9.89 psi and 1g	1,690	10,570	14,550

Table 3- Actuator loads for the fatigue and limit load test conditions 5:

The actuator loads for the revised fatigue and residual strength loading conditions are listed in Table 3-6.

Loading Condition	Load per Frame Actuator, lbs	Load per Skin Hoop Actuator, lbs	Load per Skin Axial Actuator, lbs
8.9 psi and 1.25g	1,530	9,510	16,220
10.24 psi and 1g	1,800	10,910	14,930

Table 3-6: Actuator loads for the revised fatigue and residual strength loading conditions

An initial strain survey has been conducted at 5 psi pressure and 5340 lb skin hoop, 860 lb frame, and 2590 lb skin longitudinal actuator loads. A 0.1212 frame to total hoop load ratio and a 115" pressurization length were used to calculate the frame and skin hoop actuator loads. The loads applied to the test panel at the FASTER facility resulted in frame radial link compression. The finite element model predicted tension in the frame radial links. To resolve this discrepancy, the boundary conditions in the finite element model were refined as follows. The local cylindrical coordinate systems were constructed for the skin loaders. These coordinate systems had origins at the fulcrum point locations. The skin loaders were simulated by straight rigid elements with the displacement constraints applied in the local coordinate systems at the ends not attached to the skin as shown in Figure 3-56. One translational DOF corresponding to the load direction was unconstrained for each link. Two rotational DOF were unconstrained for the skin hoop links, and all rotational DOF were unconstrained for the skin longitudinal links. Each frame had a simulated hoop loading mechanism, in addition to an independent radial link constraint as shown in Figure 3-57. The frame hoop loaders were represented by straight rigid elements with the displacement constraints applied in the local coordinate systems at the ends not attached to the frames. One rotational and one translational DOF corresponding to the load

ENGINEERING DEPARTMENT

SHEET	3-8	NO.	4-087051-20
TOTAL	3-38		
ISSUE DATE		12/21/04	

direction were unconstrained for each frame hoop link. Also, the frame and skin loads were applied in the loader local coordinate systems to allow the loads to follow the links during the panel loading. The model with the refined boundary conditions matched the radial link compression measured during the strain survey test. Although the finite element model with the refined boundary conditions predicted less frame bending compared to the original model, there was no significant difference in the skin stress predictions at the strain survey load level.

SHEET	3-9	NO.	4-087051-20
TOTAL	3-38		
ISSUE DATE	12/21/04		

References

- [3-1] Makeev, A. and Carter, A., "Bending Stress Concentration At Stiffness Discontinuities in Typical Fuselage Skins," *Proceedings of the 6th Joint FAA/DOD/NASA Conference on Aging Aircraft*, San Francisco, California, September 16-19, 2002.
- [3-2] Pratte, D., "Federal Aviation Administration Average Weight Survey," *Air Midwest Flight 5481 Crash Public Hearing*, May 20, 2003.
- [3-3] MIL-HDBK-5H, *Metallic Materials and Elements for Aerospace Vehicle Structures*, U.S. Government Printing Office, Washington, DC, 1998.
- [3-4] J. Bakuskas, "Full-Scale Testing and Analysis of Fuselage Structure Containing Multiple Cracks," *DOT/FAA/AR-01/46*, July 2002.

SHEET	3-10	NO.	4-087051-20
TOTAL	3-38		
ISSUE DATE		12/21/04	

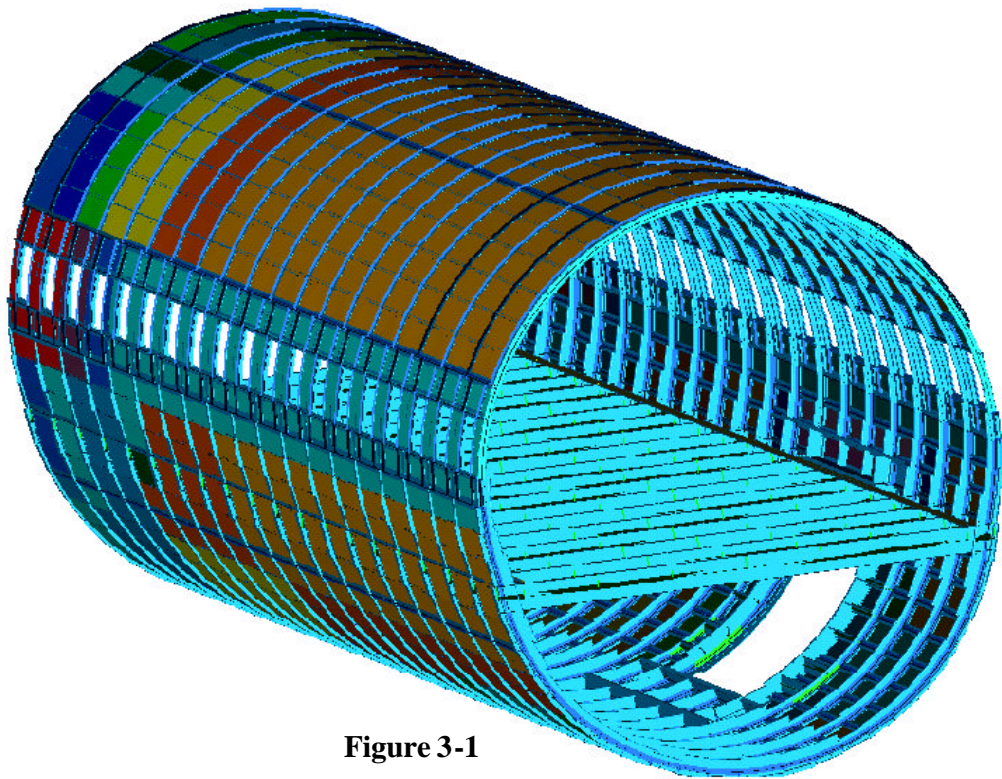


Figure 3-1

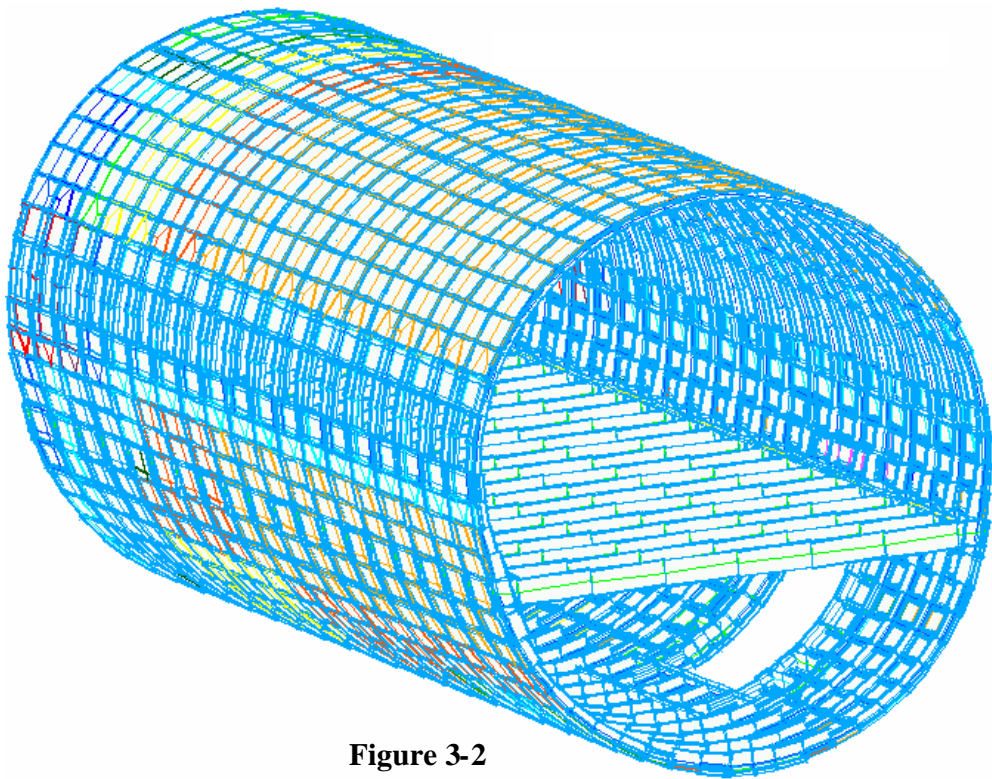


Figure 3-2

SHEET	3-11	NO.	4-087051-20
TOTAL	3-38		
ISSUE DATE	12/21/04		

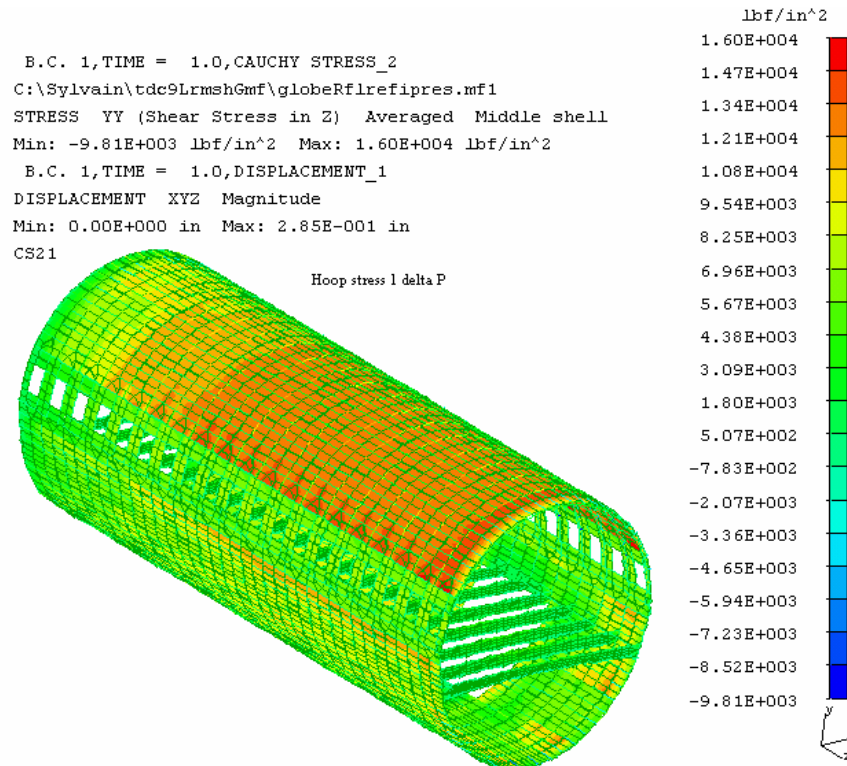


Figure 3-3

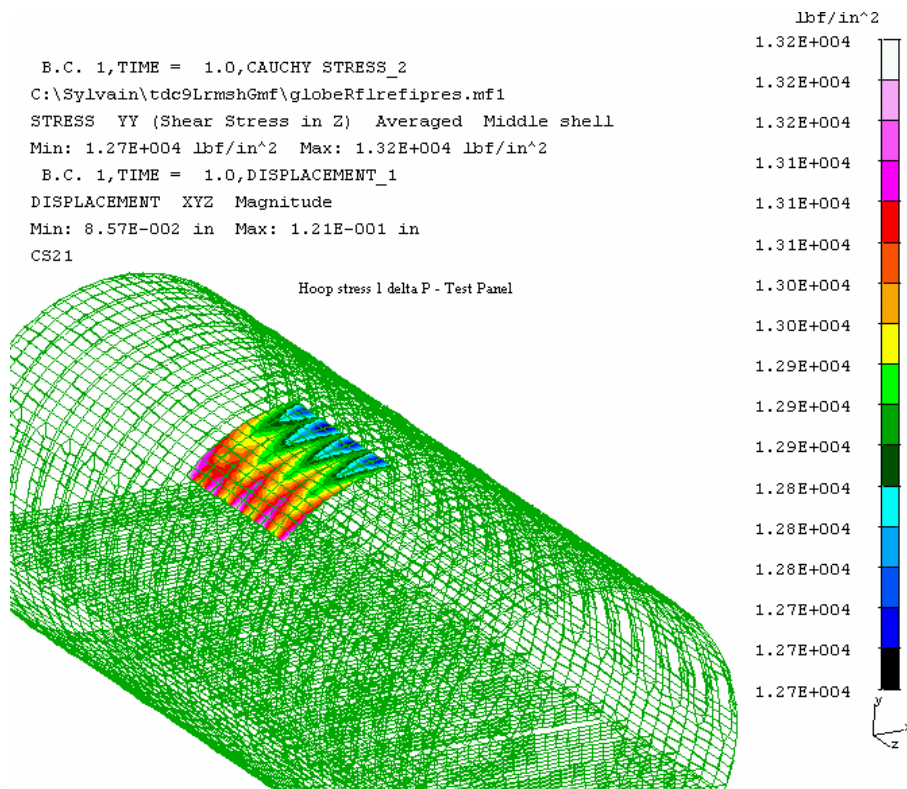


Figure 3-4

SHEET	3-12	NO.	4-087051-20
TOTAL	3-38		
ISSUE DATE	12/21/04		

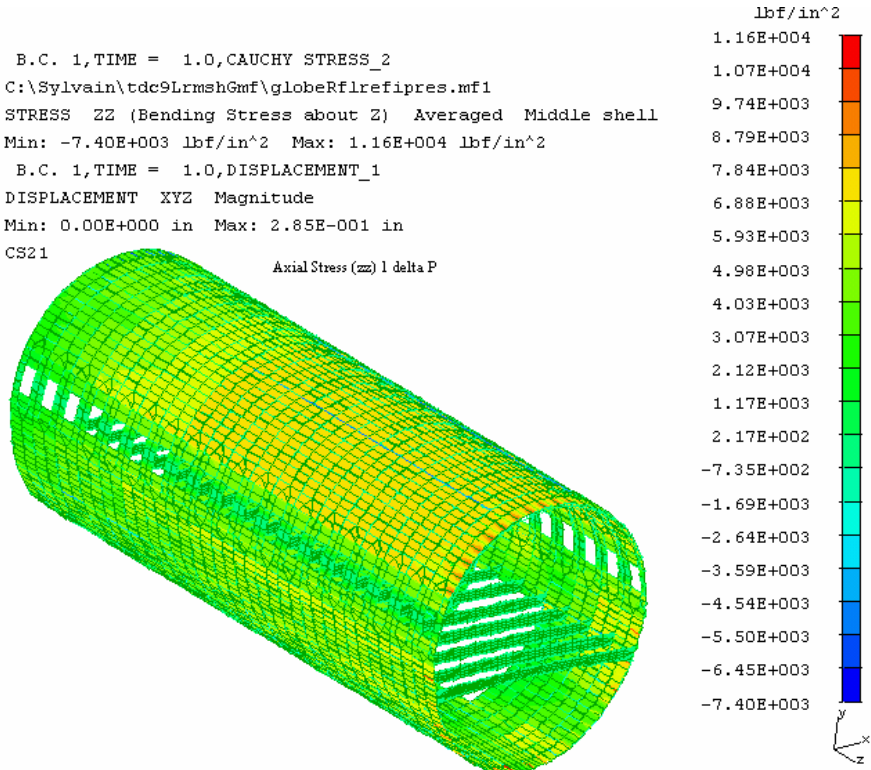


Figure 3-5

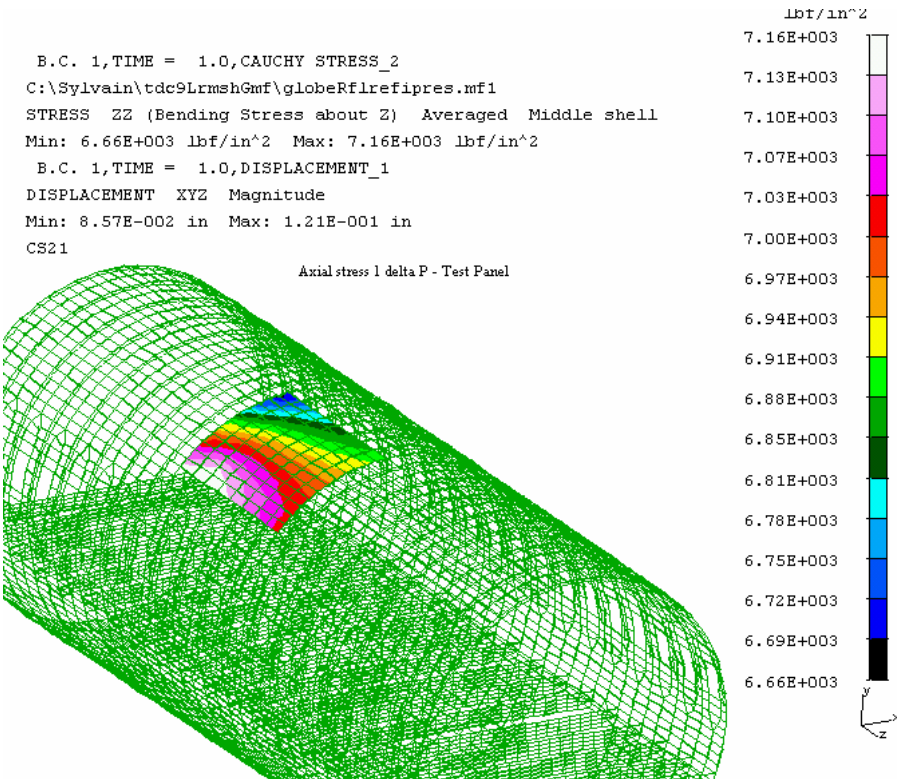


Figure 3-6

SHEET	3-13	NO.	4-087051-20
TOTAL	3-38		
ISSUE DATE	12/21/04		

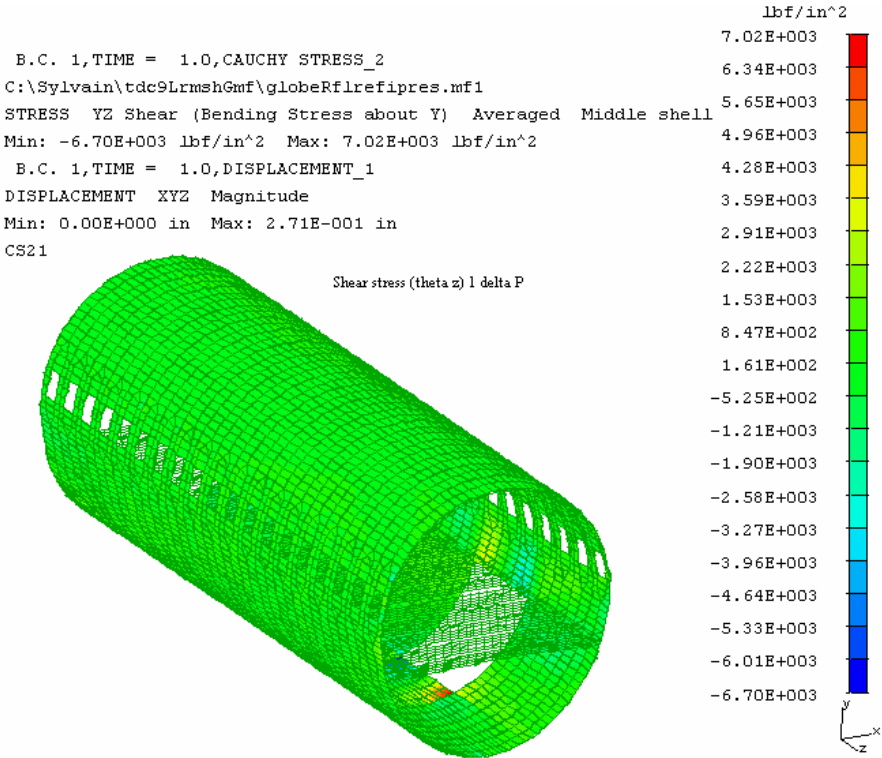


Figure 3-7

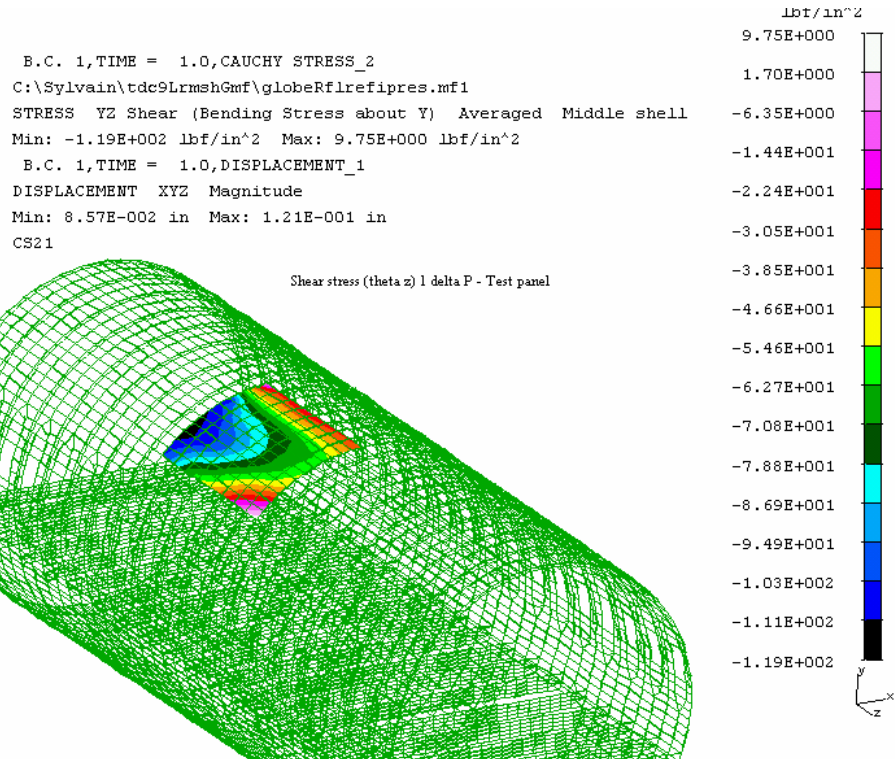


Figure 3-8

SHEET	3-14	NO.	4-087051-20
TOTAL	3-38		
ISSUE DATE	12/21/04		

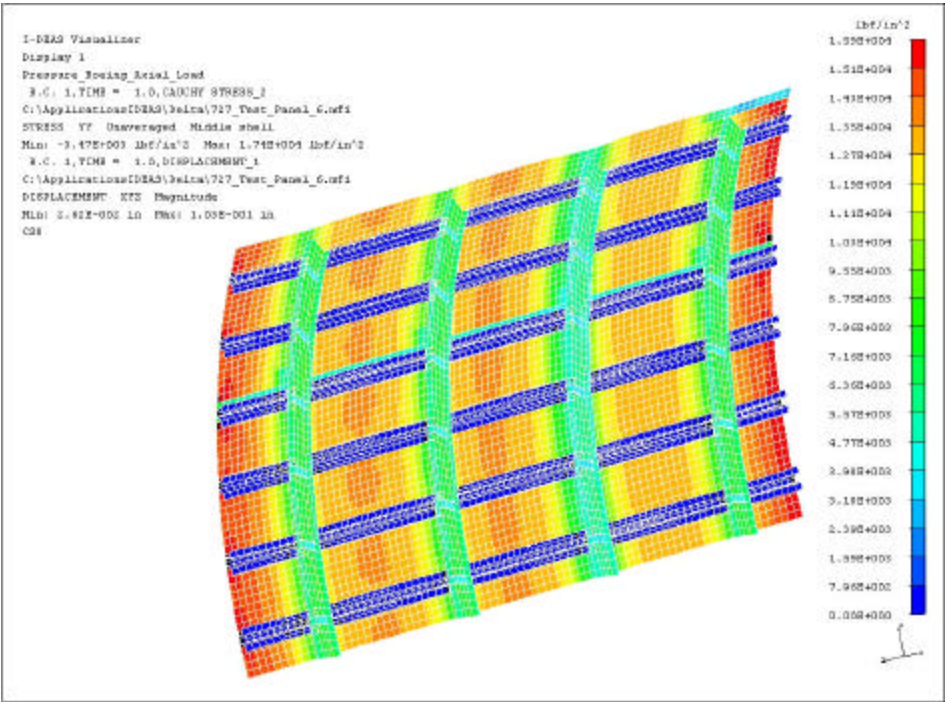


Figure 3-9

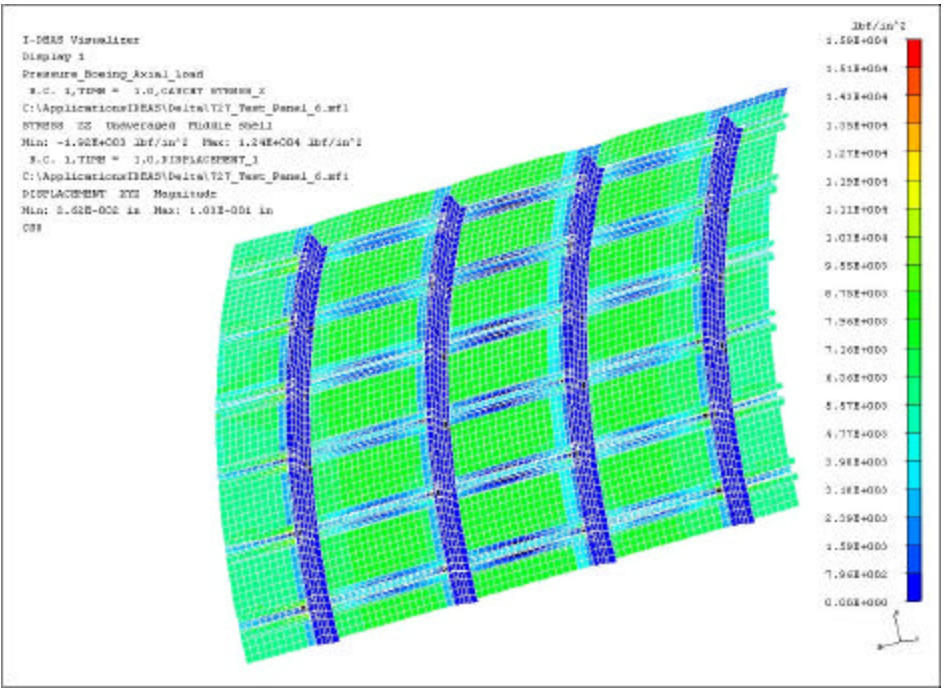


Figure 3-10

SHEET	3-15	NO.	4-087051-20
TOTAL	3-38		
ISSUE DATE	12/21/04		

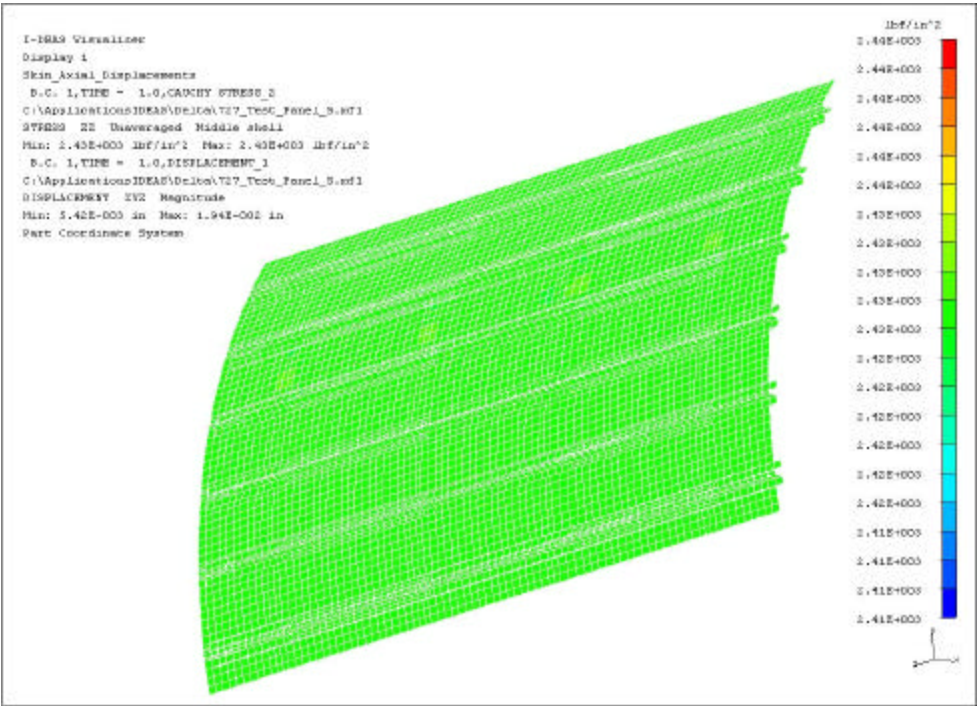


Figure 3-11

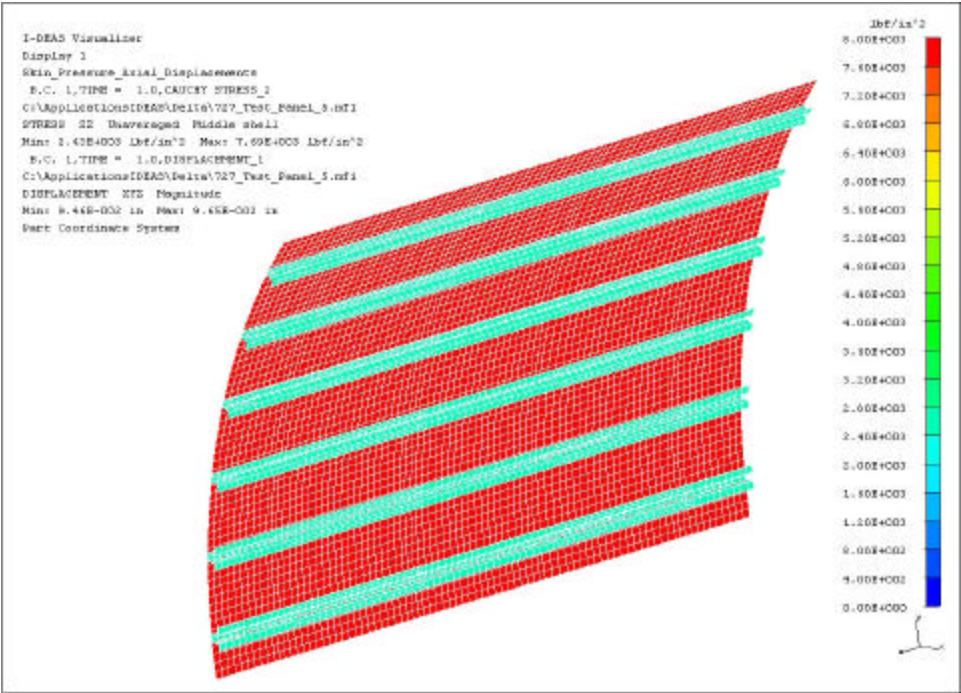


Figure 3-12

SHEET	3-16	NO.	4-087051-20
TOTAL	3-38		
ISSUE DATE	12/21/04		

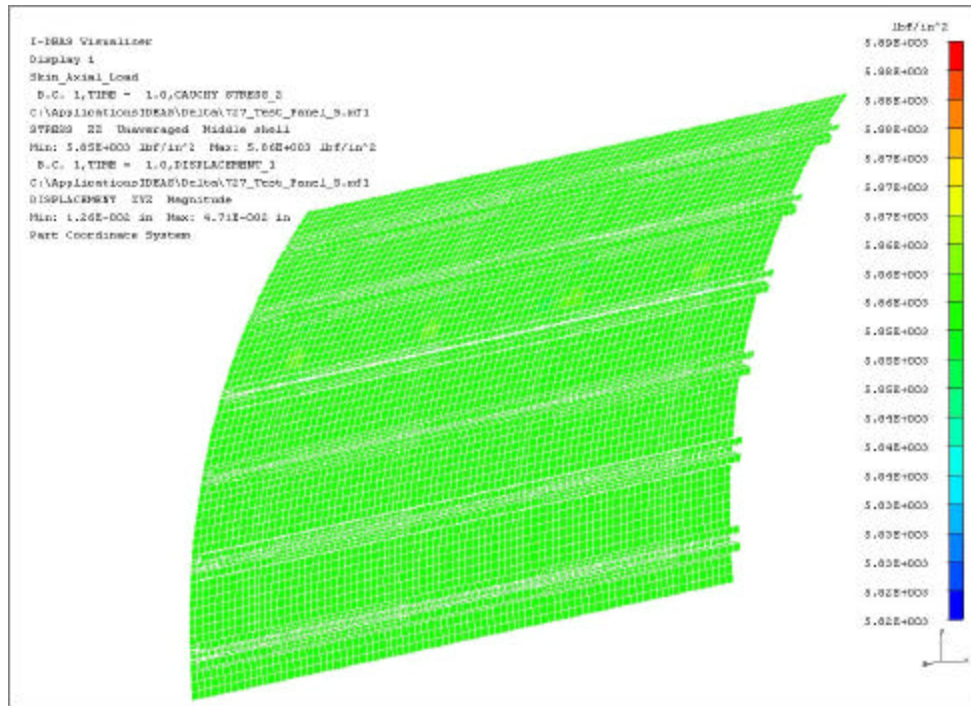


Figure 3-13

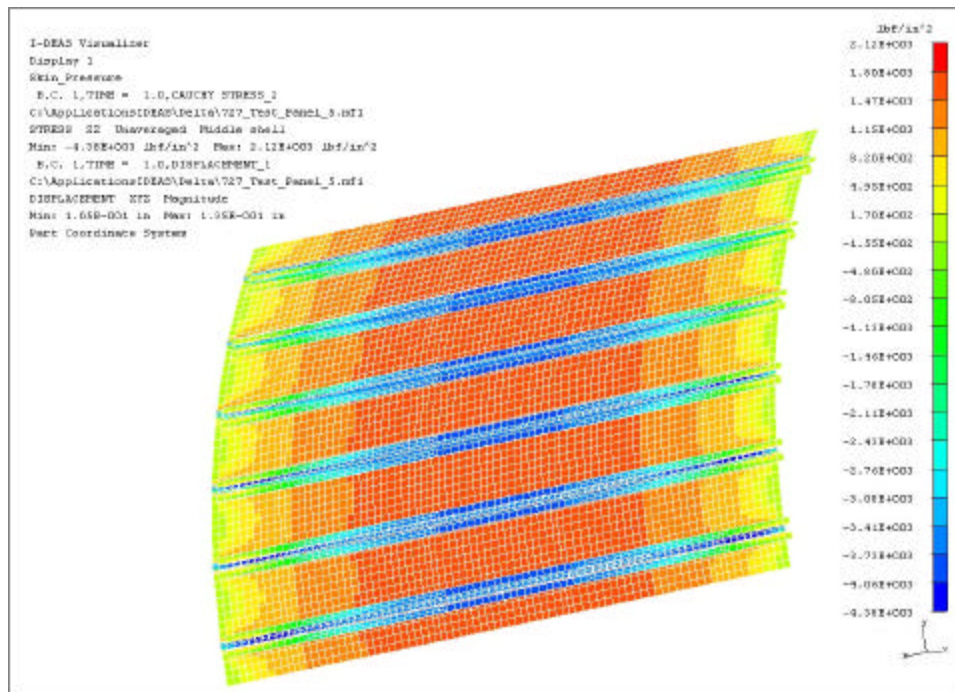


Figure 3-14

SHEET	3-17	NO.	4-087051-20
TOTAL	3-38		
ISSUE DATE	12/21/04		

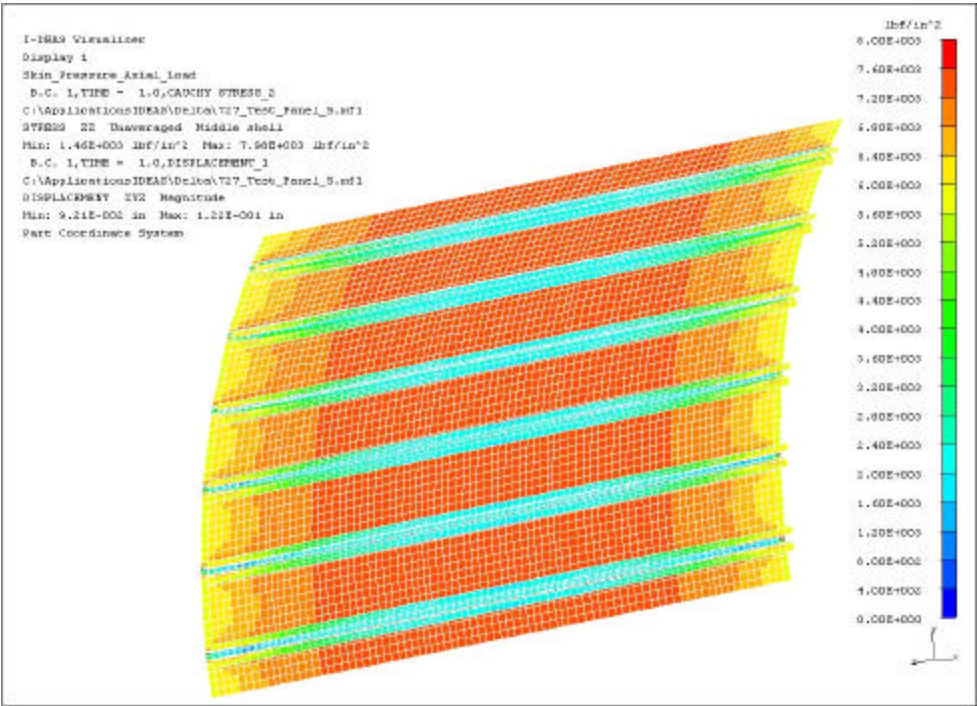


Figure 3-15

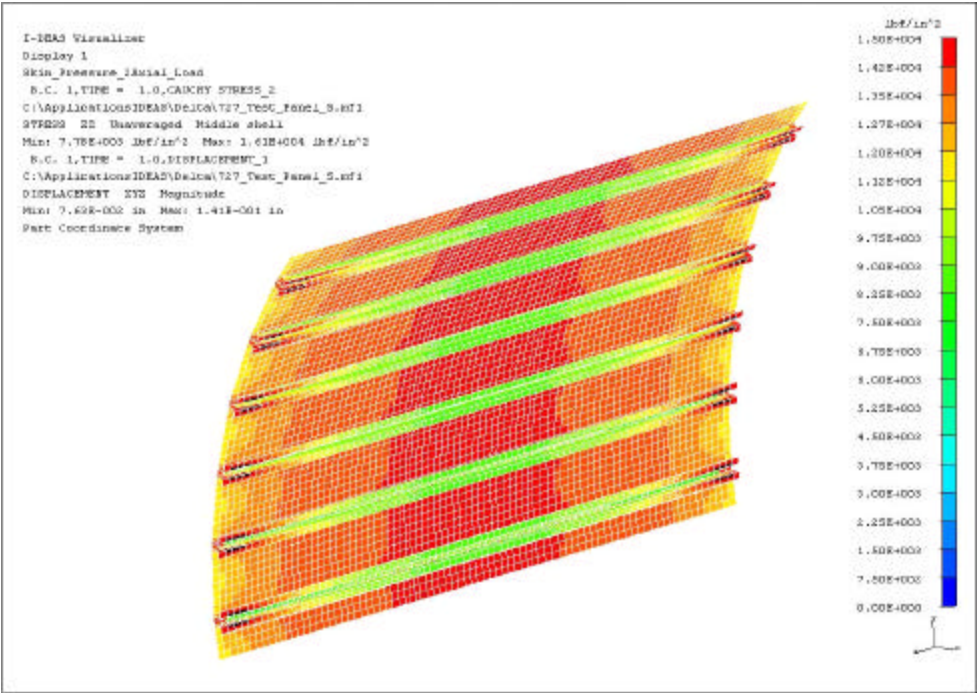


Figure 3-16

SHEET	3-18	NO.	4-087051-20
TOTAL	3-38		
ISSUE DATE	12/21/04		

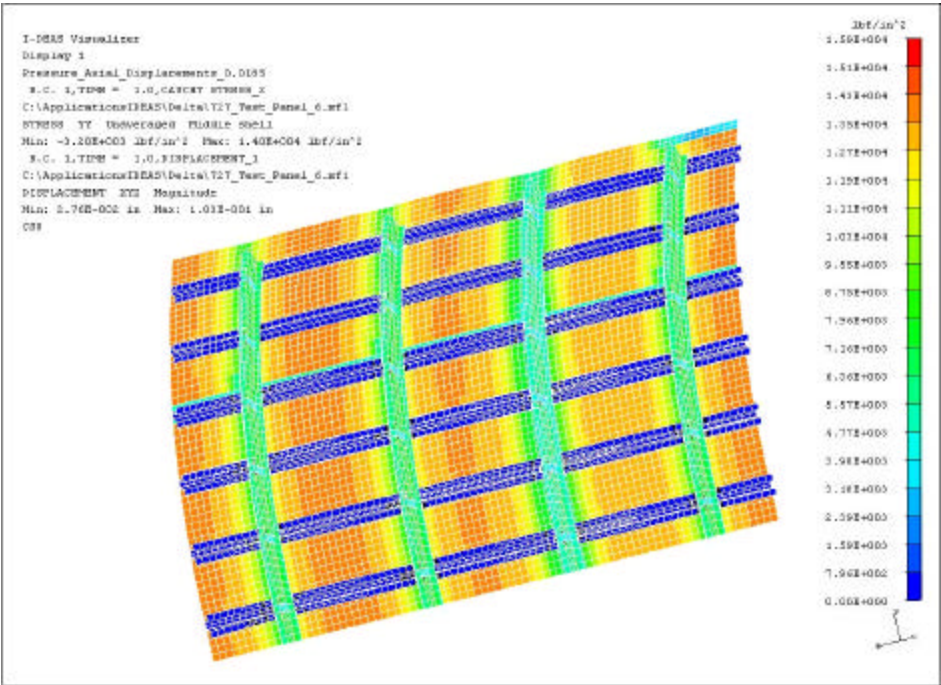


Figure 3-17

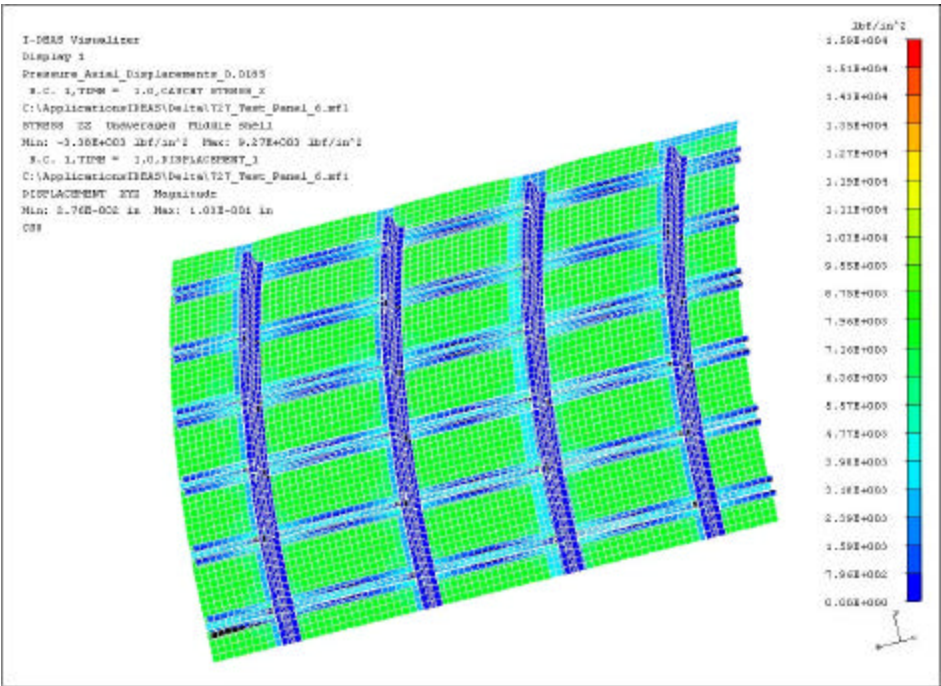


Figure 3-18

SHEET	3-19	NO.	4-087051-20
TOTAL	3-38		
ISSUE DATE	12/21/04		

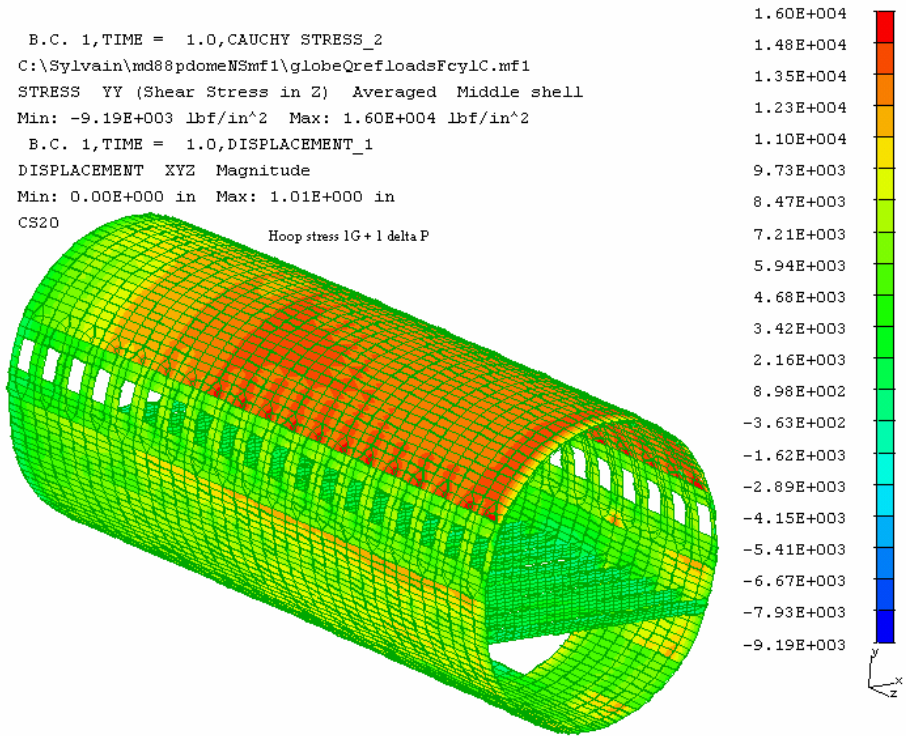


Figure 3-19

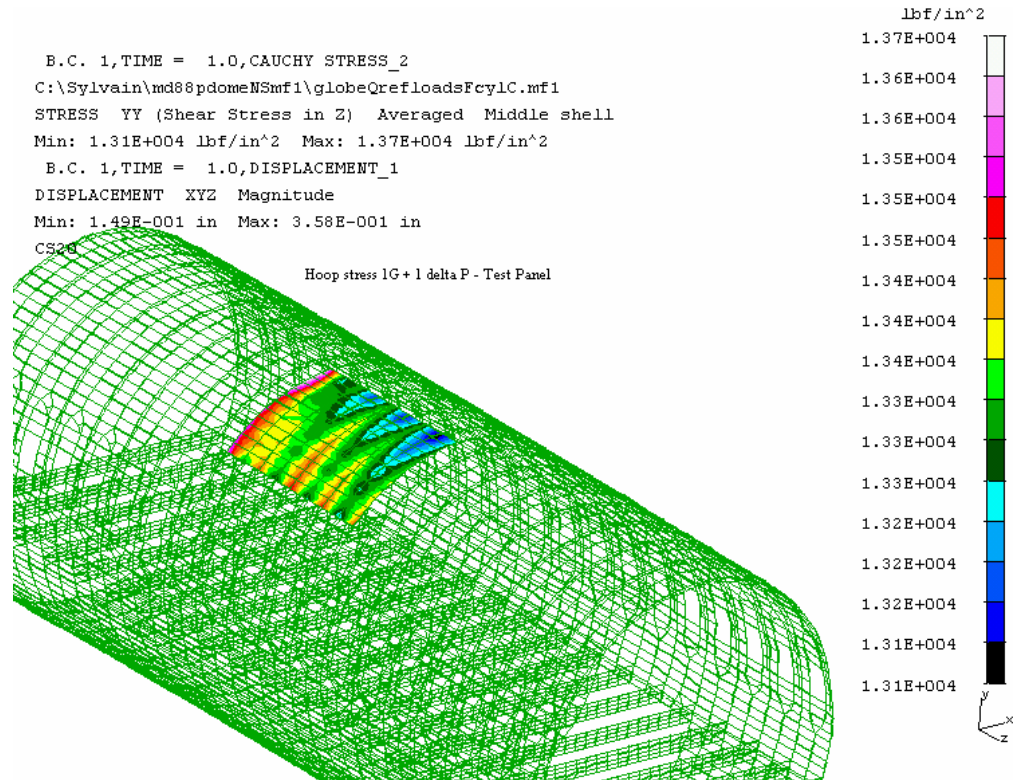


Figure 3-20

SHEET	3-20	NO.	4-087051-20
TOTAL	3-38		
ISSUE DATE	12/21/04		

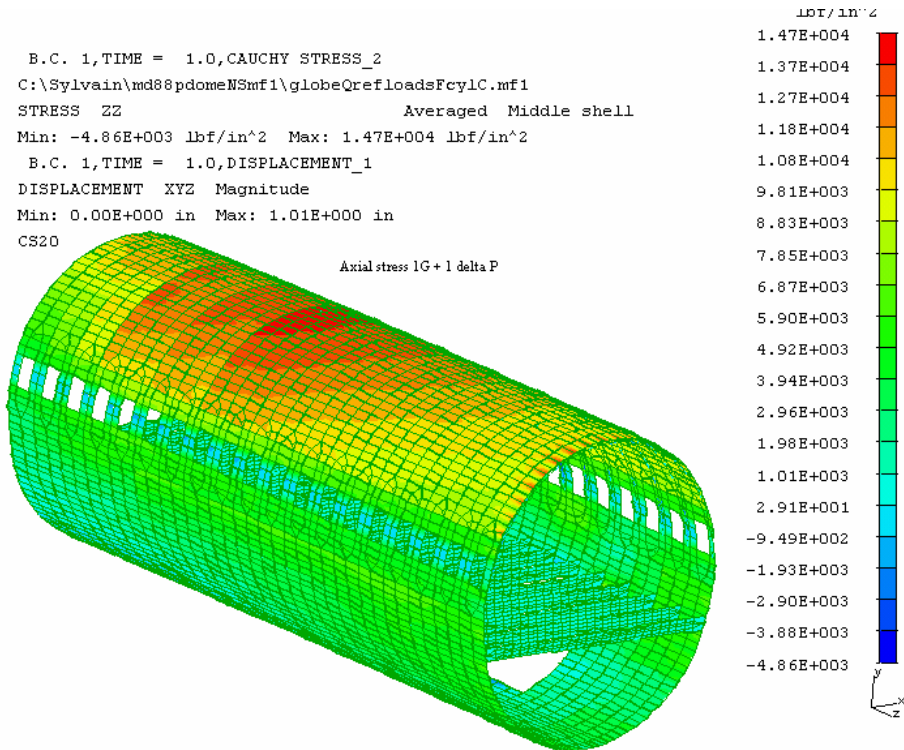


Figure 3-21

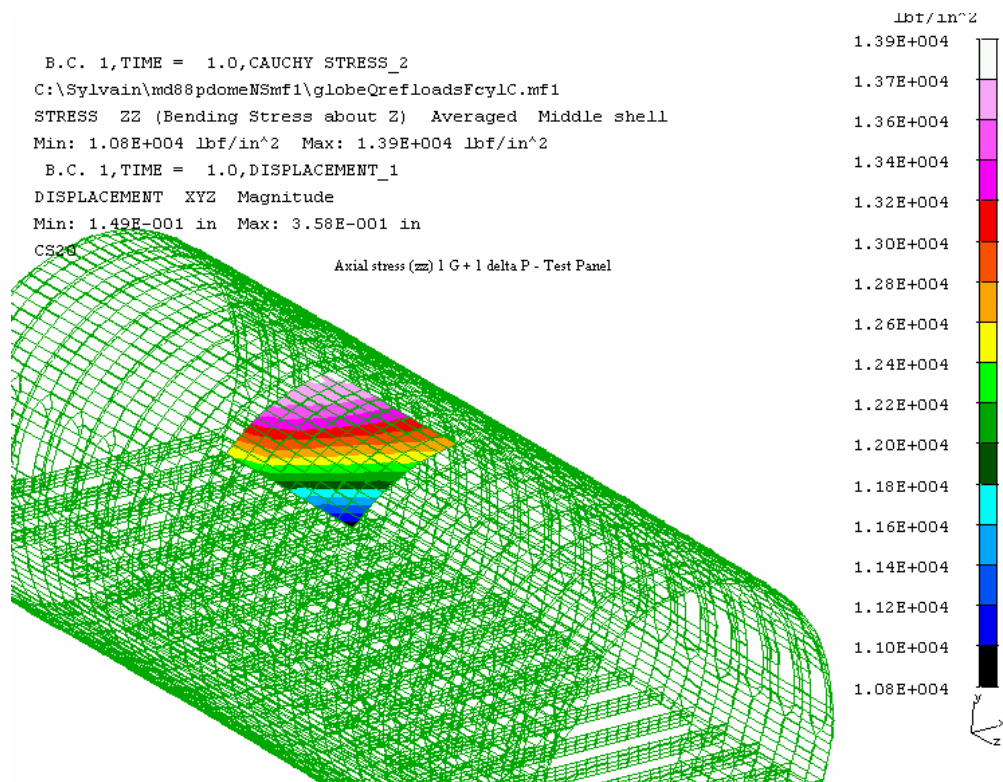


Figure 3-22

SHEET	3-21	NO.	4-087051-20
TOTAL	3-38		
ISSUE DATE	12/21/04		

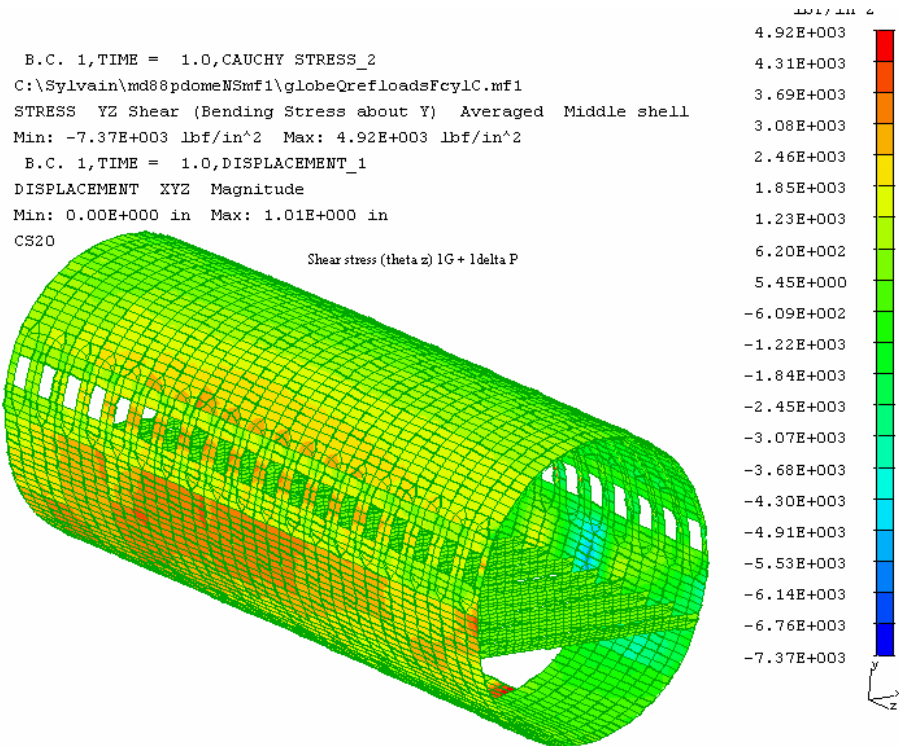


Figure 3-23

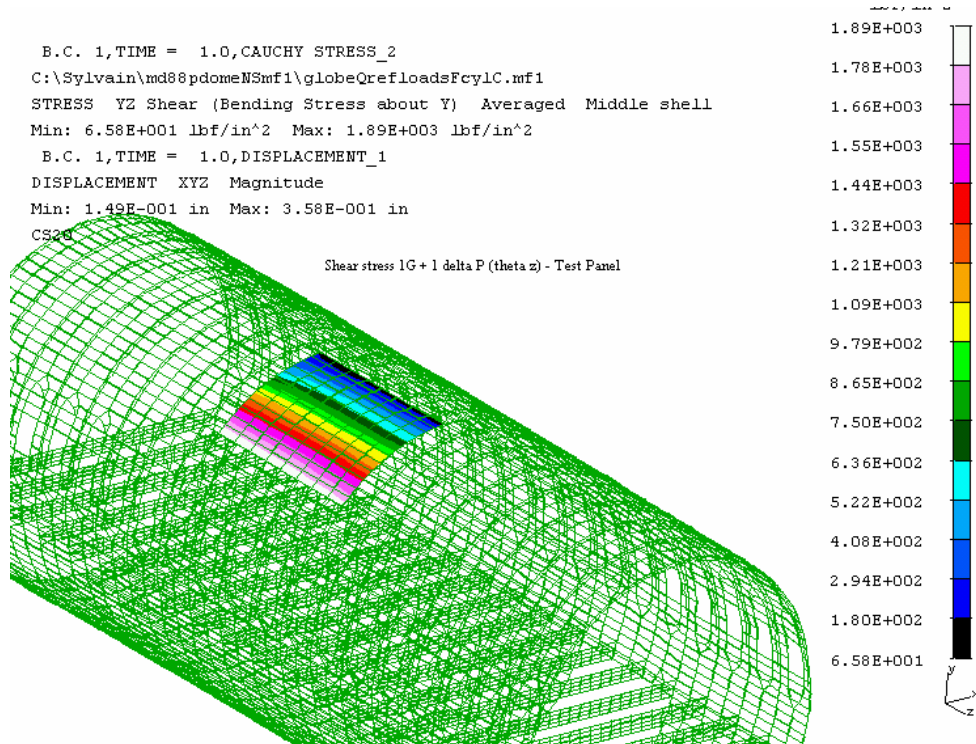


Figure 3-24

SHEET	3-22	NO.	4-087051-20
TOTAL	3-38		
ISSUE DATE	12/21/04		

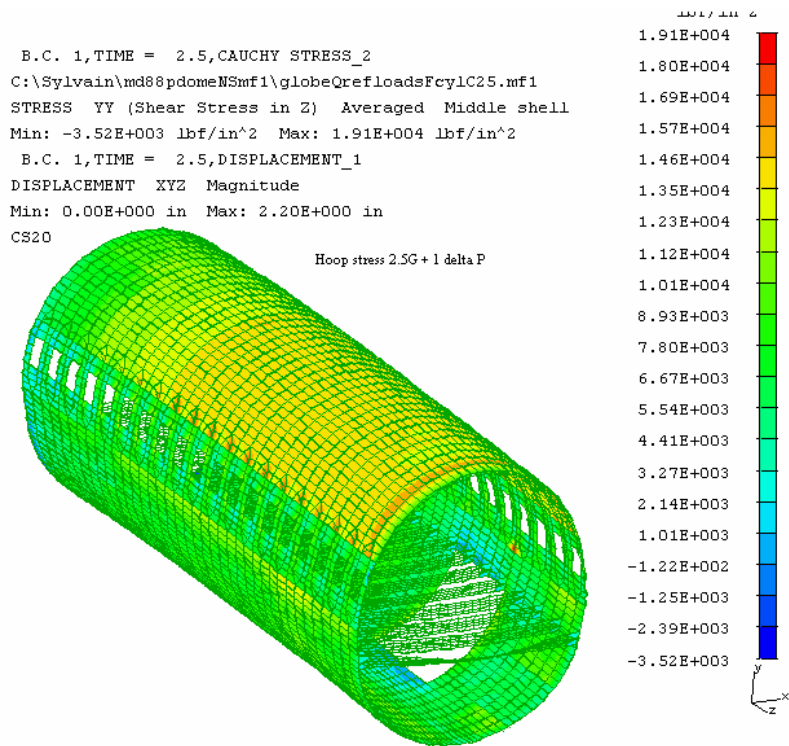


Figure 3-25

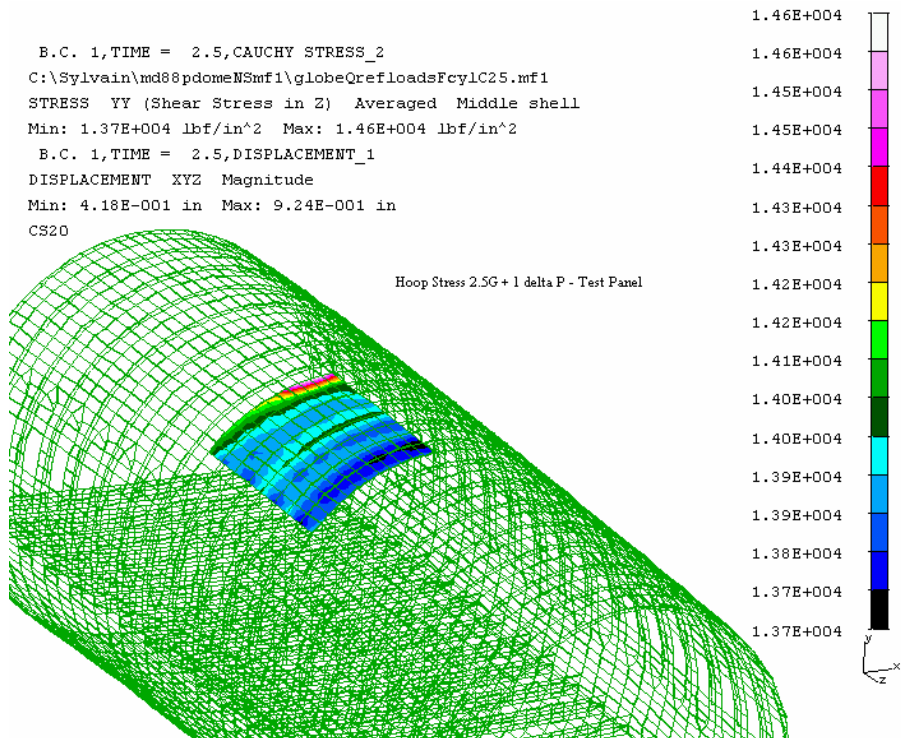


Figure 3-26

SHEET	3-23	NO.	4-087051-20
TOTAL	3-38		
ISSUE DATE	12/21/04		

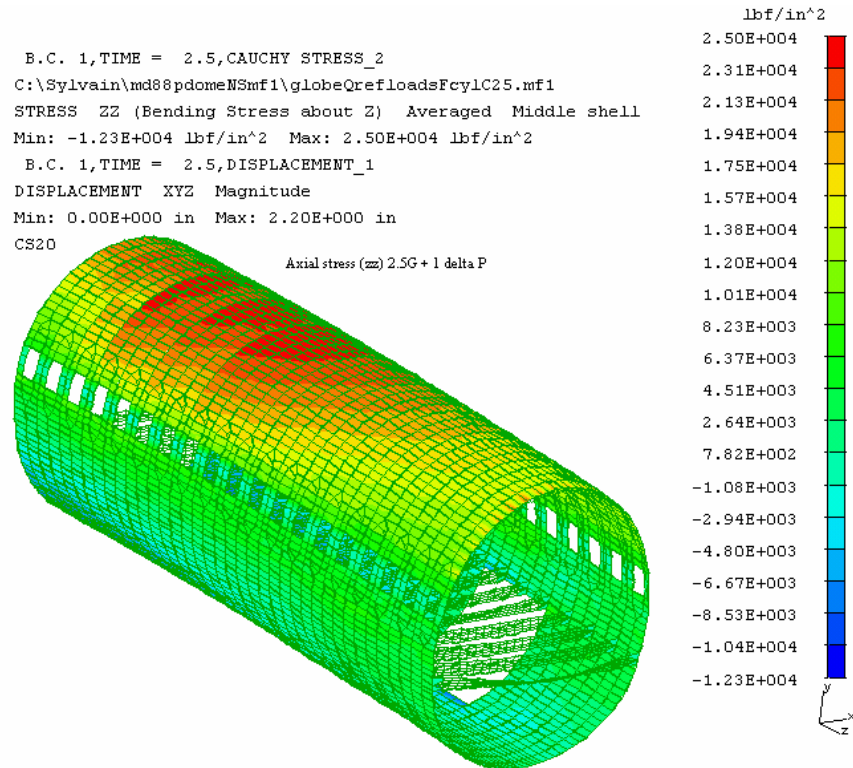


Figure 3-27

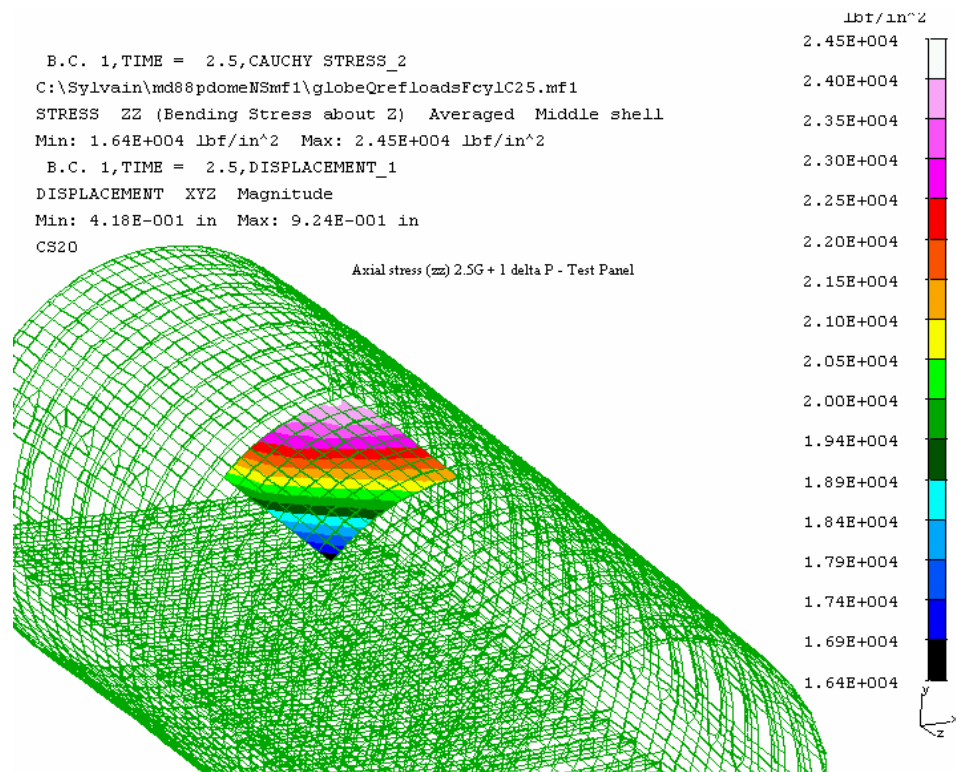


Figure 3-28

SHEET	3-24	NO.	4-087051-20
TOTAL	3-38		
ISSUE DATE	12/21/04		

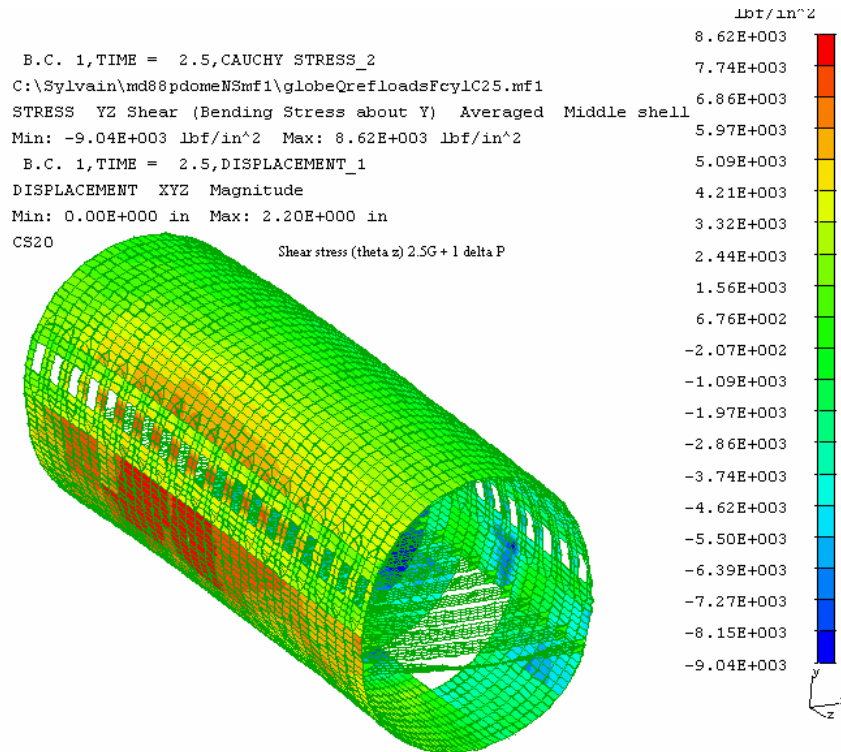


Figure 3-29

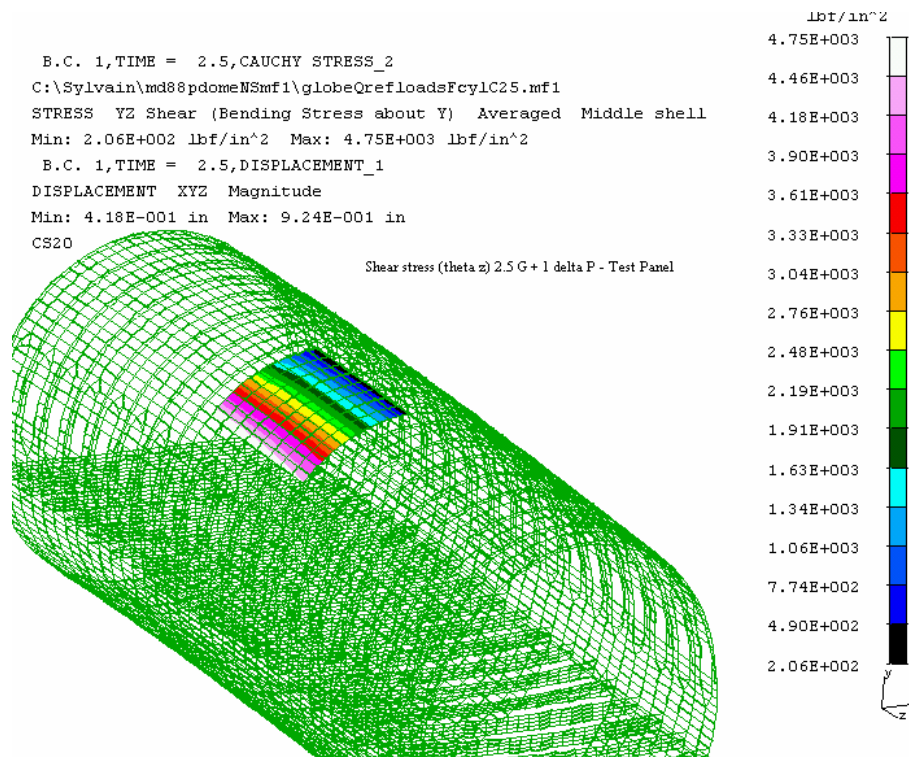


Figure 3-30

SHEET	3-25	NO.	4-087051-20
TOTAL	3-38		
ISSUE DATE	12/21/04		

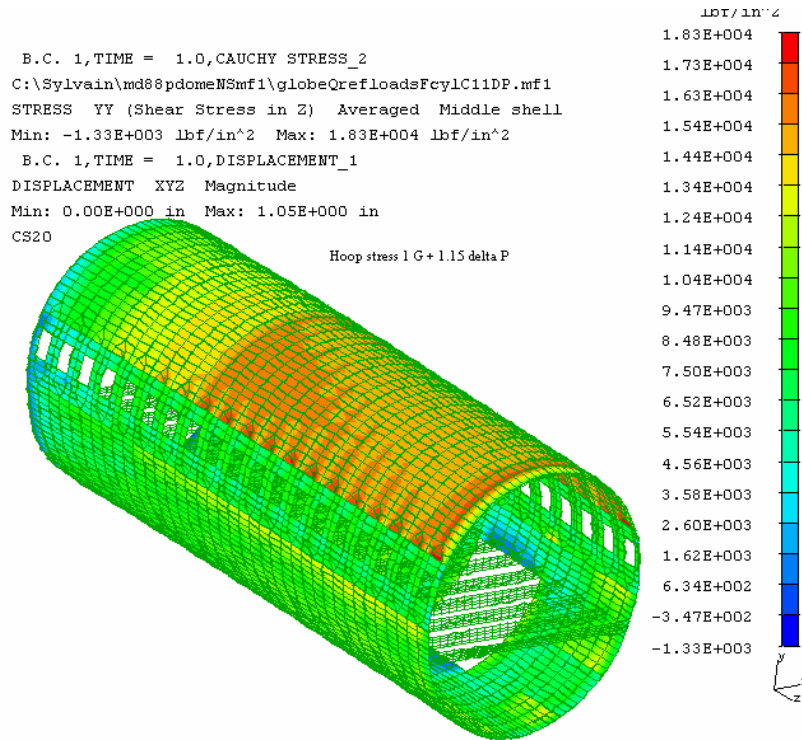


Figure 3-31

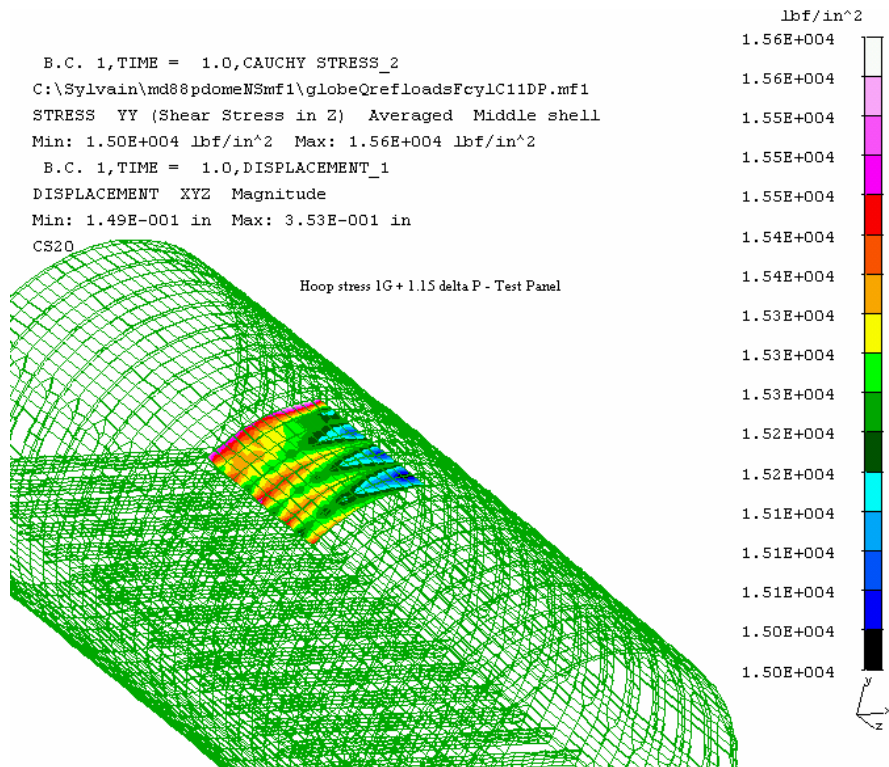


Figure 3-32

SHEET	3-26	NO.	4-087051-20
TOTAL	3-38		
ISSUE DATE	12/21/04		

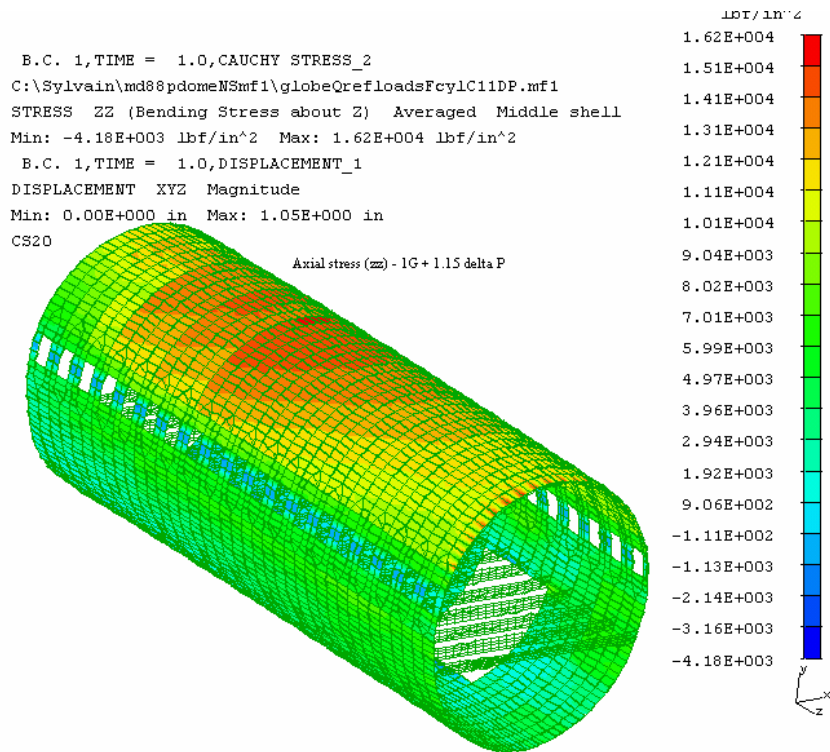


Figure 3-33

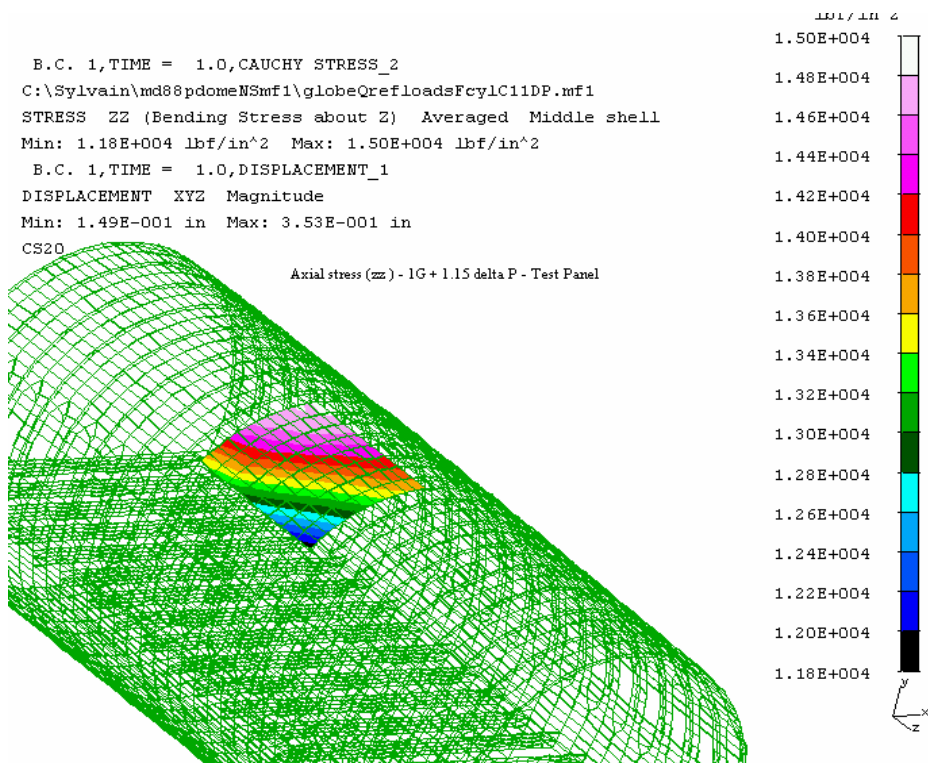


Figure 3-34

SHEET	3-27	NO.	4-087051-20
TOTAL	3-38		
ISSUE DATE	12/21/04		

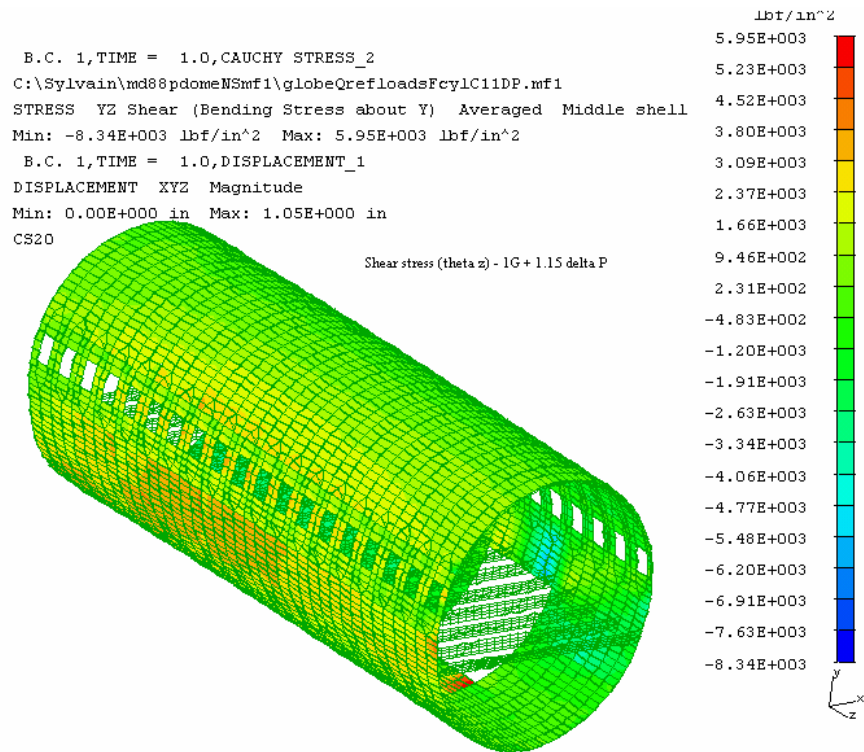


Figure 3-35

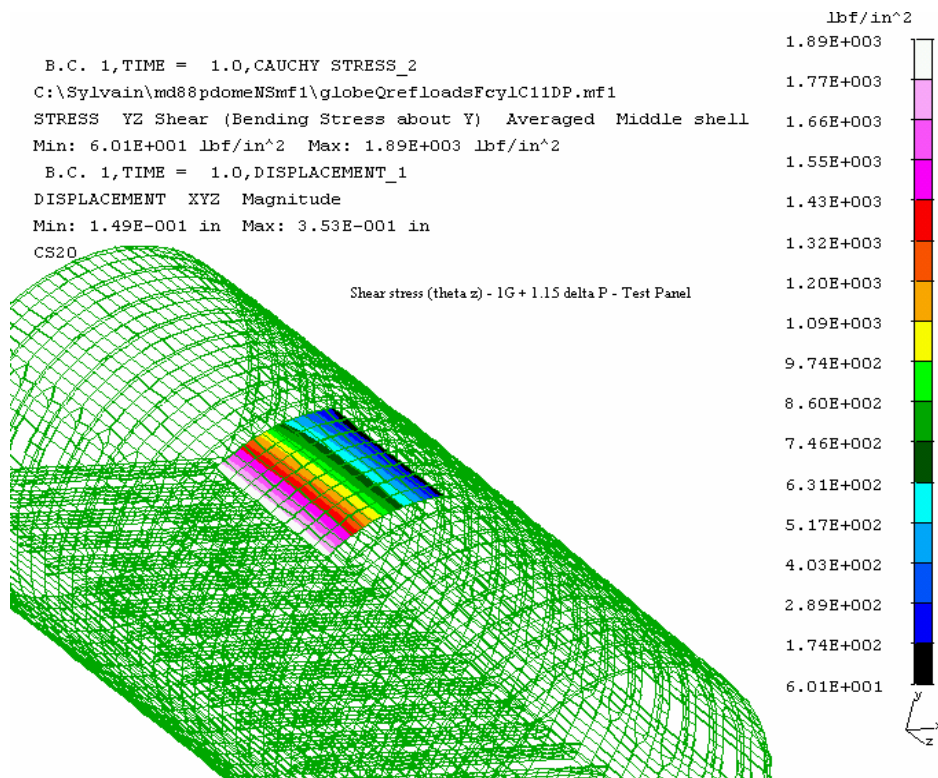


Figure 3-36

SHEET	3-28	NO.	4-087051-20
TOTAL	3-38		
ISSUE DATE	12/21/04		

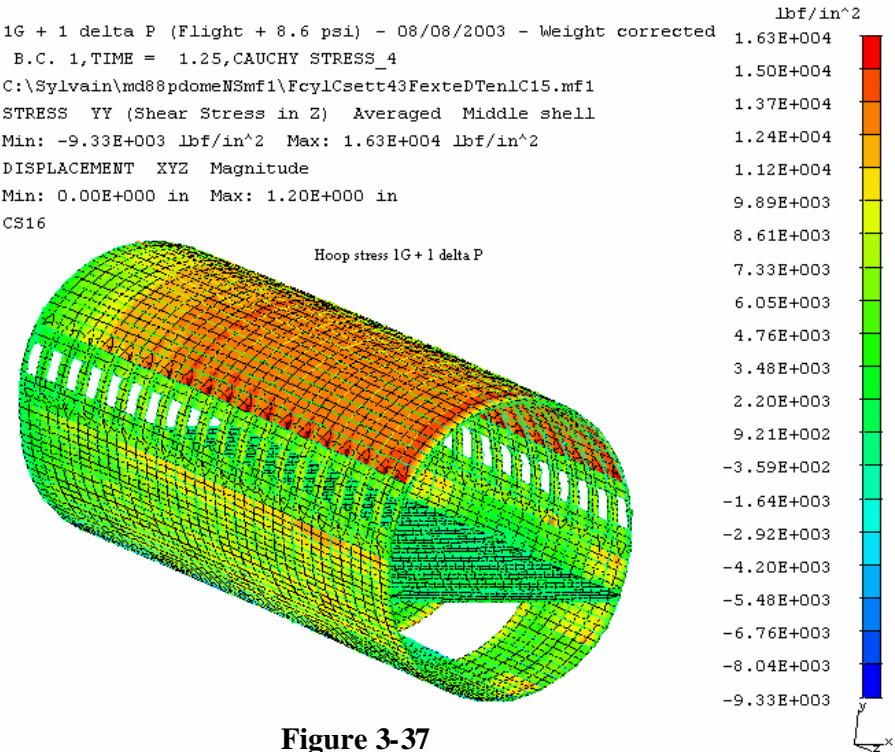


Figure 3-37

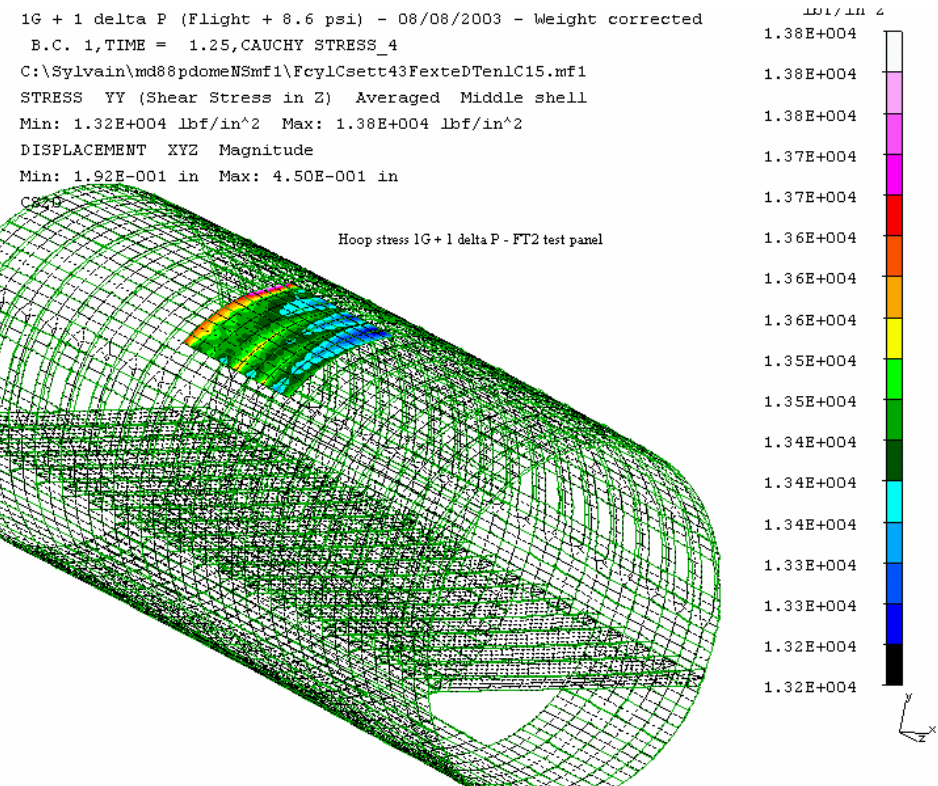
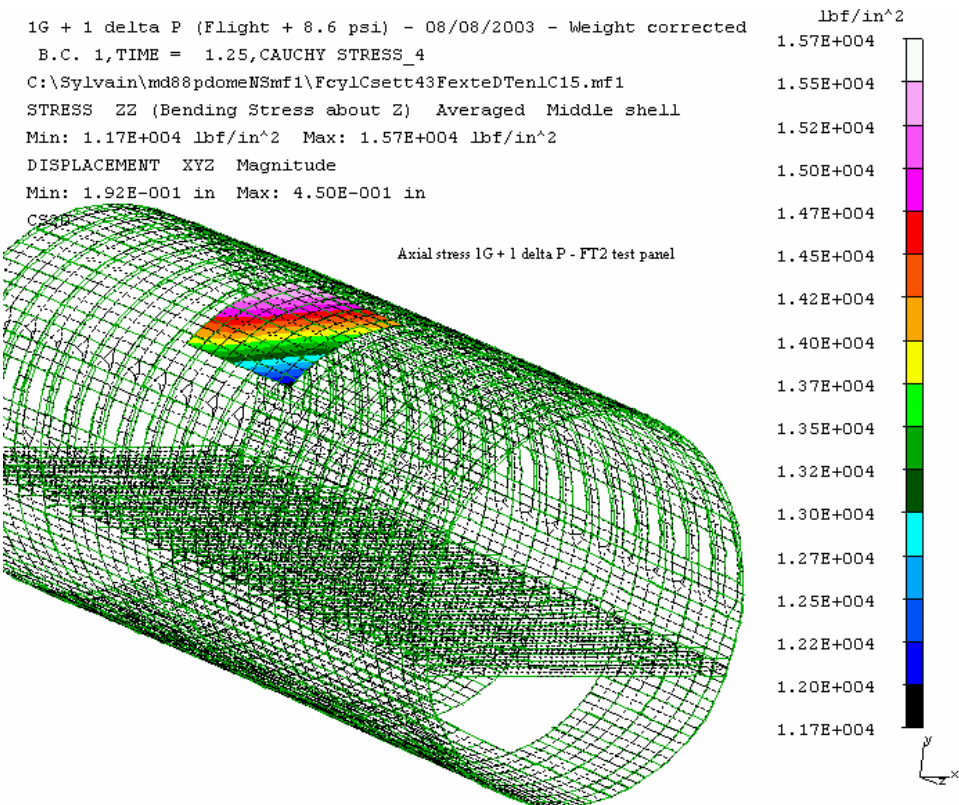
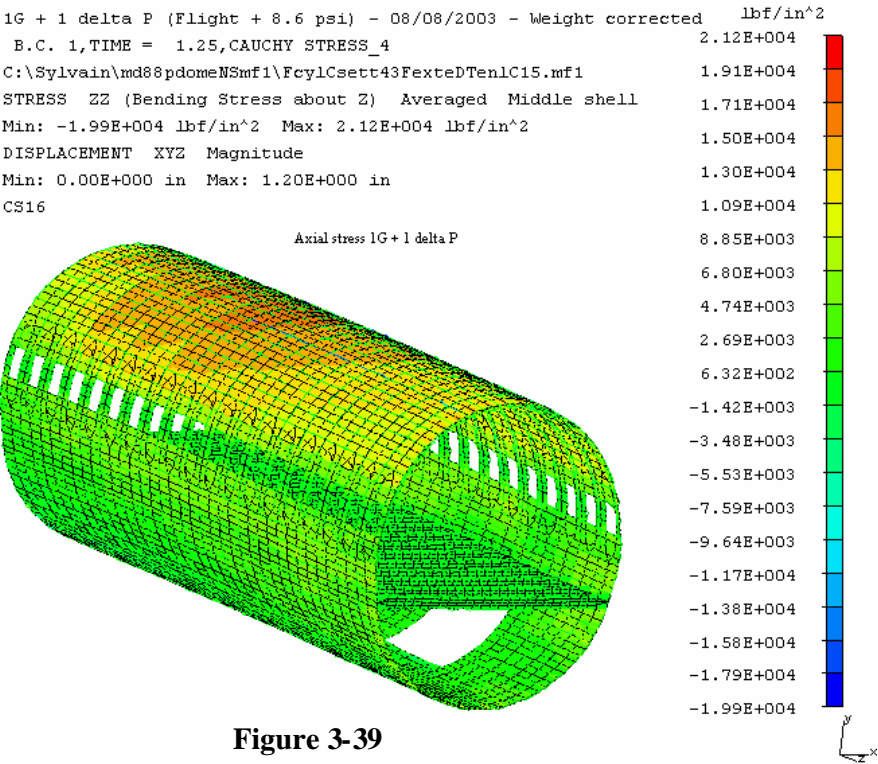


Figure 3-38

SHEET	3-29	NO.	4-087051-20
TOTAL	3-38		
ISSUE DATE	12/21/04		



SHEET	3-30	NO.	4-087051-20
TOTAL	3-38		
ISSUE DATE	12/21/04		

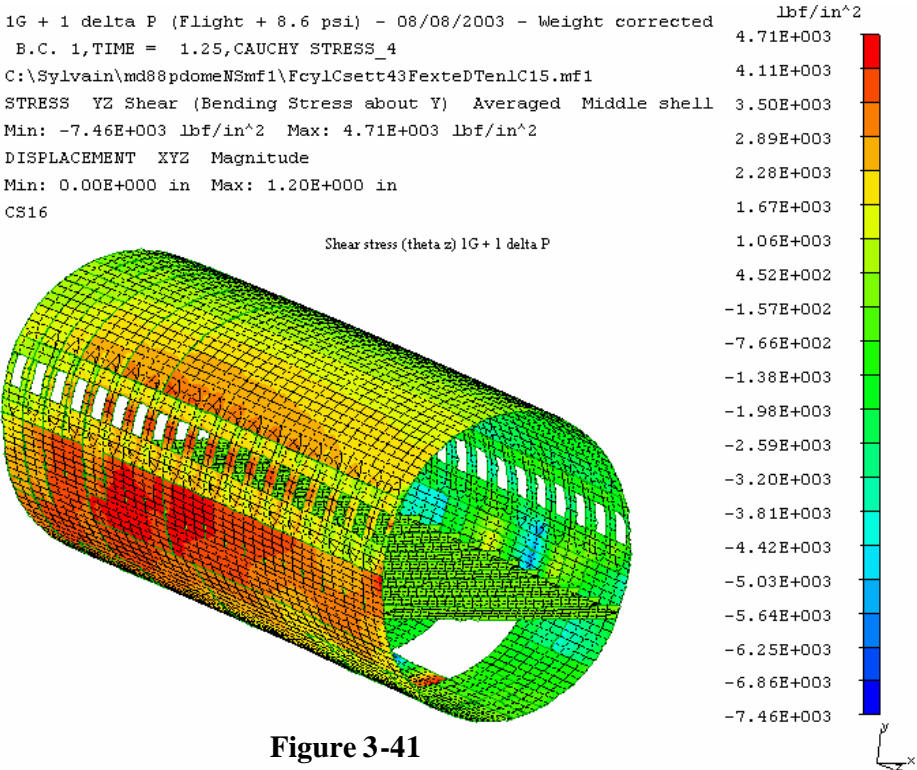


Figure 3-41

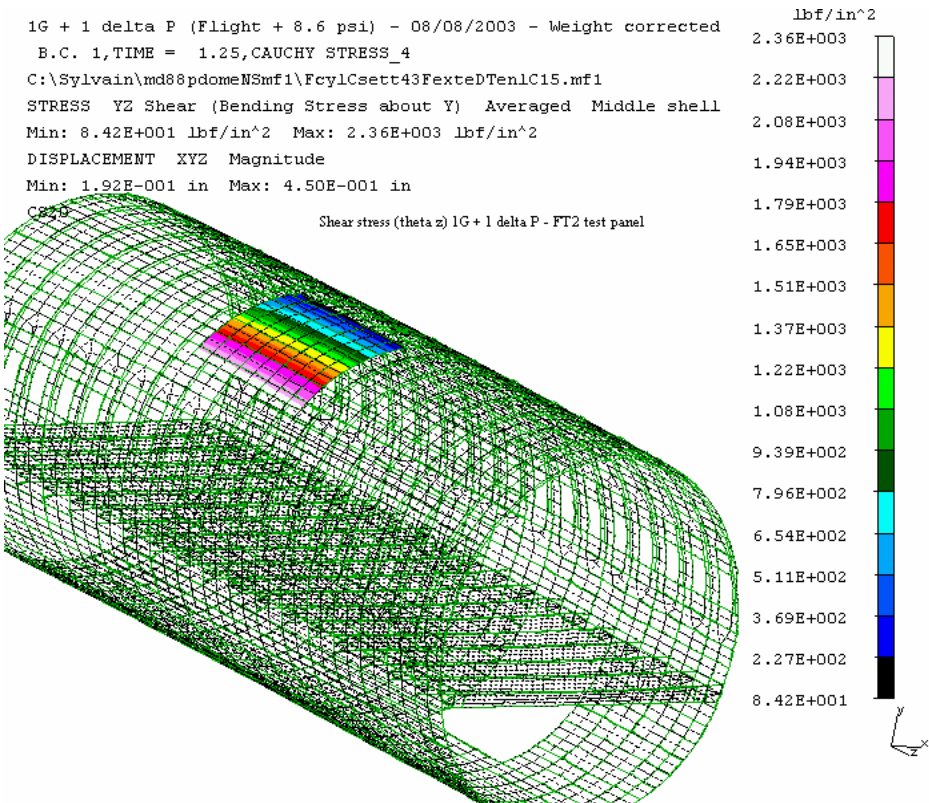


Figure 3-42

ENGINEERING DEPARTMENT

SHEET	3-31	NO.	4-087051-20
TOTAL	3-38		
ISSUE DATE	12/21/04		

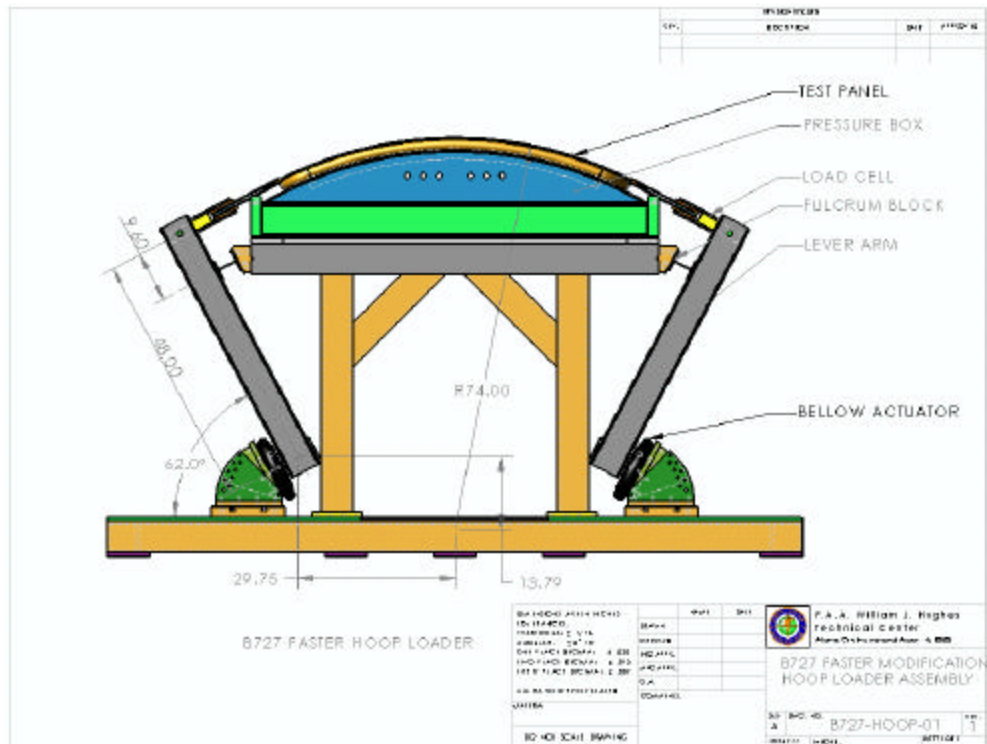


Figure 3-43

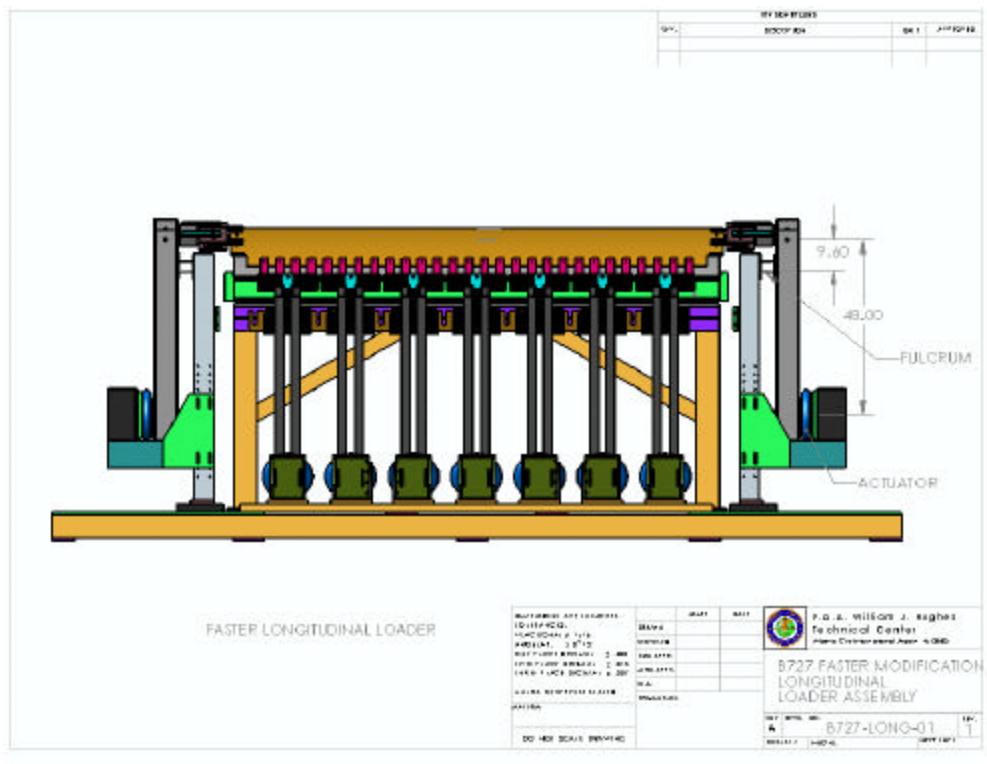


Figure 3-44

SHEET	3-32	NO.	4-087051-20
TOTAL	3-38		
ISSUE DATE	12/21/04		

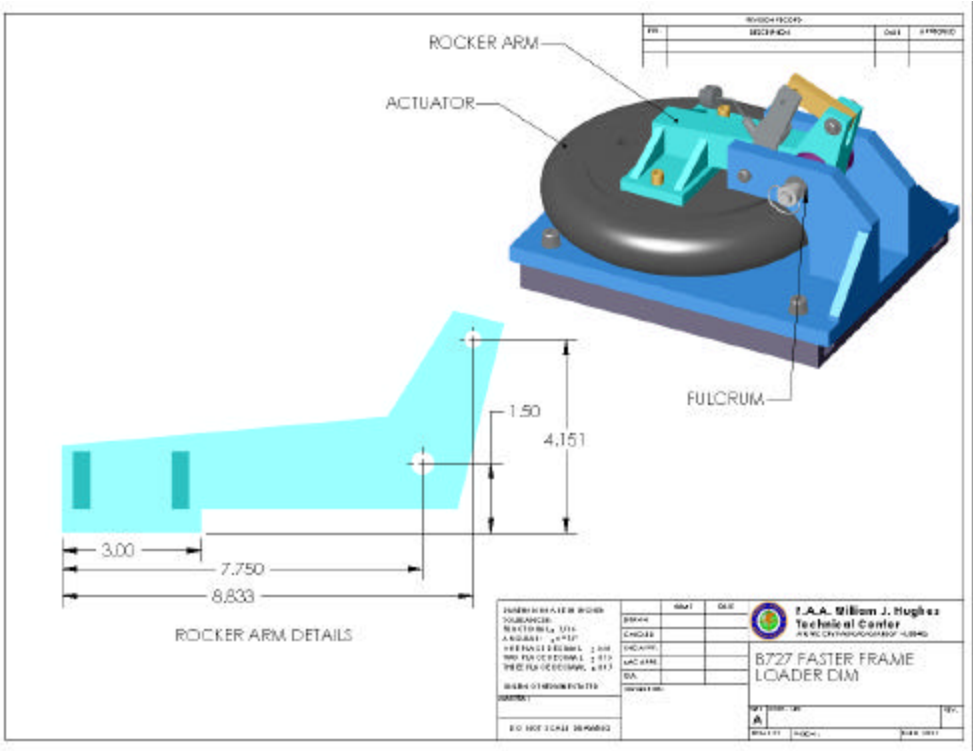


Figure 3-45

SHEET	3-33	NO.	4-087051-20
TOTAL	3-38		
ISSUE DATE	12/21/04		

FT2 Original BC

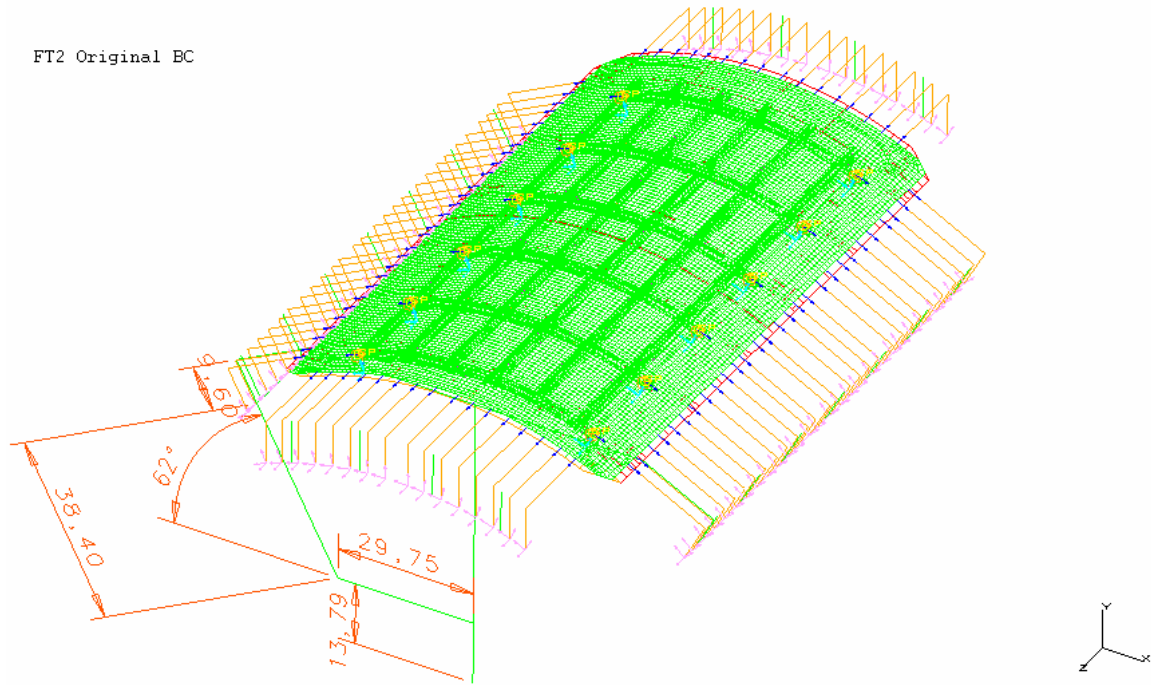


Figure 3-46

FT2 Frames with Original BC

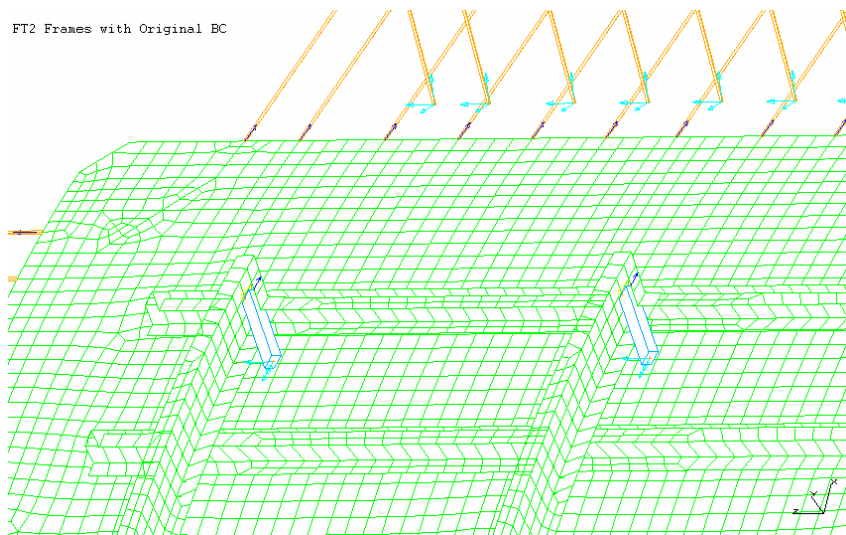


Figure 3-47

SHEET	3-34	NO.	4-087051-20
TOTAL	3-38		
ISSUE DATE	12/21/04		

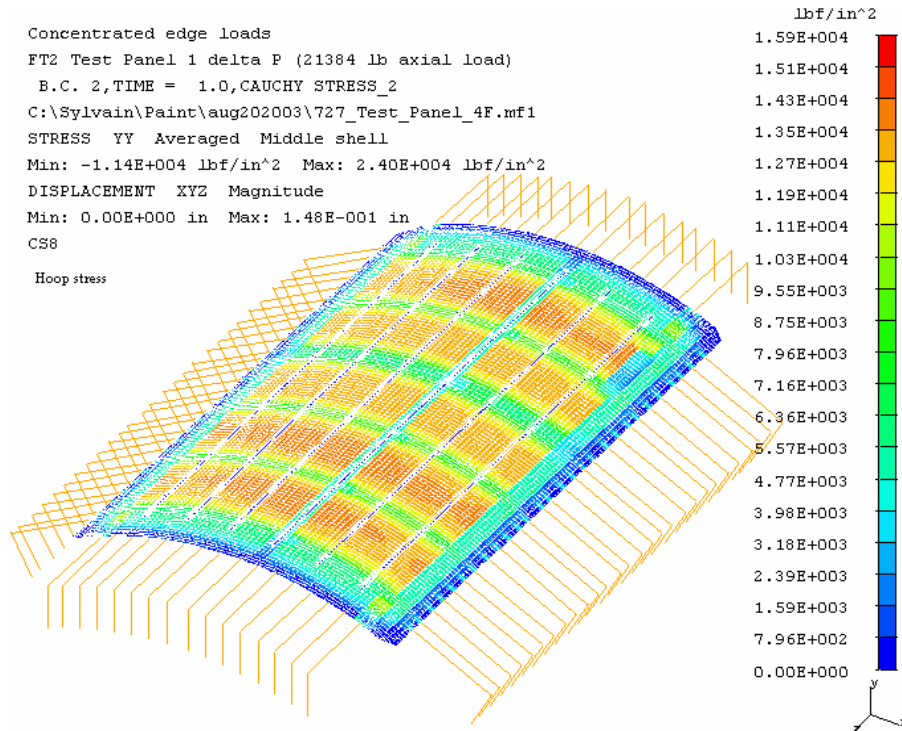


Figure 3-48

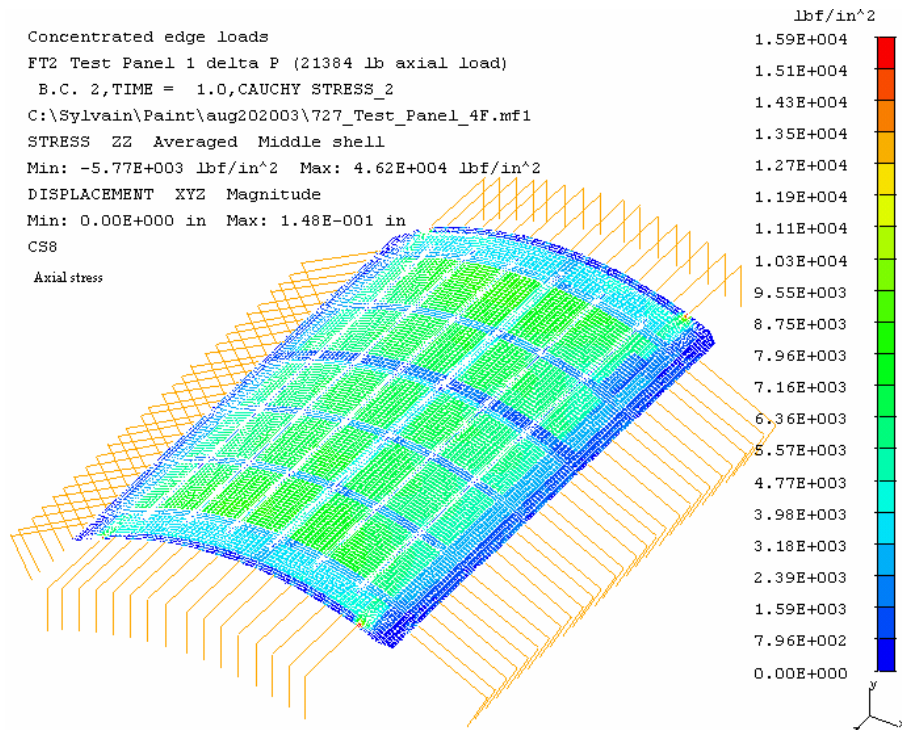
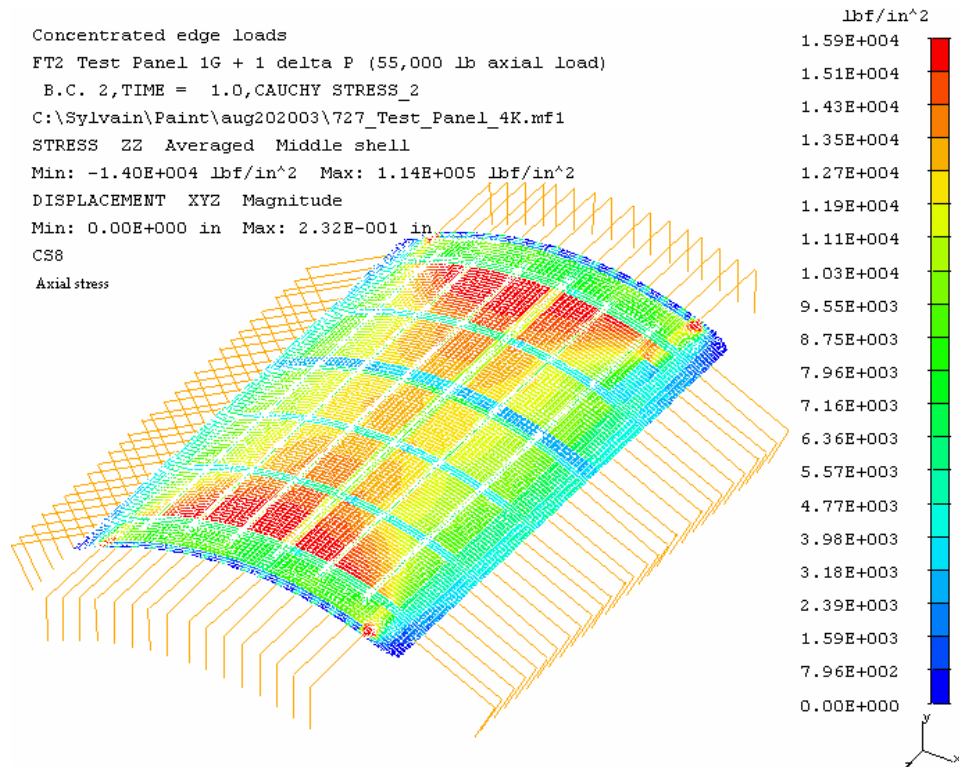
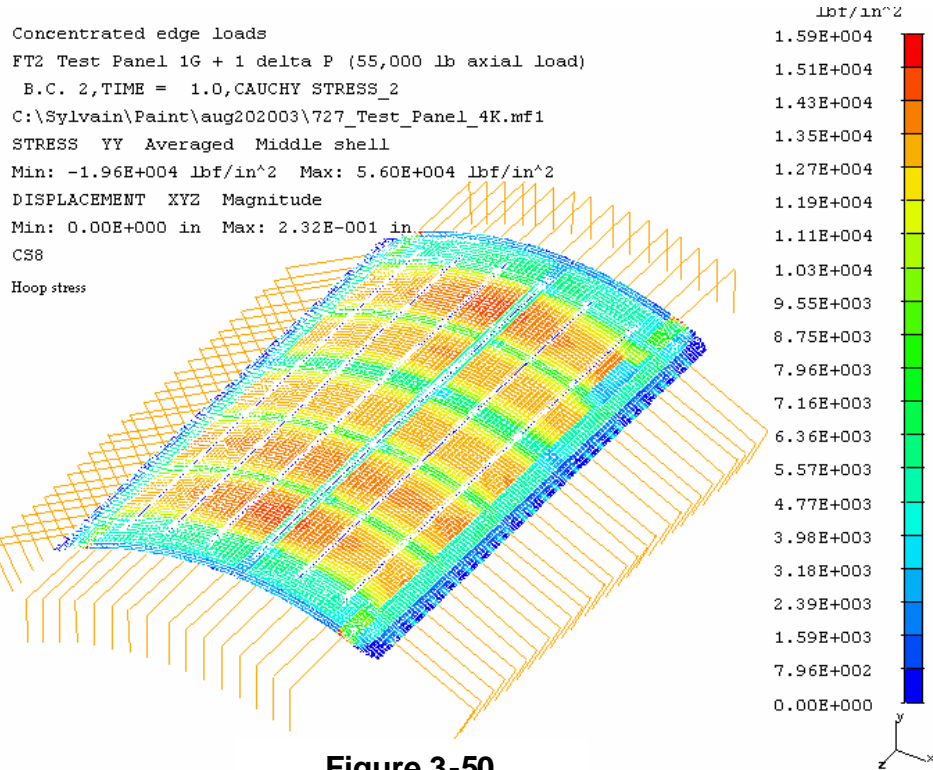


Figure 3-49

ENGINEERING DEPARTMENT

SHEET	3-35	NO.	4-087051-20
TOTAL	3-38		
ISSUE DATE	12/21/04		



SHEET	3-36	NO.	4-087051-20
TOTAL	3-38		
ISSUE DATE	12/21/04		

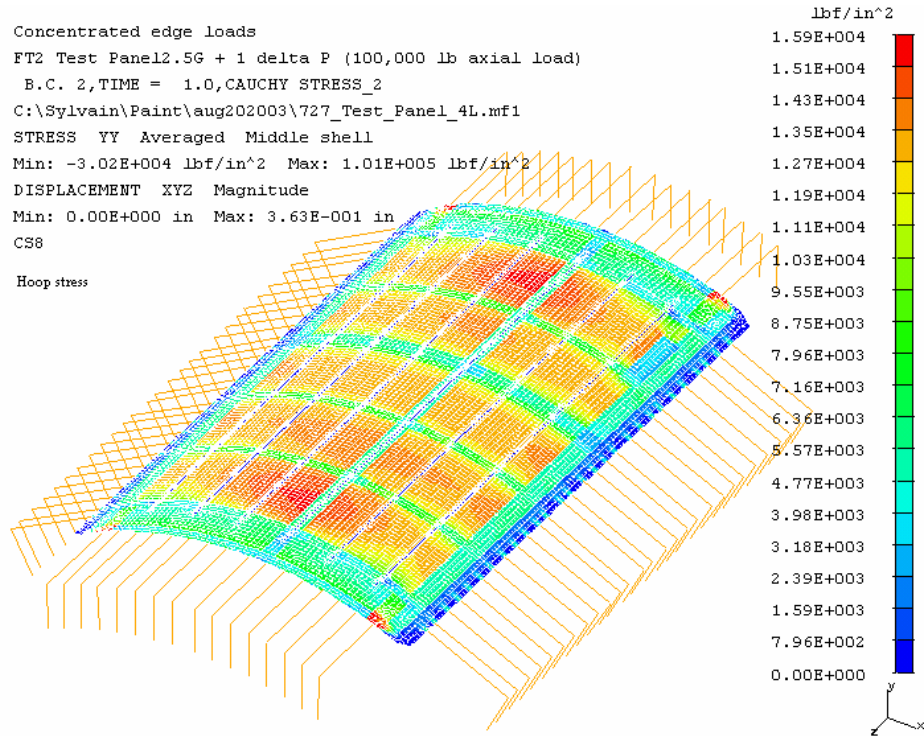


Figure 3-52

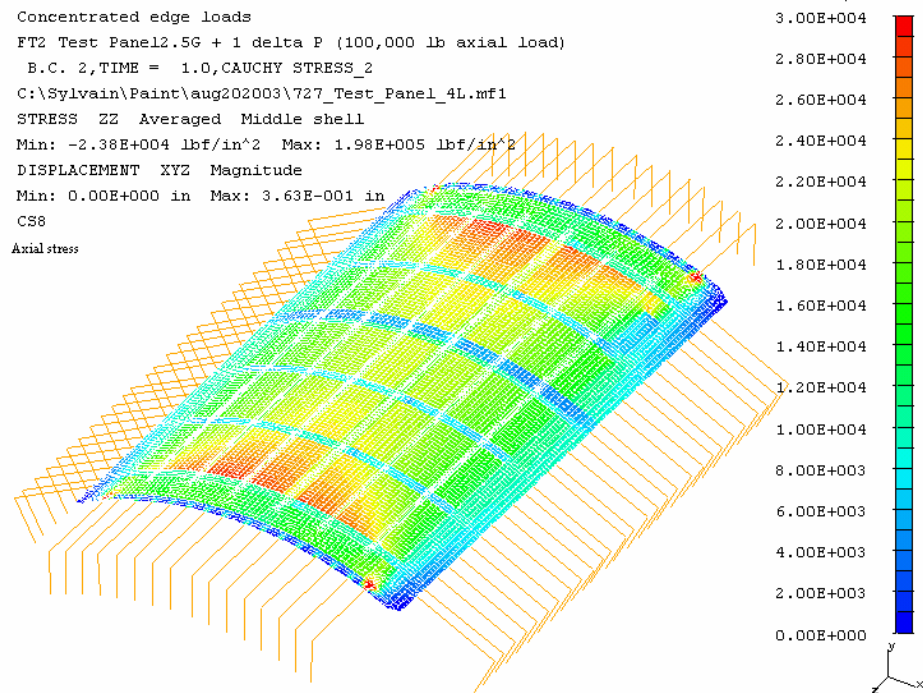


Figure 3-53

SHEET	3-37	NO.	4-087051-20
TOTAL	3-38		
ISSUE DATE	12/21/04		

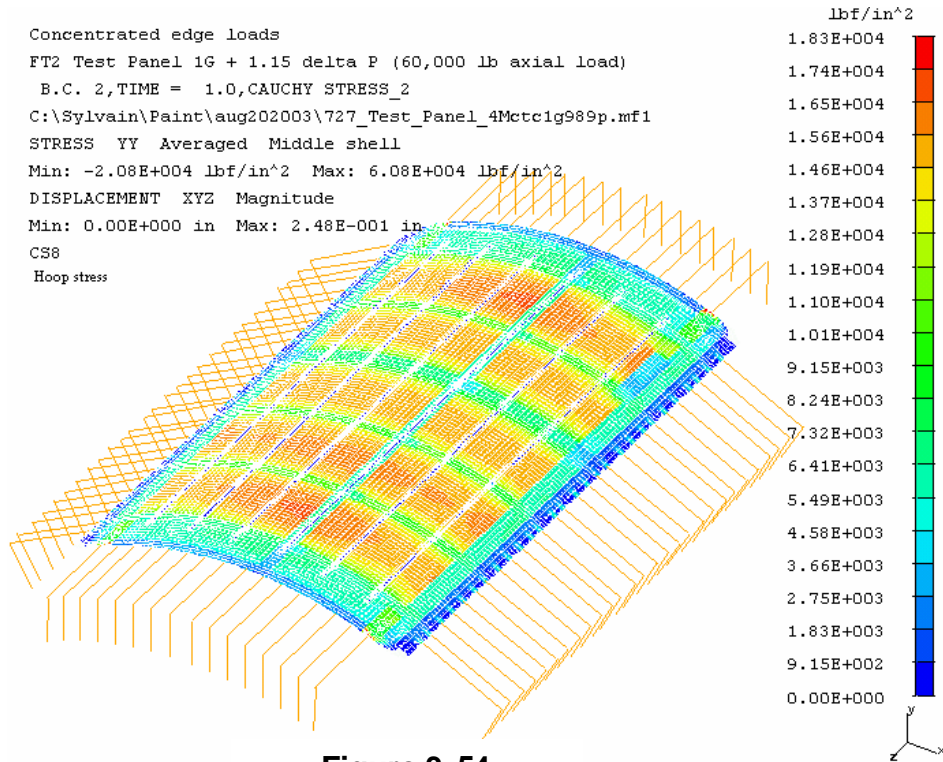


Figure 3-54

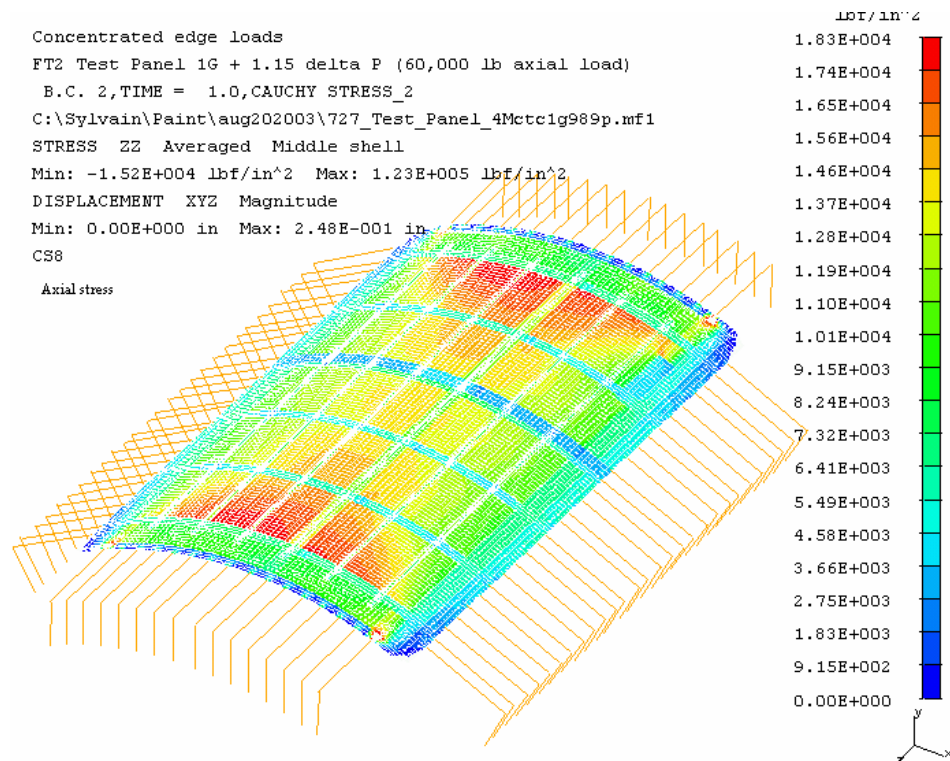
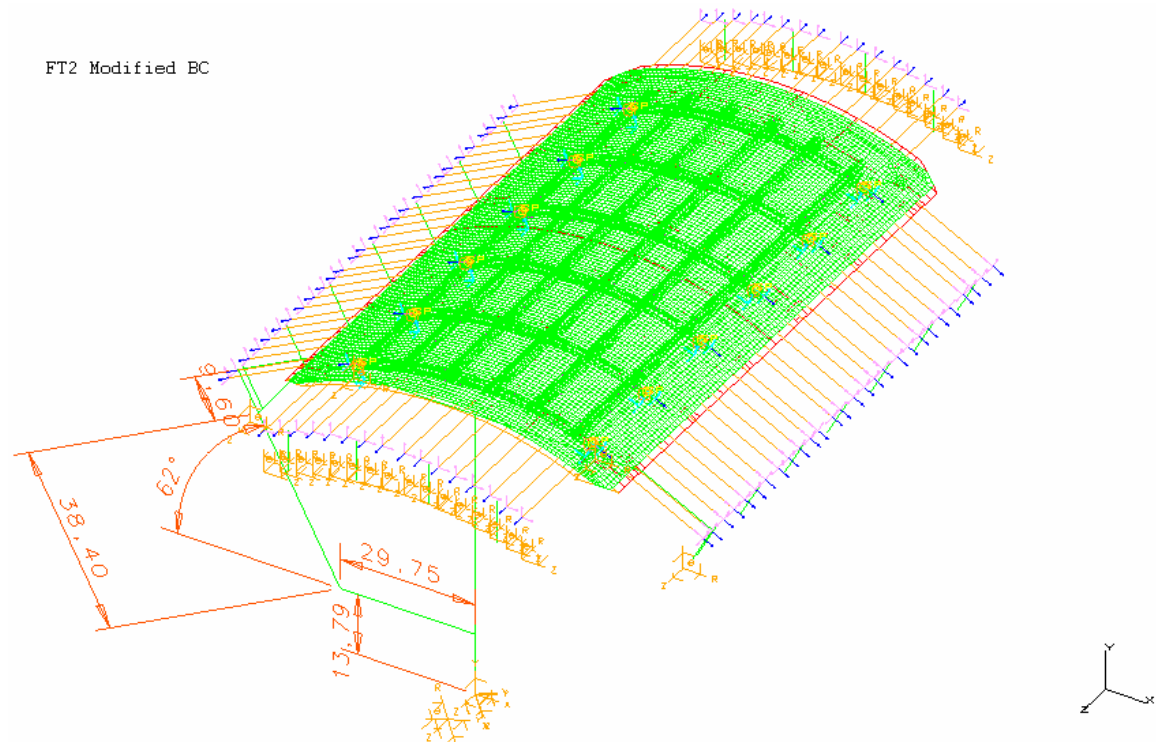
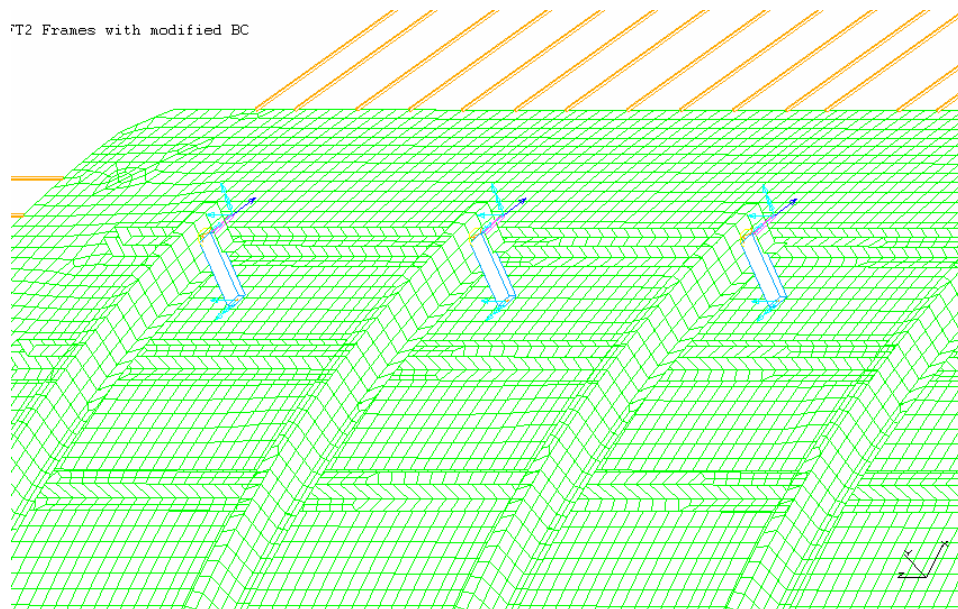


Figure 3-55

SHEET	3-38	NO.	4-087051-20
TOTAL	3-38		
ISSUE DATE	12/21/04		

**Figure 3-56****Figure 3-57**

SHEET	4-1	NO.	4-087051-20
TOTAL	4-21		
ISSUE DATE		12/22/04	

CHAPTER 4: FT1, FT3, AND FT4 FINITE ELEMENT ANALYSIS

Note: The FT1 actuator loads for the revised loading conditions are listed in Table 4-3. The FT3 and FT4 actuator loads are listed in Tables 4-4 and 4-5, respectively.

Geometrically nonlinear finite element analysis was accomplished in order to predict FASTER loads for the FT1, FT3, and FT4 test panels. Multi-level stiffness models were developed in IDEAS finite element code.

The FT1 test panel structure, located forward of the FT2 test panel in the fuselage Section 43, has similar geometry to the FT2 test panel. The same FASTER skin hoop and frame loads for the FT1 and FT2 panels are expected. The FASTER skin axial load required for the FT1 panel needs to be determined.

The global model of the B727-200 fuselage Section 43 was extended forward to the frame station 440 to accommodate the FT1 test panel. The unmodified FT1 test panel structure is located between the frame stations 480 and 580, and stringers 2 and 7. The loads include skin internal pressure, axial loads due to the pressure and bending applied at the frame station 440, and shear loads due to the weight of the aircraft, passengers and cargo, applied at the frame station 440 and distributed throughout the model (See chapter 3).

Figures 1-6 show the skin hoop, axial, and shear stress contour plots predicted by the global model for the 8.6 psi pressure and the combined 8.6 psi pressure and 1g positive maneuver loading cases. The stiffened axial stress for the 8.6 psi loading condition is 7.53 ksi. An 11 ksi lower bound to the average axial stress for the combined 8.6 psi pressure and 1g positive maneuver condition per the existing beam-

SHEET	4-2	NO.	4-087051-20
TOTAL	4-21		
ISSUE DATE	12/22/04		

type solution is similar to the global model prediction. An FT1 panel area model created on the same geometry as the fuselage global model, with a refined mesh of the same type elements as in the global model, and with the edge displacement boundary conditions mapped from the global model, predicts membrane stress values matching the global model predictions.

In order to develop a stiffness model of the FT1 test panel, minor changes to the FT2 test panel model geometry were required to account for a different butt splice location and changed edge reinforcement thicknesses. The estimated skin hoop load, frame load, and skin axial load resulting in the skin 13.7 ksi hoop membrane stress and 14.3 ksi hoop surface stress for 8.6 psi pressure, and the skin 15.7 ksi hoop membrane stress and 16.5 ksi hoop surface stress for 9.89 psi pressure conditions, and the estimated lower bound axial stresses in the critical test area are listed in Table 4-1.

Loading Condition	Load per Frame, lbs	Skin Total Hoop Load, lbs	Skin Total Axial Load, lbs
8.6 psi	1,465	64,368	21,384
8.6 psi and 1g	1,465	64,368	38,400
8.6 psi and 2.5g	1,465	64,368	63,924
9.89 psi and 1g	1,685	74,023	41,608

Table 4-1: Estimated lower bound axial stresses in the critical test area

The contour plots for the axial and hoop stresses due to 8.6 psi pressure, and combined 8.6 psi pressure and 1g flight loading conditions are shown in Figures 4-6 through 4-10. The similarity of the predicted skin hoop and frame loads between the FT1 and FT2 test panels for these loading cases was used to estimate the loads for the combined 8.6 psi pressure and 2.5g flight, and 9.89 psi pressure and 1g flight limit load conditions in Table 4-1. The FASTER facility provides 6 frame, 7 skin hoop and 4 skin axial load control points. The actuator loads for the fatigue and limit load test conditions are listed in Table 4-2.

SHEET	4-3	NO.	4-087051-20
TOTAL	4-21		
ISSUE DATE	12/22/04		

Loading Condition	Load per Frame Actuator, lbs	Load per Skin Hoop Actuator, lbs	Load per Skin Axial Actuator, lbs
8.6 psi and 1.25g	1,470	9,200	10,660
9.89 psi and 1g	1,690	10,570	10,370

Table 4-2: Actuator loads for the fatigue and limit load test conditions

The actuator loads for the revised fatigue and residual strength loading conditions are listed in Table 4-3.

Loading Condition	Load per Frame Actuator, lbs	Load per Skin Hoop Actuator, lbs	Load per Skin Axial Actuator, lbs
8.9 psi and 1.25g	1,510	9,520	10,940
10.24 psi and 1g	1,800	10,910	10,670

Table 4-3: Actuator loads for the revised fatigue and residual strength loading conditions

The stiffness models were also developed for the FT3 and FT4 test panels. In addition to the axial and hoop loads, a self-equilibrating set of two couples of uniformly distributed shear forces, simulating the loads from the shear fixture, is applied to the skin in accordance with the shear fixture geometry shown in Figures 4-11 and 4-12. The skin axial and shear loads are determined based on matching the stresses at a location in the critical test area to stresses from the existing global model through an iterative procedure. The skin hoop to frame load ratios were determined from the unmodified test panel area models. The total hoop load applied to the panels equilibrates the hoop load due to internal pressure. The FT3 and FT4 panels have different geometry compared to the FT1 and FT2 panels, resulting in different hoop stress levels. The FT3 and FT4 panel hoop, axial, and shear stress contour plots for the fatigue and residual strength loading conditions are shown in Figures 4-13 through 4-24. The test panel models are meshed with linear shell elements. To check the convergence of the finite element results, a parabolic element mesh was created for the FT3 panel. The model comparison for the skin stress results in the critical test area shows less than 2% difference between the linear and

SHEET	4-4	NO.	4-087051-20
TOTAL	4-21		
ISSUE DATE	12/22/04		

parabolic element formulations. The fatigue load skin stress contour plots predicted by the model meshed with parabolic elements are shown in Figures 4-25 through 4-27.

The FT3 panel actuator loads for are listed in Table 4-4.

Loading Condition	Load per Frame Actuator, lbs	Load per Skin Hoop Actuator, lbs	Load per Skin Axial Actuator, lbs	Shear Load, lbs/in
8.9 psi and 1.25g	1,550	9,490	20,730	167
10.24 psi and 1g	1,870	10,840	19,620	134

Table 4-4: FT3 panel actuator loads

The FT4 panel actuator loads for are listed in Table 4-5.

Loading Condition	Load per Frame Actuator, lbs	Load per Skin Hoop Actuator, lbs	Load per Skin Axial Actuator, lbs	Shear Load, lbs/in
8.9 psi, 1.25g, and 10% limit fin gust	1,480	9,550	19,630	139
10.24 psi and 1g	1,700	10,990	17,760	84

Table 4-5: FT4 panel actuator loads

Modifications to FT1 Axial Loads:

At Q9, the axial loads for the FT1 test panel were revised, since the axial loads for FT2 test panel which were obtained using the exact same approach described in the previous section and the previous chapter (FT2), lead to cracking outside the lap joint during the test (See chapter 9). Therefore, the 25% additional body loads added during FT2 panel loads derivation to the Section 43 global model was removed and re-accomplished the matching of axial stresses at certain specific location (Between STR-4 and STR-5, FS 520-FS 540) on FT1 test panel to the exact same location on the global fuselage

SHEET	4-5	NO.	4-087051-20
TOTAL	4-21		
ISSUE DATE	12/22/04		

section 43 model for the 8.9 psi + 1.25G (Fatigue) and the 10.24 psi + 1G (Residual strength) load cases. This procedure is illustrated in figures 4-28 through 4-31. The loads obtained thus have been tabulated in the table 4-6 below.

Loading Condition	Load per Frame Actuator, lbs	Load per Skin Hoop Actuator, lbs	Load per Skin Axial Actuator, lbs
8.9 psi and 1.25g	1,510	9,520	8,900
10.24 psi and 1g	1,800	10,910	8,500

Table 4- 6: Modified actuator loads for the revised fatigue and residual strength loading conditions

SHEET	4-6	NO.	4-087051-20
TOTAL	4-21		
ISSUE DATE	12/22/04		

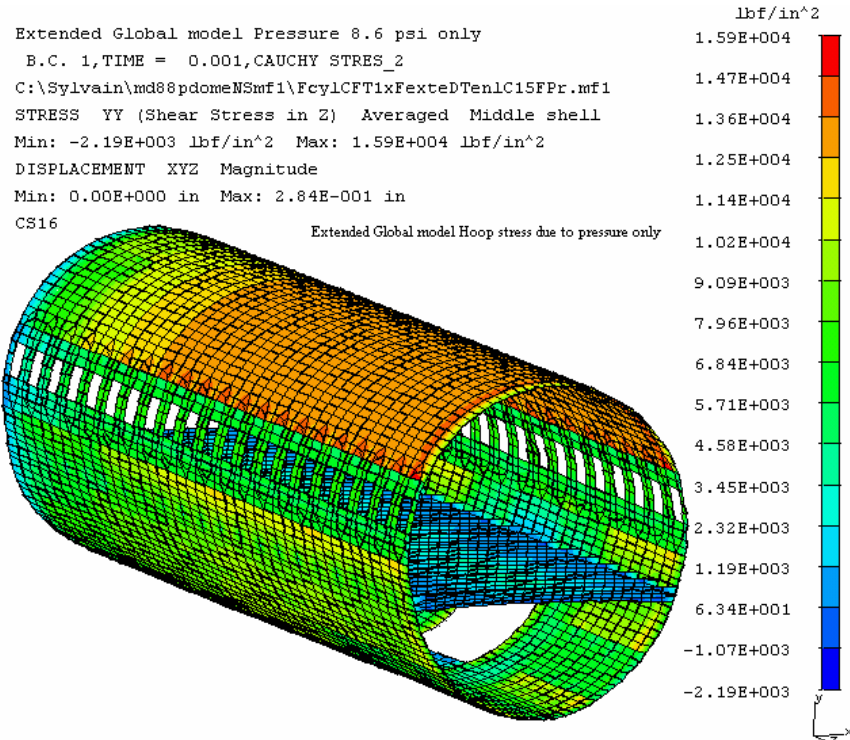


Figure 4-1

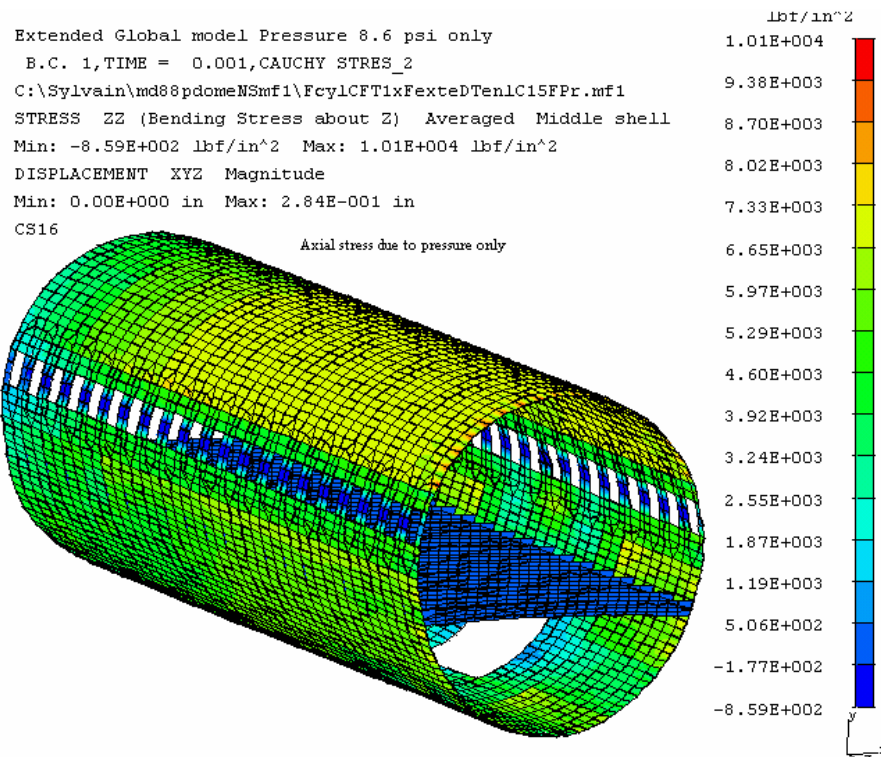
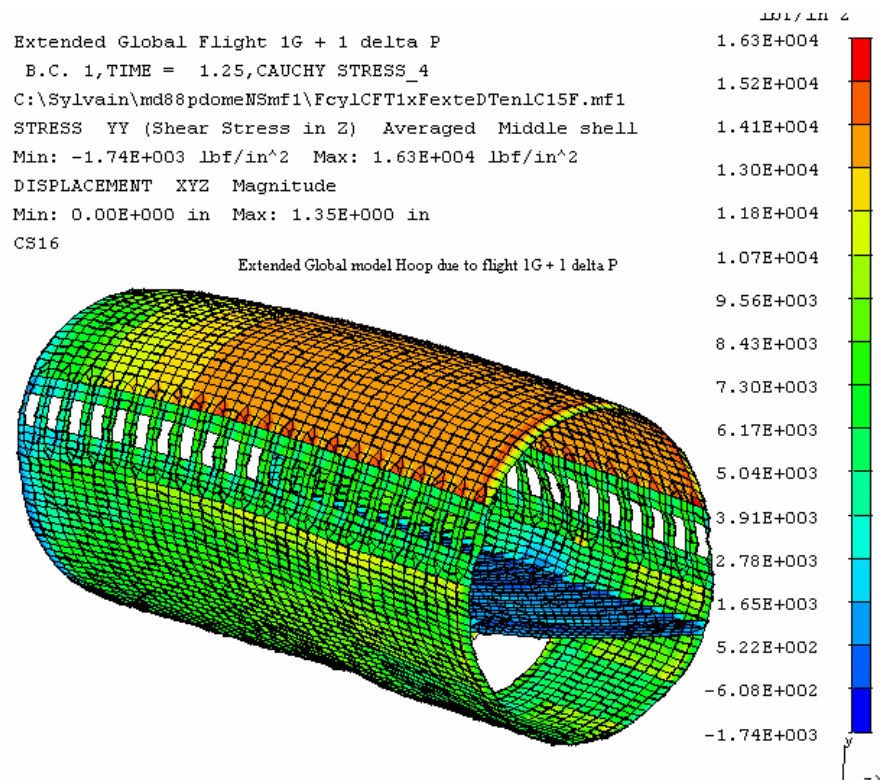
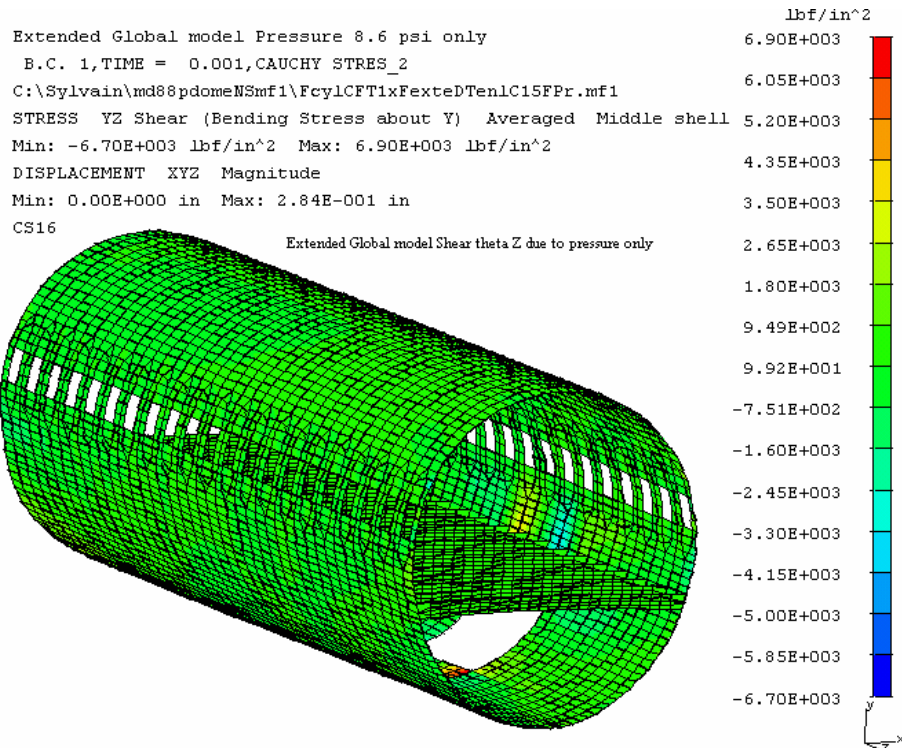


Figure 4-2

SHEET	4-7	NO.	4-087051-20
TOTAL	4-21		
ISSUE DATE	12/22/04		



ENGINEERING DEPARTMENT

SHEET	4-8	NO.	4-087051-20
TOTAL	4-21		
ISSUE DATE	12/22/04		

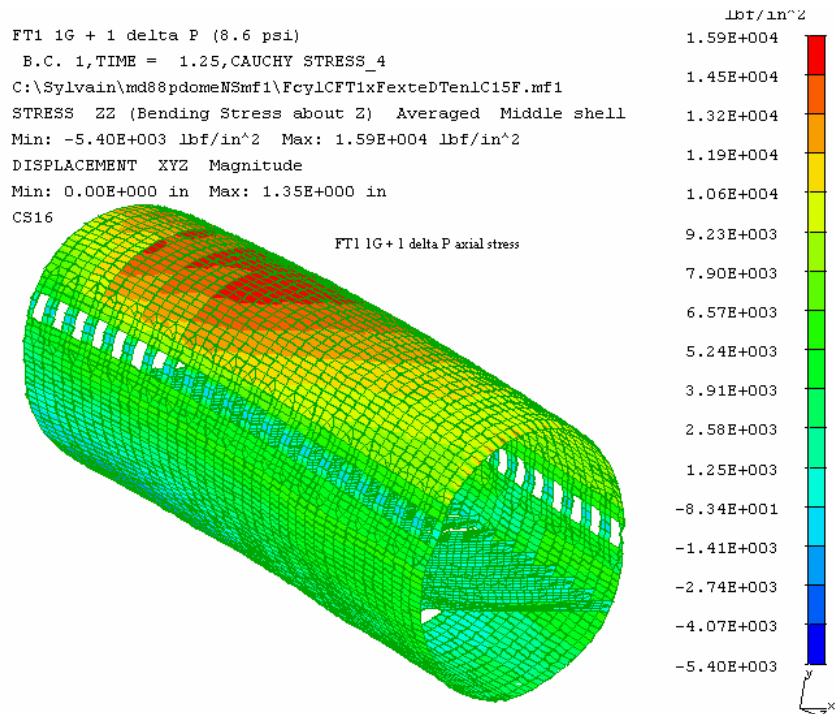


Figure 4-5

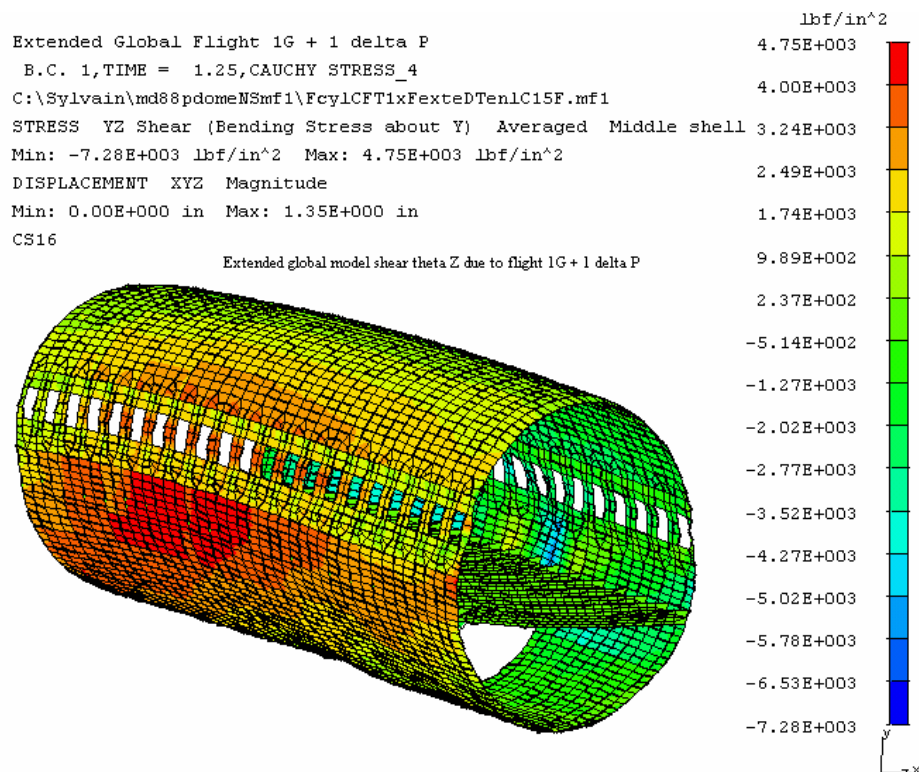


Figure 4-6

SHEET	4-9	NO.	4-087051-20
TOTAL	4-21		
ISSUE DATE	12/22/04		

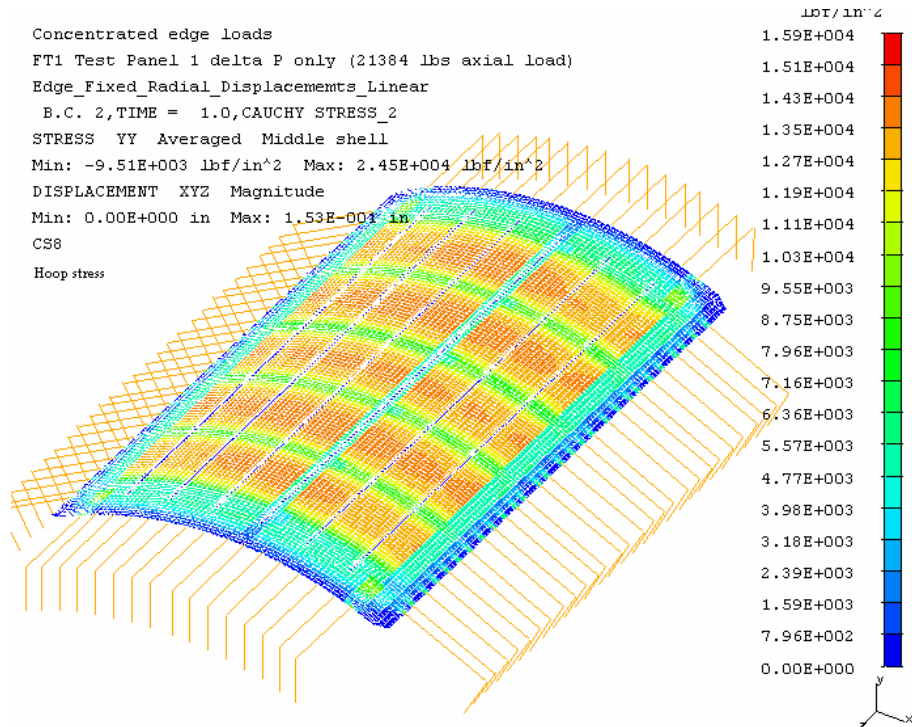


Figure 4-7

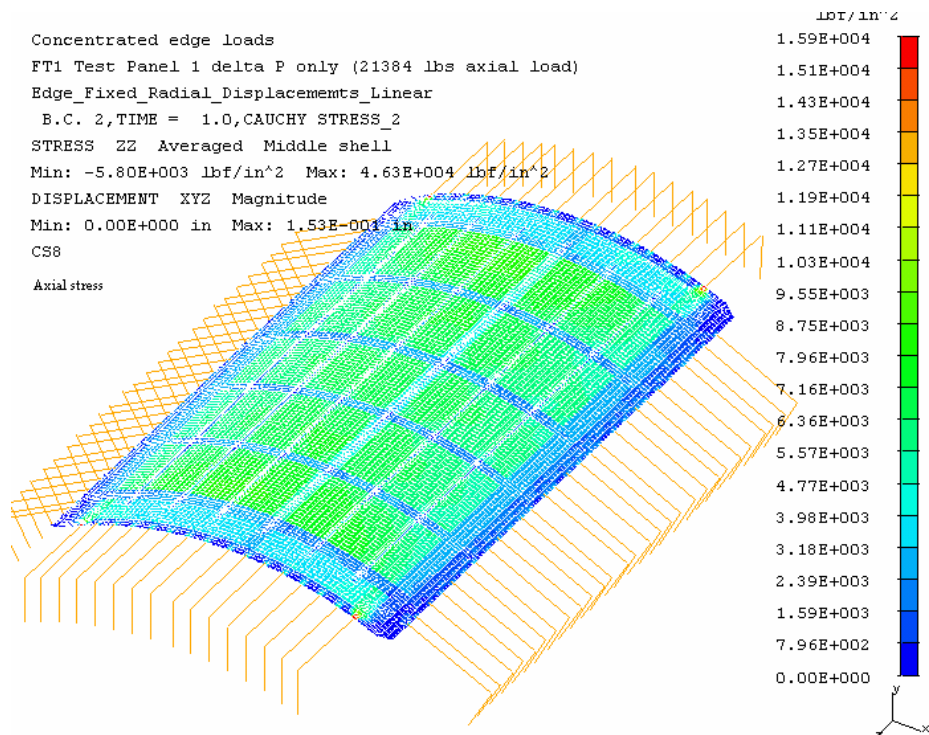


Figure 4-8

SHEET	4-10	NO.	4-087051-20
TOTAL	4-21		
ISSUE DATE	12/22/04		

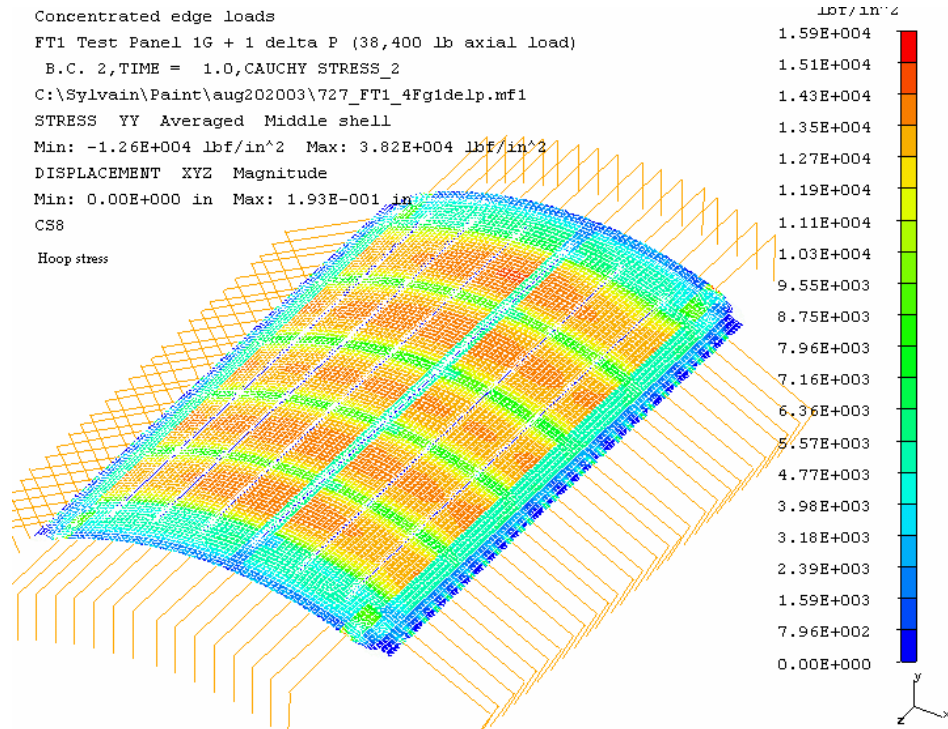


Figure 4-9

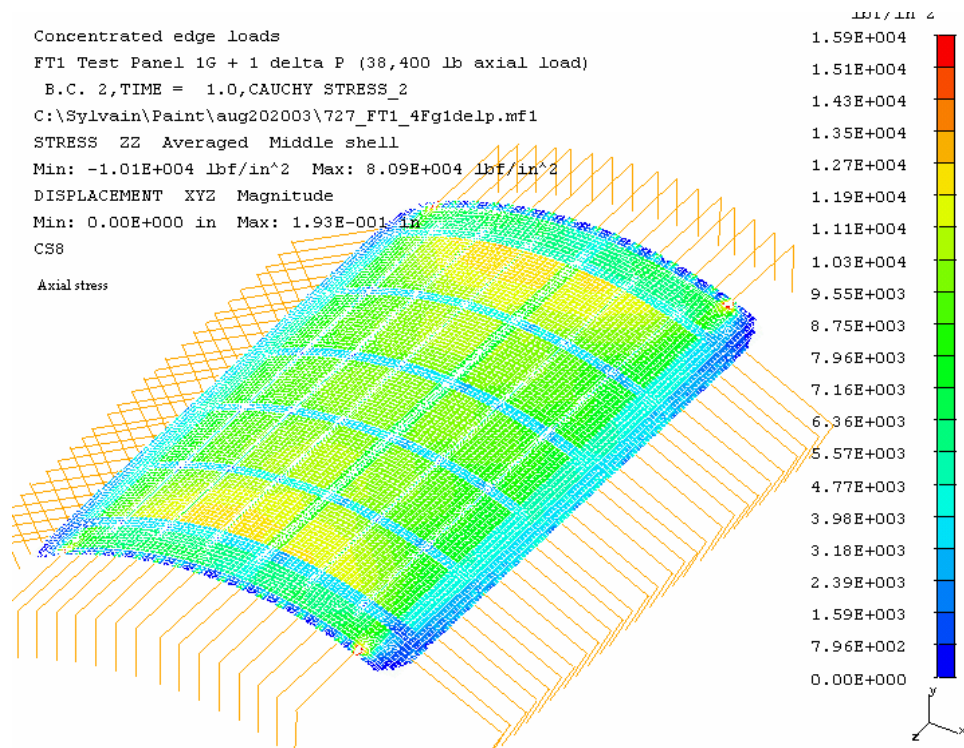


Figure 4-10

SHEET	4-11	NO. 4-087051-20
TOTAL	4-21	
ISSUE DATE		12/22/04



SHEET	4-12	NO.	4-087051-20
TOTAL	4-21		
ISSUE DATE	12/22/04		

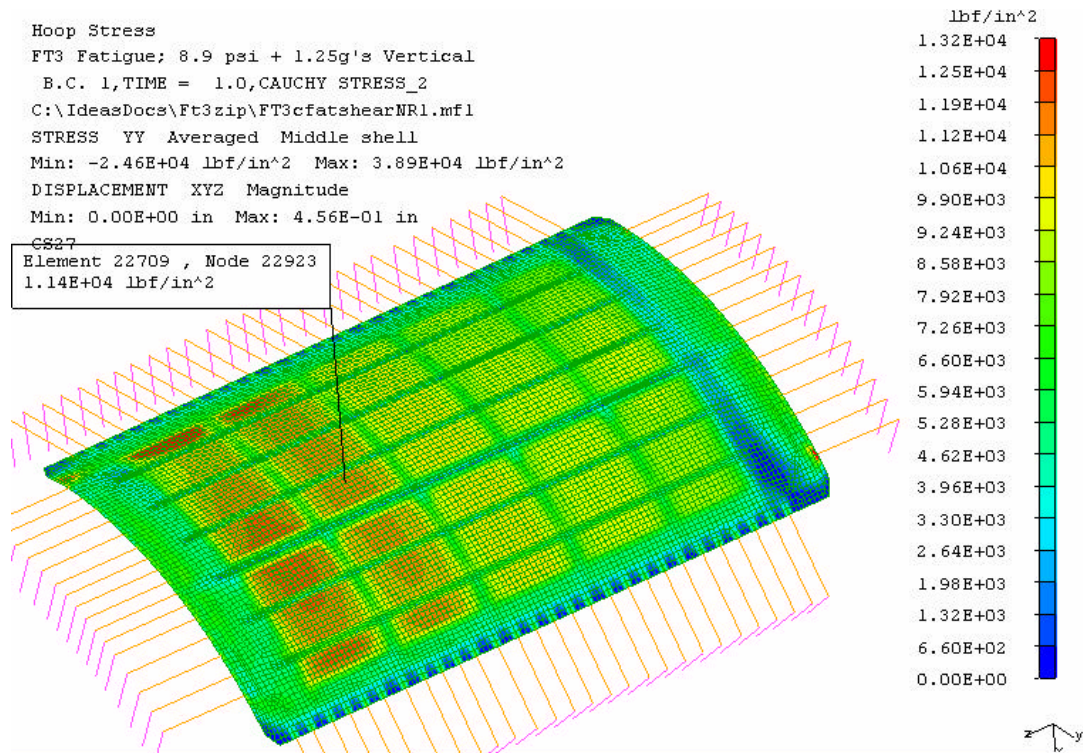


Figure 4-13

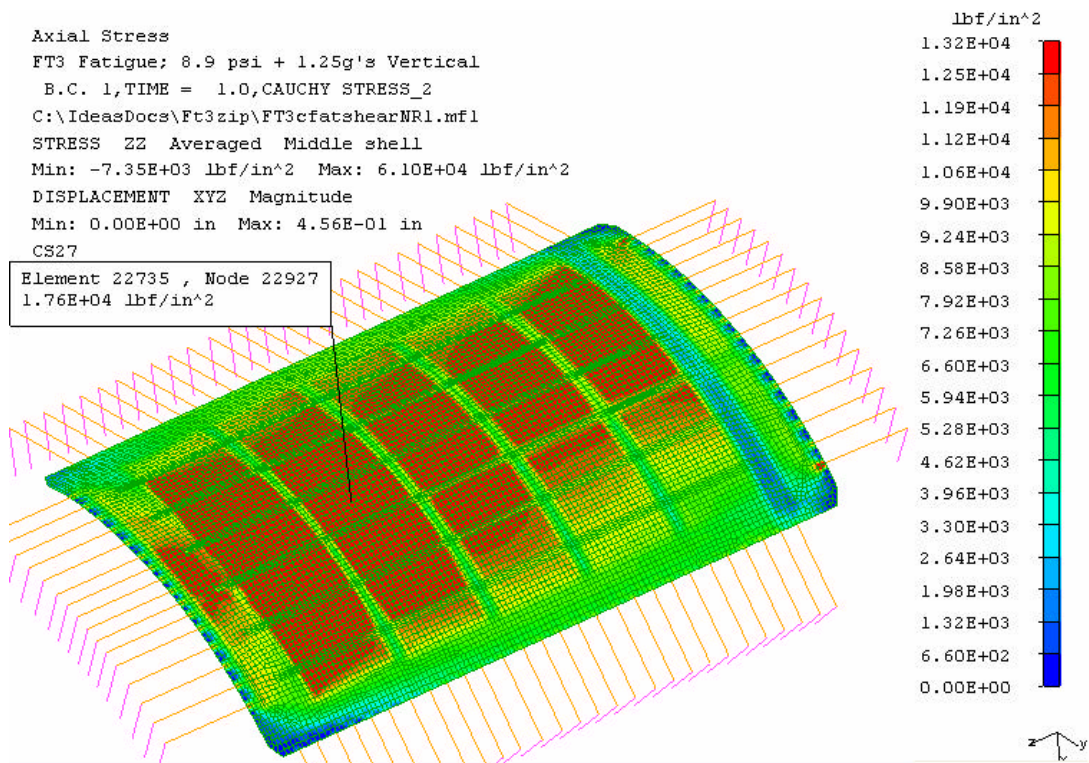


Figure 4-14

SHEET	4-13	NO.	4-087051-20
TOTAL	4-21		
ISSUE DATE	12/22/04		

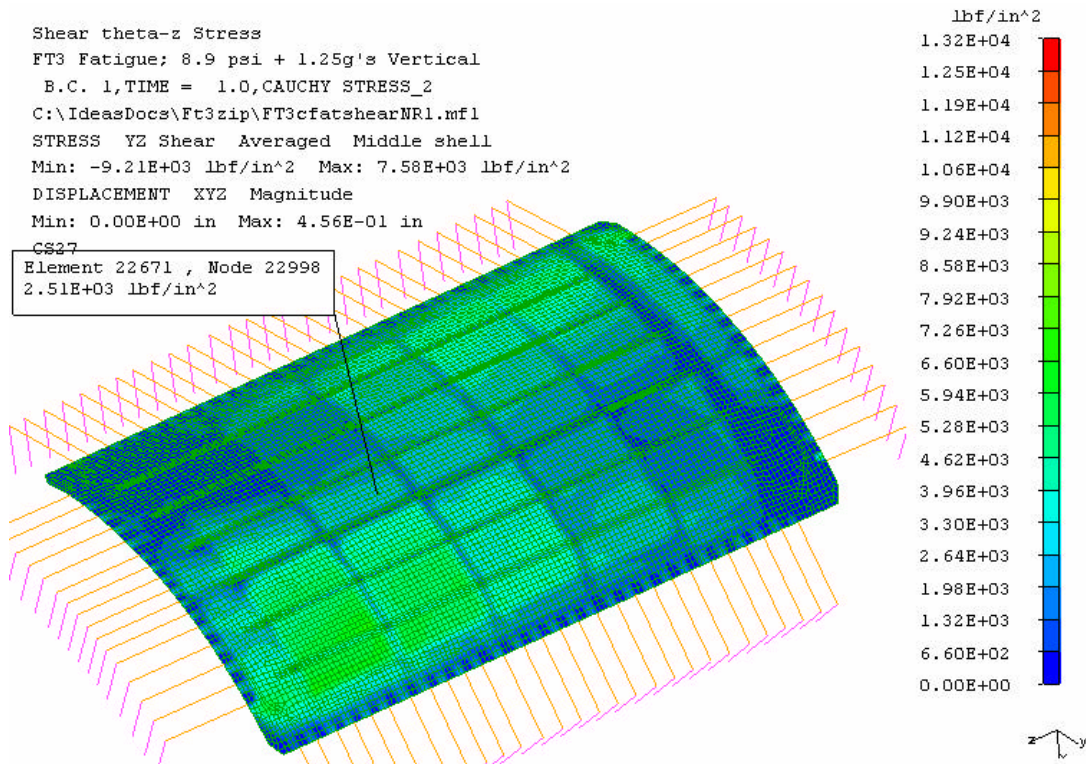


Figure 4-15

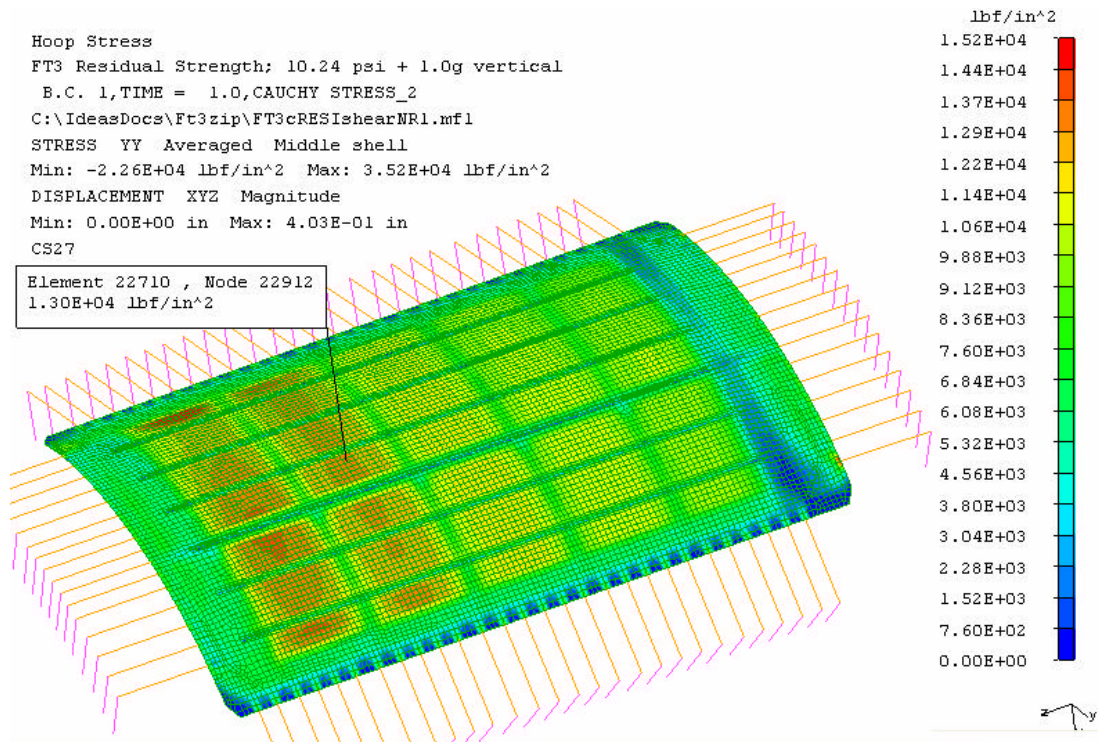


Figure 4-16

SHEET	4-14	NO.	4-087051-20
TOTAL	4-21		
ISSUE DATE	12/22/04		

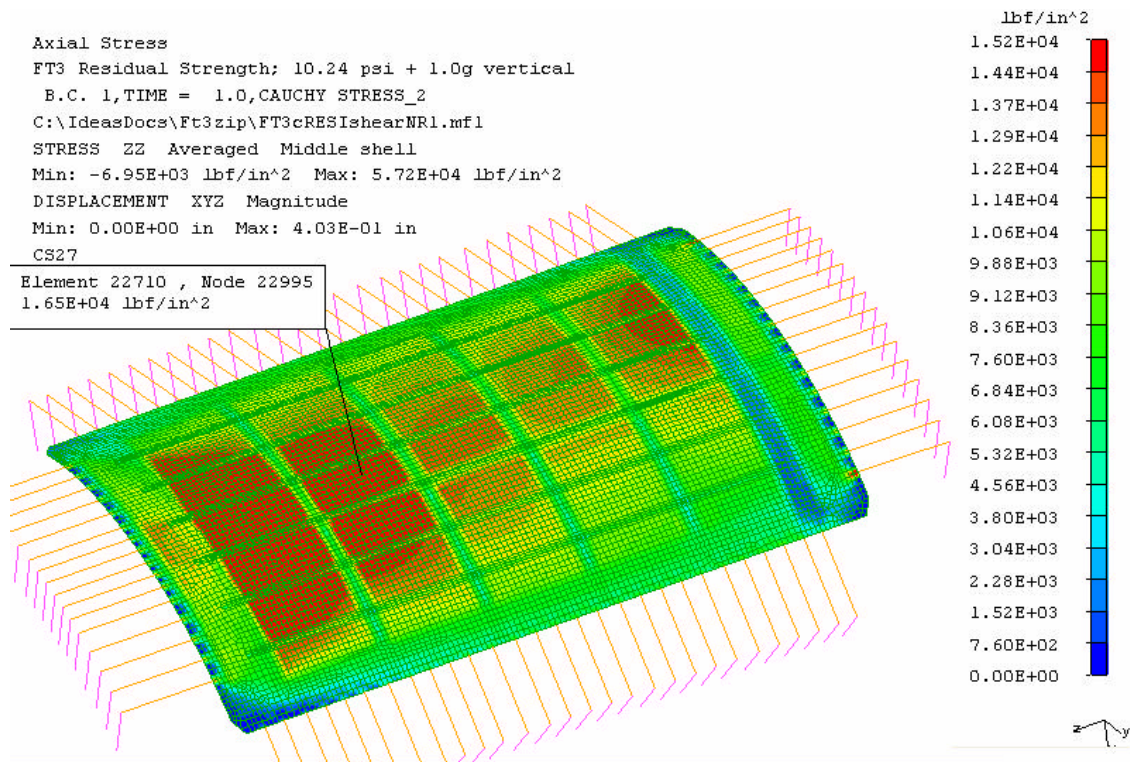


Figure 4-17

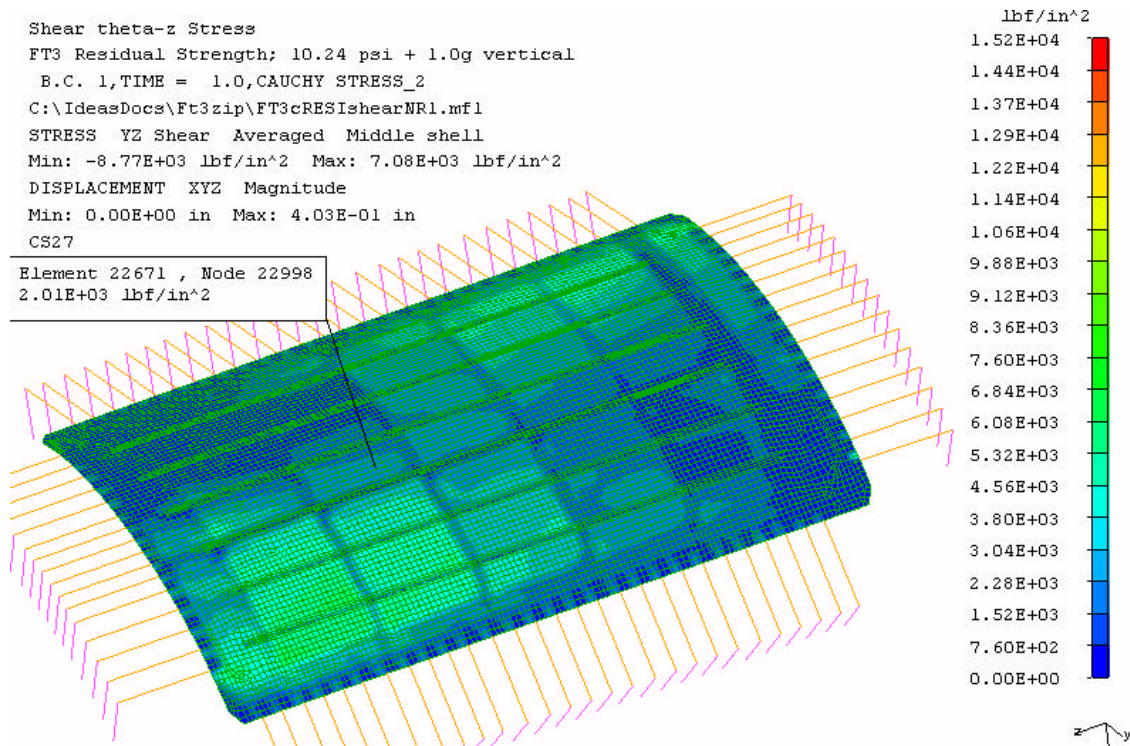


Figure 4-18

SHEET	4-15	NO.	4-087051-20
TOTAL	4-21		
ISSUE DATE	12/22/04		

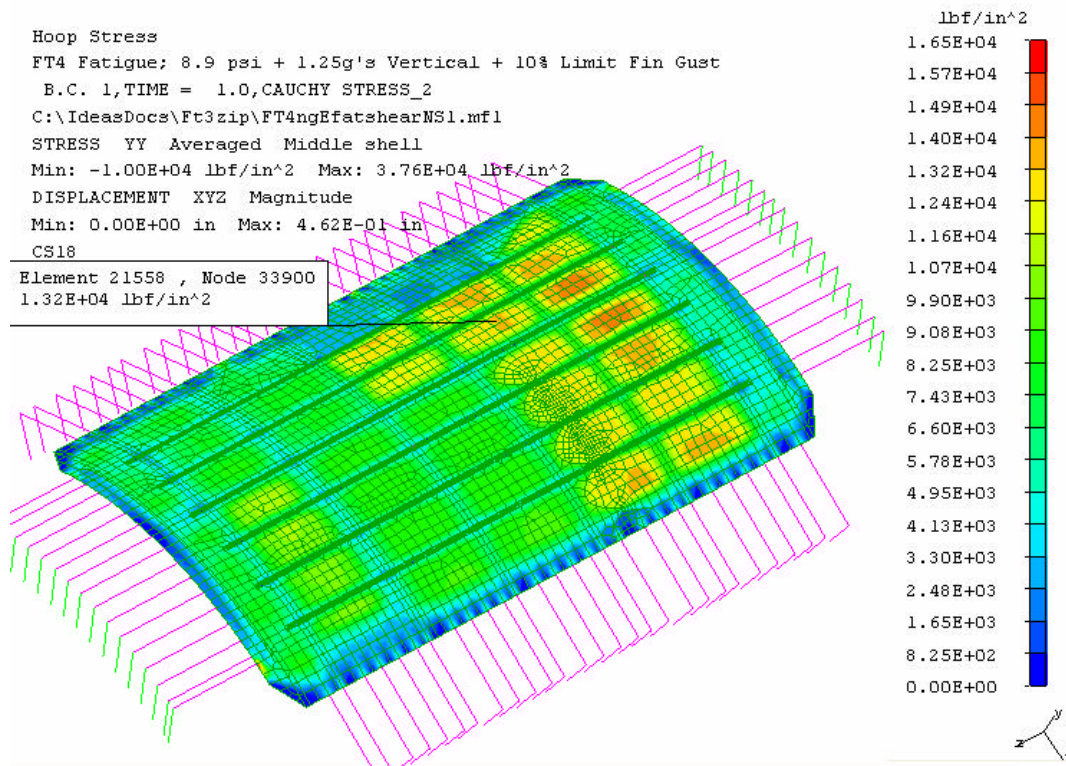


Figure 4-19

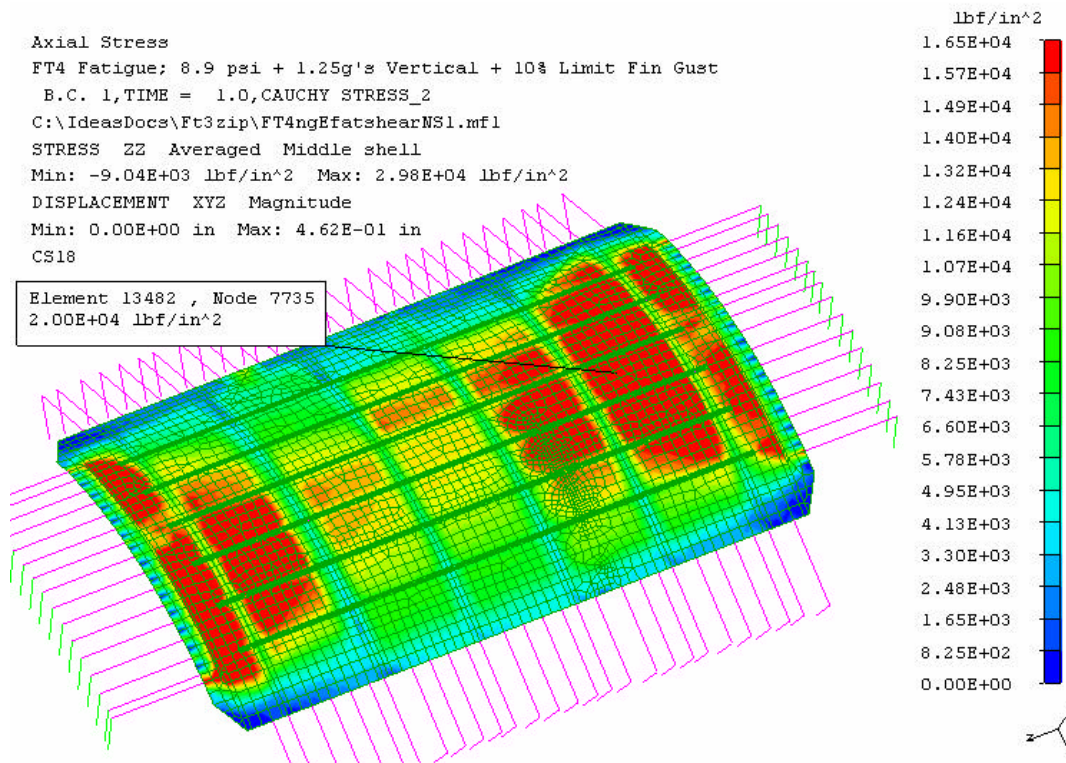


Figure 4-20

SHEET	4-16	NO.	4-087051-20
TOTAL	4-21		
ISSUE DATE	12/22/04		

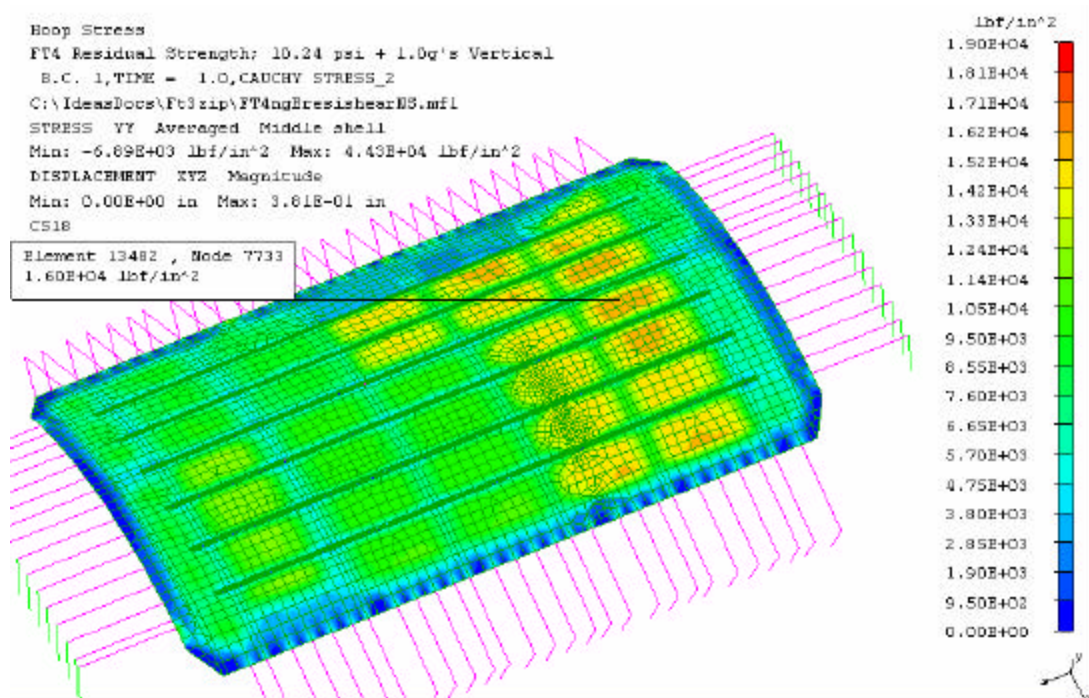


Figure 4-21

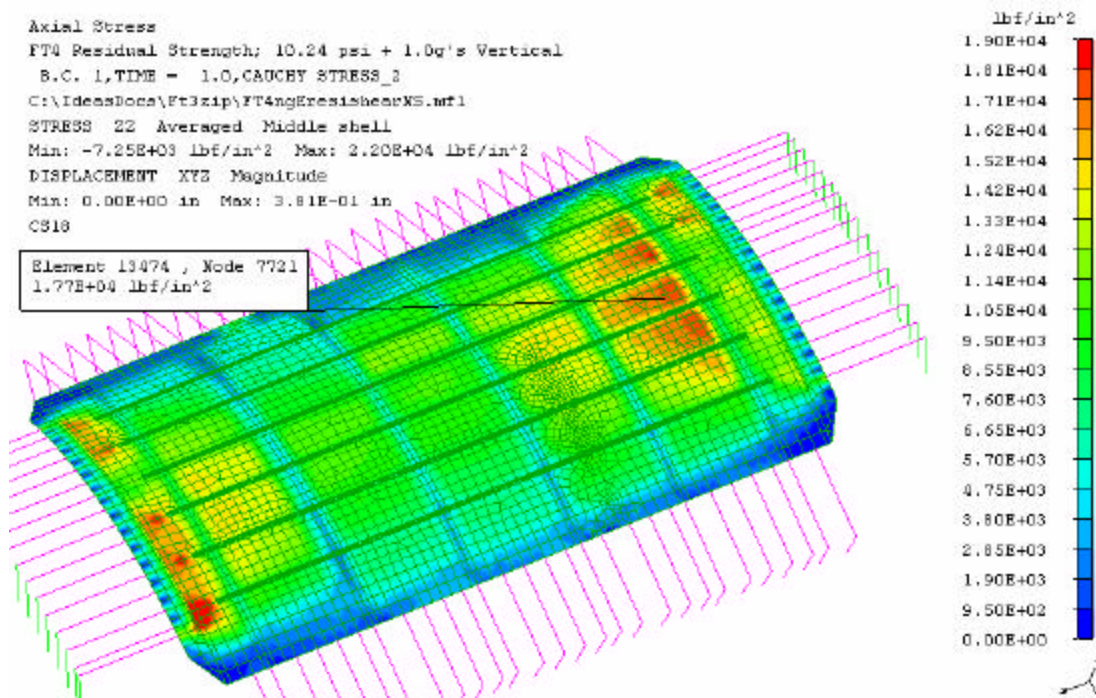


Figure 4-22

SHEET	4-17	NO.	4-087051-20
TOTAL	4-21		
ISSUE DATE	12/22/04		

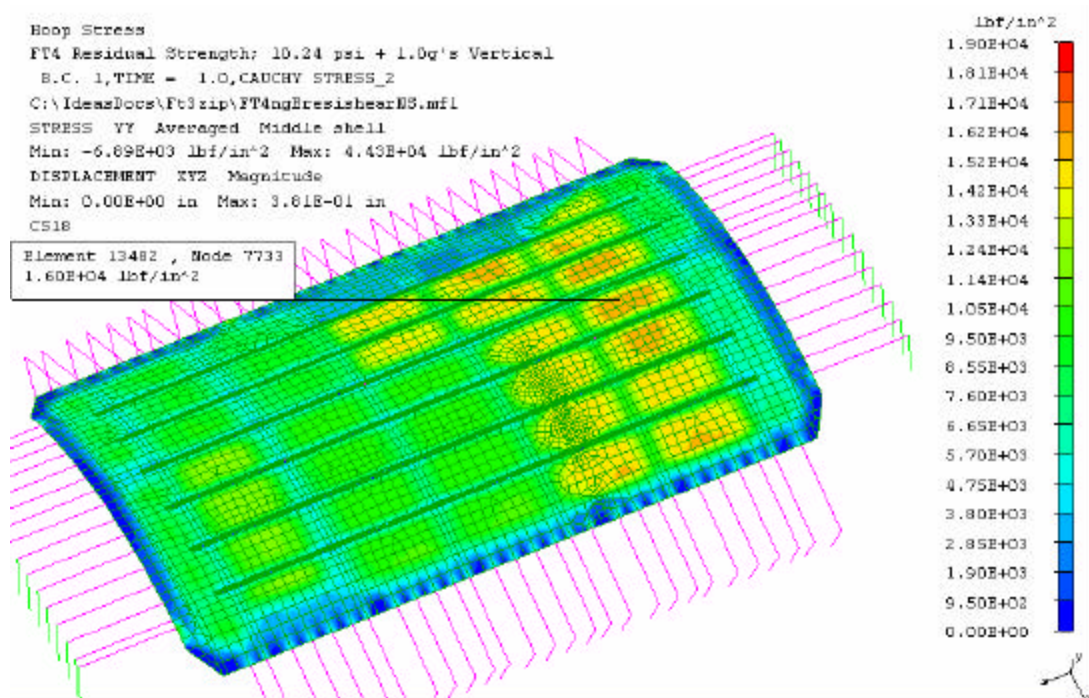


Figure 4-23

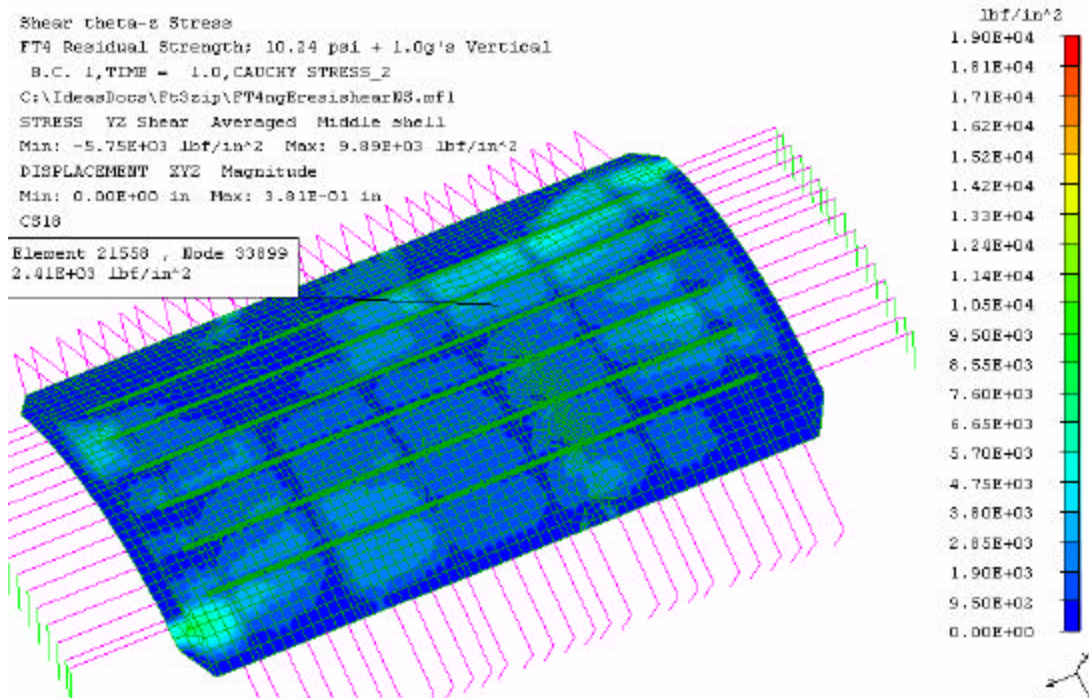


Figure 4-24

SHEET	4-18	NO.	4-087051-20
TOTAL	4-21		
ISSUE DATE	12/22/04		

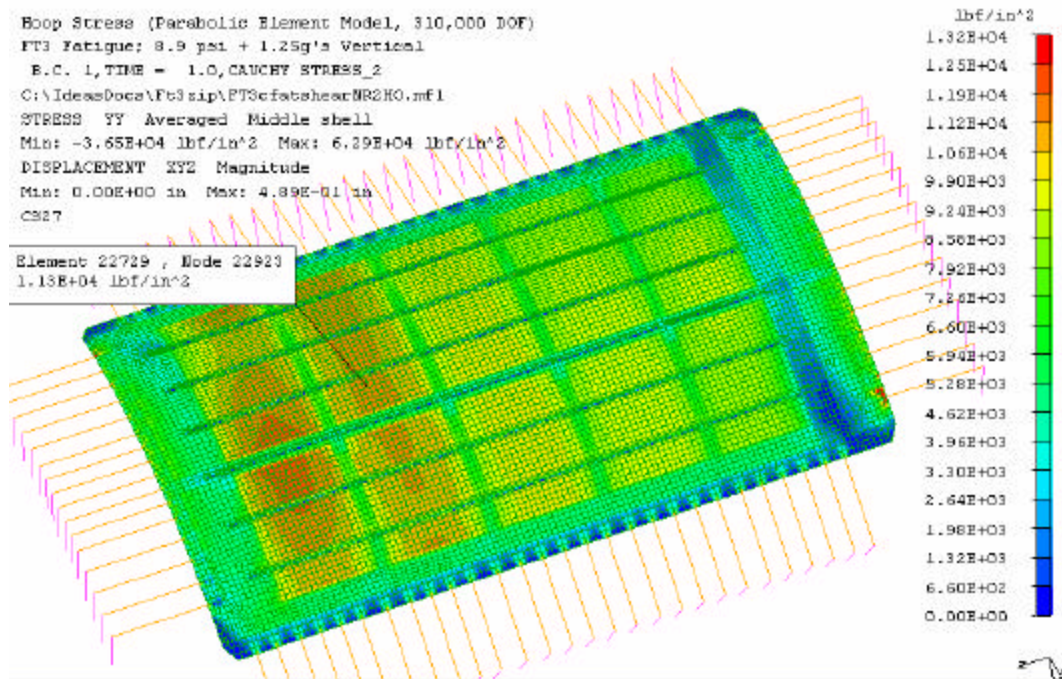


Figure 4-25

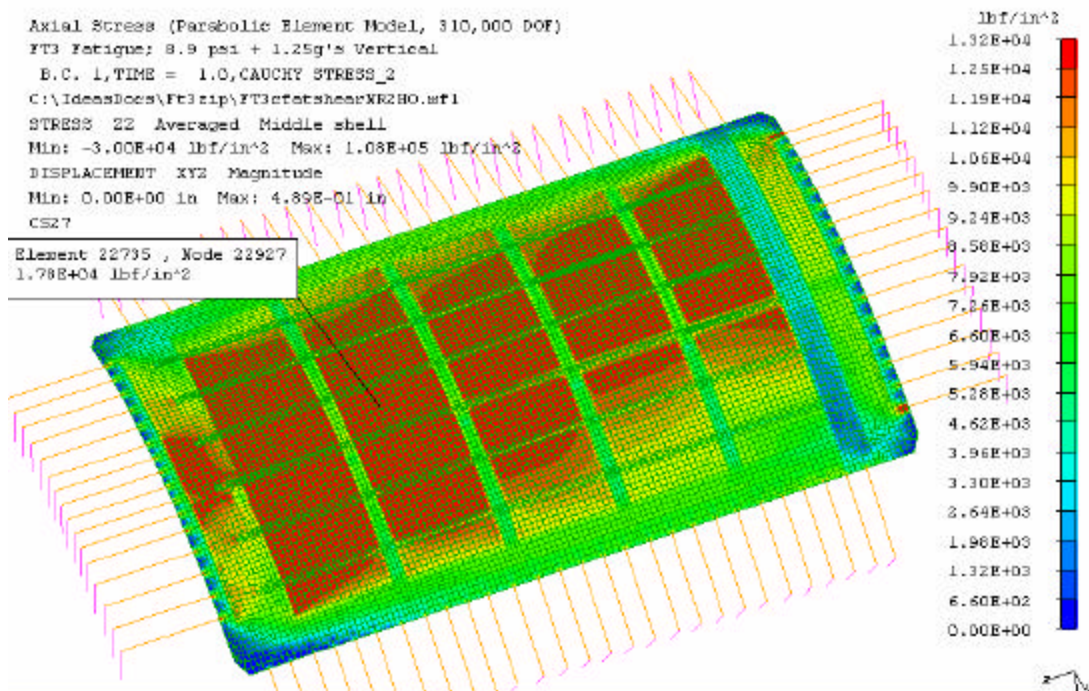


Figure 4-26

SHEET	4-19	NO.	4-087051-20
TOTAL	4-21		
ISSUE DATE	12/22/04		

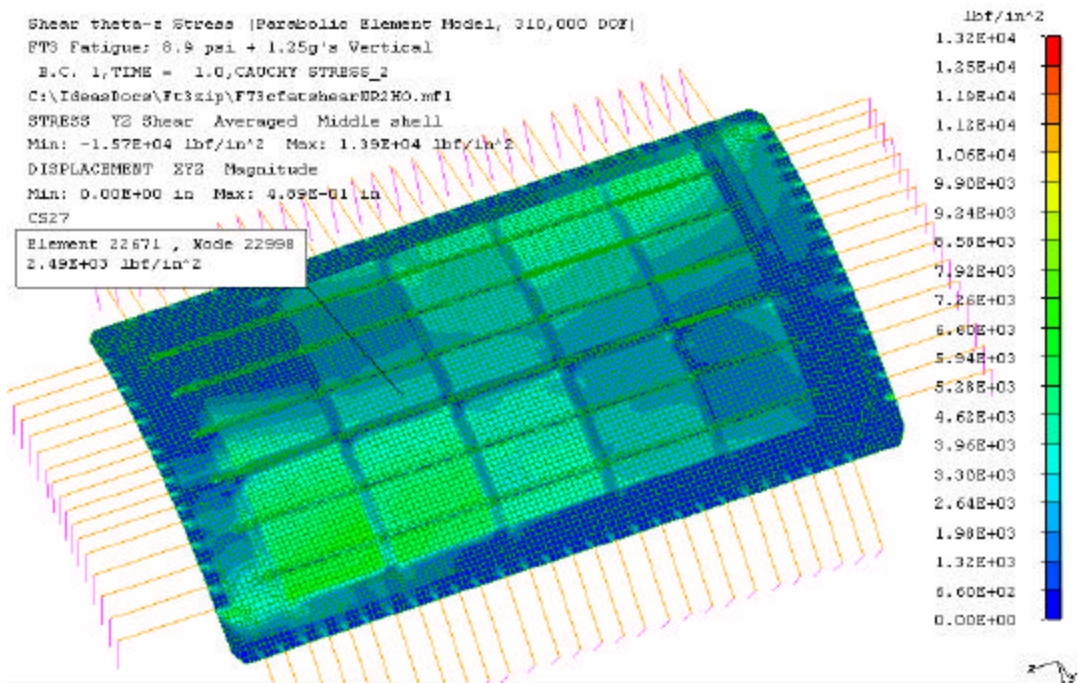


Figure 4-27

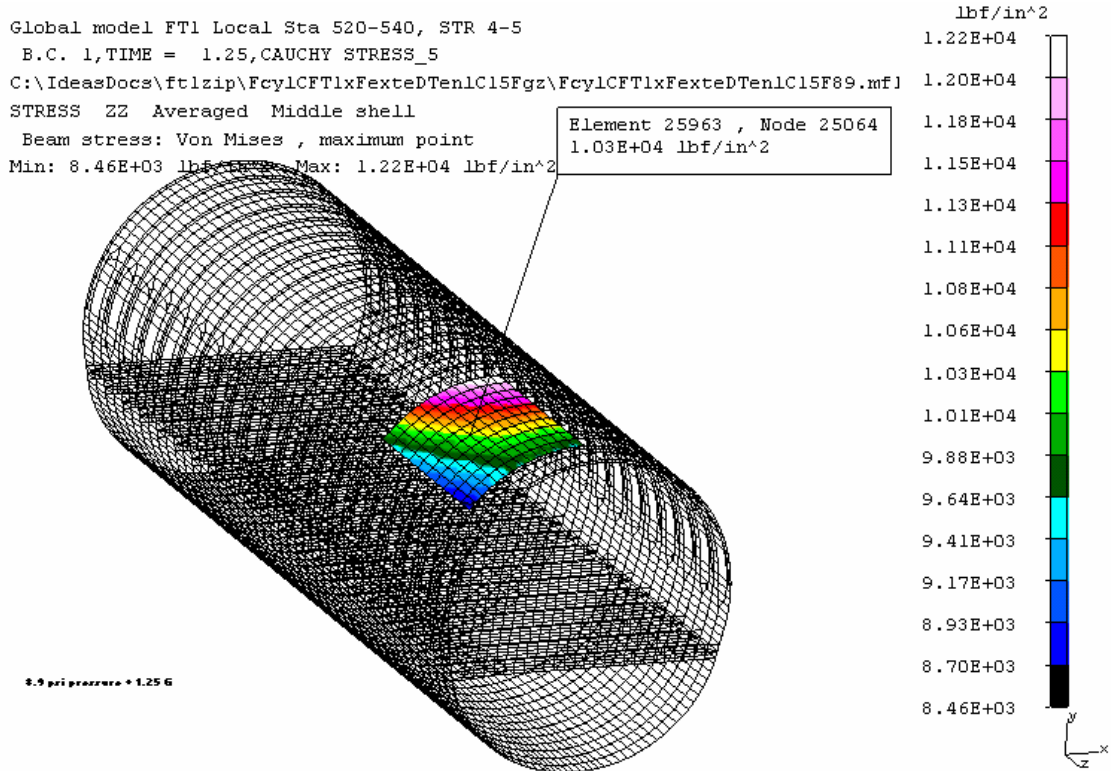


Figure 4-28: Fuselage section 43 global model with fatigue loads (8.9 psi + 1.25g)

SHEET	4-20	NO.	4-087051-20
TOTAL	4-21		
ISSUE DATE	12/22/04		

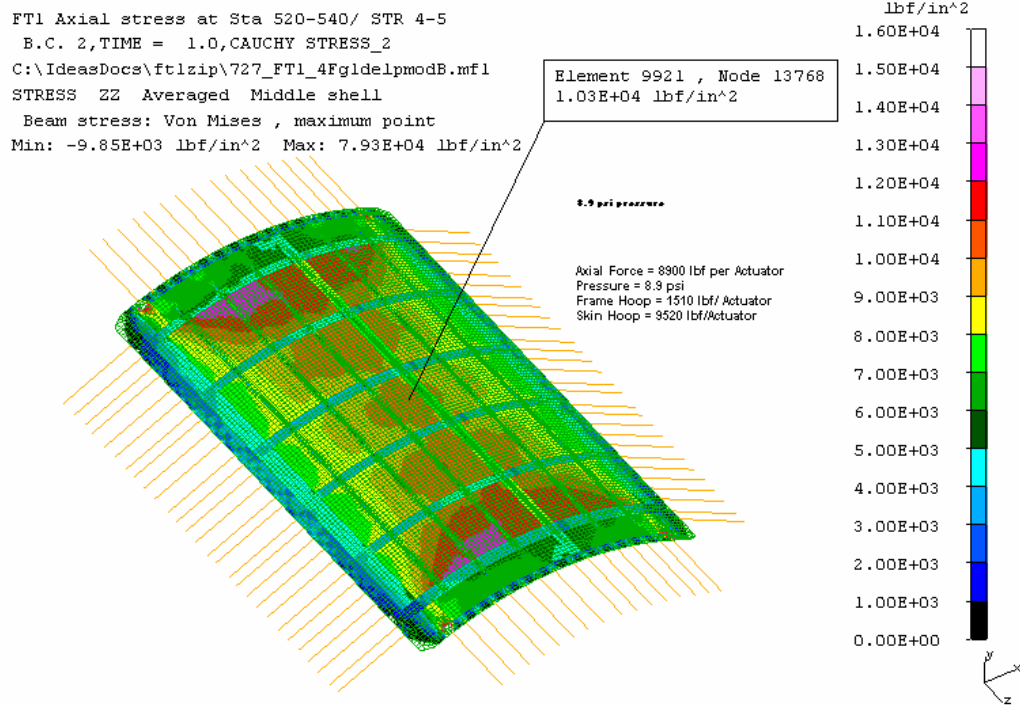
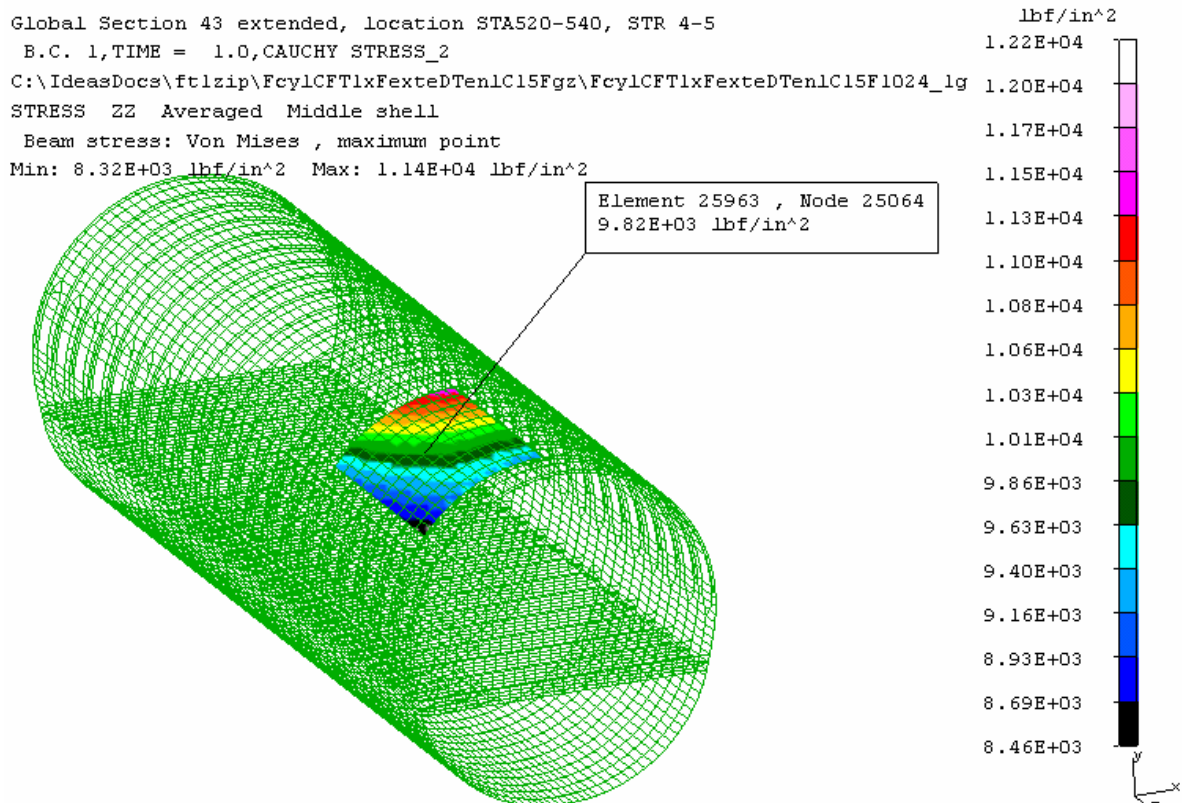
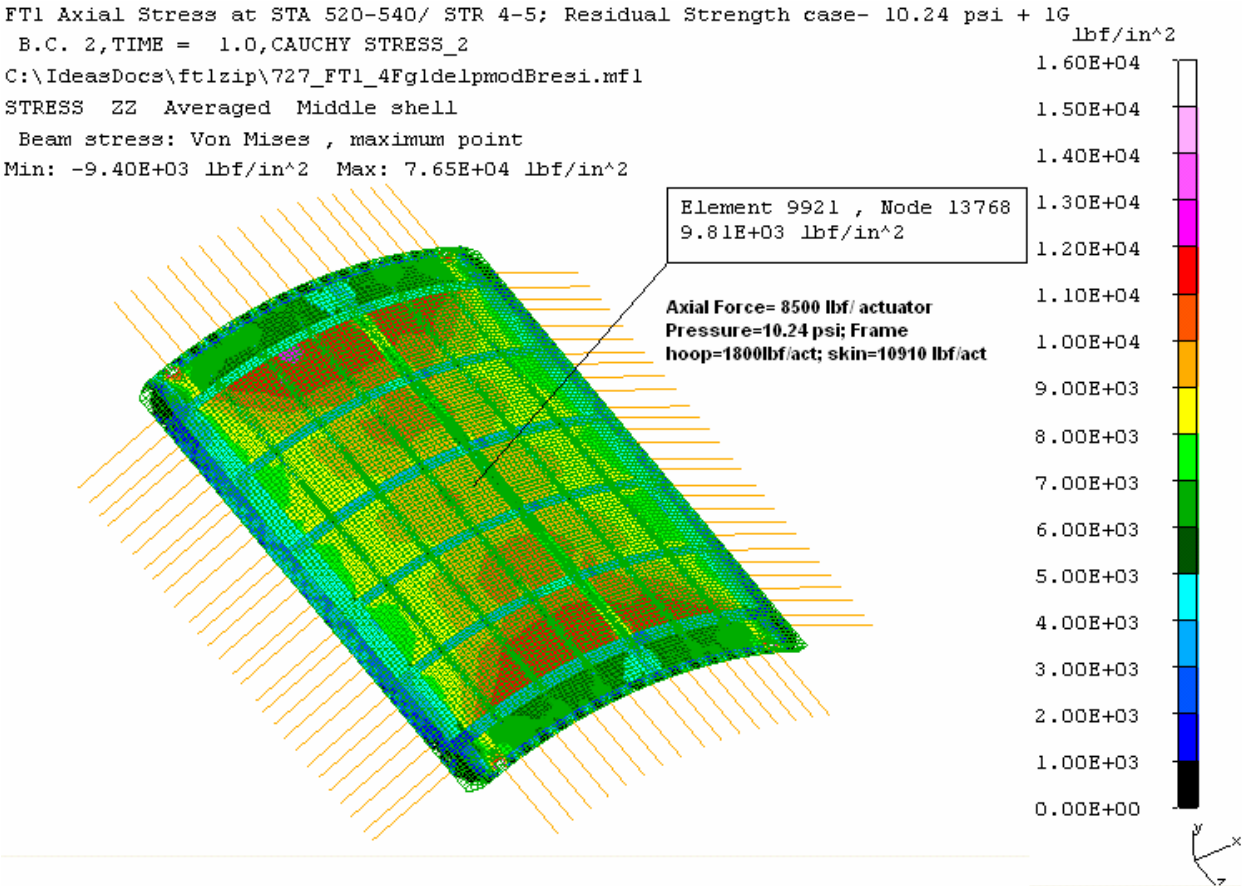


Figure 4-29: FT1 test panel with fatigue loads (8.9 psi + 1.25g)



SHEET	4-21	NO.	4-087051-20
TOTAL	4-21		
ISSUE DATE	12/22/04		

Figure 4-30: Section 43 global model with limit load (10.24 psi + 1g)



SHEET	5-1	NO.	4-087051-20
TOTAL	5-12		
ISSUE DATE	01/30/04		

CHAPTER 5: HALF BAY SHELL MODEL

In order to make pre-test crack growth calculation in the FT1, FT2 and FT3 test panel stringer 4L lap joint, the detailed stress distribution as a function of fuselage station is required. This stress distribution was determined by the creation of three non-linear displacement finite element models which include two to three circumferential bays and one half of a longitudinal bay. Symmetry about the bay center line is assumed and validated by intermediate models. The bays chosen were BS 500 to BS 560, BS 640 to BS 660, and BS 720C to BS 720D based on service history these bays are most likely to develop cracks first and the global finite element model shows the adjacent bays to have a slightly lower stress level due to the BS 681 butt splice in FT2 and the increase in skin thickness in FT3. The models extend from stringer 3 at the upper end to stringers 5 at the lower end. This provides enough distance from the lap joint to sort out eccentricities due to the lap splice. The models were created using COSMOSM 1.75A finite element software utilizing QUAD4 thin shell elements for all details. All major structural details are modeled with the exception of the fasteners that connect the shear ties to the frames and stringers, the fasteners that connect stringers 3 and 5 to the skin and the bonding adhesive that attaches the tear strap and lap splice doubler to the skin. The models have between 80,000 to 102,000 degrees of freedom. The basic model geometry can be seen in Figure 5-1.

Fastener Compliance

The fasteners were modeled as cylindrical shells that connect the upper skin to the lower skin and the stringer to the lower skin. The properties of the shells were determined by iterative runs of finite element strip models with the approximate predicted load applied to the strip. The displacement and bypass stress in five different finite element strip models were compared to strain compatibility calculations which utilized classical methods for calculation of fastener compliance. The fastener compliance was calculated using methodology that is similar to that found in NACA Technical Note No. 1051 and the strip compliance was calculated using Hooke's Law. The strip model element sizes and shapes were identical to those used in the final model. The cylindrical fastener shell properties were changed until the displacement results were within 1% calculated and the bypass stresses were within 5% of that calculated. An example of the strip models is shown in Figure 5-2.

SHEET	5-2	NO.	4-087051-20
TOTAL	5-12		
ISSUE DATE	01/30/04		

Boundary Conditions and Applied Loads

The boundary conditions at the upper and lower edges of the model were that of symmetry utilizing a local cylindrical coordinate system. The frame and tear strap edge of the model also utilized symmetrical boundary conditions. The mid bay edge of the model used displacements taken from the fuselage global model. The basic displacement boundary conditions can be seen in Figure 5-3.

The only loads applied to the model were that of 8.9 psi pressure to the entire inner surface of the upper and lower skins and a load around the fastener holes to make up for the missing area of the hole. The basic loading can be seen in Figure 5-4.

Results

The model was run using displacements for a 1.25 G flight condition and 8.9 psi pressure. The bypass stresses in the lap joint compare very well with those predicted and the axial stress is comparable to intermediate model results. The model will not be considered validated until after it is compared to strain gauge readings from the test panel. The deformed shape FT2 can be seen in Figure 5- 5. The FT2 axial membrane stress results can be seen in Figure 5-6.

In order to determine a stress gradient to be used for crack growth calculations at the critical lower fastener row, the circumferential stress below the lower row in the lap joint was plotted against it's location in the frame bay. The FT2 circumferential stresses in this area can be seen in Figure 5-7. The stress in line with the fastener locations was plotted at 3 times the fastener hole diameter below the fastener holes. The plots can be seen in Figure 5-8, Figure 5-9, and Figure 5-10.

SHEET	5-3	NO. 4-087051-20
TOTAL	5-12	
ISSUE DATE		01/30/04

Figures

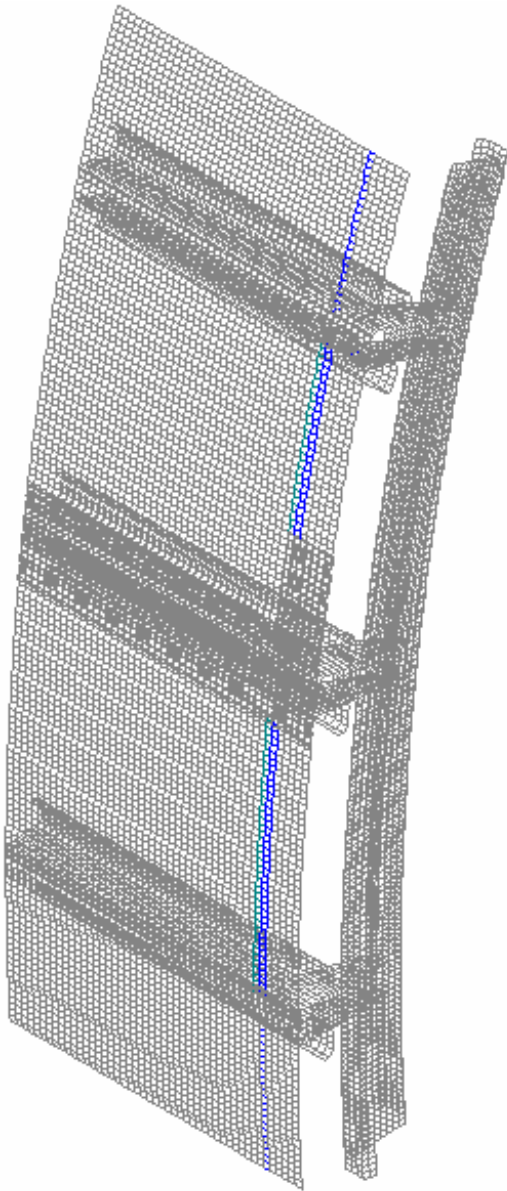


Figure 5-1 Model Geometry

SHEET	5-4	NO. 4-087051-20
TOTAL	5-12	
ISSUE DATE		01/30/04

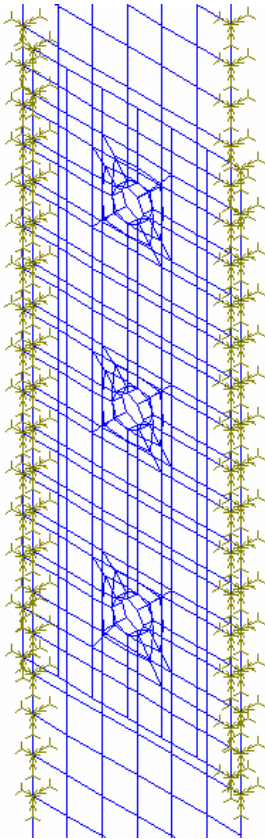


Figure 5-2. Strip Model

SHEET	5-5	NO.	4-087051-20
TOTAL	5-12		
ISSUE DATE	01/30/04		

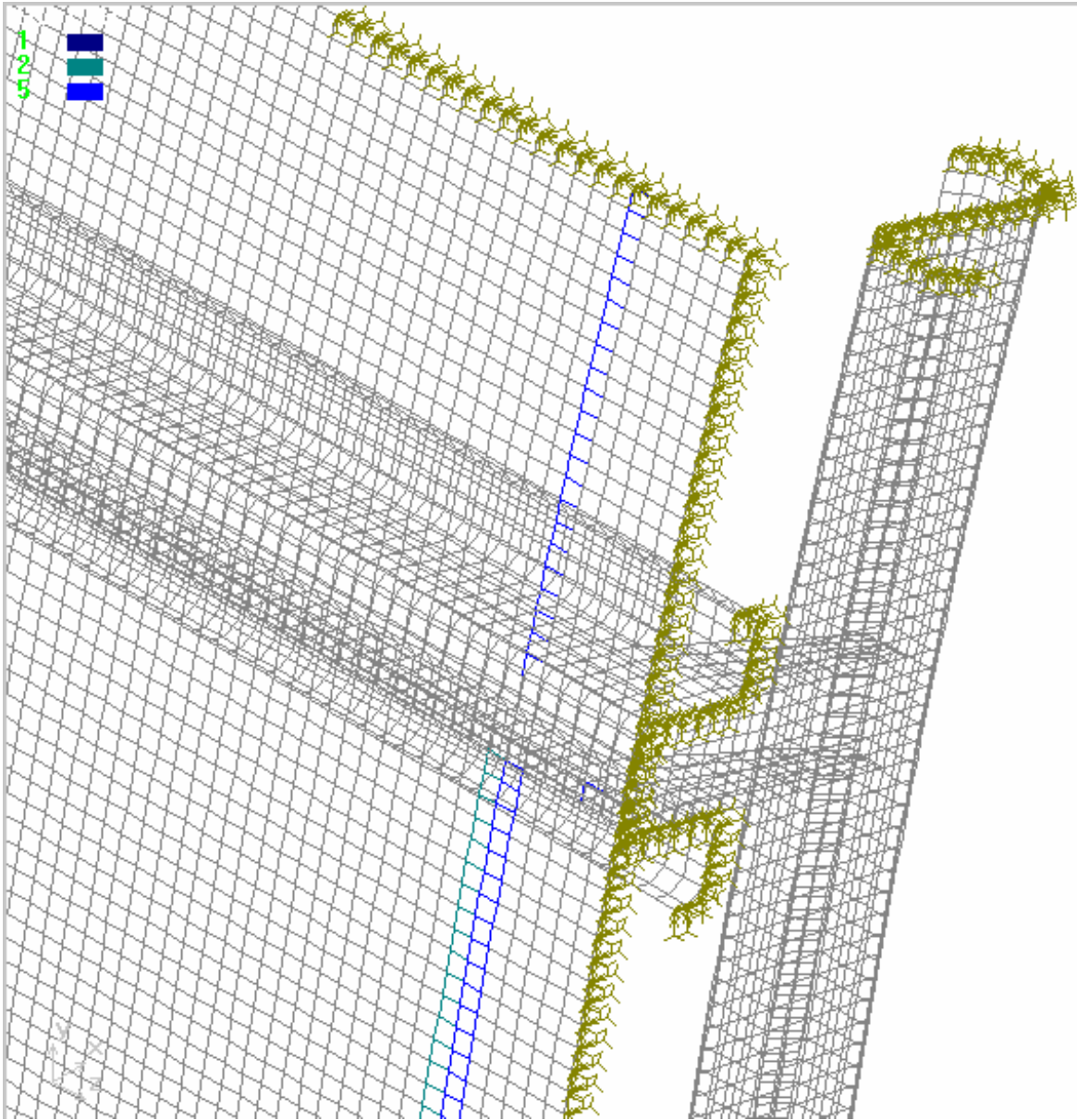


Figure 5-3: Displacement Boundary Conditions

SHEET	5-6	NO. 4-087051-20
TOTAL	5-12	
ISSUE DATE		01/30/04

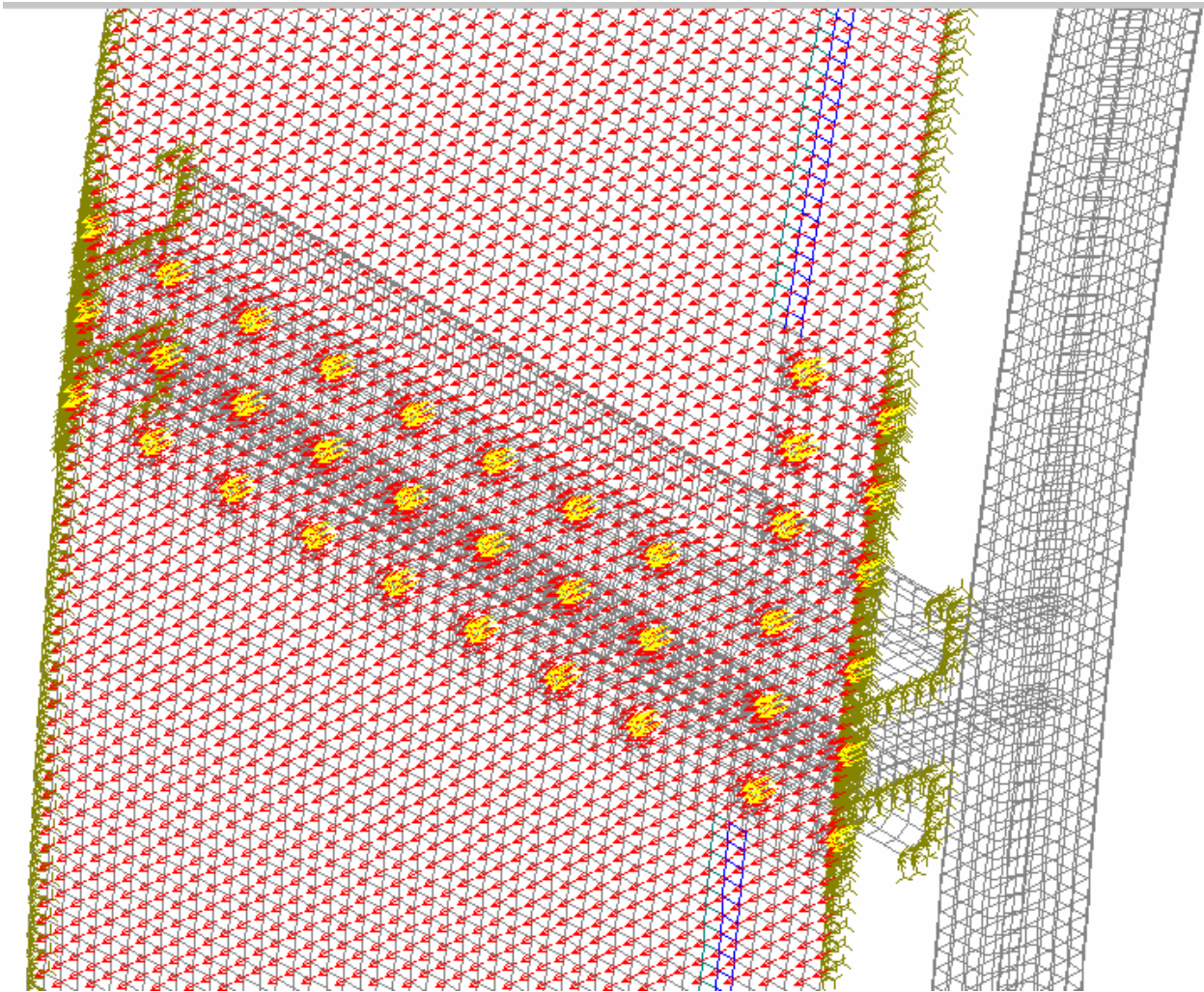


Figure 5-4 Pressure Loads

SHEET	5-7	NO.	4-087051-20
TOTAL	5-12		
ISSUE DATE	01/30/04		

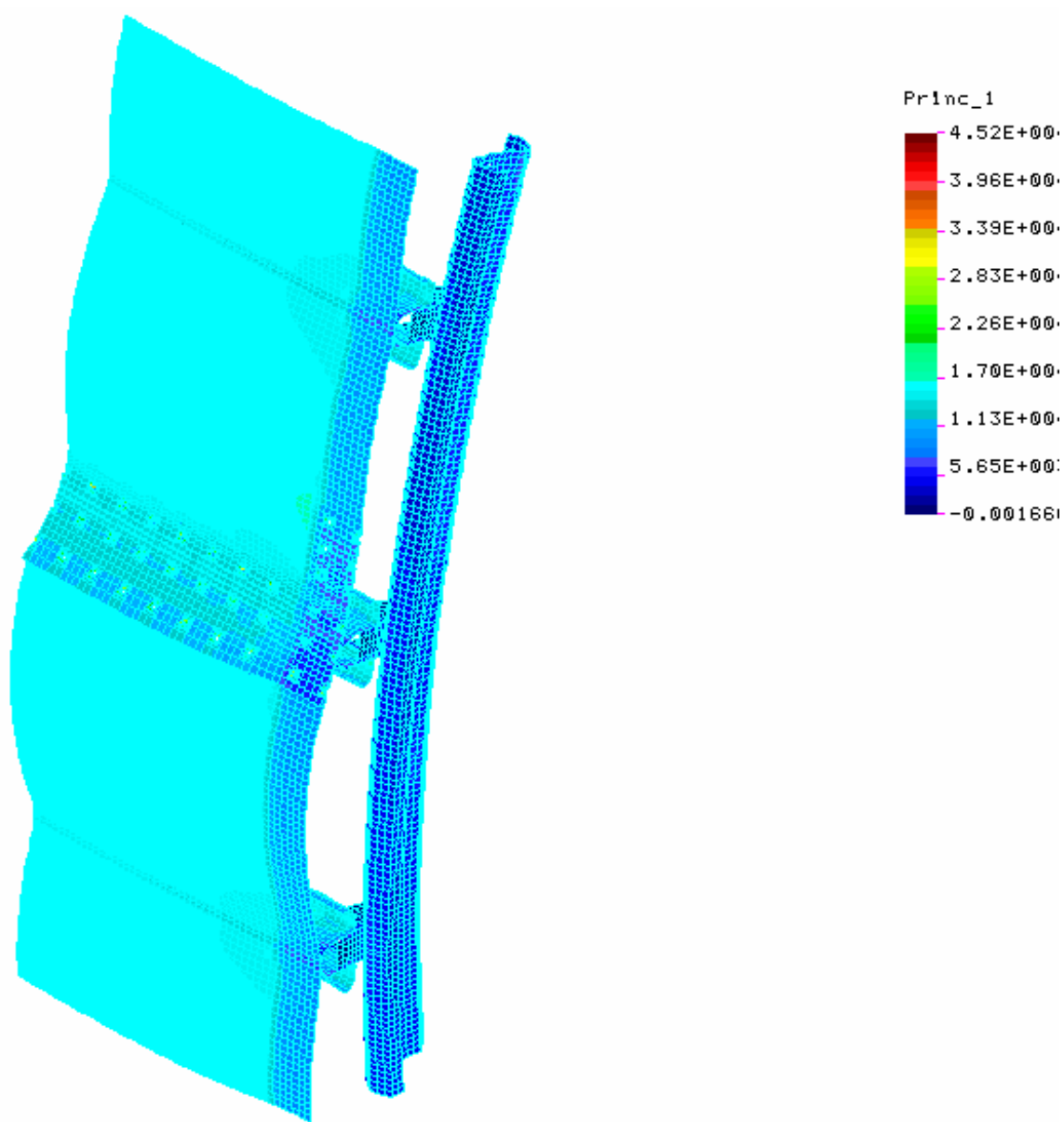


Figure 5- 5 Deformed Shape at 36:1

SHEET	5-8	NO.	4-087051-20
TOTAL	5-12		
ISSUE DATE	01/30/04		

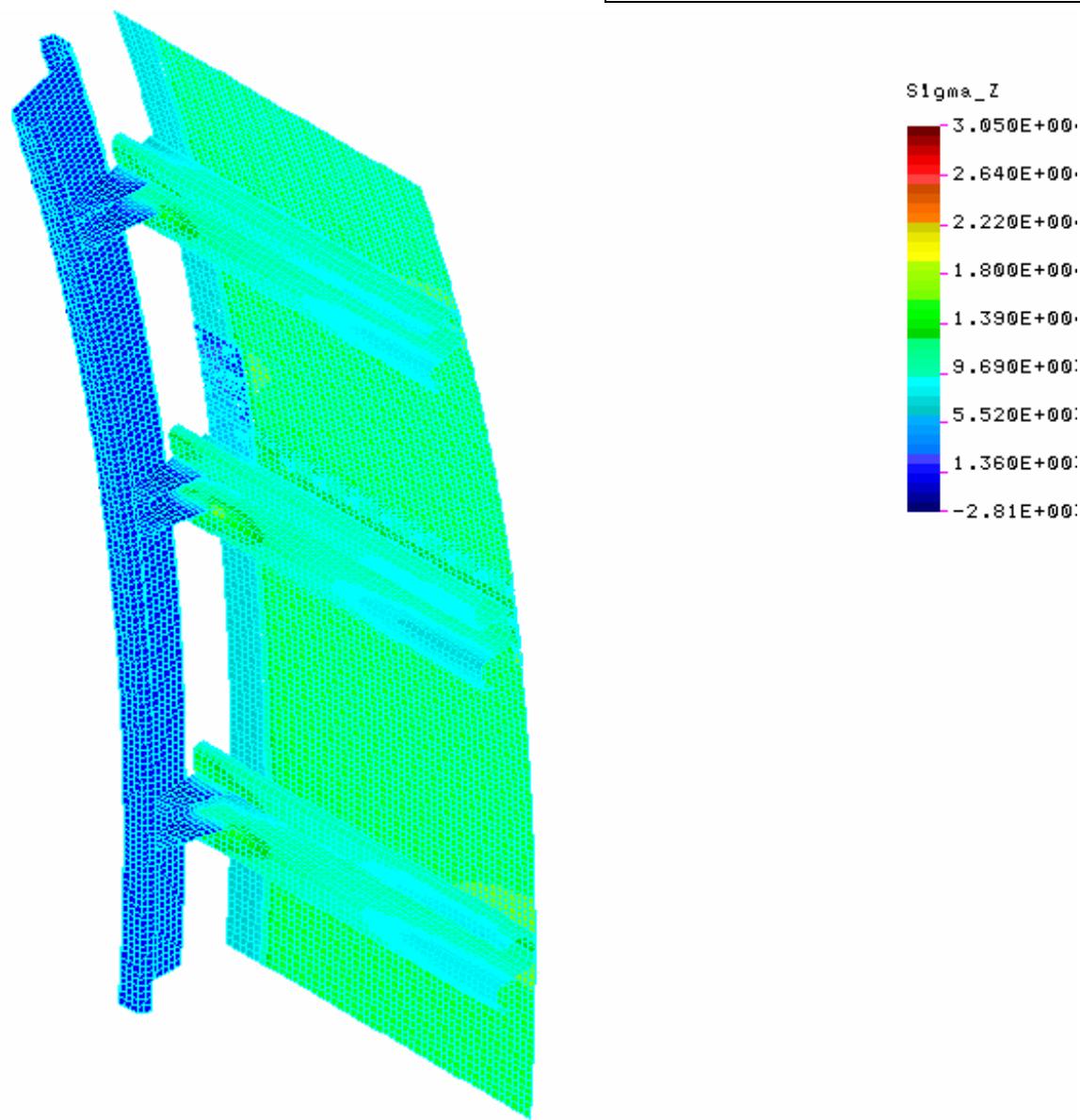


Figure 5-6 Axial Membrane Stress

SHEET	5-9	NO. 4-087051-20
TOTAL	5-12	
ISSUE DATE		01/30/04

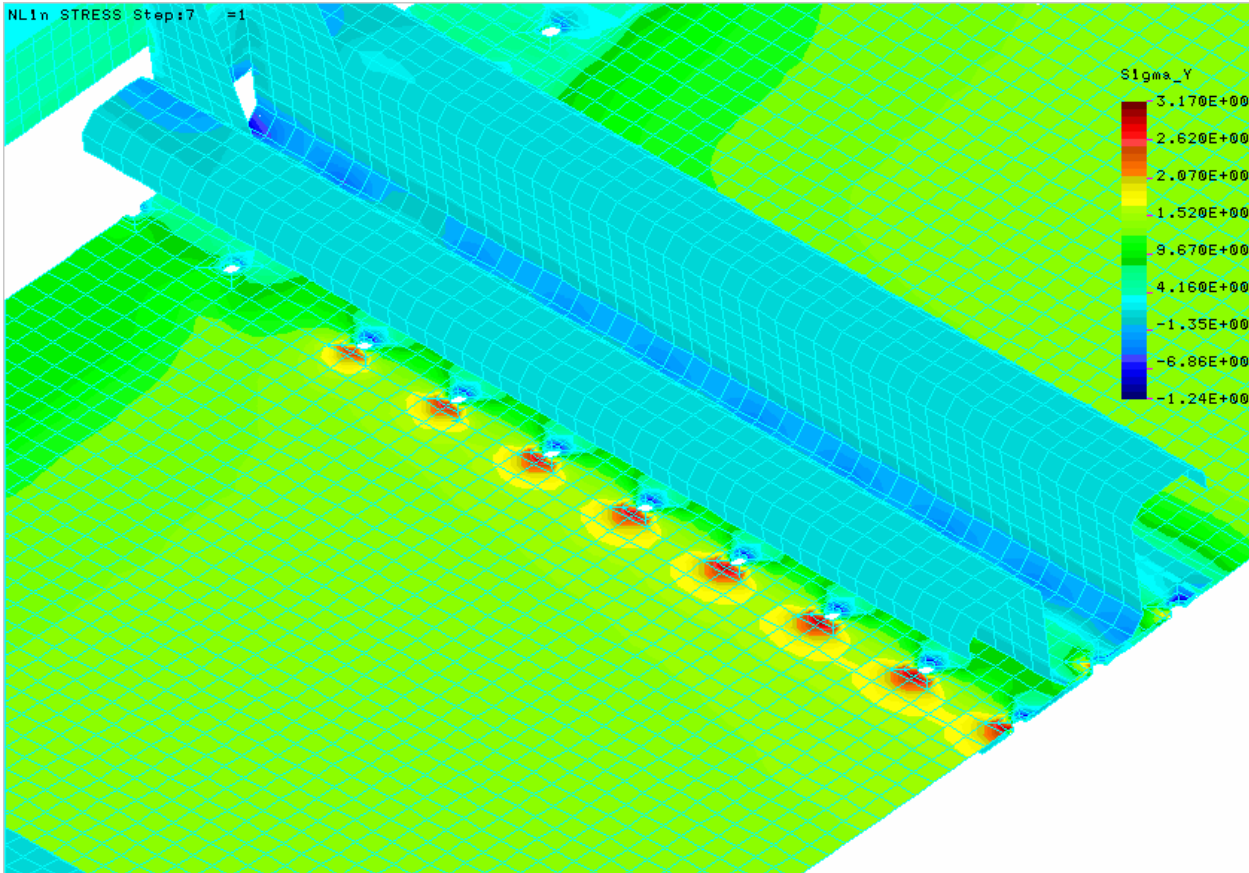
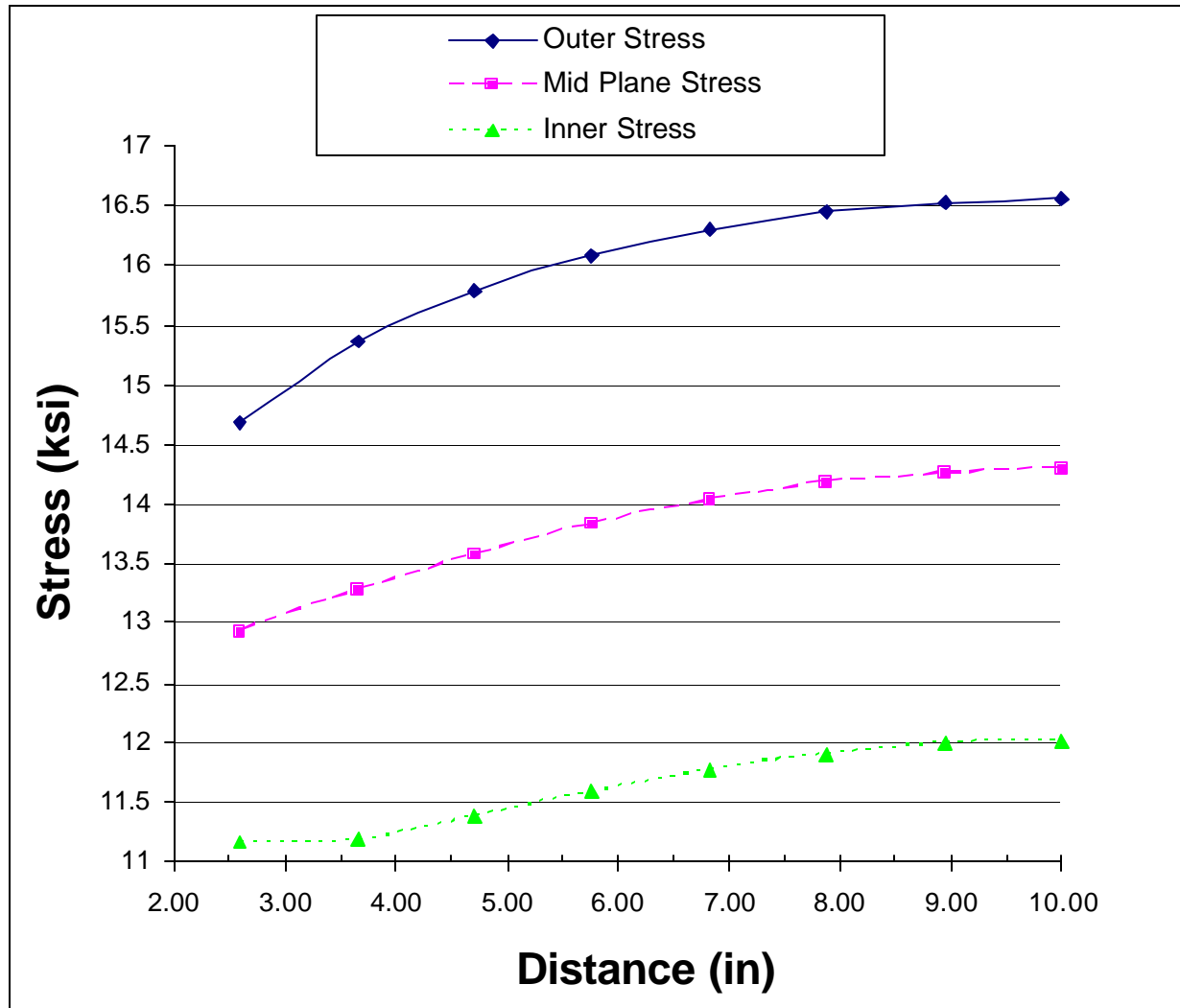


Figure 5-7 Outer Surface Circumferential Stress

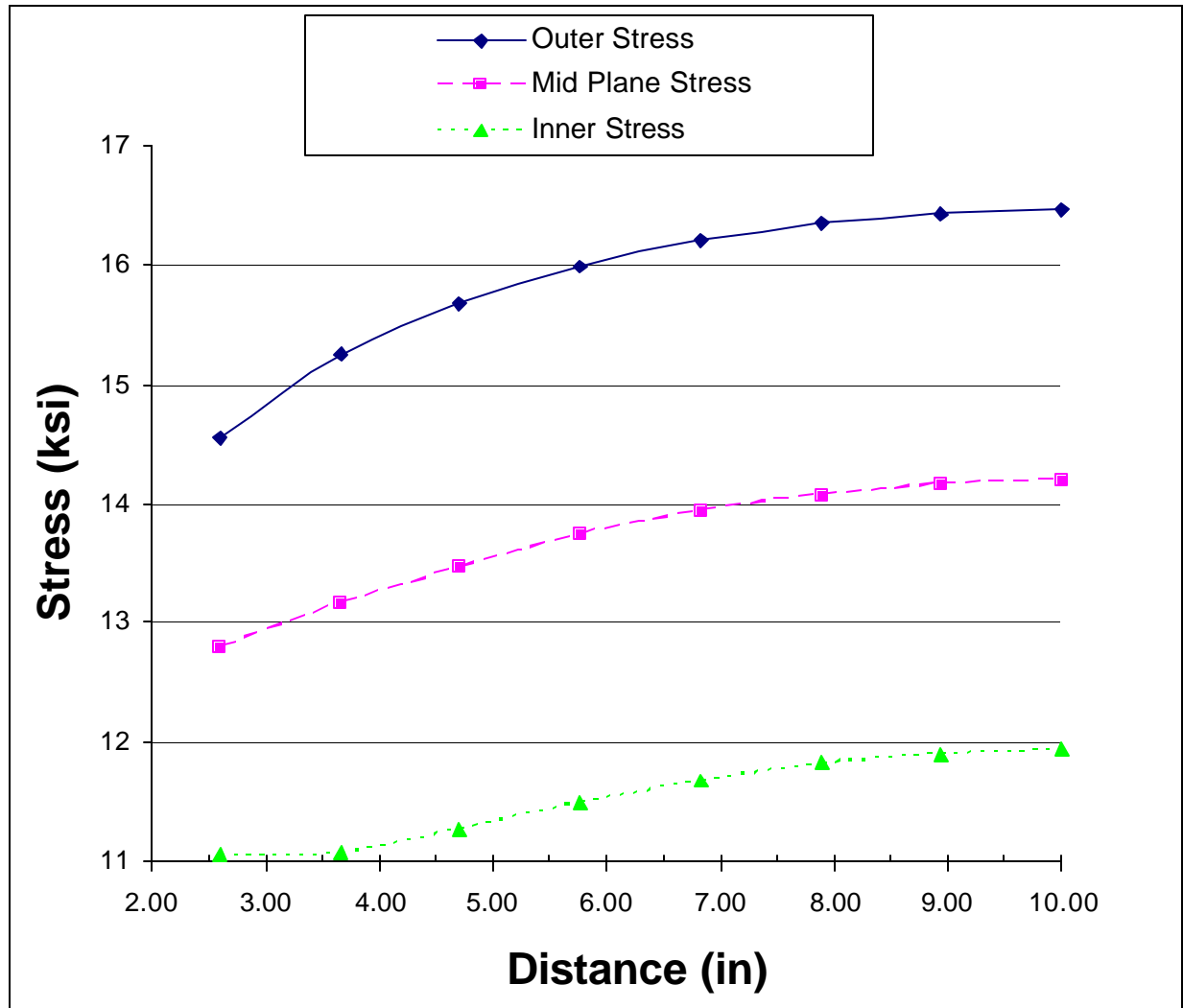
SHEET	5-10	NO.	4-087051-20
TOTAL	5-12		
ISSUE DATE	01/30/04		



Distance	Outer Stress	Mid Plane Stress	Inner Stress
2.60 in	14.69 ksi	12.93 ksi	11.17 ksi
3.66 in	15.37 ksi	13.28 ksi	11.19 ksi
4.71 in	15.78 ksi	13.58 ksi	11.38 ksi
5.77 in	16.08 ksi	13.84 ksi	11.59 ksi
6.83 in	16.3 ksi	14.04 ksi	11.78 ksi
7.89 in	16.45 ksi	14.18 ksi	11.91 ksi
8.94 in	16.53 ksi	14.26 ksi	11.99 ksi
10.00 in	16.56 ksi	14.29 ksi	12.02 ksi

Figure 5-8 FT1 Circumferential Stress VS Frame Bay Location at 3D

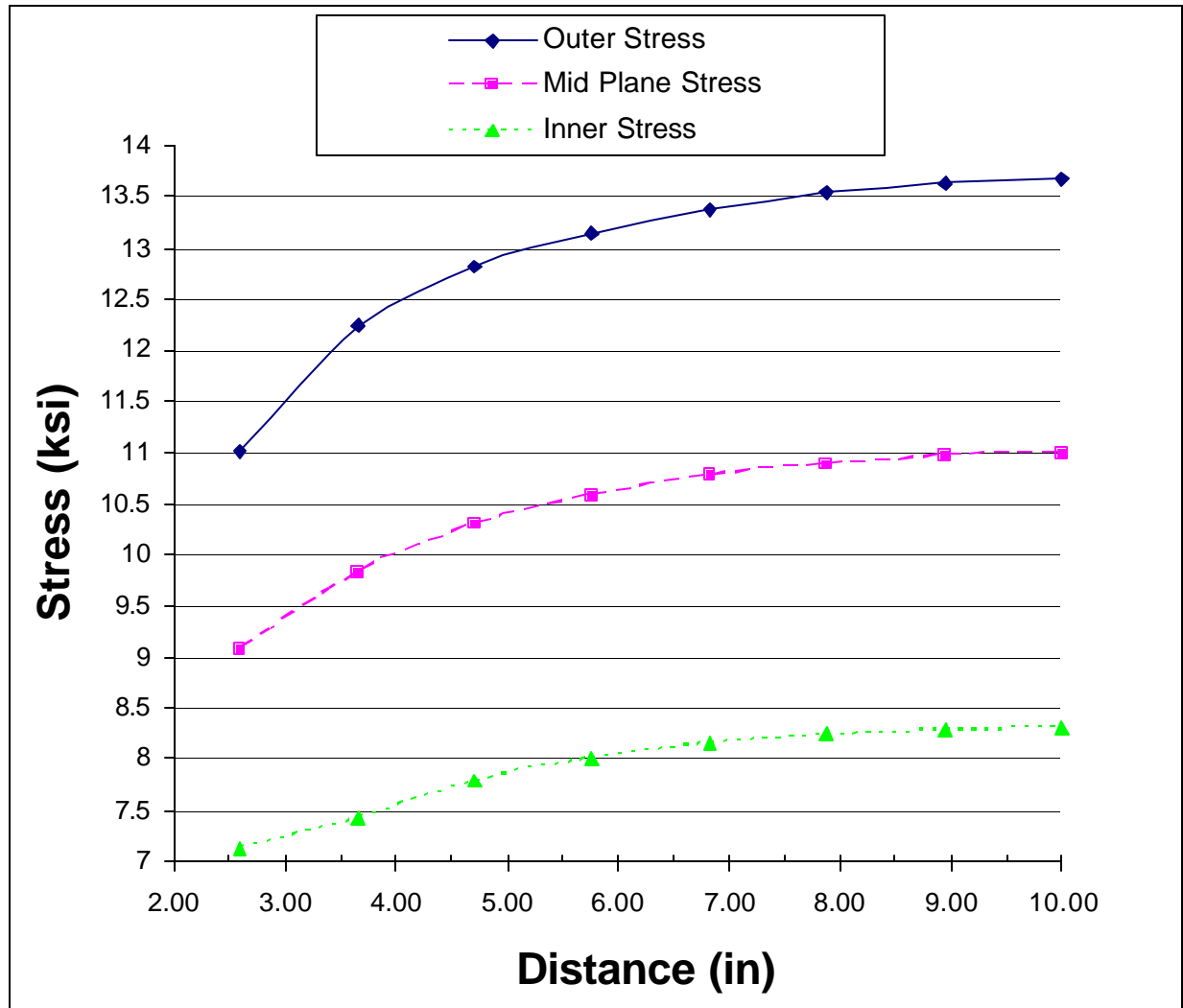
SHEET	5-11	NO. 4-087051-20
TOTAL	5-12	
ISSUE DATE		01/30/04



Distance	Outer Stress	Mid Plane Stress	Inner Stress
2.60 in	14.56 ksi	12.81 ksi	11.06 ksi
3.66 in	15.25 ksi	13.17 ksi	11.08 ksi
4.71 in	15.67 ksi	13.47 ksi	11.27 ksi
5.77 in	15.98 ksi	13.74 ksi	11.5 ksi
6.83 in	16.2 ksi	13.94 ksi	11.68 ksi
7.89 in	16.35 ksi	14.08 ksi	11.82 ksi
8.94 in	16.43 ksi	14.17 ksi	11.9 ksi
10.00 in	16.46 ksi	14.2 ksi	11.93 ksi

Figure 5-9 FT2 Circumferential Stress VS Frame Bay Location at 3D

SHEET	5-12	NO.	4-087051-20
TOTAL	5-12		
ISSUE DATE	01/30/04		



Distance	Outer Stress	Mid Plane Stress	Inner Stress
2.60	11.02	9.073	7.13
3.66	12.25	9.837	7.423
4.71	12.81	10.3	7.784
5.77	13.15	10.58	8.017
6.83	13.38	10.77	8.159
7.89	13.54	10.89	8.247
8.94	13.63	10.97	8.297
10.00	13.67	10.99	8.313

Figure 5-10 FT3 Circumferential Stress VS Frame Bay Location at 3D

SHEET	6-1	NO.	4-087051-20
TOTAL	6-32		
ISSUE DATE		12/22/04	

CHAPTER 6: STRESS STATE AT THE FASTENER HOLE

This chapter includes discussion of several FEA analyses to determine the detailed stress state at the critical fastener hole. This stress state is complex, as it is a function of the far field fuselage hoop and longitudinal stresses, plus the local effects of joint eccentricity, fastener bending, and residual stresses from the rivet installation process. At this point, several independent models have been created to address individual aspects of the problem. The goal is to create an integrated model that incorporates effects from all of these stress sources.

2-D Rivet Installation Simulation

Finite element analysis was accomplished to identify requirements for accurate simulation of residual stresses due to rivet installation in a typical B727 forward fuselage stringer 4 lap joint. Nonlinear axisymmetric and 3D models were developed.

Axisymmetric modeling simplifies the parametric analysis as it enables capturing fine geometry resolution necessary for accurate local stress results within a model that allows for practical run times.

Axisymmetric models ranging from 5000 to 30000 DOF were developed in this work. The rivet installation simulation requires solving a contact problem that involves both material and geometric nonlinearities. A 90 deg. angle between the normals to contact surfaces in the undeformed state complicates the contact simulation. The analysis requires about 150 nonlinear load increments that include from 2 to 11 iterations.

An axisymmetric finite element model is shown in Figure 1. A 60" thick 2024-T3 Aluminum upper skin and a 40" thick 2024-T3 Aluminum lower skin are joined with a BACR15CE5D5 2017-T4 Aluminum rivet. The rivet is 5/32" in diameter and 0.312" long [6-1,6-2]. The rivet hole diameter is 0.162" that is within the 0.159" and 0.165" limits listed in Ref. [6-2]. The model is 0.5" wide. The Young modulus, the Poisson ratio, and the yield strength for 2024-T3 and 2017-T4 Aluminum are listed in Ref. [6-3]. The inelastic stress-strain relationship for 2017-T4 Aluminum is assumed the same as for 2024-T4 Aluminum. Inelastic material behavior with isotropic hardening is selected. The rivet displacements are applied through parts meshed with elements that are about 100 times stiffer than the rivet material. A

SHEET	6-2	NO.	4-087051-20
TOTAL	6-32		
ISSUE DATE		12/22/04	

0.2 coefficient of friction is assigned for all surface contacts. A 0.13" applied rivet displacement results a 0.08" tail height representative of measurements. Such tail height is within the 0.05" and 0.1" limits listed in Ref. [2]. Symmetry boundary conditions are assumed at the skin right surfaces. The model is meshed with four-node reduced integration axisymmetric elements CAX4R in ABAQUS finite element code.

Figure 6-2 shows the initial model configuration. Figure 6-3 depicts the deformed shape and the residual hoop stress contour plot. The skin residual hoop tension at the hole surface and tension away from the hole is consistent with the finite element results of Ref.[6-4].

Effects of local geometry on the stress were further investigated. Simplification of the rivet head geometry, shown in Figure 6- 4, improves the convergence and does not significantly affect the residual stress state in the lower skin as shown in Figure 6- 5. Constraining the vertical displacements at the rivet head surface eliminates the need in modeling the upper tool.

Increasing the rivet hole diameter within the allowable limits [6-2] as shown in Figure 6- 6 does not affect the residual stress state in the lower skin in accordance with Figure 6- 7. If the hole size in the upper skin is larger compared to the hole size in the lower skin as shown in Figure 6- 8, the residual hoop compression in the lower skin at the hole surface is reduced in accordance with Figure 6- 9. If surface defects depicted in Figure 6-10 - Figure 6- 14 are introduced, the lower skin residual hoop stresses change to tension as shown in Figs. 6-11, 6-13, and 6-15. The presence of drill shavings at the skin faying surfaces results in the hoop tension at the lower skin faying surface as shown in Figure 6- 16 - Figure 6- 19. Also, reducing the coefficient of friction to 0.05 results in lower skin hoop tension at the hole surface. See Figure 6- 20 and Figure 6- 21 for the geometry and hoop residual stress contour plots.

The presence of wet sealant between the upper and lower skin faying surfaces is considered next. The sealant is simulated with low stiffness hyperelastic elements. An Aluminum segment representing a drill shaving blocking the sealant flow into the rivet hole is placed at the hole surface. Figure 6-22 shows the undeformed model configuration. The hoop stress contour plots for 2 loading steps are shown in

SHEET	6-3	NO.	4-087051-20
TOTAL	6-32		
ISSUE DATE	12/22/04		

Figures 6-23 and 6-24. Figure 6-25 shows the residual hoop stress contour plot. High residual hoop tensile stress values are obtained in areas susceptible to cracking in accordance with inspection results.

The axisymmetric finite element model results indicate that local geometry details and the state of adhesive during the riveting significantly affect the skin residual stresses, and therefore, have to be accounted for.

The service findings indicate there are no symmetric rivets in aircraft lap joints. Axisymmetric models are not capable of capturing this phenomenon. A simple 3D model is shown in Figure 6-26. The model is 0.5" wide and 1" long. A 0.2 coefficient of friction is assigned for all surface contacts. The sealant is not modeled. The rivet head vertical displacements are constrained and a 0.13" vertical displacement is applied to the rivet tail. Symmetry boundary conditions are assumed at the skin lateral surfaces. The model is meshed with eight-node reduced integration brick elements C3D8R in ABAQUS finite element code. If there is no clearance between the rivet and the skin in the initial state, the deformation is symmetric as shown in Figure 6-27. If a clearance is present, the deformation is not symmetric. Figure 6-28 shows the deformed geometry and the maximum principal residual stress contour plot.

Based on the results of this sensitivity analysis, a 3D finite element model that captures local geometry features representative of the service hole quality, and accounts for the presence of sealant is needed for accurate simulation of the skin residual stresses due to the rivet installation.

SHEET	6-4	NO.	4-087051-20
TOTAL	6-32		
ISSUE DATE		12/22/04	

3-D Joint Analysis

To accurately determine the stress states around the rivet holes in skin in the lap joint area, a 3D FEA analysis of the joint was performed. The intent of this analysis is to determine the stress state around the lower skin rivet hole due to service loads only. The next step is to superimpose the residual stress due to installation from the previous analysis (Rivet installation simulation) and reapply service loads to accurately determine the stress state around the rivet hole to validate the typical cracking found around the lower row of fastener holes in the lower skin of the lap joint.

The baseline model was flat without the fuselage curvature with dimensions as shown in Figure 6- 29 and 6-30. Enforced displacement was applied to the lower skin to match a far field hoop stress of 14.7 ksi in the lower skin. A geometric non linear run of this model did not converge in EDS/IDEAS. Therefore, it was decided to incorporate the fuselage curvature with 74.0 inches as the radius and extend the model circumferentially to half bay on either sides and apply symmetric boundary conditions and pressure to the skin (see Figure 6- 31). Contacts were defined between the upper skin, lower skin and the rivets. The rivets were connected to the ground with very weak springs in order to prevent the rigid body motion of the rivets. The level of mesh refinement was the same as the baseline model as shown in Figure 6- 30. The model did not converge since the mesh refinement on the rivet and near the rivet holes was not adequate. The mesh was then locally refined on the rivet and near the rivet holes as shown in Figure 6- 32. The model still did not converge in IDEAS. The same model however converged using ABAQUS at FAA technical center at Atlantic City, NJ. The model was geometric nonlinear with lower reduced integrated hexahedral elements (C3D8R) with about 330,000 degrees of freedom. The contacts between the upper skin, the lower skin and the rivets were given a coefficient of friction of 0.2 based on ref [4]. The material property was assumed linear. The model had symmetric boundary conditions at the edges. A pressure of 7.5 psi (87.1% of 8.6 psi) was applied based on the results of the FT2 symmetric model as shown in Figure 6- 33. The stress distribution in the lowermost rivet hole in the lower skin is very much in line with the cracking pattern observed in the stringer 4 lap joint (see Figure 6- 34). The peak maximum principal stress in this region is about 52 ksi (see Figure 6- 35).

SHEET	6-5	NO.	4-087051-20
TOTAL	6-32		
ISSUE DATE		12/22/04	

The strip model was further modified such that the circumferential symmetric boundary conditions lie on the inflection points based on the half bay model. Therefore the model was extended up to the inflection points as shown in Figure 6- 36, keeping the other aspects of the model the same as the previous iteration. The peak maximum principal stress was 55.8 ksi (see Figure 6- 37). The stress distribution on the lower rivet hole on the lower skin remained the same as before (see Figure 6- 38). Since the stress is more than the yield of 40 ksi for the material 2024-T3, a non linear stress-strain curve was defined for the skin as shown in Figure 6- 39. The analysis was rerun with a higher pressure of 7.75 psi (87.1 % of 8.9 psi). The peak maximum principal stress was 46 ksi on the lower rivet hole of the lower skin as shown in Figure 6- 40. The peak plastic strain equivalent was around 0.2% (see

Figure 6- 41). It should be remembered that the stringer has not been represented in the model. The stringer will provide some additional stiffness to the joint. To get around the task of modeling the stringer in detail, the stringer was represented as a radial spring with an arbitrary stiffness. The stiffness of this spring or in combination with a torsional spring can be tuned to match a far field stress of 14.7 ksi on the lower skin.

Figure 6- 41 shows the work in progress, wherein the stringer has been represented as an extensional spring with an arbitrary stiffness of 1000 lbf/in. A pressure of 8.9 psi was applied. The far field stress is only about 9 ksi and therefore the spring stiffness has to be reduced.

A more straight forward approach may be model the stringer and the frame as shells to account for their stiffness contribution and apply pressure of 8.9 psi. This work will be completed in the near future.

It can be concluded that the stress levels on the lap joint with the stringer excluded and due to the service loads alone is quite high (more than the yield strength of 48 ksi for 2024-T3 Al). The maximum plastic strain equivalent is 0.2%. It should be noted that the rivets in the model are not interference fit. An interference fit will contribute to some compressive stress which will reduce the overall stress levels. Also the stress levels might lower if the residual stresses due to installation are added to the model. If compressive hoop stress is produced in the close proximity of the rivet hole surface, it might help reduce the overall stress levels. As mentioned before, the stringer and the frame should be modeled for a more accurate representation of the joint and this work is currently in progress.

SHEET	6-6	NO.	4-087051-20
TOTAL	6-32		
ISSUE DATE		12/22/04	

Displacements in the baseline 3D strip model without the radial and torsional springs and a pressure of 7.75 psi compared well with the half bay shell model with stringers and a pressure of 8.9 psi. The comparisons are shown in figures 6-43 and 6-44.

During Q9 an attempt was made to map the residual stresses due to rivet installation onto the baseline strip model to establish the procedure of stress mapping. The residual stresses from a 2D axisymmetric rivet model were input as initial conditions to the strip model. One row of hex elements around the each rivet hole were oriented in their respective local rivet hole cylindrical coordinate system. Eight element sets were created through the thickness for each rivet hole and the six stress components were applied directly as shown in Figure 6-45. The analysis was carried out in 2 steps. The residual stresses were applied in the first step and the model was allowed to equilibrate. The pressure load was applied in the second step. Figure 6-46 shows the strip model at the end of the first step. Figures 6-47 and 6-48 show the lower skin and the upper skin respectively at the end of the first step. Figures 6-49 and 6-50 show the lower skin and the upper skin respectively at the end of the second step.

2D axisymmetric baseline model results were mapped at this stage since that mapping is less complex to implement than 3D mesh-to-mesh mapping. With this methodology established, work is currently in progress to map from the 3D individual installation tests. Other 3D mapping procedures will also be concurrently tried for validation.

SHEET	6-7	NO. 4-087051-20
TOTAL	6-32	
ISSUE DATE		12/22/04

FIGURES

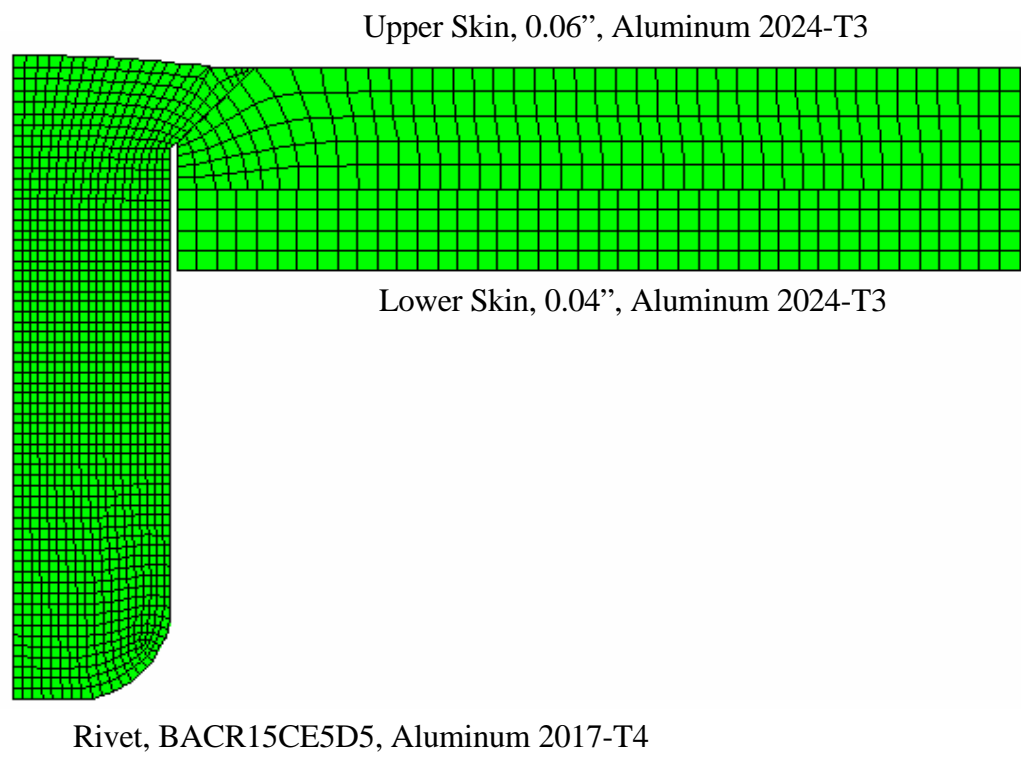


Figure 6-1: Axisymmetric Model Geometry

SHEET	6-8	NO.	4-087051-20
TOTAL	6-32		
ISSUE DATE	12/22/04		

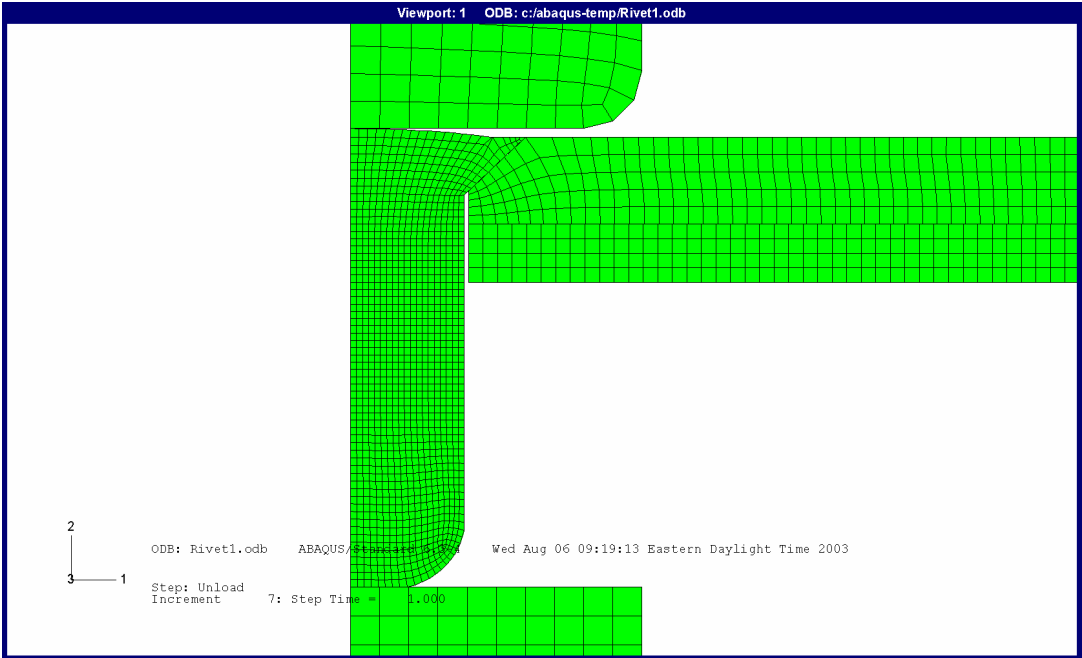


Figure 6-2: Axisymmetric Model, Initial Configuration

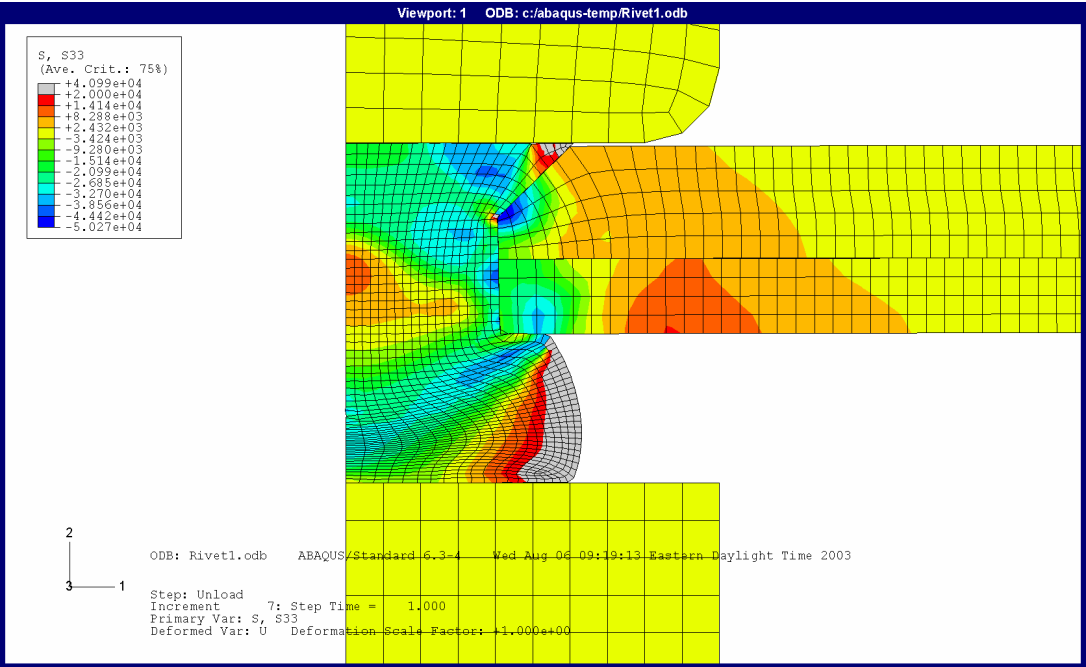


Figure 6-3: Axisymmetric Model, Residual Hoop Stress

SHEET	6-9	NO.	4-087051-20
TOTAL	6-32		
ISSUE DATE	12/22/04		

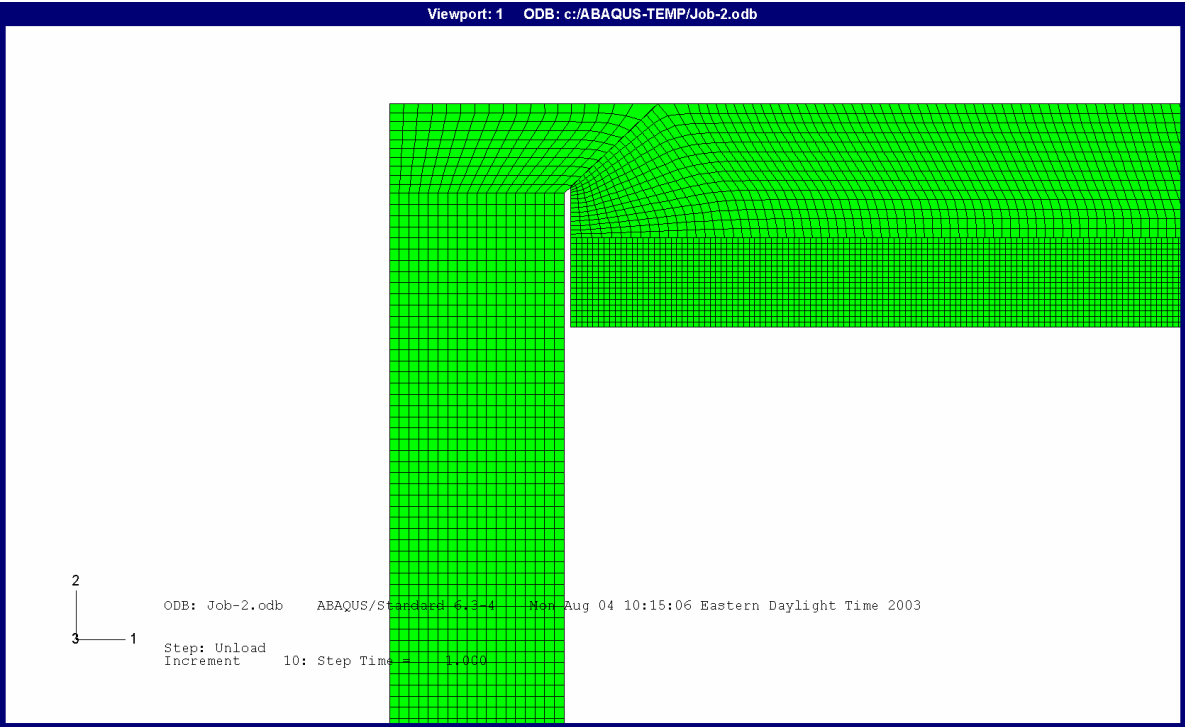


Figure 6- 4: Simplified Model, Initial Configuration

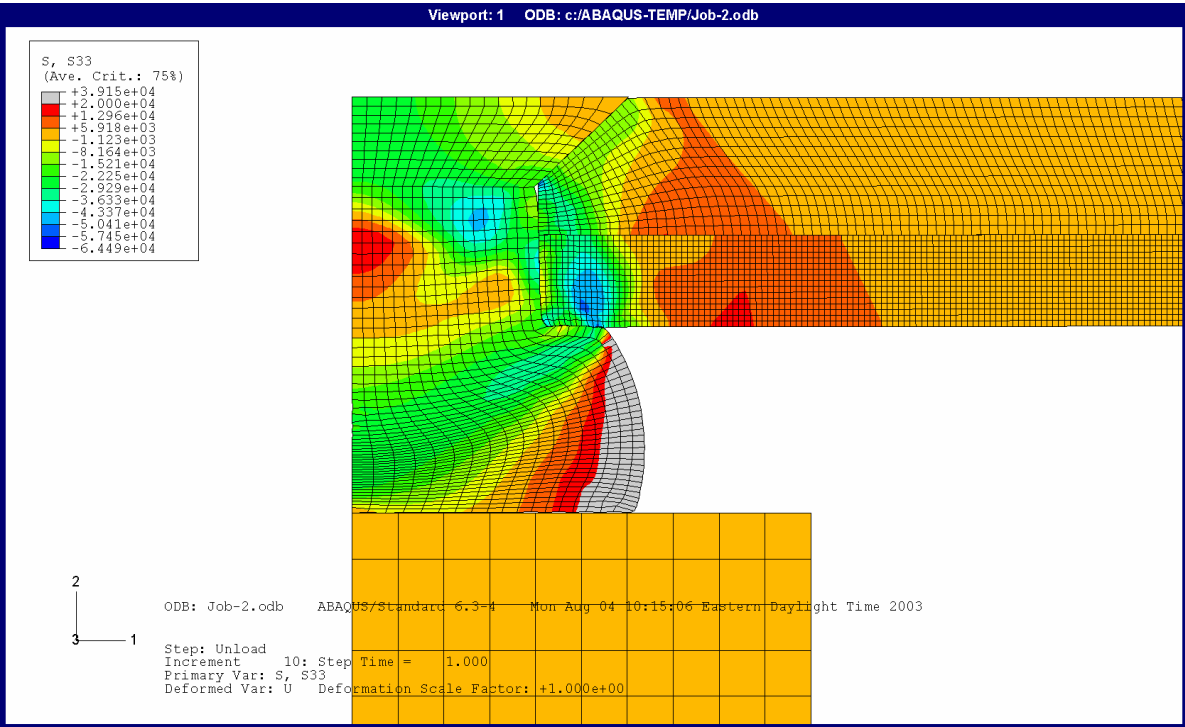


Figure 6- 5: Simplified Model, Residual Hoop Stress

SHEET	6-10	NO.	4-087051-20
TOTAL	6-32		
ISSUE DATE	12/22/04		

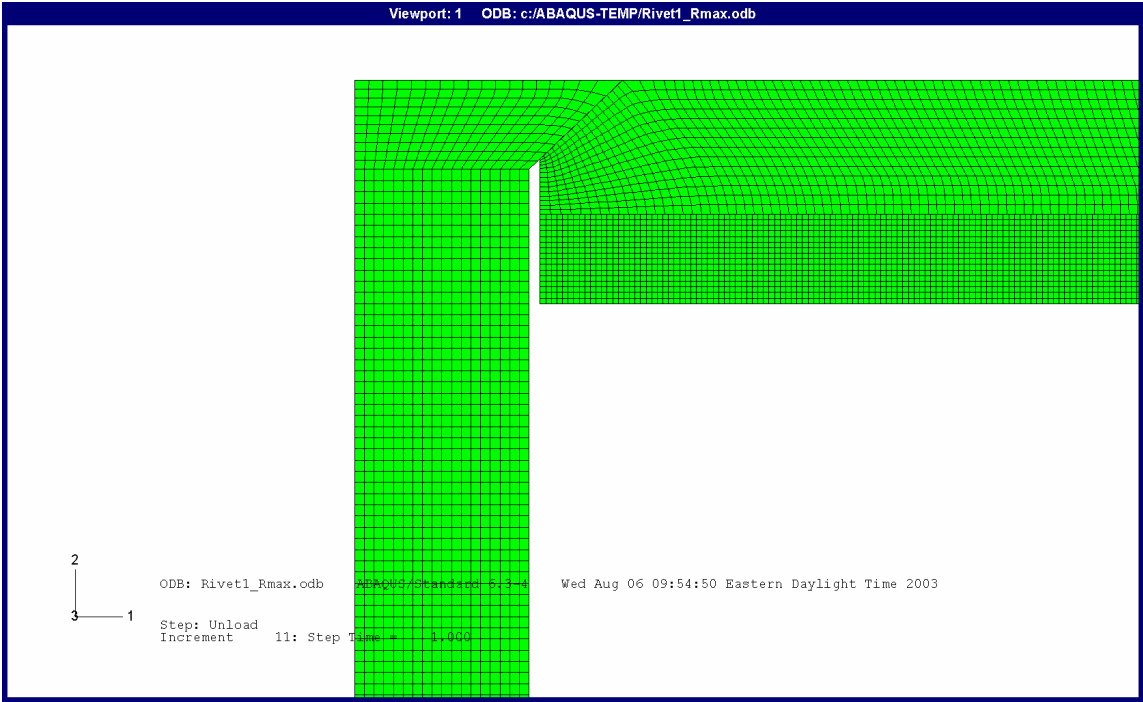


Figure 6- 6: Increased Rivet Hole Diameter, Initial Configuration

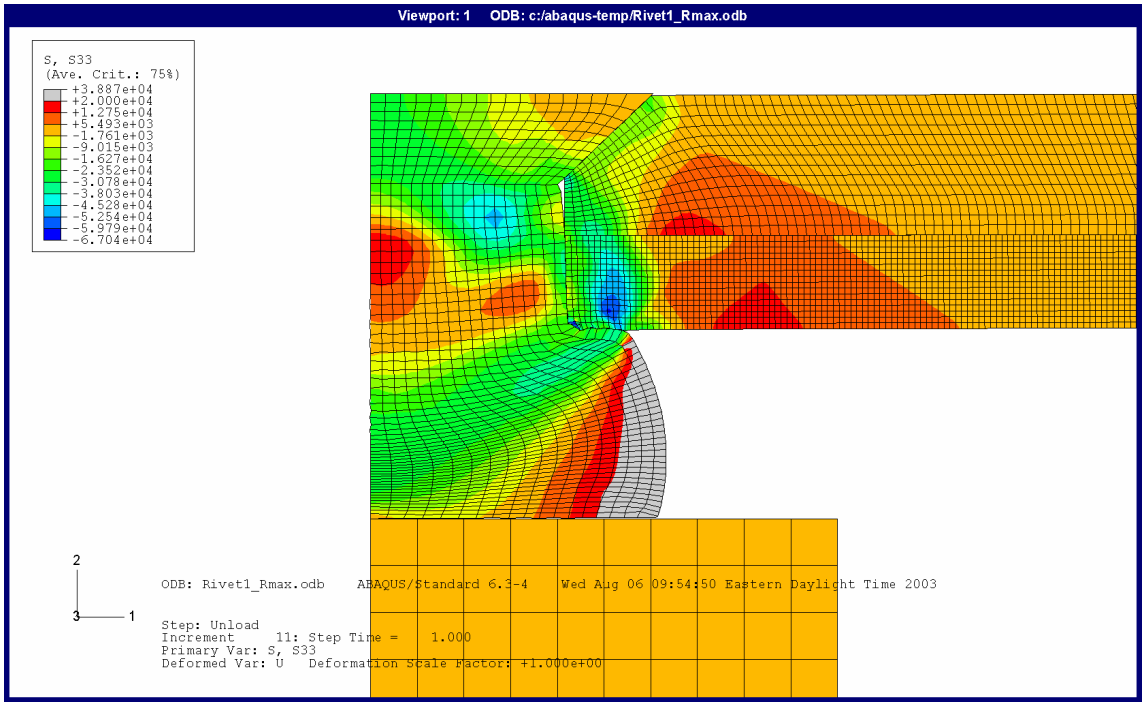


Figure 6- 7: Increased Rivet Hole Diameter, Residual Hoop Stress

SHEET	6-11	NO.	4-087051-20
TOTAL	6-32		
ISSUE DATE	12/22/04		

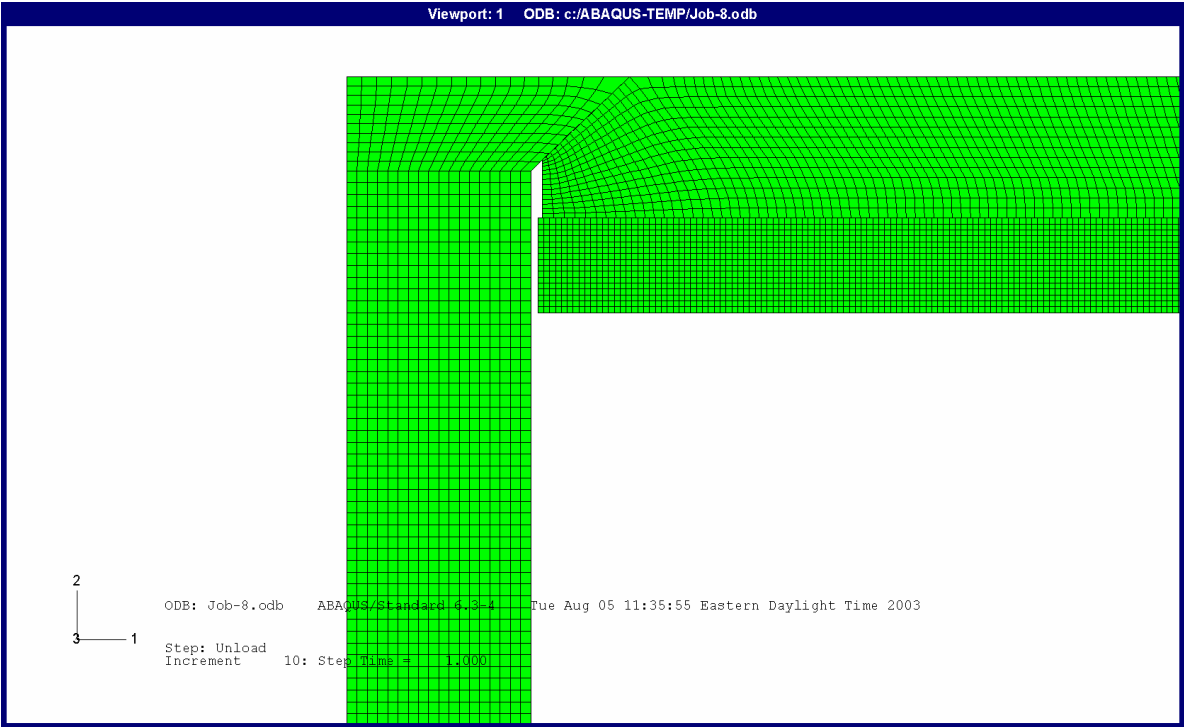


Figure 6- 8: Increased Upper Skin Hole Diameter, Initial Configuration

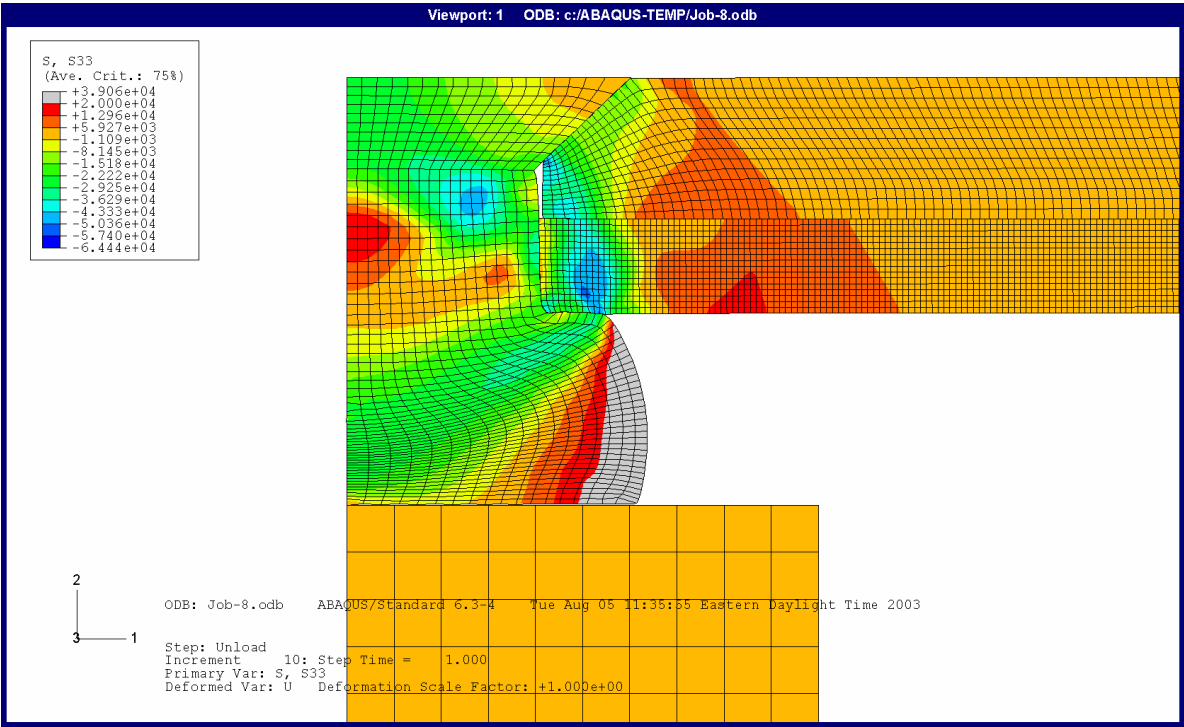


Figure 6- 9: Increased Upper Skin Hole Diameter, Residual Hoop Stress

SHEET	6-12	NO.	4-087051-20
TOTAL	6-32		
ISSUE DATE	12/22/04		

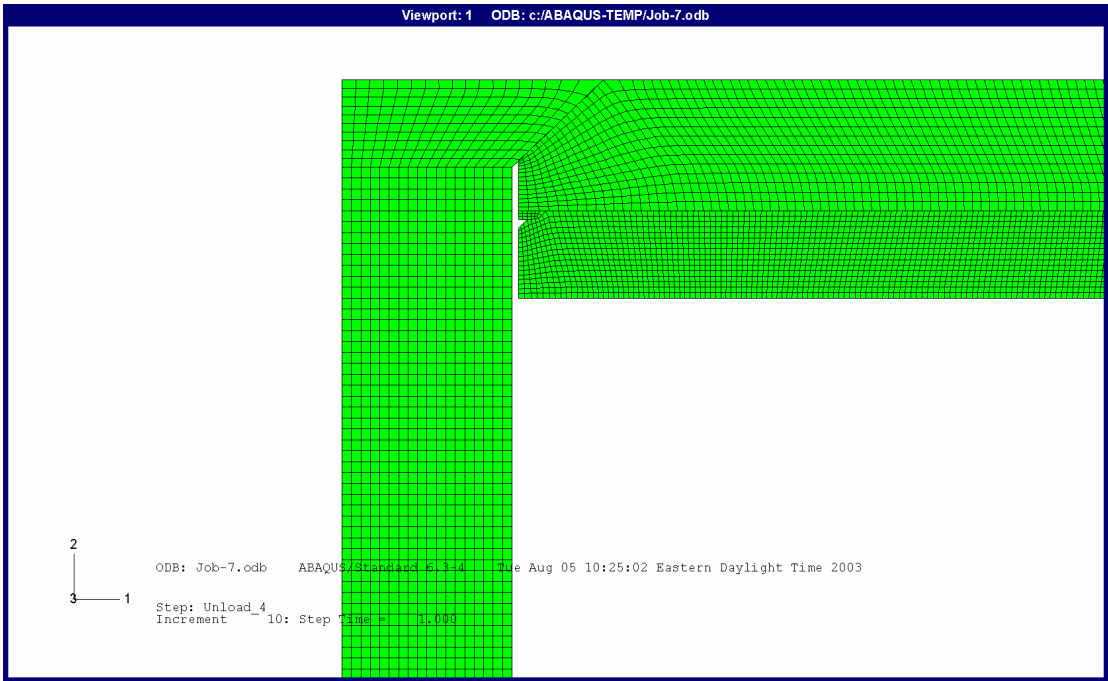


Figure 6-10: Surface Defects, Initial Configuration

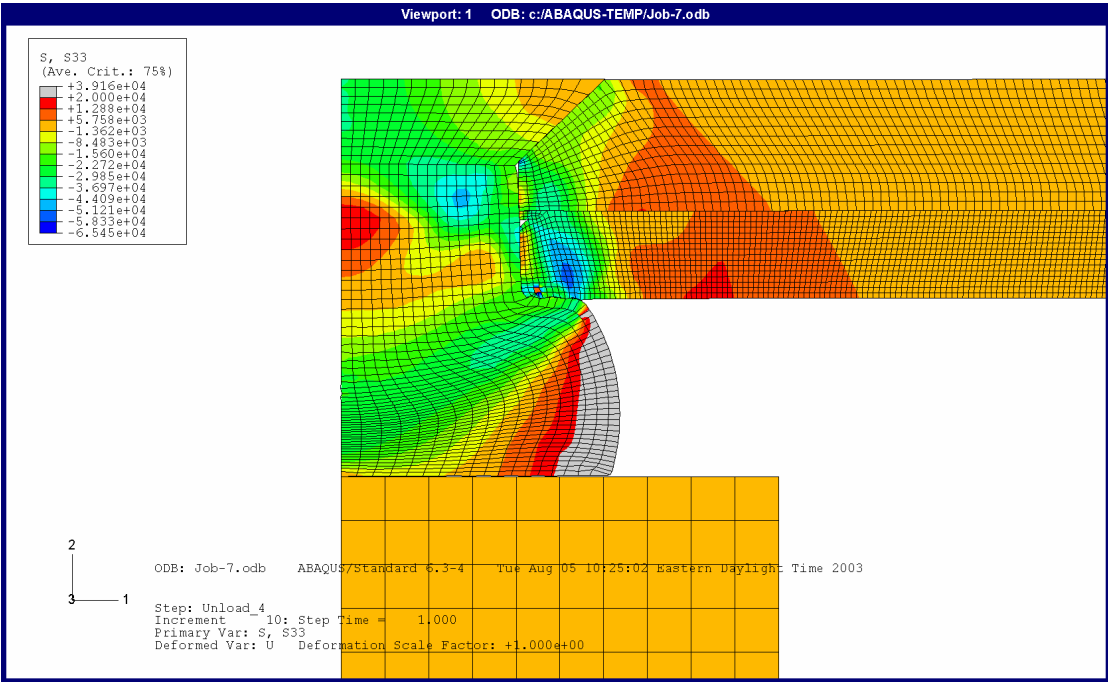


Figure 6-11: Surface Defects, Residual Hoop Stress

SHEET	6-13	NO.	4-087051-20
TOTAL	6-32		
ISSUE DATE	12/22/04		

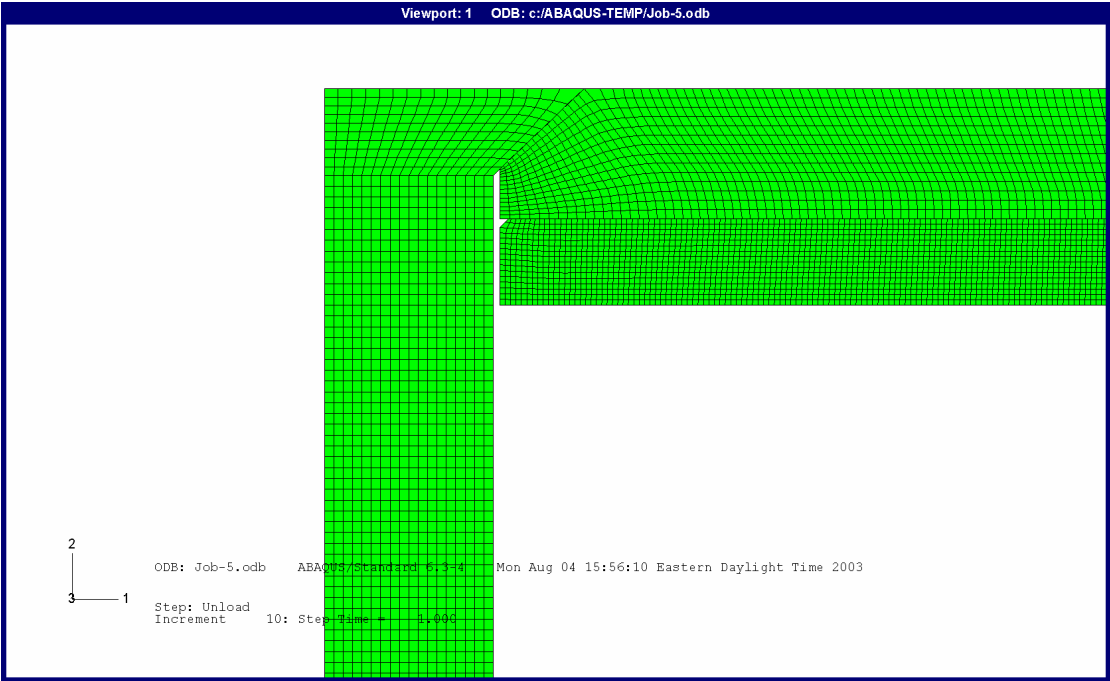


Figure 6-12: Surface Defects, Initial Configuration

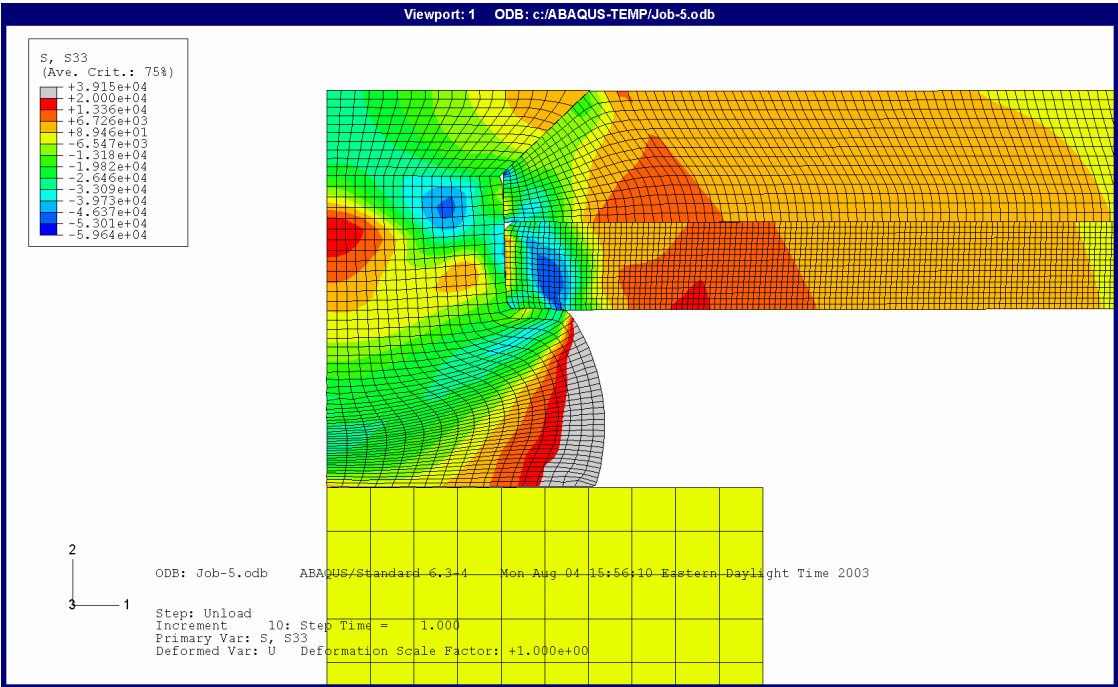


Figure 6- 13: Surface Defects, Residual Hoop Stress

SHEET	6-14	NO.	4-087051-20
TOTAL	6-32		
ISSUE DATE	12/22/04		

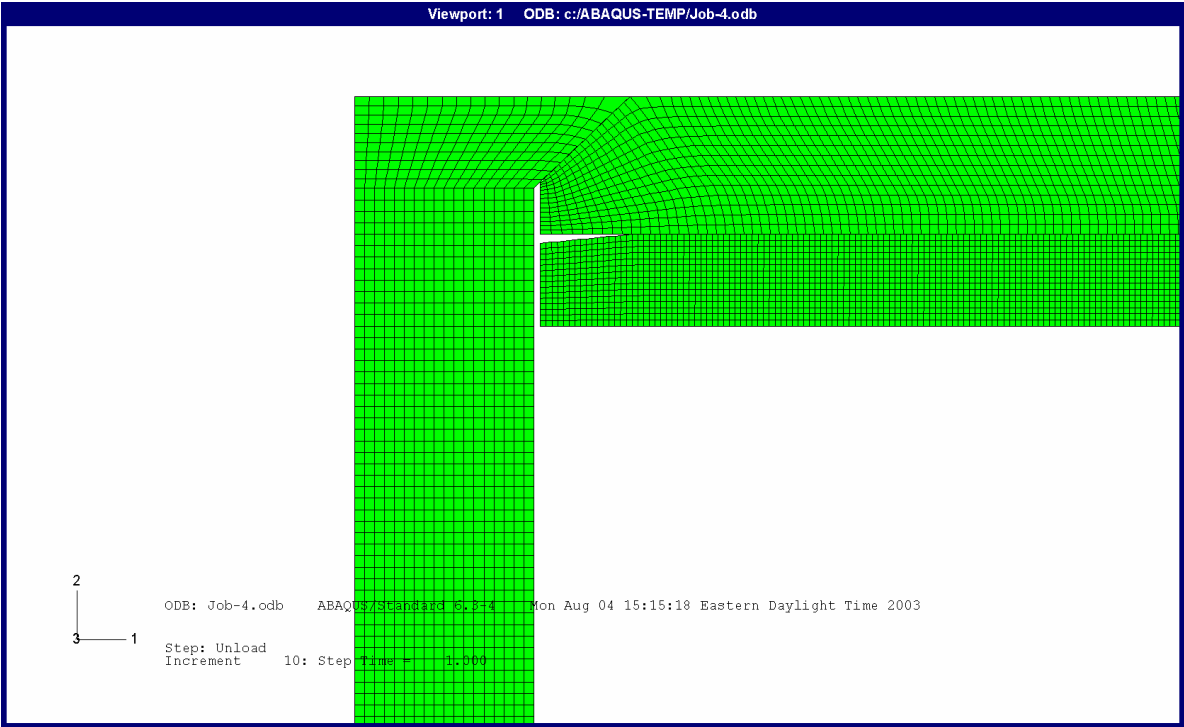


Figure 6- 14: Surface Defects, Initial Configuration

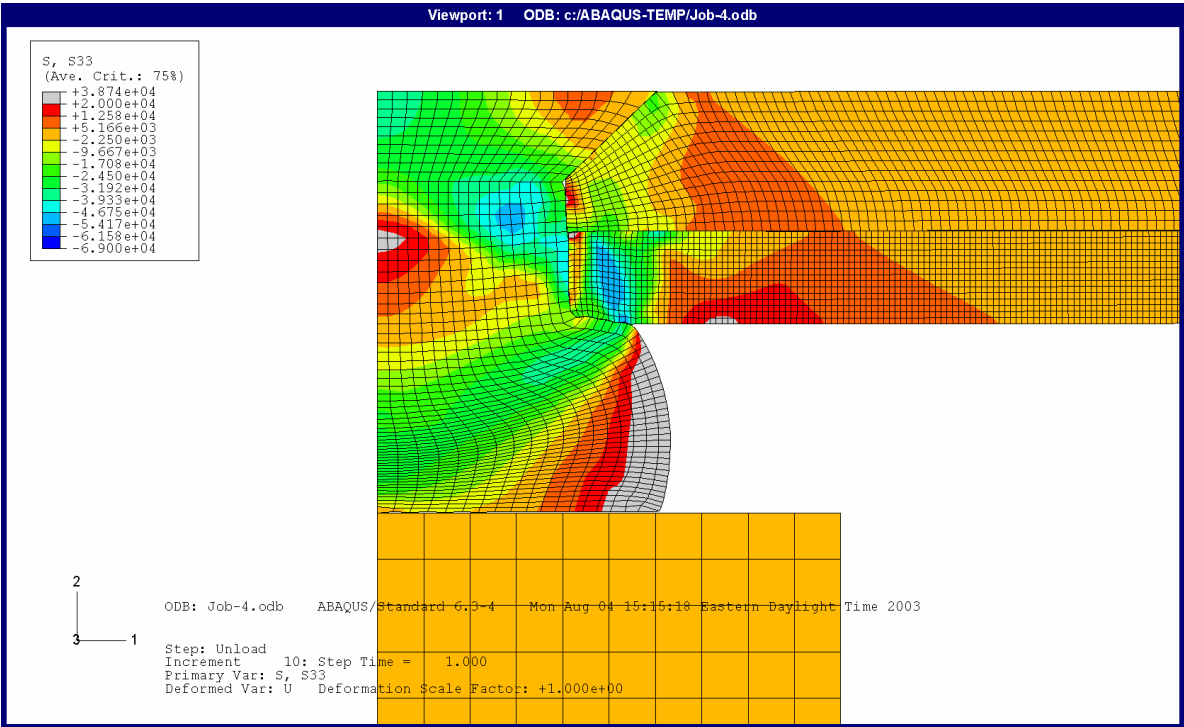


Figure 6- 15: Surface Defects, Residual Hoop Stress

SHEET	6-15	NO.	4-087051-20
TOTAL	6-32		
ISSUE DATE	12/22/04		

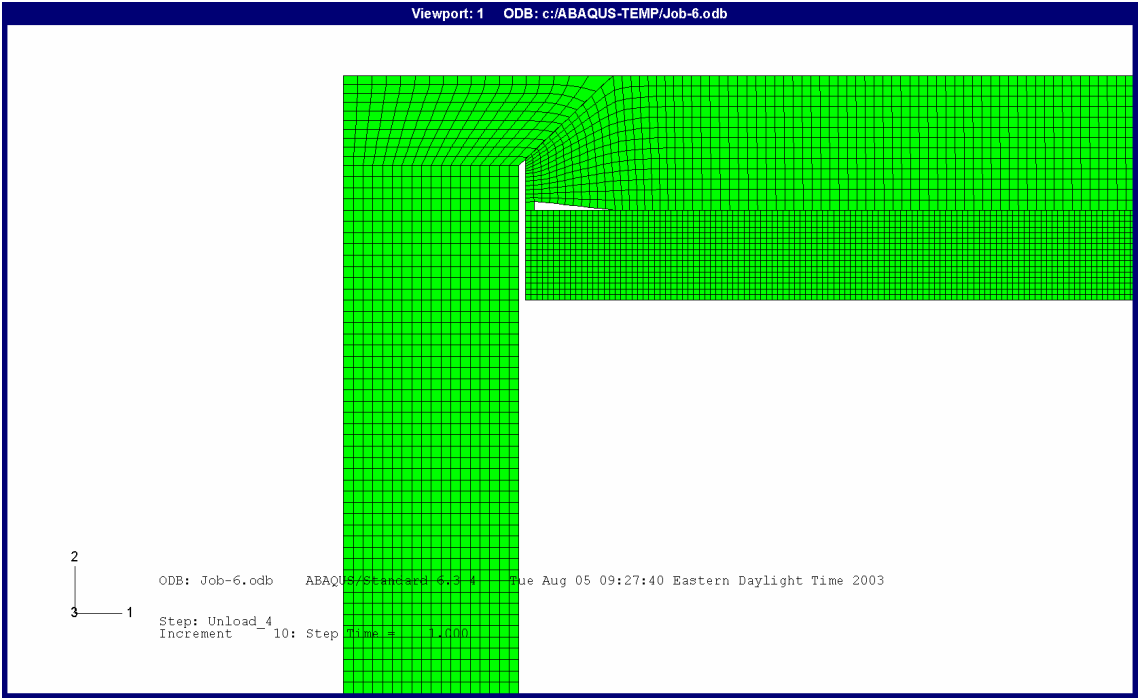


Figure 6- 16: Drill Shavings, Initial Configuration

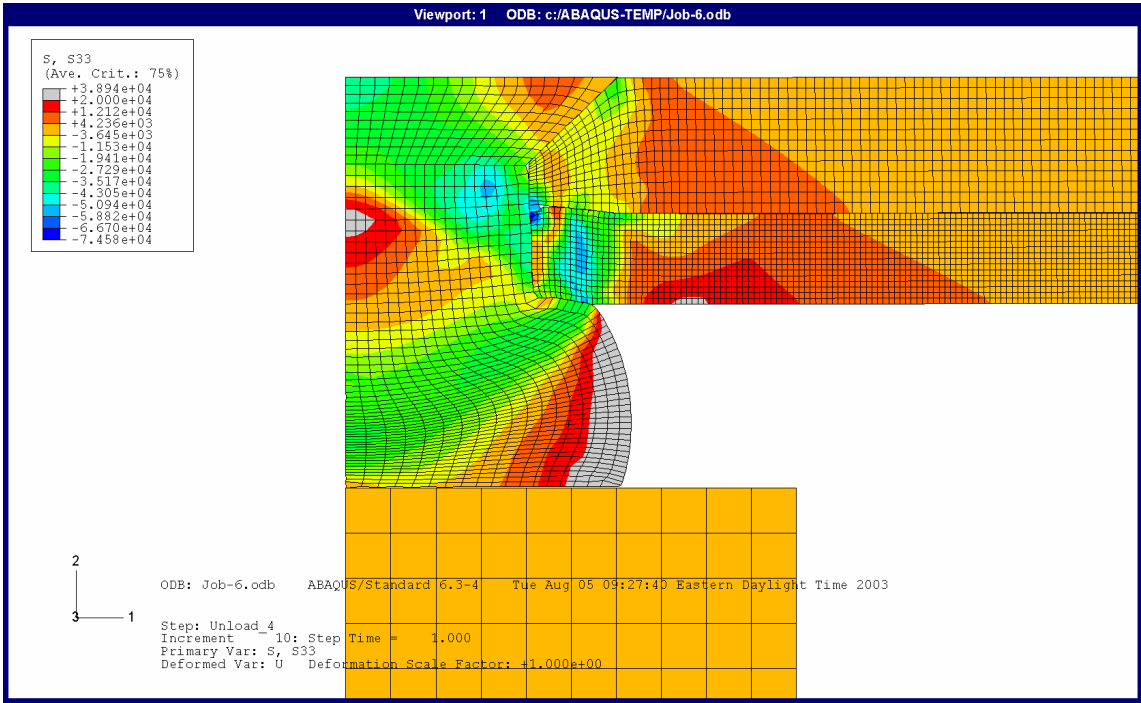


Figure 6- 17: Drill Shavings, Residual Hoop Stress

SHEET	6-16	NO.	4-087051-20
TOTAL	6-32		
ISSUE DATE	12/22/04		

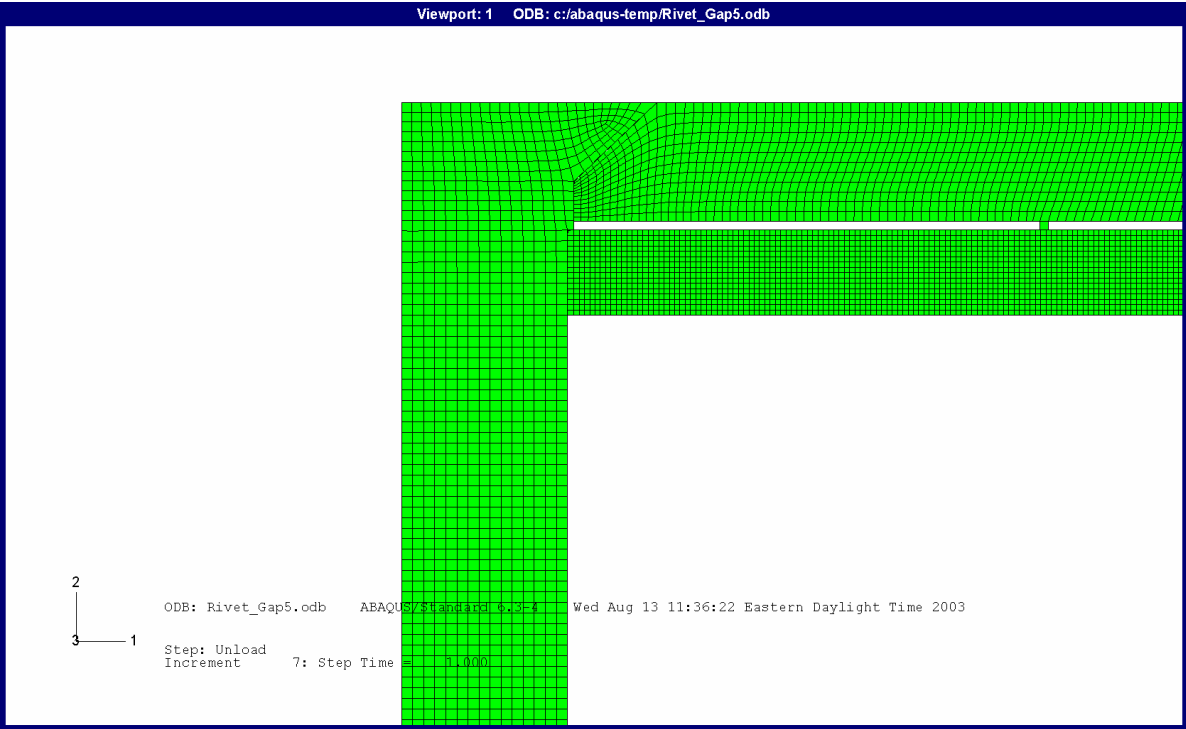


Figure 6- 18: Drill Shavings, Initial Configuration

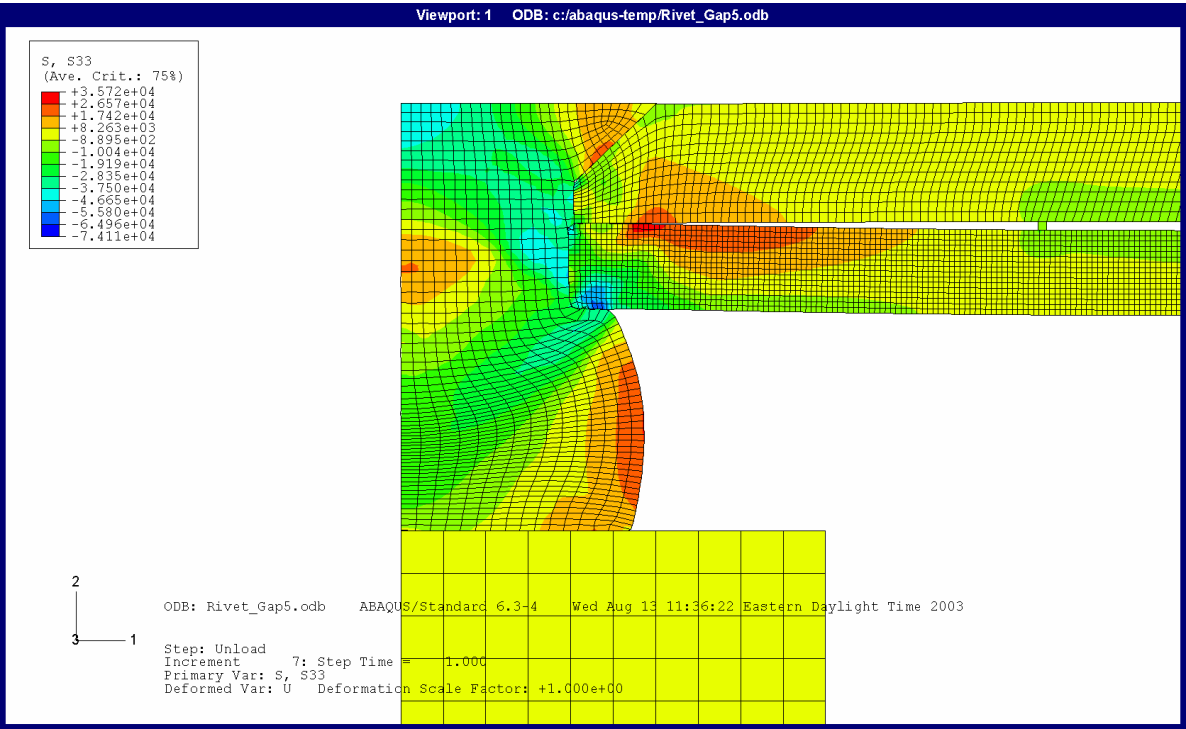


Figure 6- 19: Drill Shavings, Residual Hoop Stress

SHEET	6-17	NO.	4-087051-20
TOTAL	6-32		
ISSUE DATE	12/22/04		

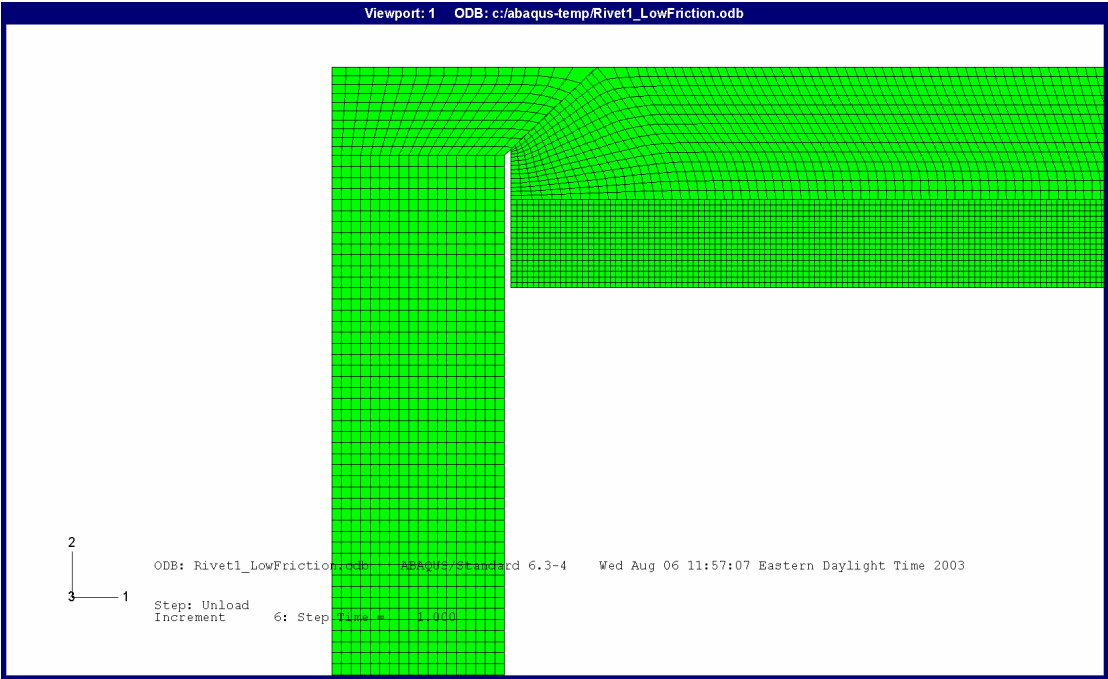


Figure 6- 20: Reduced Coefficient of Friction, Initial Configuration

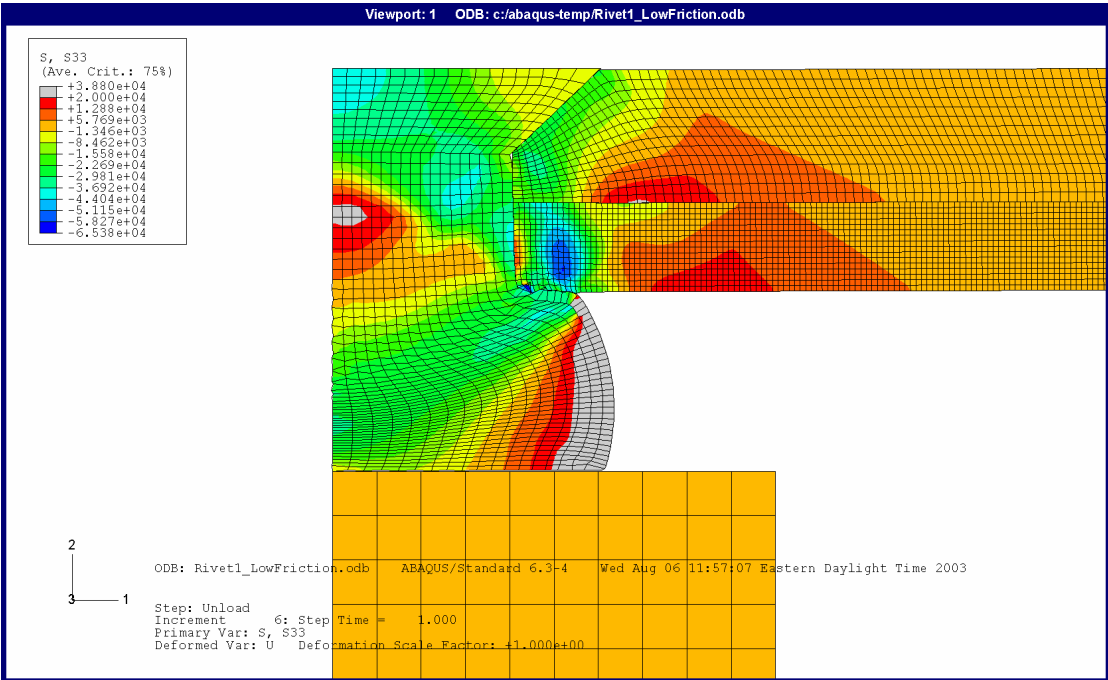


Figure 6- 21: Reduced Coefficient of Friction, Residual Hoop Stress

SHEET	6-18	NO.	4-087051-20
TOTAL	6-32		
ISSUE DATE	12/22/04		

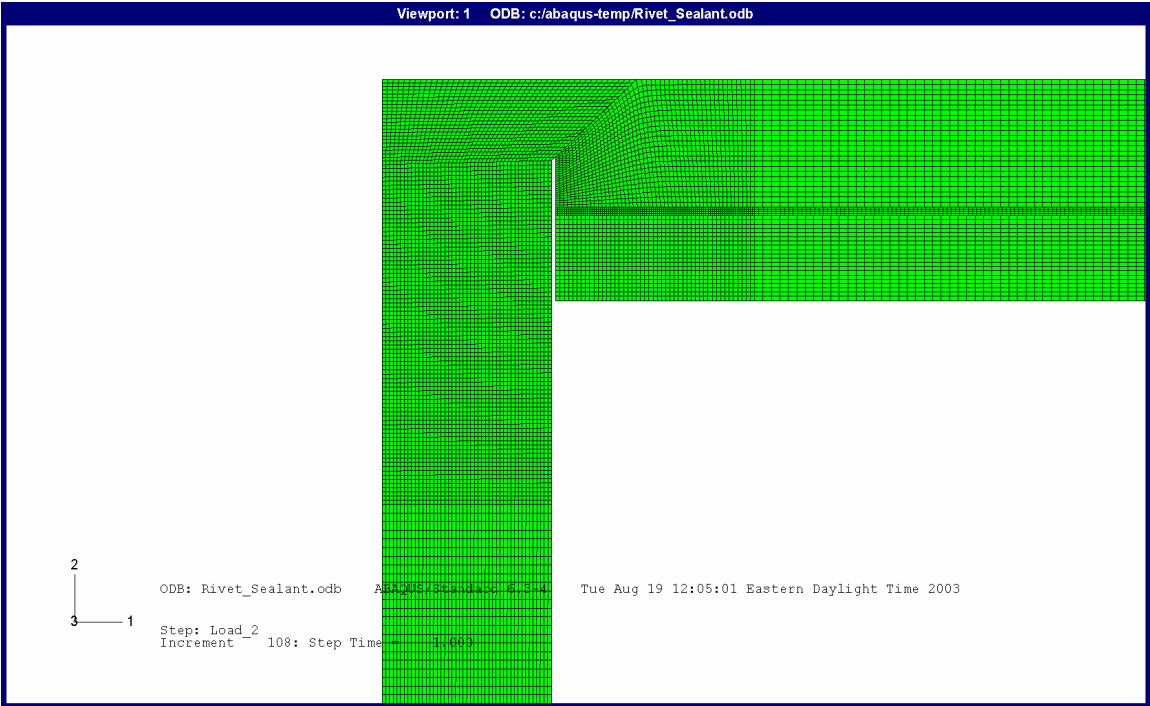


Figure 6- 22: Wet Sealant and Drill Shavings, Initial Configuration

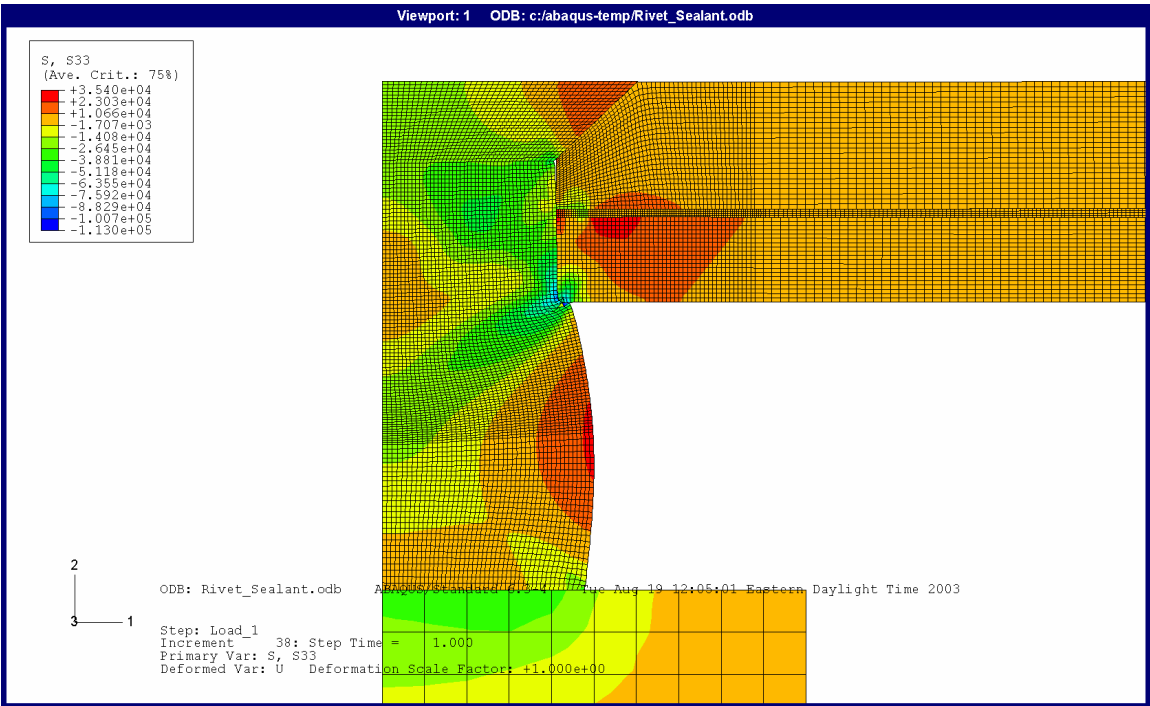


Figure 6- 23: Wet Sealant and Drill Shavings, Load Step 1

SHEET	6-19	NO.	4-087051-20
TOTAL	6-32		
ISSUE DATE	12/22/04		

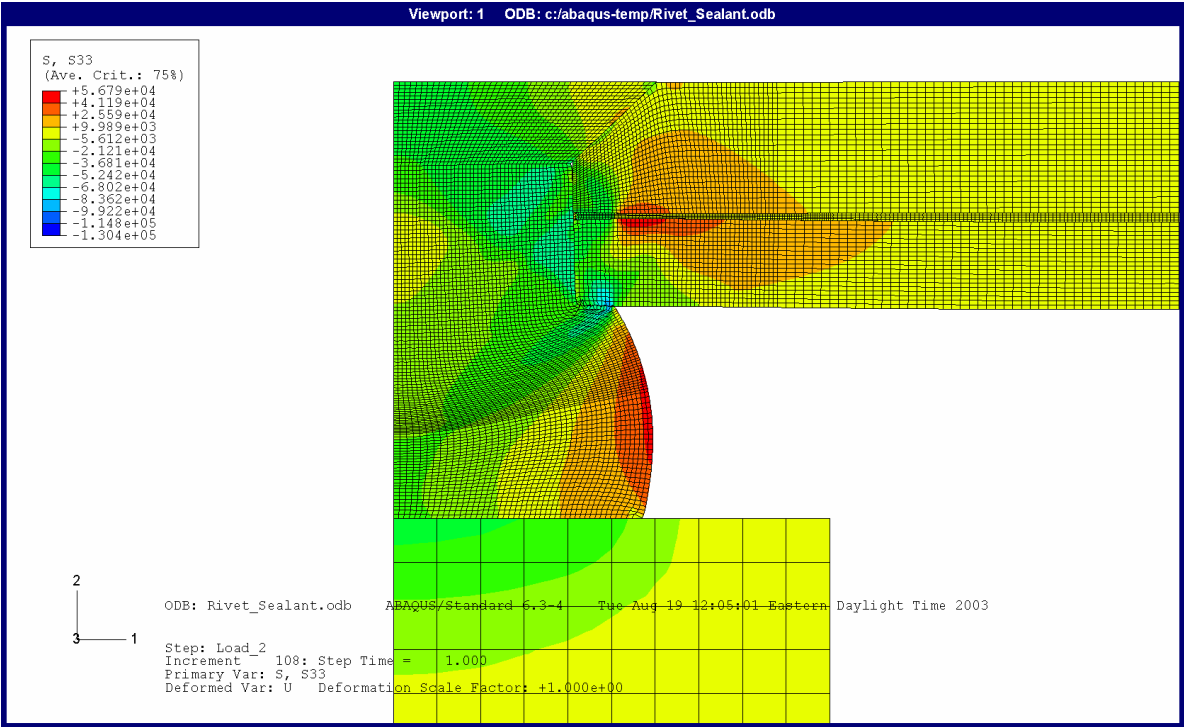


Figure 6- 24: Wet Sealant and Drill Shavings, Load Step 2

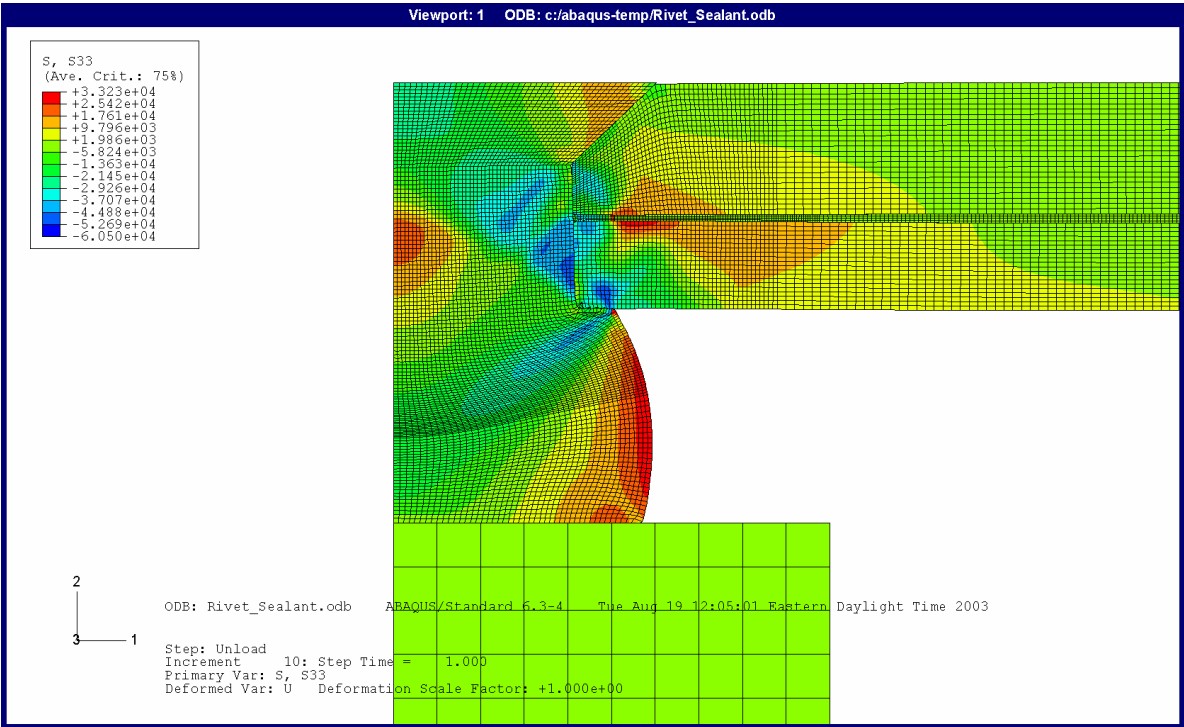


Figure 6- 25: Wet Sealant and Drill Shavings, Residual Hoop Stress

SHEET	6-20	NO.	4-087051-20
TOTAL	6-32		
ISSUE DATE	12/22/04		

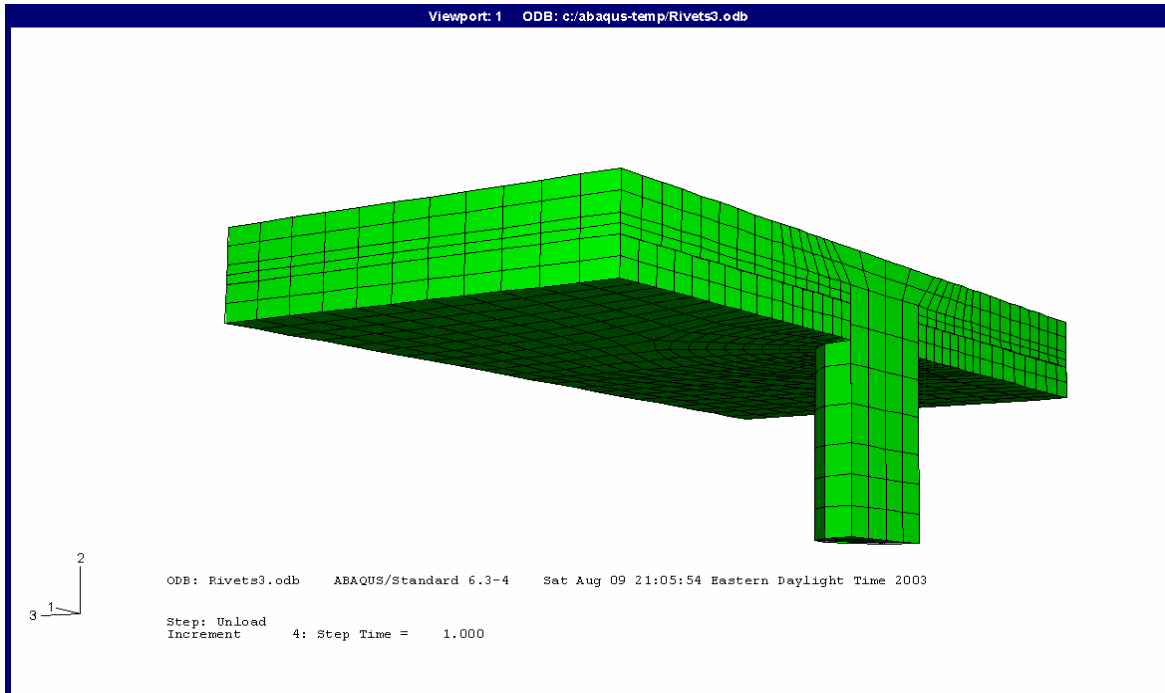


Figure 6- 26: 3D Model Without Clearance, Initial Configuration

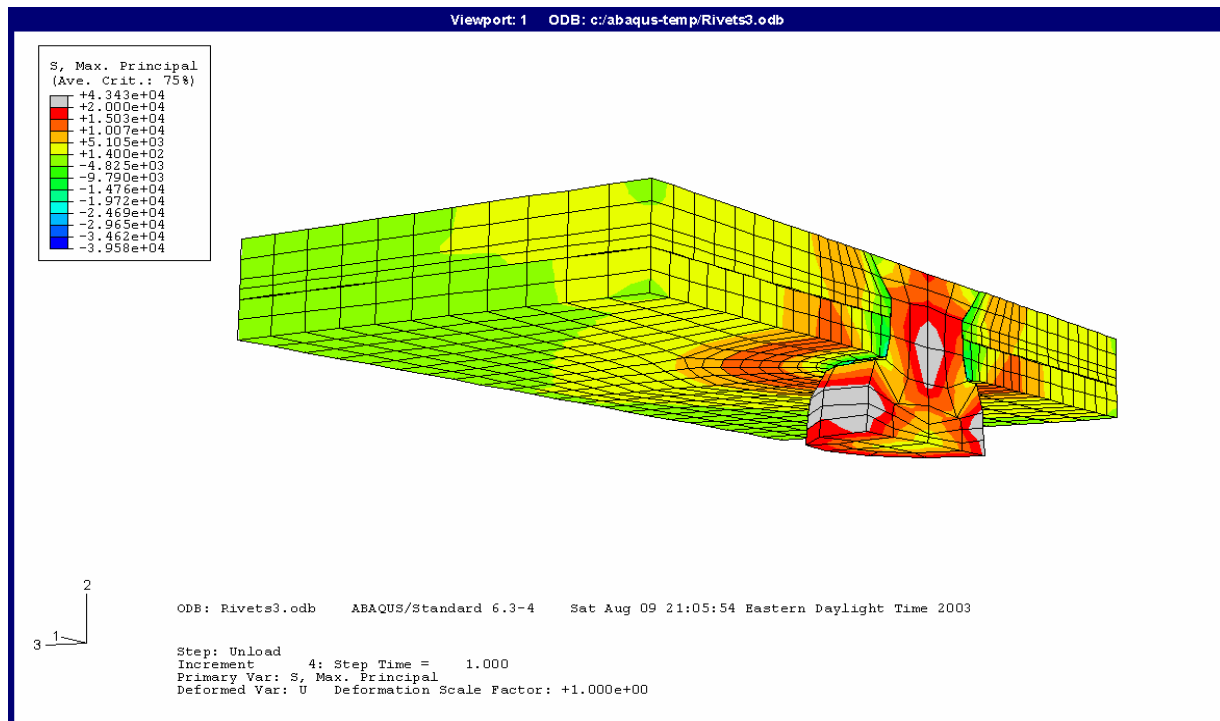


Figure 6- 27: 3D Model Without Clearance, Residual Stress State

SHEET	6-21	NO.	4-087051-20
TOTAL	6-32		
ISSUE DATE	12/22/04		

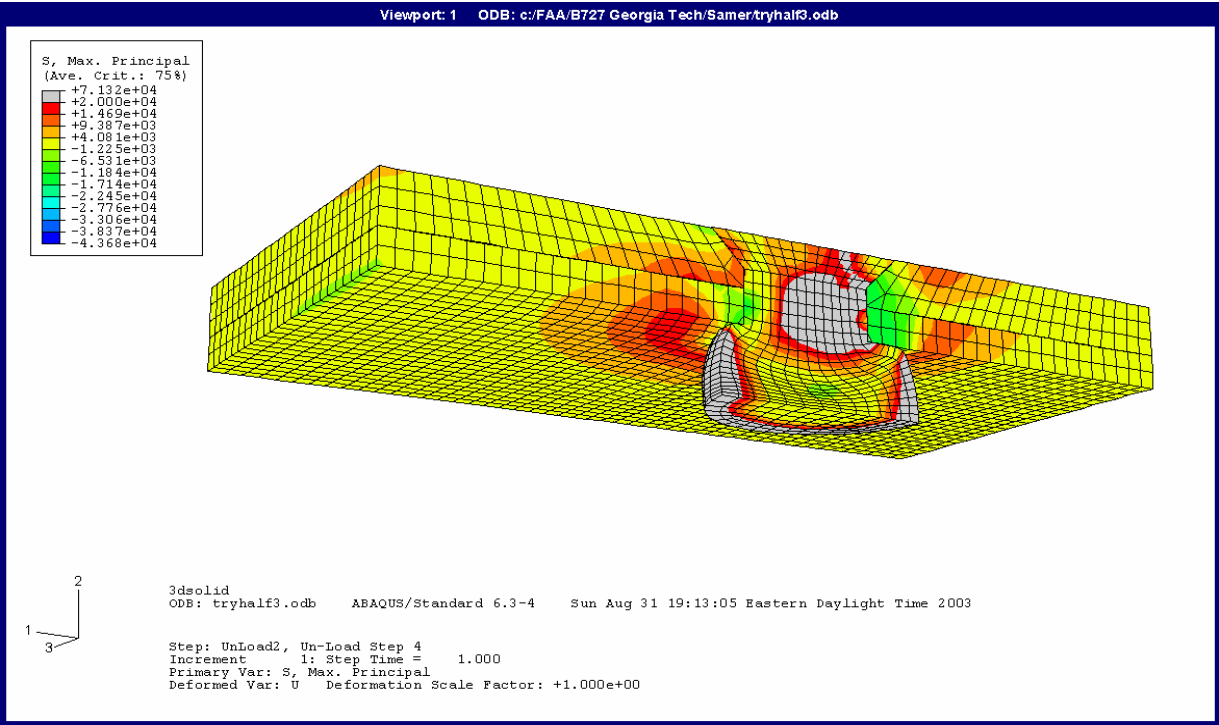


Figure 6- 28: 3D Model With Clearance, Residual Stress State

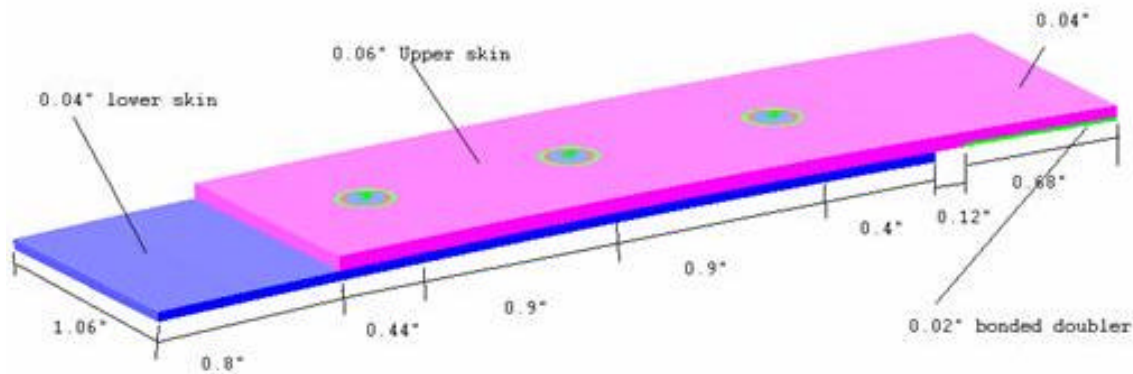


Figure 6- 29: Flat Strip Model Dimensions

SHEET	6-22	NO.	4-087051-20
TOTAL	6-32		
ISSUE DATE	12/22/04		

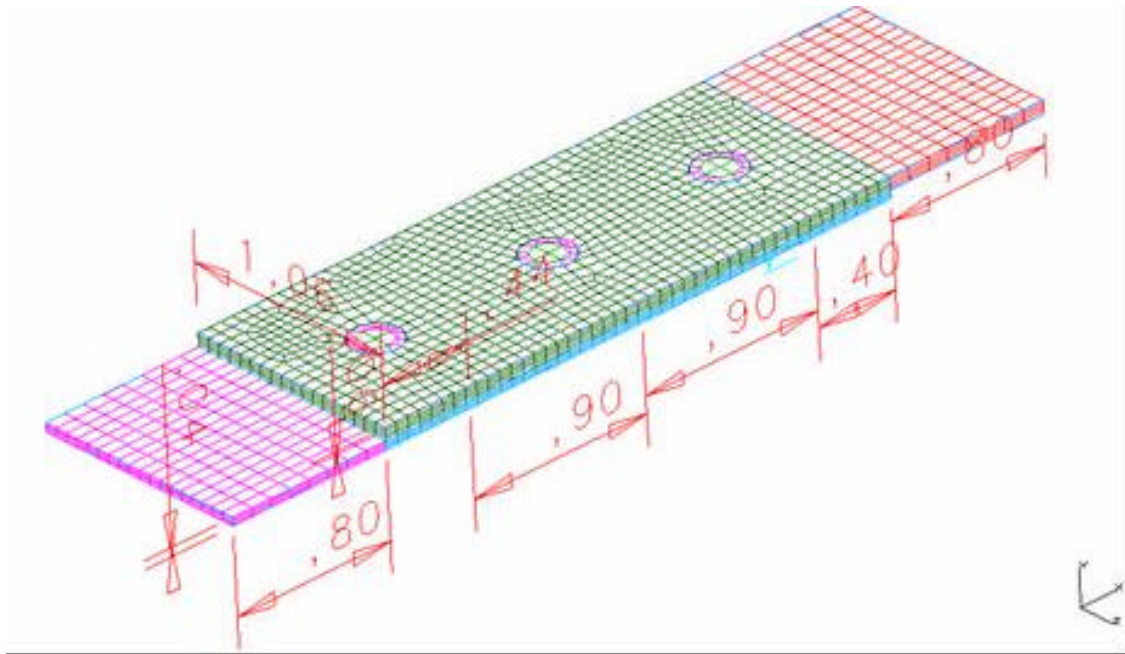


Figure 6- 30: Flat Strip Model Baseline Mesh

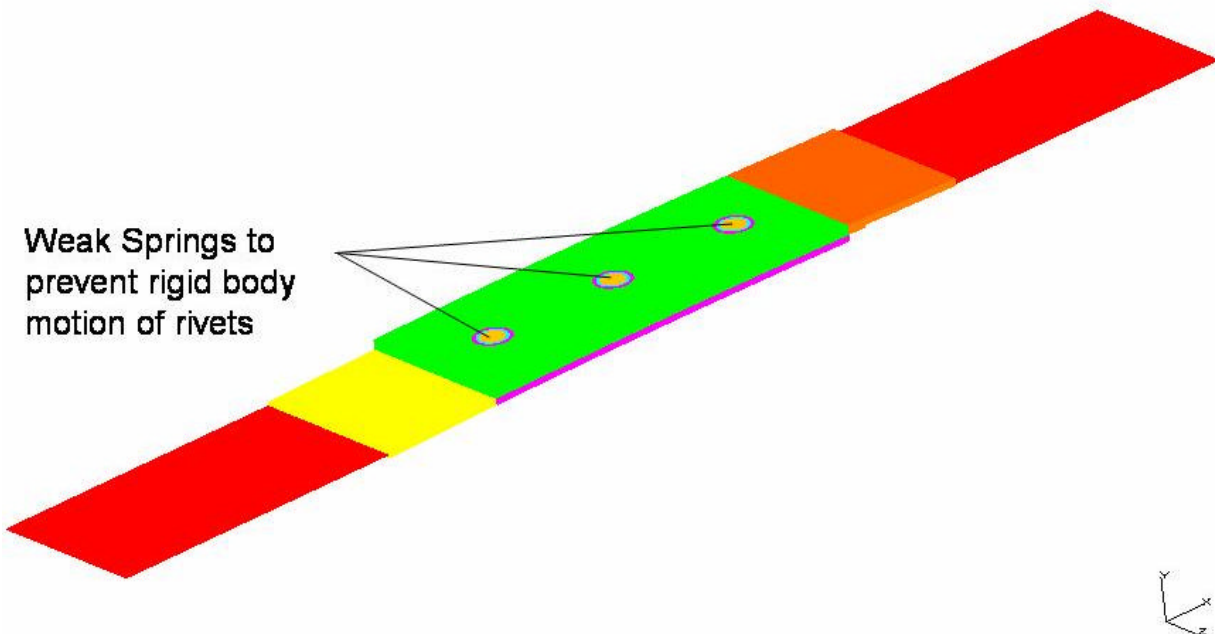


Figure 6- 31: Modified Strip Model Extended to Half Bay

SHEET	6-23	NO.	4-087051-20
TOTAL	6-32		
ISSUE DATE	12/22/04		

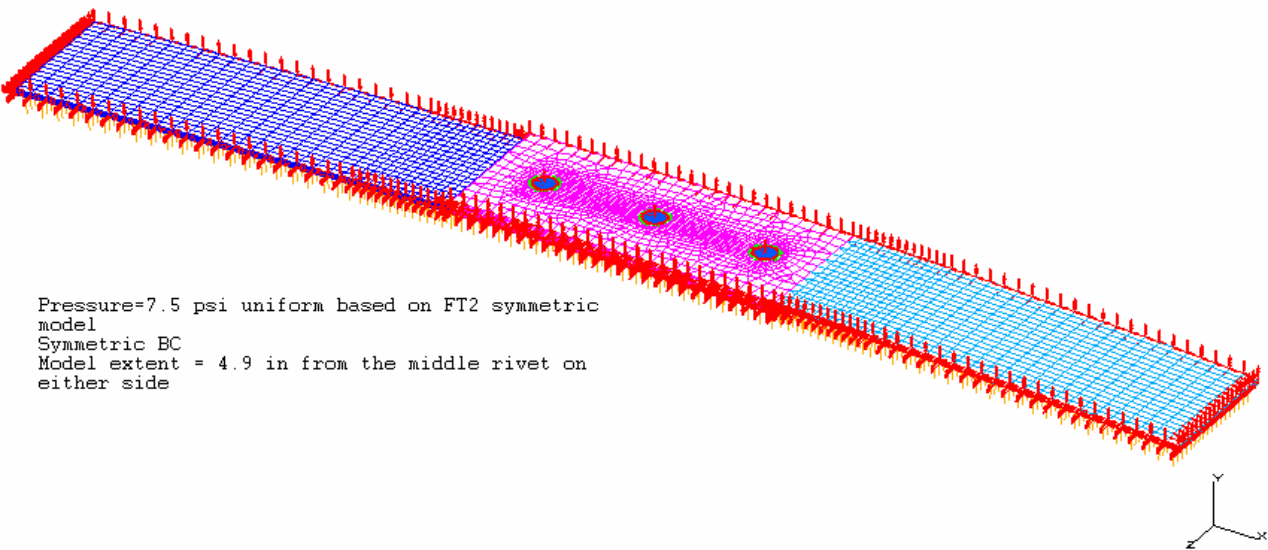


Figure 6- 32: Modified Strip Model Extended to Half Bay (Mesh with BCs)

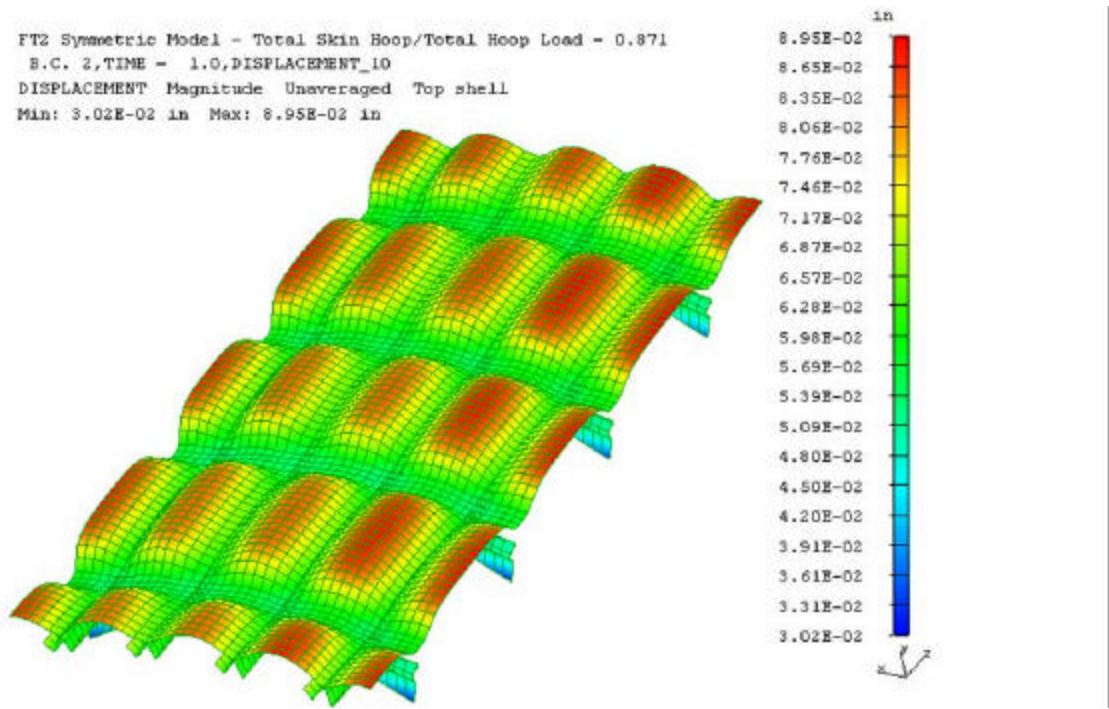


Figure 6- 33: FT2 Symmetric Model

SHEET	6-24	NO.	4-087051-20
TOTAL	6-32		
ISSUE DATE	12/22/04		

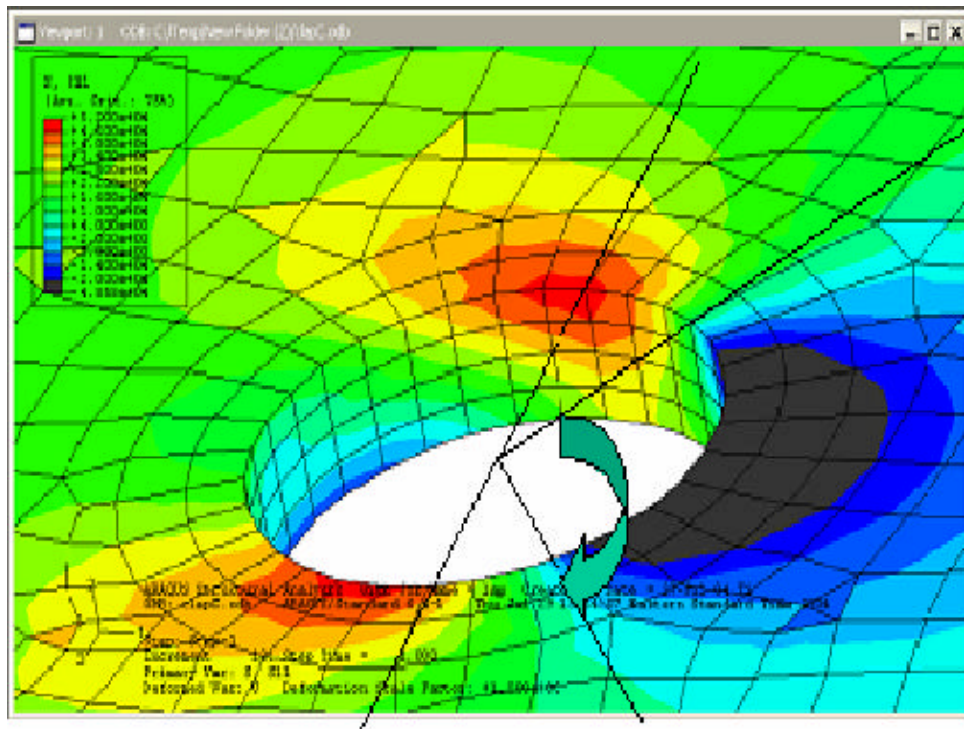


Figure 6- 34: Modified Strip Extended to Half Bay, Hoop Stress in Lower Skin

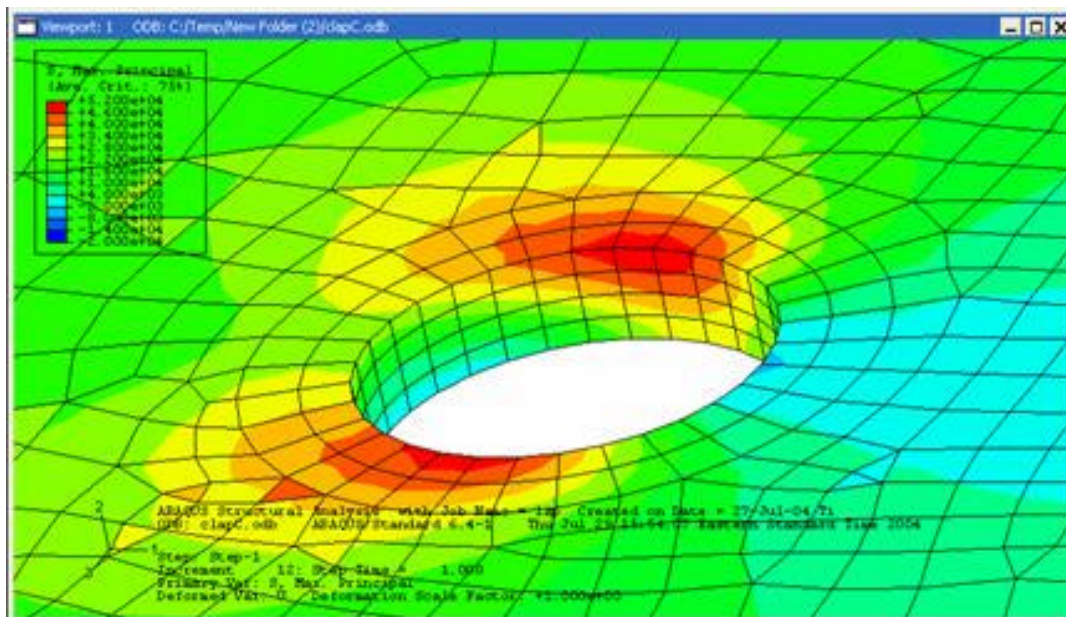


Figure 6- 35: Modified Strip Model Extended to Half Bay, Maximum Principal Stress in the Lower Skin

SHEET	6-25	NO.	4-087051-20
TOTAL	6-32		
ISSUE DATE	12/22/04		

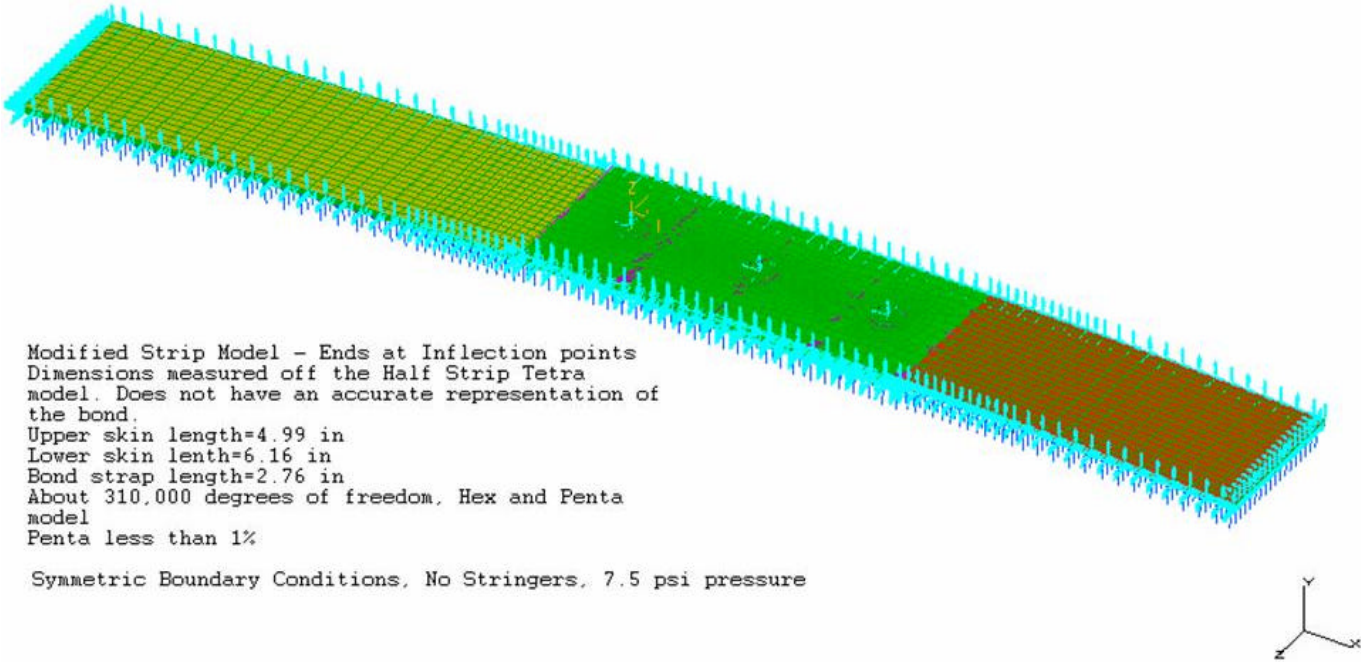


Figure 6- 36: Strip Model Extending up to the Inflection Point

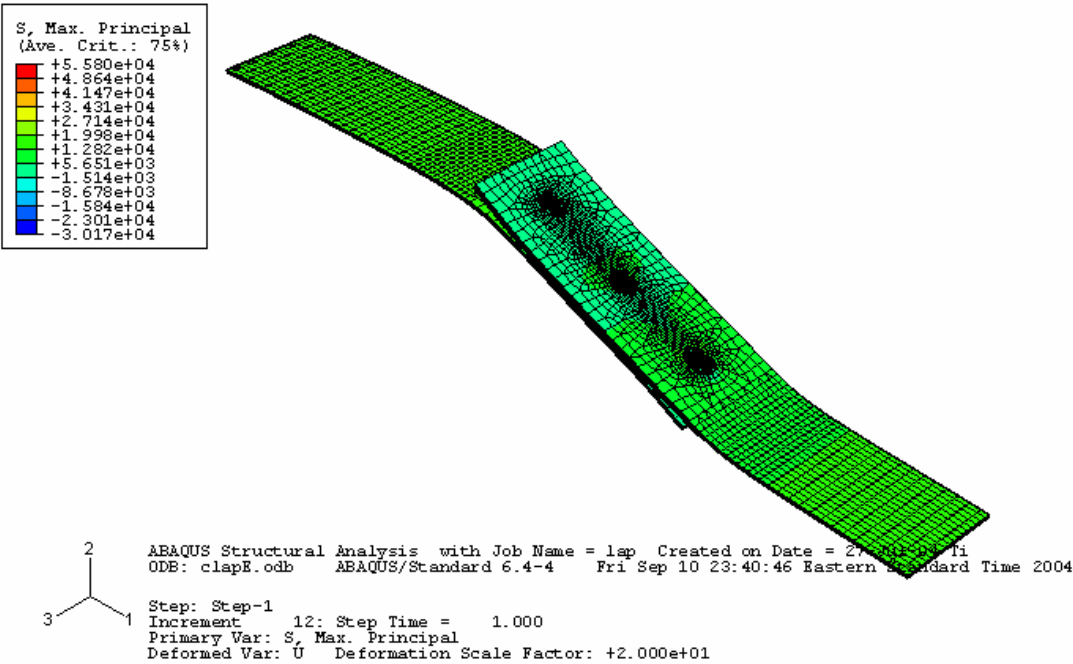


Figure 6- 37: Strip Model extending up to Inflection Point, Max Principal Stress Plot

SHEET	6-26	NO.	4-087051-20
TOTAL	6-32		
ISSUE DATE	12/22/04		

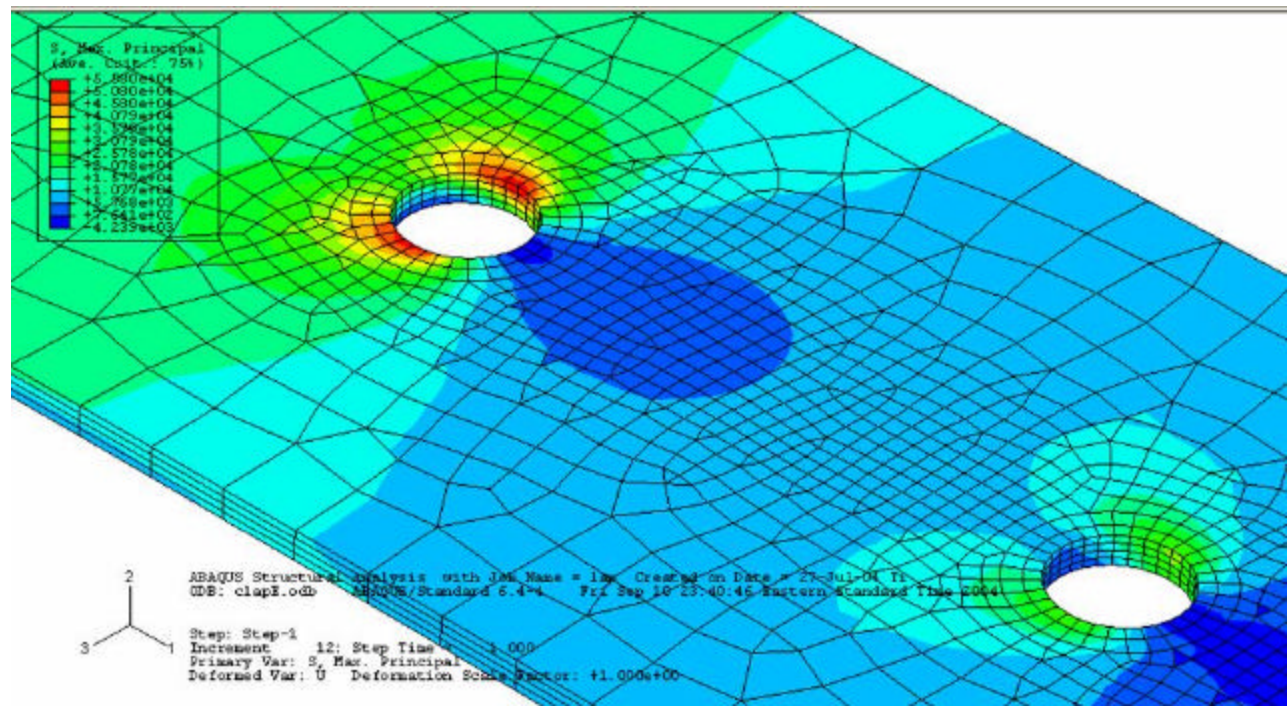


Figure 6- 38: Strip Model Extending up to Inflection Point, Max Principal in Lower Skin

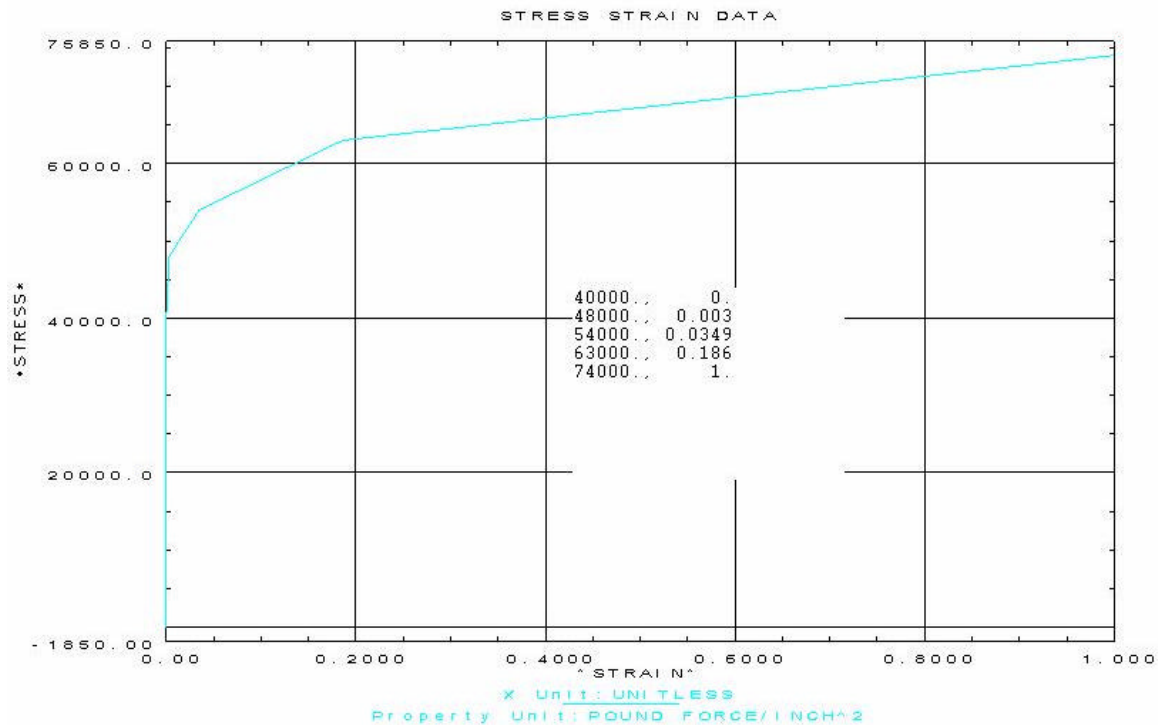


Figure 6- 39: Stress-Strain Curve for 2024-T3 Al

SHEET	6-27	NO.	4-087051-20
TOTAL	6-32		
ISSUE DATE	12/22/04		

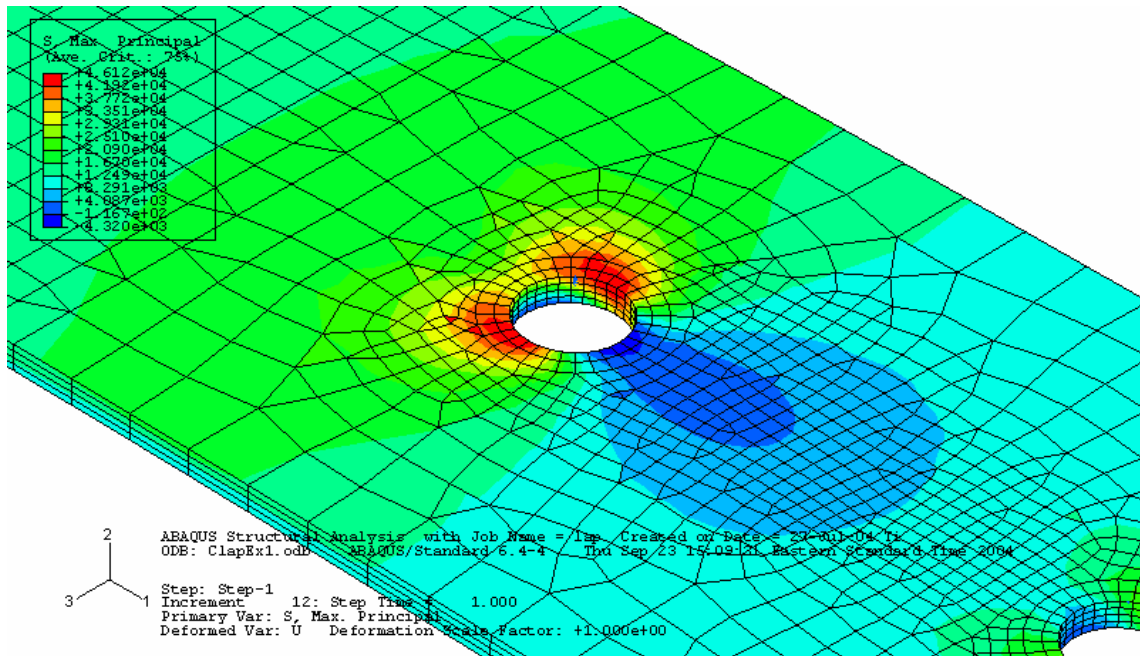


Figure 6- 40: Strip Model Extending up to Inflection Point, Max Principal Stress in Lower Skin (Non-Linear Material)

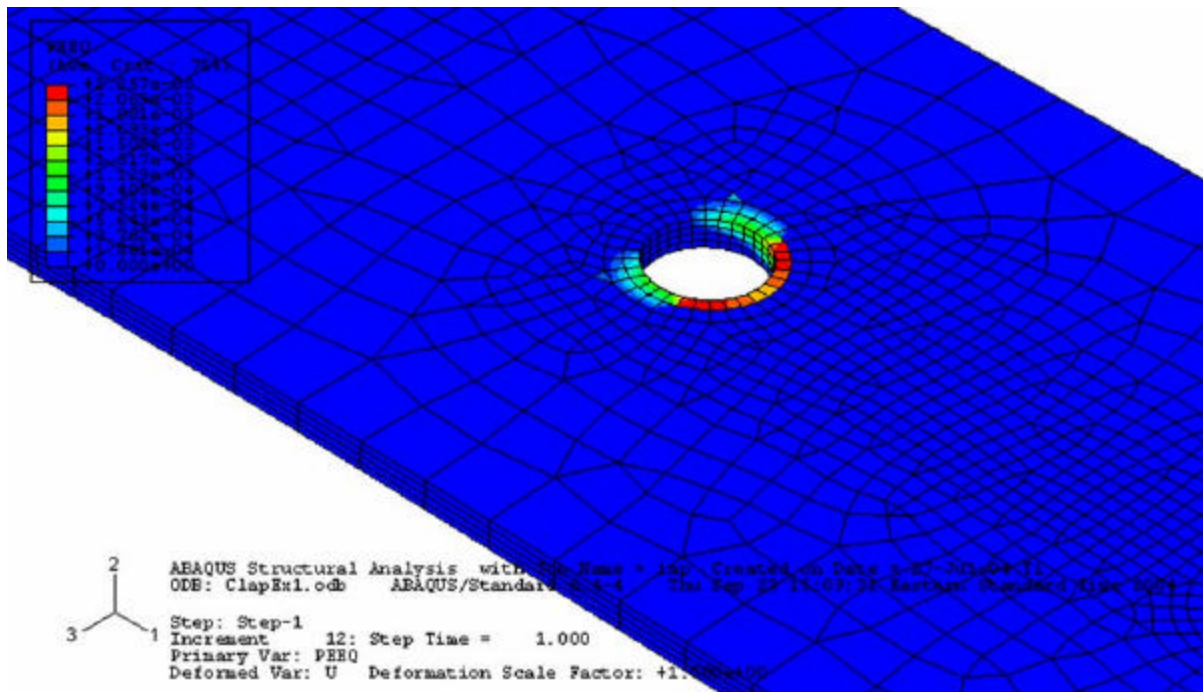


Figure 6- 41: Strip Model Extending up to Inflection Point, Plastic Strain Equivalent in Lower Skin (Non-Linear Material)

SHEET	6-28	NO.	4-087051-20
TOTAL	6-32		
ISSUE DATE	12/22/04		

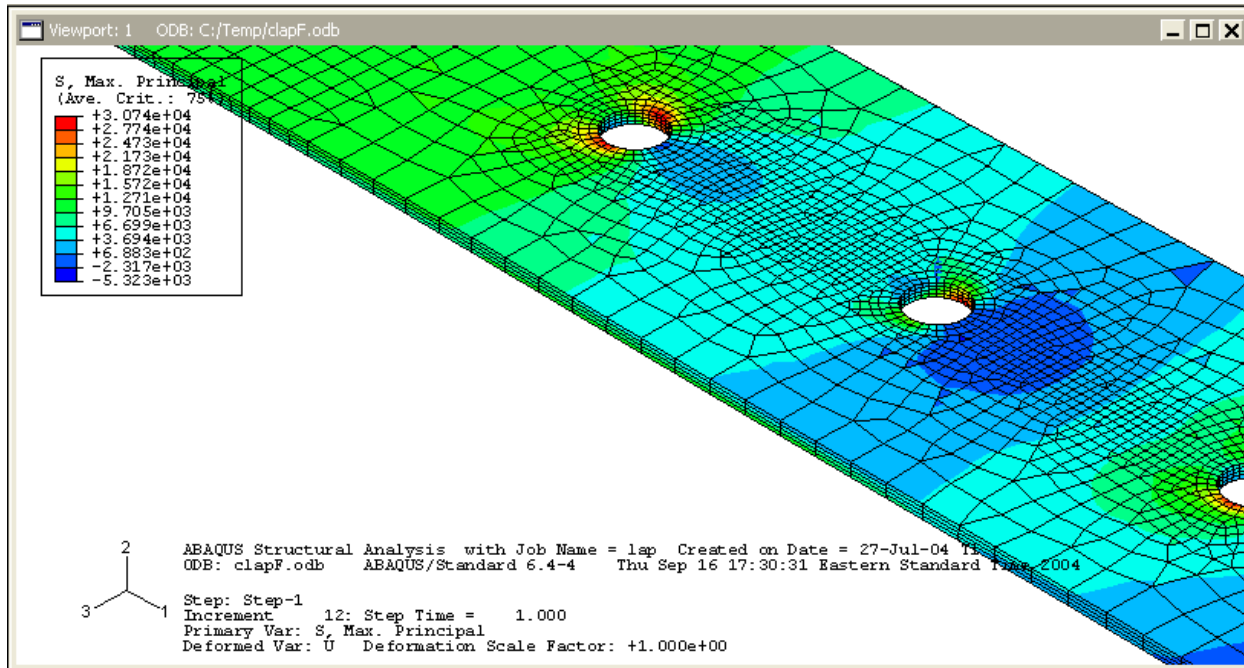


Figure 6- 42: Strip Model Extended Up To Inflection Point, Stringer Represented As Spring (Max Principal Stress In Lower Skin)

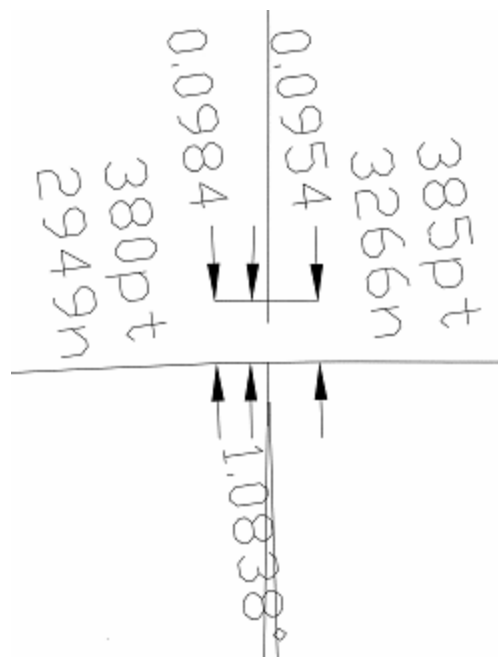


Figure 6-43: Displacements Of Mid Fastener From Half Bay Model

SHEET	6-29	NO.	4-087051-20
TOTAL	6-32		
ISSUE DATE	12/22/04		

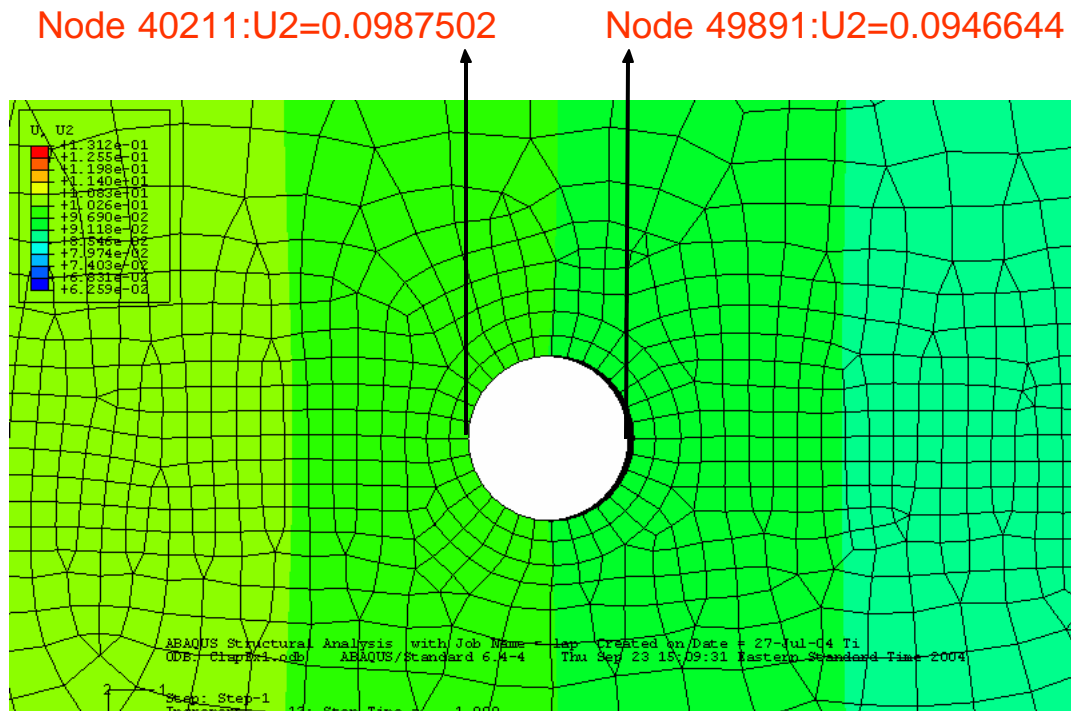


Figure 6-44: Displacements At Mid-Fastener From Baseline Strip Model

***INITIAL CONDITIONS, TYPE=STRESS**

LC20A,	-10000,	-15000,	-10000,	-2000,	0.0,	0.0
LC20B,	-20000,	-15000,	-15000,	-2000,	0.0,	0.0
LC20C,	-30000,	-15000,	-20000,	-6000,	0.0,	0.0
LC20D,	-40000,	-15000,	-25000,	2000,	0.0,	0.0
LC20E,	-40000,	-15000,	-35000,	-2000,	0.0,	0.0
LC20F,	-45000,	-15000,	-35000,	-4000,	0.0,	0.0
LC20G,	-50000,	-15000,	-30000,	-6000,	0.0,	0.0
LC20H,	-55000,	-15000,	-30000,	7000,	0.0,	0.0

Figure 6-45: Stress Results From Axi-Symmetric Model Applied As Initial Conditions To The Strip Model On Eight Segments Through The Thickness Of The Rivet Hole

SHEET	6-30	NO.	4-087051-20
TOTAL	6-32		
ISSUE DATE	12/22/04		

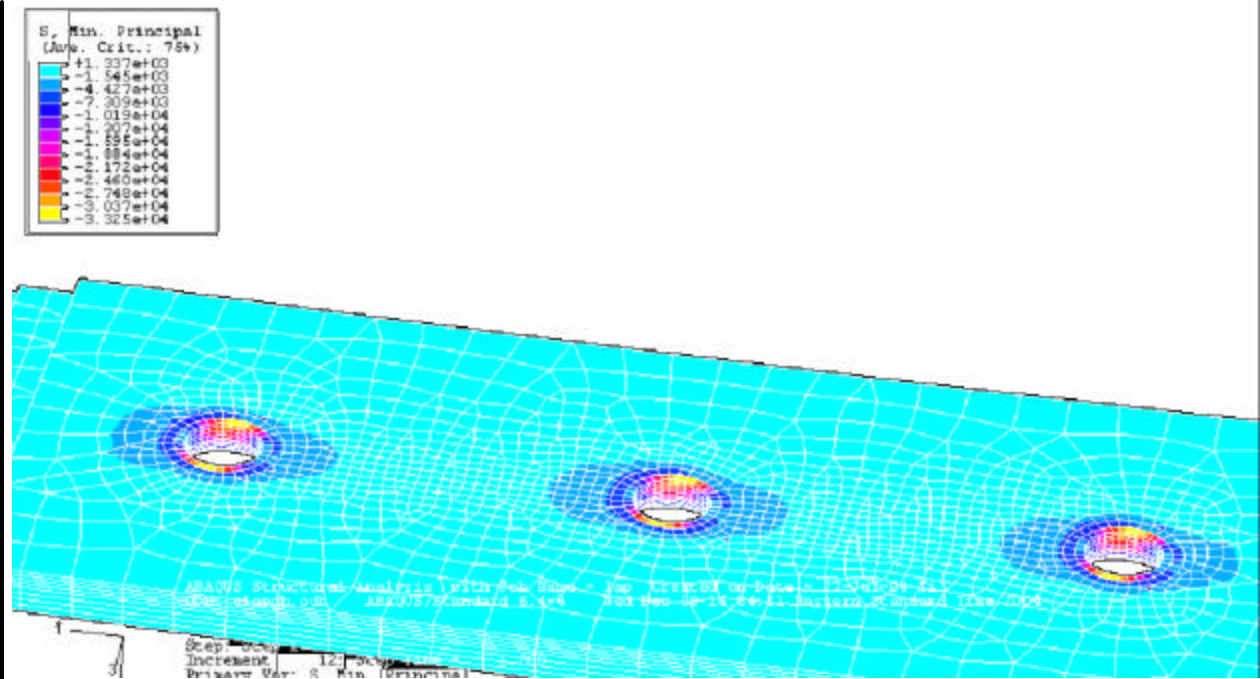


Figure 6-46: The Strip Model At The End Of Step 1(Apply Residual Stresses) To The Rivet Hole).

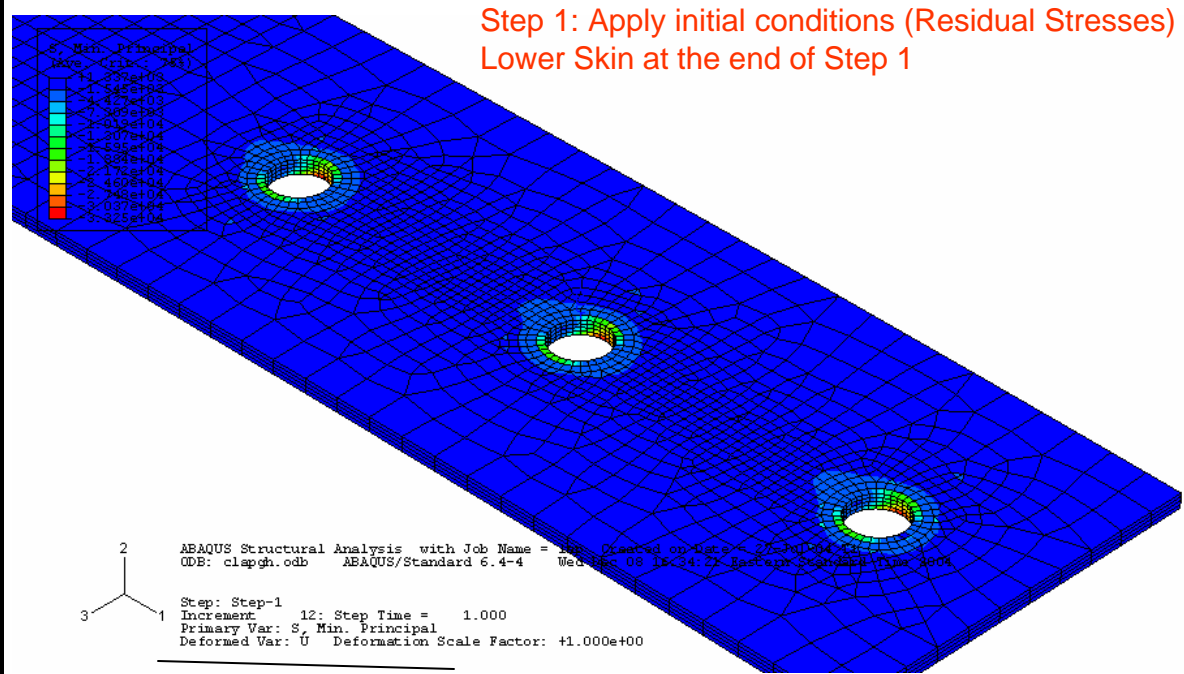


Figure 6-47: The Lower Skin At The End Of The First Step (Apply Residual Stresses).

SHEET	6-31	NO.	4-087051-20
TOTAL	6-32		
ISSUE DATE	12/22/04		

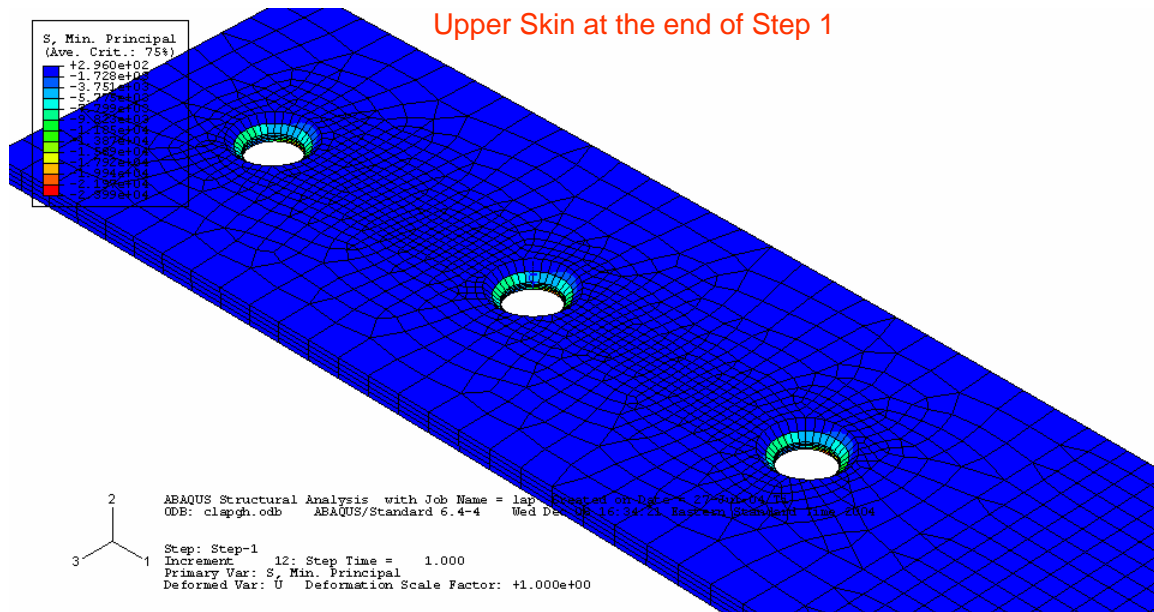


Figure 6-48: The Upper Skin At The End Of The First Step (Apply Residual Stresses).

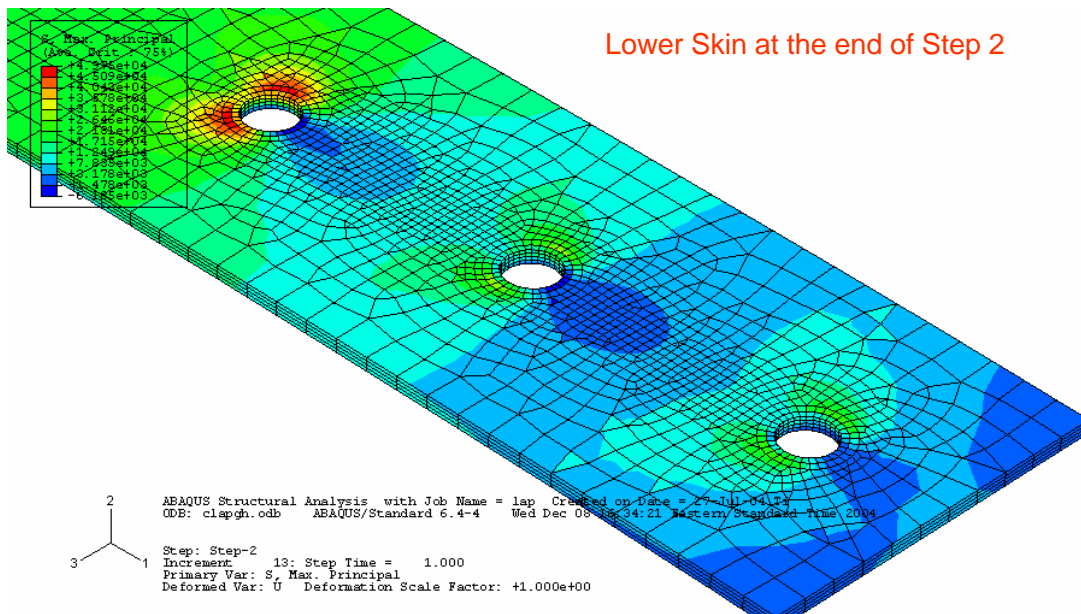


Figure 6-49: The Lower Skin At The End Of The Second Step (Apply Pressure).

SHEET	6-32	NO.	4-087051-20
TOTAL	6-32		
ISSUE DATE		12/22/04	

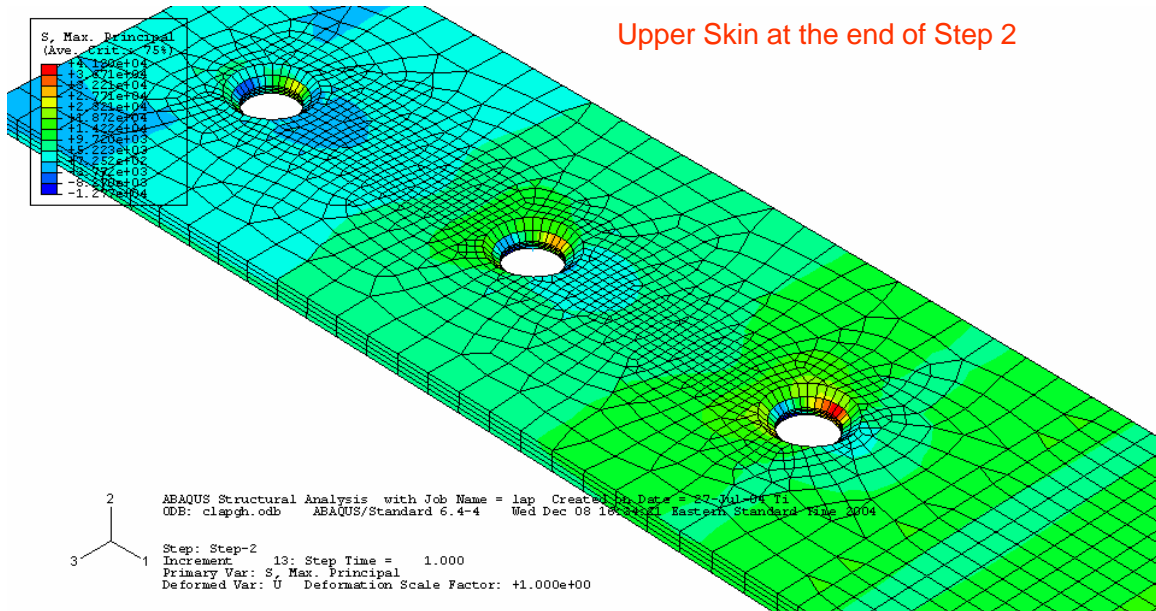


Figure 6-50: The Upper Skin At The End Of The Second Step (Apply Pressure).

REFERENCES

- [6-1] BACR15CE Boeing Part Standard, June 26, 1956, Rev (BF), December 19, 2002
- [6-2] Boeing 727 Structural Repair Manual, D6-4062, Rev 95, May 25, 2003.
- [6-3] MIL-HDBK-5H, Metallic Materials and Elements for Aerospace Vehicle Structures, U.S. Government Printing Office, Washington, DC, 1998.
- [6-4] M. P. Szolwinski and T. N. Farris, "Linking Riveting Process Parameters to the Fatigue Performance of Riveted Aircraft Structures," *Proceedings of the 40th AIAA/ASME/ASCE/ASC Structures, Structural Dynamics and Materials Conference*, St Louis, MO, April 1999, pp. 1208-1218.

SHEET	7-1	NO.	4-087051-20
TOTAL	7-28		
ISSUE DATE	12/22/04		

CHAPTER 7: CRACK GROWTH ANALYSIS

This chapter includes the discussion of all crack growth models developed to correlate the state of MSD at any time. The Local Crack Growth section addresses the crack state at a single hole, potentially including complex effects such as rivet residual stresses and multi-crack (“starburst”) cracking profiles. The MSD Propagation Simulation section addresses the propagation of multiple cracks at every fastener hole, including interaction effects and the varying stress distribution along the aircraft.

Local Crack Growth Analysis

The stress intensity function for a simple crack configuration in a fastener hole is well established in the technical literature (see Appendix B). During Q8, preliminary investigations were conducted with FADD2D [7-1] to evaluate its capabilities with respect to this project and to test out avenues of further research. FADD2D is a two-dimensional boundary element analysis program that seems well suited to evaluate crack profiles other than diametric. All analysis has been accomplished in 2D plane stress, so any effects due to skin bending and fastener clamp-up are ignored. The goal of the analysis was to conduct a comparative analysis of configurations with starburst cracking, leading to some preliminary conclusions.

The four FADD models considered are shown in Figure 7- 1. The hole in each model has four cracks, as shown in Figure 7- 2. The cracks are allowed to propagate from this starting state, leading to the configurations and SIF plots shown in Figure 7- 3 through Figure 7-5. Some observations from this analysis sequence are:

- In all models, Cracks 1 and 2 dominate. In the tensile only case these cracks grow normal to the far field stress, while in the tensile/bearing case the cracks propagate at an angle to the far field stress. This pattern has also been seen in the Damage Characterization.
- In all models, Cracks 3 and 4 arrest. These secondary cracks appear to have an influence proportional to their arc distance from the main crack; Crack 1 is always less dominant, apparently due to Crack 4. Similarly, Crack 4 arrests earlier than Crack 3.

SHEET	7-2	NO.	4-087051-20
TOTAL	7-28		
ISSUE DATE	12/22/04		

- The above observations remain unchanged with a changed edge location. The presence of the free edge does not appear significant to the character of growth.
- Based on the comparisons in Figure 7-6 and Figure 7-7, a diametric strip model is a conservative model of starburst cracking.

While these observations are valid for the current series of models, further work will be accomplished to determine their validity in general. In particular, the arrest behavior of the secondary cracks shown in Figure 7-8 may depend heavily on the pre-existence of cracks 1 and 2; if the initiation sequence is changed, this arrest may not occur. This issue is one of several areas for planned work outlined within the Detailed Work Plan.

SHEET	7-3	NO.	4-087051-20
TOTAL	7-28		
ISSUE DATE	12/22/04		

MSD Propagation Simulation

A numerical crack growth simulation tool was developed to model the growth of independent cracks from each hole in the MSD susceptible joint. The simulation is run in MS Excel, as shown in Figure 7-9. The values of far-field stress are taken from the Half Bay Shell Model. The hole location numbers use the naming convention established in the Initial Database Report and outlined in the Test Plan Data Retrieval Packages.

Each row of the simulation contains the crack length of both sides of each hole at a given cycle measurement. Each row is a step in the numerical simulation, and the cycle difference between rows is termed the simulation step size.

During Q4 and Q5, the simulation was used to generate predictions within the Test Plan Analysis. However, the simulation was developed as a general tool for propagating an arbitrary lap joint MSD state based on a varying stress distribution. Therefore, this simulation or future revision may be used to:

- generate pre-test predictions for all FASTER test panels
- generate prediction updates during a FASTER test based on a measured MSD distribution.
- propagate random MSD damage states as part of a Monte-Carlo simulation

During Q8, the MSD simulation was compared against striation count data for one frame bay (i.e., 15 holes). As discussed in a subsequent section, this comparison shows good correlation between simulation and actual crack growth, and serves to validate the simulation model. During Q9, the MSD simulation was used in a Monte Carlo approach to predict the distribution of crack arrays at DSG resulting from a preliminary EIFS distribution. Future work will compare the simulation results to the characterization data from additional bays, in addition to the bulleted list of objectives above.

SHEET	7-4	NO.	4-087051-20
TOTAL	7-28		
ISSUE DATE	12/22/04		

Stress Intensity Calculation

At each step, the crack tip stress intensity function (SIF) is calculated for each crack tip. The SIF is superimposed from three established solutions:

- The nominal β for diametric corner cracks becoming diametric oblique thru-cracks from a loaded hole, taken from USAF AFGROW [7-2];
- The interference factor $\beta_{\text{interference}}$ for adjacent unequal length cracks from Murakami [7-3];
- The finite width correction factor F_w from the USAF Damage Tolerance Design Manual [7-4]

The SIF at any crack length is calculated as

$$\text{SIF}(c) \equiv \sigma \sqrt{\pi c} \frac{\beta}{F_w} \beta_{\text{interference}},$$

where

c : crack length

σ : far field stress

$$F_w: \text{ the finite width correction factor, } F_w = \sqrt{\frac{w}{\pi(r-c)} \tan\left(\frac{\pi(r+c)}{w}\right)}$$

In effect, this approach replaces the conservative finite-width model of adjacent MSD with a specific correction factor. If the adjacent crack is the same length, this replacement has little effect, as a finite width model is a reasonable approximation of equal length MSD.

Stress State

For locations with a lower skin thickness of 0.040", the far field stress at each hole is taken from the 1/2 bay shell model discussed in the previous section. The bending at the fastener is derived using the approach from de Rijck and Fawaz [7-5] (based on Hartman and Schivje [7-6]) In summary, the stress intensity is calculated from:

- Stress Range: 12.81 ksi adjacent to the tearstraps increasing to 14.2 ksi midbay

SHEET	7-5	NO.	4-087051-20
TOTAL	7-28		
ISSUE DATE	12/22/04		

- Bending: 85% at all fasteners. This calculation assumes a rivet tilt β of 0.5° , with the 0.020" doubler acting as a non-working spacer.

Diametric Corner and Thru Cracks

Within AFGROW, the β calculation for diametric corner cracks uses a complex set of semi-empirical formulas based on Newman and Raju [7-7]. After the crack transitions to an oblique thru crack, AFGROW uses an interpolation algorithm of published tables of β values, including Fawaz [7-8,7-9]. In both cases, additional correction factors for finite width effects are included.

Since the MSD simulation is optimized for the very specific case of 727 lap joint cracking, reproducing the AFGROW SIF calculation within the simulation is unnecessarily complex. Instead, a single AFGROW run was conducted with the appropriate parameters to capture $\beta(c)$ for the complete run:

Model: Diametric Corner Cracks becoming Oblique Thru Cracks
 Width: 1.07" (typical fastener spacing)
 Thickness: 0.040"
 Bypass Stress: 61% (i.e., 39% load transfer at the first fastener)
 Bending: 85%
 Crack Size: $a = c = 50 \times 10^{-6}$ "

Based on this run, $\beta(C)$ was incorporated into the MSD simulation as a stepwise polynomial fit:

$$\beta(C) = -42103.28190786 C^3 + 3723.33566434 C^2 - 130.02932579 C + 4.5206899 \text{ for } C < 0.0416488 \text{ (corner crack)}$$

$$\beta(C) = -130187.91333294 C^5 + 87086.68287498 C^4 - 22524.24751596 C^3 + 2828.96383824 C^2 - 177.60562607 C + 6.33387229 \text{ for } 0.0416488 < C < 0.2 \text{ (short thru crack)}$$

$$\beta(C) = 2418.39711589 C^4 - 2393.69025414 C^3 + 881.75146161 C^2 - 141.71721318 C + 9.73600309 \text{ for } C > 0.2 \text{ (long thru crack)}$$

Interference Factor

The calculation of the interference β is complex, for it requires evaluation of the formulae below (written in a MathCAD format):

SHEET	7-6	NO.	4-087051-20
TOTAL	7-28		
ISSUE DATE	12/22/04		

$$K(A, B, L) := \int_0^{\frac{\pi}{2}} \left(1 - k(A, B, L)^2 \cdot \sin^2(\theta)\right)^{-\frac{1}{2}} d\theta$$

$$E(A, B, L) := \int_0^{\frac{\pi}{2}} \left(1 - k(A, B, L)^2 \cdot \sin^2(\theta)\right)^{\frac{1}{2}} d\theta$$

$$k(A, B, L) := \left[1 - \frac{L^2 - (A + B)^2}{L^2 - (A - B)^2}\right]^{\frac{1}{2}}$$

$$\beta_{\text{interaction}}(A, B) := \frac{\sqrt{(L - A + B) \cdot (L - A - B)}}{2 \cdot A} \cdot \left(\frac{L + A - B}{L - A - B} \cdot \frac{E(A, B, L)}{K(A, B, L)} - 1 \right)$$

where A is the crack length, B is the adjacent crack length, and L is the distance between crack centers. For this simulation, L is equal to the lap joint fastener spacing.

Within the simulation, a set of VBA functions use Simpson's integration rule to calculate the value of the elliptic integrals. This calculation is computationally intensive for any pair of crack lengths. However, for short cracks, there is no appreciable interaction and the interaction β -factor is either equal to 1 or increasing slightly. Therefore, the determination of the interaction β -factor is accomplished one of two ways:

- For large cracks, when MSD propagation is sensitive to the interaction β -factor, the value is calculated explicitly using the above formulae. For example, explicit calculation was done during the simulation of Phase 3 of the testing in the Test Plan Analysis.
- For smaller cracks, when MSD propagation is not sensitive, the interaction β -factor is linearly interpolated from values in $\beta(a_1, a_2)$ table lookup (see Figure 7-11). This method substantially reduces the computational effort of the calculation, as is necessary for a high volume of calculations required for a Monte Carlo simulation. Note that because of the increasing slope of the β -factor, linear interpolation results in a conservative (higher) estimate of the true value.

SHEET	7-7	NO.	4-087051-20
TOTAL	7-28		
ISSUE DATE	12/22/04		

Growth Rate Calculation

Throughout the simulation, the crack growth rate (da/dN) is calculated using the methods in NASGRO v3[7-10]. The calculation uses the Modified Forman equation for growth rate as a function of ΔK and Stress Ratio (R), including threshold stress intensity, critical stress intensity, and closure effects:

Crack growth rate:

$$dN da_{msd}(A) := \frac{1}{C (1-f)^n} \cdot \left[\left(\frac{\Delta K_{msd}(A)}{ksi \cdot \sqrt{in}} \right)^{-n} \cdot \left(1 - \frac{\Delta K_{th}(A)}{\Delta K_{msd}(A)} \right)^{-p} \cdot \left(1 - \frac{\Delta K_{msd}(A)}{K_c} \right)^q \right]$$

$$dadN_{msd}(A) := \frac{1}{dN da_{msd}(A)}$$

SIF threshold:

$$\Delta K_{th}(A, \sigma_{min}, \sigma_{max}) := \Delta K_0 \cdot \left(\frac{4}{\pi} \cdot \tan \left(1 - \frac{\sigma_{min}}{\sigma_{max}} \right) \right) \cdot \left(\frac{A}{A + a_0} \right)^{0.5}$$

Closure/stress ratio effect

$$A_0 := \left(0.825 - 0.34 \cdot \alpha + 0.05 \cdot \alpha^2 \right) \cdot \cos \left(SR \cdot \frac{\pi}{2} \right)^{\frac{1}{\alpha}}$$

$$A_1 := (0.415 - 0.071 \cdot \alpha) \cdot SR$$

$$A_3 := 2 \cdot A_0 + A_1 - 1$$

$$A_2 := 1 - A_0 - A_1 - A_3$$

$$f_R(R) := \begin{cases} \max \left(\left[R \cdot A_0 + A_1 \cdot R + A_2 \cdot R^2 + A_3 \cdot R^3 \right] \right) & \text{if } R > 0 \\ A_0 + A_1 \cdot R & \text{otherwise} \end{cases}$$

Empirical constants:

$$C := 0.244 \cdot 10^{-7} \quad \alpha := 1.5 \quad \Delta K_0 := 2.9 \cdot ksi \cdot \sqrt{in} \quad SR := 0.3 \quad q := 1.0 \quad p := 0.5$$

$$n := 2.601 \quad A_k := 1 \quad B_k := 1 \quad K_{Ic} := 29 \cdot ksi \cdot \sqrt{in} \quad a_0 := 0.004 \cdot in$$

SHEET	7-8	NO.	4-087051-20
TOTAL	7-28		
ISSUE DATE	12/22/04		

Crack Growth Increment

The simulation solves for the crack length at the following step through numerical solution of the differential equation for crack growth rate:

$$\frac{da}{dN} = f(a, N)$$

where a is the crack length, and N is cycles, and $f(a, N)$ is calculated using the SIF and Modified Forman rate equations. A fourth order Runge-Kutta method[7-11] determines the crack length for the following step. The simulation step size can be changed based on the crack growth rate, but the Runge-Kutta step size is typically $1/20^{\text{th}}$ of the simulation step size. The simulation step size is typically 1000 cycles.

Pre-Test Predictions

The assumed initial crack distribution is important to the analysis. However, one conclusion from the Damage Characterization to date is that the scatter in fatigue crack initiation is a function of many unknowns other than stress, so a crack distribution based primarily on stress cannot necessarily capture service effects in an individual bay. However, a crack growth simulation which starts with an equal length flaw at every location is a reasonable approach to test prediction, and was used for the FT2 and FT1 Pre-Test Predictions. See the Test Plan Analysis for further discussion.

Note that at Q8 the SIF derivation changed to allow simulation of corner crack propagation. However, this change did not significantly affect predictions of the thru crack phase. The revised simulation will be used for future test predictions.

SHEET	7-9	NO.	4-087051-20
TOTAL	7-28		
ISSUE DATE	12/22/04		

Validation

During Q8, the MSD simulation was validated through comparison to striation count data for a complete frame bay FS 540 – FS 560 along S-4R (see Q8 Damage Characterization). The validation process compared crack length vs cycle data from three sources:

- Striation spacing vs distance to origin measured using Scanning Electron Microscopy (see Figure 7-12). Striation spacing is an empirical measurement of crack growth rate at a single location on fracture surface. Point-to-point integration over all locations leads to a cycles vs crack length curve.
- An AFGROW strip model of a diametric corner cracks becoming oblique thru cracks within a finite-width, using the parameters listed in the Stress Intensity section of this chapter (see Figure 7- 10)
- The MSD simulation, with results specific to each hole.

The process for aligning curves from these data sources is shown on the midbay hole data in Figure 7-15. Since the current crack state at 59,497 airframe cycles is the known condition, the striation count data and the simulation are aligned at this point. The striation count is grown backwards from the current state. The starting MSD distribution for the simulation was iterated until the predicted state at 59,497 airframe cycles reflects the actual current state. Note that data from the striation count was not used to “tune” the simulation; the two data sources are simply juxtaposed on the same curve, and plots where the data coincide indicates a good model fit.

The AFGROW strip model and the MSD simulation are essentially identical in the small corner crack regime, where the effect of adjacent crack interaction is negligible. So, the AFGROW model results are aligned with the MSD simulation results such that the two models overlap in this region. This juxtaposition demonstrates the conservative prediction of the strip model; for cracks where the adjacent crack is small, crack growth predicted by the strip model can be appreciably faster than the simulation and the striation data. Also, it allows the AFGROW model to be used to determine an equivalent initial flaw size (EIFS) for each hole.

SHEET	7-10	NO.	4-087051-20
TOTAL	7-28		
ISSUE DATE	12/22/04		

The comparisons between the AFGROW strip, MSD simulation, and striation count data are shown in Figure 7-15 through Figure 7-20. On average, the MSD simulation is a good fit to the striation count data, particularly for cracks longer than the 0.040" skin thickness (see Figure 7-21). The simulation does not fit well within the corner crack regime, in part because of the complex, multi-origin nature of the service cracks. These complex effects, in addition to crack angle, starburst cracking, or rivet residual stress effects, are not modeled in the analysis.

As shown in Figure 7-22 and Figure 7-23, the current state of damage in the FS 540 – FS 560 4R frame bay was propagated forward under service loads using the MSD simulation. As the simulation does not explicitly check for failure under residual strength requirements, criteria defining several failure conditions are calculated separately. Figure 7-22 shows the predicted length vs. cycle plot for the longest crack in the frame bay had the aircraft remained in service. With the exception of the 1" tip-to-tip, the listed failure criteria have been conservatively applied to the AFGROW strip model. The conclusion is that MSD link-up in this frame bay under JAR 25.571 loads would be predicted between 70,000 and 80,000 cycles. Note that this frame bay is not necessarily the worst bay in the aircraft, so the first predicted linkup may occur earlier.

Equivalent Initial Flaw Distribution

The equivalent initial flaw size is determined as the crack length at 0 cycles from the AFGROW strip model. The EIFS distribution for this frame bay is tabulated in Figure 7-24, and shown as a histogram in Figure 7-25. The resulting EIFS average of 4 μm should be compared to the 12 μm mean determined by Fawaz [7-12], and to the 50 μm - 100 μm range used successfully in Harris, Piascik, and Newman [7-13]. It is important to note that this crack size is "equivalent" in the sense that the analysis produces the correct MSD array at 60,000 cycles; it is not an accurate reflection of the state of damage at zero cycles, and in many cases the crack origins on the respective fracture surface are not located at the hole corner. Also, this EIFS is strongly tied to the analysis method used, as it ignores small crack effects.

During Q9, a Weibull distribution was fit to the EIFS data as shown in Figure 7- 26. The resulting distribution (shape factor $\alpha = 1.22$, characteristic life $\beta = 108.1 \times 10^6$ in.) provides a stochastic starting

SHEET	7-11	NO.	4-087051-20
TOTAL	7-28		
ISSUE DATE	12/22/04		

point for each crack location in a Monte Carlo simulation. It is important to remember that since this distribution was derived from a limited data set, it has two important shortcomings:

- There is no data derived from large cracks, such as the 20 inch lap joint crack discussed in the preamble to AD 99-04-22;
- There is no data derived from holes characterized and found with no cracks.

With these omissions, the distribution generated cannot completely predict the initiation of MSD in service. However, this distribution is reasonable to use for methodology development of the MSD propagation simulation.

Monte Carlo Simulation

A simulation is conducted by generating stochastic array of cracks within a frame bay at zero cycles from the EIFS as shown in Figure 7- 27. The MSD simulation is entirely deterministic, and results in a predicted crack array at 60,000 cycles. After accomplishing 1,000 runs of the simulation, the array of results was analyzed statistically as shown in Table 1.

The histogram of all final crack lengths is shown in Figure 7- 28. The maximum crack length from the simulation is 0.349 in., which is considerably longer than the 0.185" maximum found within this frame bay or the 0.225" maximum found to date on the subject aircraft (see Damage Characterization reports). However, the distribution of cracks measured up to Q9 are qualitatively consistent with the simulation results. The histogram of primary crack lengths from the Q9 Database (normalized to an equivalent area) are shown with the histogram of Monte Carlo simulation results in Figure 7- 29.

Statistical results from these 1,000 Monte Carlo runs include:

- 54.7% of runs result in cracks longer than 0.234", the 90% POD crack size for external LFEC inspection.
- 10.8% of those runs result in 2 cracks in a single bay longer than 0.234".

The maximum crack length in the frame bay has also been calculated for each Monte Carlo run. This histogram for maximum hole-to-tip crack length is shown in Figure 7- 30, and the histogram for maximum tip-to-tip crack length is shown in Figure 7- 31. Results of that analysis include:

SHEET	7-12	NO.	4-087051-20
TOTAL	7-28		
ISSUE DATE	12/22/04		

- 1.0% of runs result in hole-to-tip cracks larger than 0.273", the crack size associated with ligament yielding of a 1.07" wide strip at residual strength conditions.
- The largest tip-to-tip crack was 0.733", below the 1" tip-to-tip criteria for sparse MSD link-up.

This MSD simulation models the behavior of MSD on the subject airplane. Additional work would be required to extend these results to other airplanes. Future work on the MSD simulation will include:

- Improvement of the empirical EIFS distribution to address the identified shortcomings.
- Incorporation of the Probabilistic Neural Network Initiation model into the deterministic MSD simulation (see Chapter 8)
- Validation of the MSD simulation against characterization data from additional frame bays and the FASTER test panels.

SHEET	7-13	NO.	4-087051-20
TOTAL	7-28		
ISSUE DATE	12/22/04		

References

- [7-1] Fracture Analysis by Distributed Dislocations in 2 Dimensions, Analysis code by C. Chang and M. Mear (UT Austin), User Interface by NASA Langley and AS&M Inc.
- [7-2] J. A. Harter, AFGROW Users Guide And Technical Manual, AFRL-VA-WP-TR-2004-XXXX, Final Report For The Period 4/2/87-6/07/04, June 2004.
- [7-3] Y. Murakami et al., Stress Intensity Factors Handbook, Pergamon Press, New York, 1990
- [7-4] J. Gallagher, Damage Tolerant Design Handbook, University of Dayton Research Institute, prepared for Air Force Wright Aeronautical Laboratories, Wright-Patterson Air Force Base, Ohio, 1983.
- [7-5] J. J. M de Rijck and S. Fawaz, "A Simplified Approach For Stress Analysis Of Mechanically Fastened Joints", Fourth Joint DOD/FAA/NASA Conference on Aging Aircraft, May 2000.
- [7-6] A. Hartman and J. Schijve, "The Effect Of Secondary Bending On Fatigue Strength Of 2024-T3 Alclad Riveted Joints", NLR TR 69116 U, 1969.
- [7-7] Newman, J.C., and Raju, I.S., "Stress Intensity Factor Equations for Cracks in Three-Dimensional Bodies Subjected to Tension and Bending Loads," Chapter 9, Computational Methods in the Mechanics of Fracture, Elsevier Science Publishers B.V., 1986
- [7-8] Fawaz, S.A., "Application of the Virtual Crack Closure Technique to Calculate Stress Intensity Factors for Through Cracks with an Elliptical Crack Front," Engineering Fracture Mechanics, 59 (1998), pp. 327-342.
- [7-9] S. A. Fawaz, "Stress Intensity Factor Solutions For Part-Elliptical Through Cracks," Engineering Fracture Mechanics Vol 63, pp 209-226, 1999.
- [7-10] JSC-22267A, "Fatigue Crack Growth Computer Program 'NASA FLAGRO' Version 2.0, Revision A, 1994.
- [7-11] Scheid, F., Schaum's Outline of Theory and Problems of Numerical Analysis, Second Edition, 1989.
- [7-12] S. A. Fawaz, Equivalent Initial Flaw Size Testing And Analysis, AFRL-VA-WP-TR-2000-3024, Final Report for 10/01/97-6/15/2000, June 2000.
- [7-13] C. E. Harris, R. S. Piascik, and J. C. Newman, Jr., "A Practical Engineering Approach To Predicting Fatigue Crack Growth In Riveted Lap Joints", Presented at the International Conference On Aeronautical Fatigue (ICAF), 1999.

SHEET	7-14	NO.	4-087051-20
TOTAL	7-28		
ISSUE DATE	12/22/04		

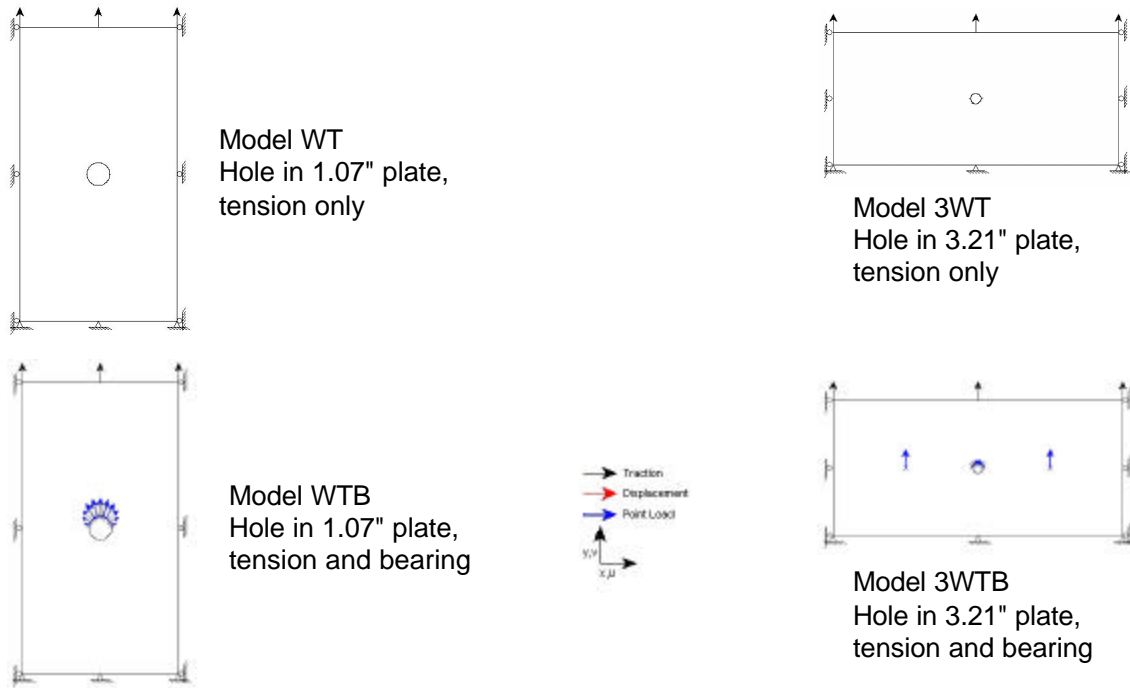
Figures

Figure 7- 1: Four FADD Models

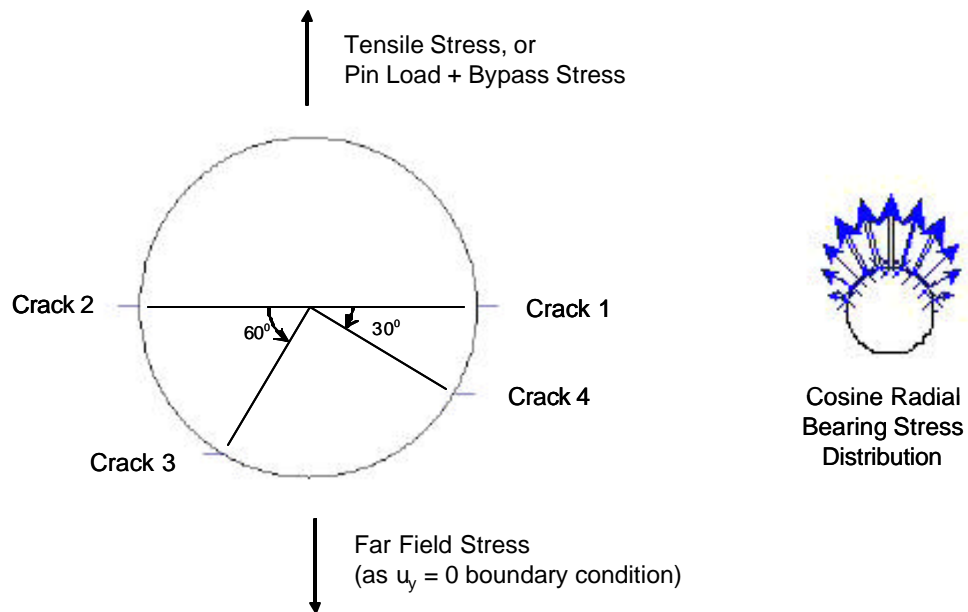


Figure 7- 2: Crack Profile in All Four FADD Models

SHEET	7-15	NO.	4-087051-20
TOTAL	7-28		
ISSUE DATE	12/22/04		

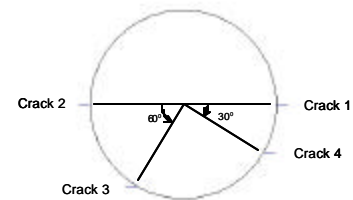
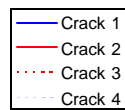
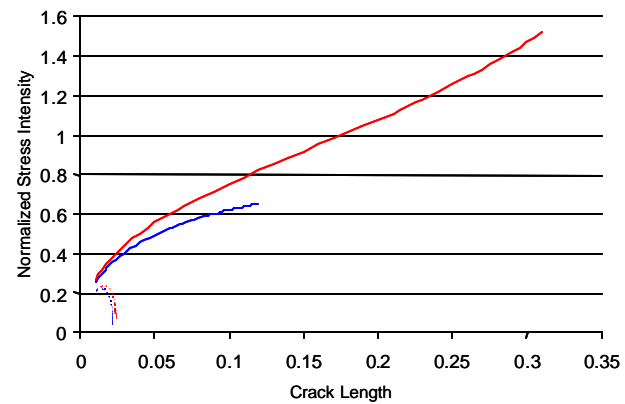
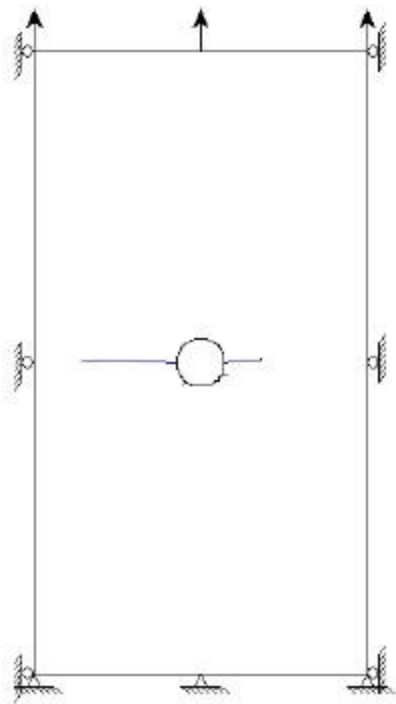


Figure 7- 3: Normalized SIF for WT Model (All Cracks)

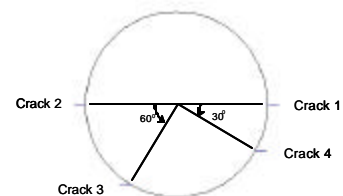
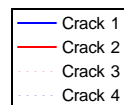
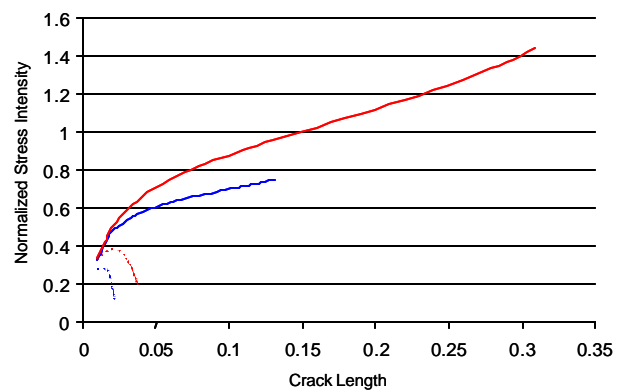
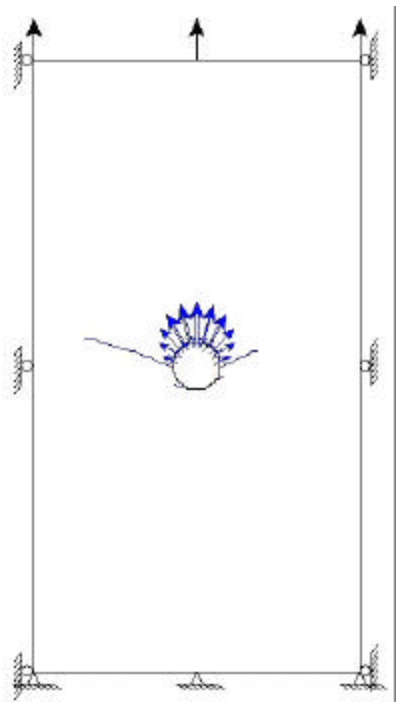


Figure 7- 4: Normalized SIF for WTB Model (All Cracks)

SHEET	7-16	NO.	4-087051-20
TOTAL	7-28		
ISSUE DATE	12/22/04		

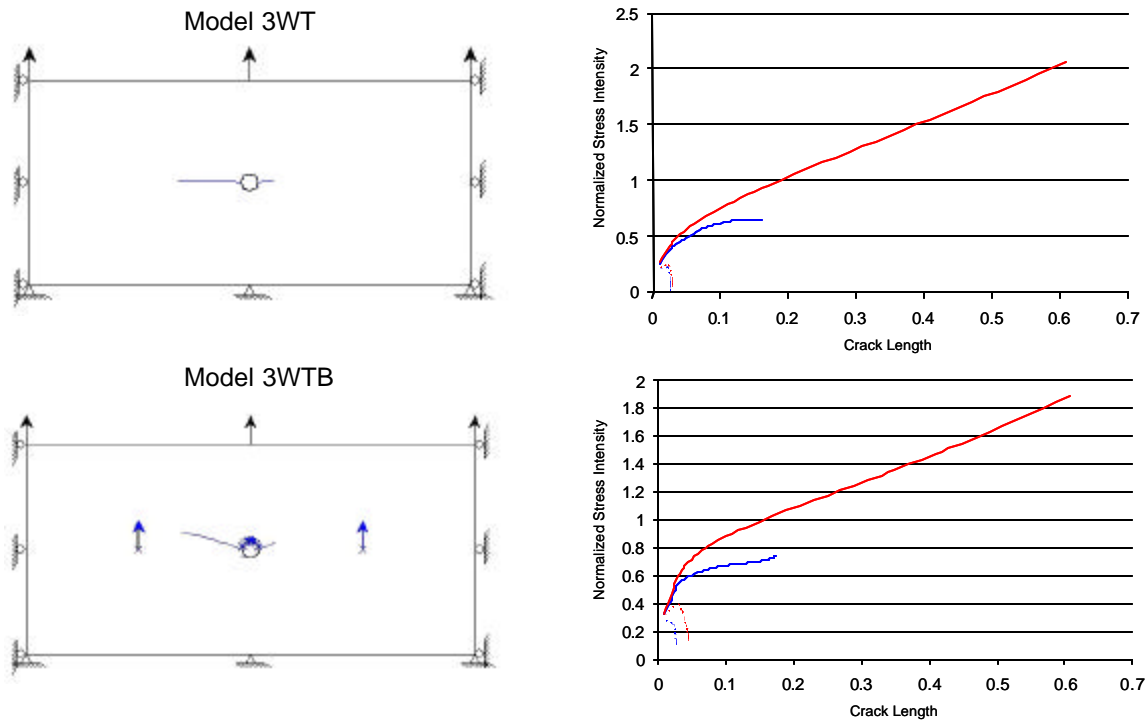


Figure 7-5: Normalized SIF for 3WT and 3WTB Models (All Cracks)

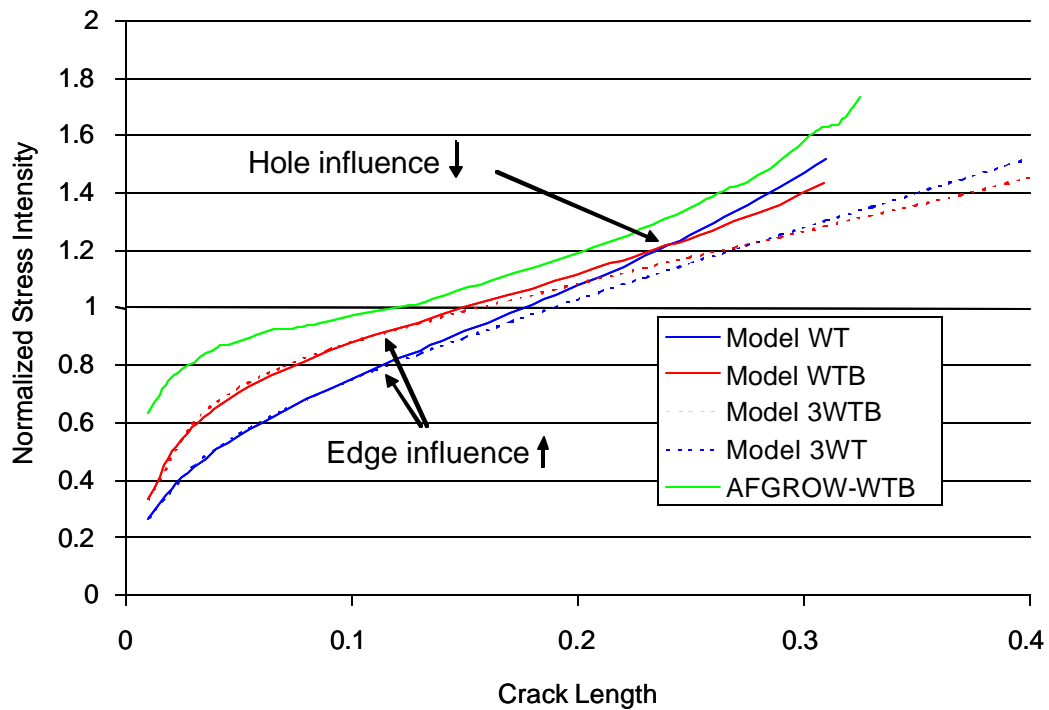


Figure 7-6: Normalized SIF for Crack 2 (All Models)

SHEET	7-17	NO.	4-087051-20
TOTAL	7-28		
ISSUE DATE	12/22/04		

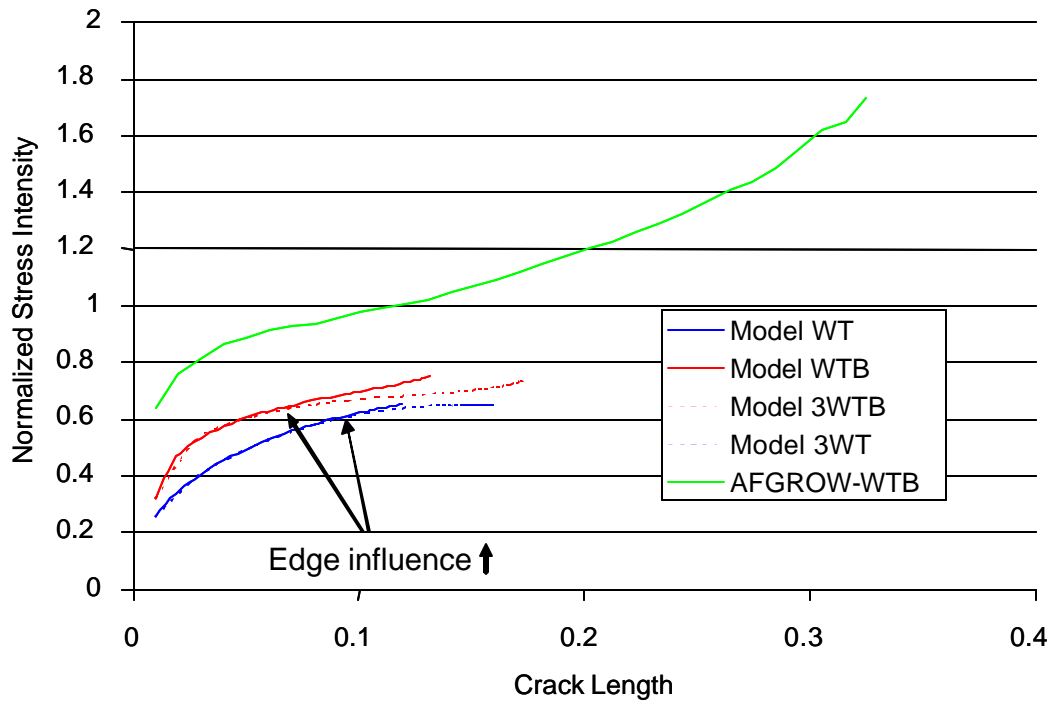


Figure 7-7: Normalized SIF for Crack 1 (All Models)

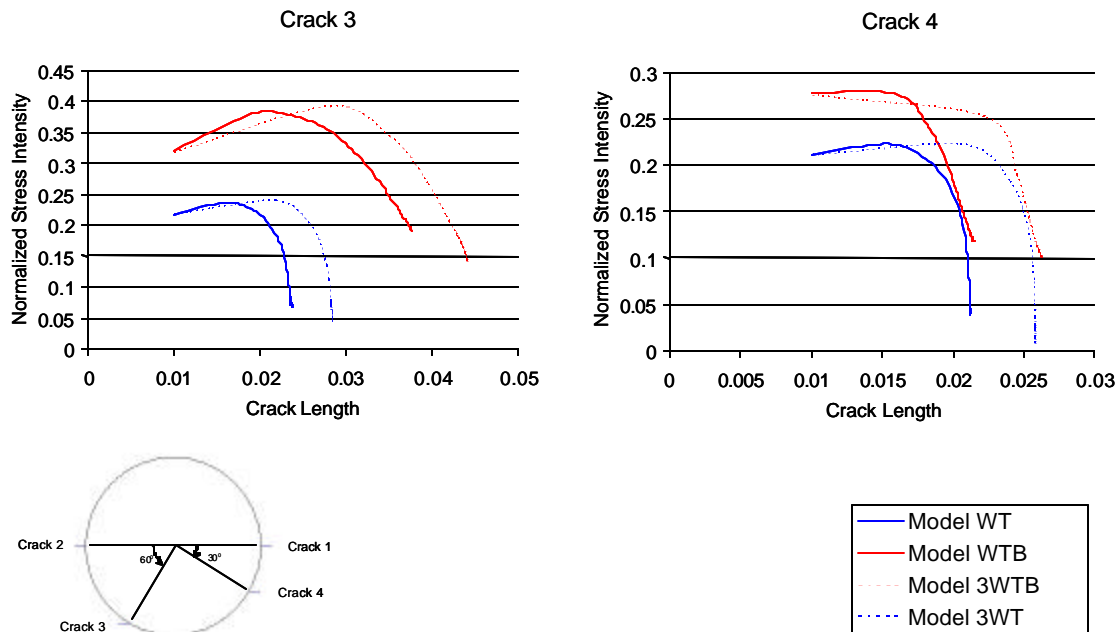


Figure 7-8: Normalized SIF for Cracks 3 and 4 (All Models)

ENGINEERING DEPARTMENT

SHEET	7-18	NO.	4-087051-20
TOTAL	7-28		
ISSUE DATE	12/22/04		

	540+02 6~4L + 1.0~LSH		540+03 6~4L + 1.0~LSH		540+04 7~4L + 1.0~LSH		540+05 7~4L + 1.0~LSH		540+06 8~4L + 1.0~LSH		540+07 9~4L + 1.0~LSH	
Fuselage Station	542.6	542.6	543.6	543.6	544.7	544.7	545.7	545.7	546.8	546.8	547.9	547.9
Dist. to frame	2.6	2.6	3.6	3.6	4.7	4.7	5.7	5.7	6.8	6.8	7.9	7.9
FF Stress	12.81	12.81	13.17	13.17	13.47	13.47	13.74	13.74	13.94	13.94	14.08	14.08
True Length at 59,497	---	---	---	---	0.151183	---	0.140258	0.0898	0.167268	0.090086	0.184176	0.112513
Predicted at 59497	0.0009	0.0009	0.0012	0.0013	0.1519	0.0017	0.1402	0.0899	0.1660	0.0905	0.1857	0.1121
Cycles												
29,497	0.0001	0.0001	0.0001	0.0001	0.0125	0.0001	0.0065	0.0014	0.0100	0.0011	0.0140	0.0017
30,497	0.0001	0.0001	0.0001	0.0001	0.0147	0.0001	0.0078	0.0016	0.0120	0.0013	0.0168	0.0020
31,497	0.0001	0.0001	0.0001	0.0001	0.0172	0.0001	0.0094	0.0018	0.0144	0.0015	0.0201	0.0024
32,497	0.0001	0.0001	0.0001	0.0001	0.0201	0.0001	0.0112	0.0021	0.0172	0.0017	0.0238	0.0029
33,497	0.0001	0.0001	0.0001	0.0001	0.0234	0.0001	0.0134	0.0025	0.0204	0.0020	0.0283	0.0034
34,497	0.0001	0.0001	0.0001	0.0001	0.0272	0.0001	0.0159	0.0030	0.0242	0.0024	0.0334	0.0042
35,497	0.0001	0.0001	0.0001	0.0001	0.0315	0.0001	0.0188	0.0035	0.0285	0.0029	0.0391	0.0051
36,497	0.0001	0.0001	0.0002	0.0002	0.0363	0.0002	0.0221	0.0042	0.0335	0.0035	0.0445	0.0062
37,497	0.0002	0.0002	0.0002	0.0002	0.0414	0.0002	0.0259	0.0051	0.0391	0.0042	0.0493	0.0076
38,497	0.0002	0.0002	0.0002	0.0002	0.0458	0.0002	0.0303	0.0061	0.0443	0.0051	0.0541	0.0093
39,497	0.0002	0.0002	0.0002	0.0002	0.0500	0.0002	0.0353	0.0074	0.0490	0.0062	0.0588	0.0113
40,497	0.0002	0.0002	0.0002	0.0002	0.0541	0.0002	0.0406	0.0089	0.0536	0.0075	0.0635	0.0136
41,497	0.0002	0.0002	0.0002	0.0002	0.0583	0.0002	0.0454	0.0107	0.0582	0.0091	0.0684	0.0164

Figure 7-9: Section of Crack Growth Simulation, Phases 1 and 2

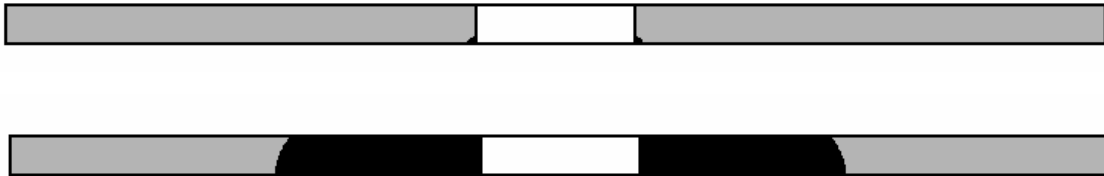


Figure 7- 10: AFGROW Model

a1/a2	5.00E-03	0.07	0.1	0.125	0.15	0.2	0.25	0.275	0.3	0.325	0.35	0.375	0.4	0.425	0.45	0.475	0.5
0.005	1.003	1.011	1.015	1.020	1.026	1.039	1.056	1.065	1.076	1.088	1.101	1.115	1.131	1.148	1.168	1.189	1.212
0.07	1.004	1.012	1.017	1.022	1.028	1.043	1.061	1.072	1.084	1.097	1.111	1.128	1.145	1.165	1.187	1.212	1.240
0.1	1.004	1.012	1.018	1.023	1.029	1.045	1.064	1.075	1.088	1.102	1.117	1.135	1.154	1.175	1.199	1.226	1.256
0.125	1.004	1.013	1.018	1.024	1.031	1.046	1.067	1.079	1.092	1.107	1.123	1.141	1.162	1.184	1.210	1.239	1.272
0.15	1.004	1.013	1.019	1.025	1.032	1.049	1.070	1.082	1.096	1.112	1.129	1.149	1.171	1.195	1.223	1.254	1.291
0.2	1.004	1.014	1.021	1.027	1.035	1.053	1.077	1.091	1.107	1.125	1.145	1.167	1.193	1.222	1.255	1.294	1.339
0.25	1.005	1.016	1.023	1.030	1.039	1.059	1.086	1.102	1.120	1.141	1.164	1.191	1.222	1.258	1.300	1.351	1.411
0.275	1.005	1.017	1.024	1.032	1.041	1.063	1.091	1.109	1.129	1.151	1.177	1.207	1.241	1.282	1.330	1.389	1.463
0.3	1.005	1.017	1.026	1.034	1.043	1.067	1.098	1.116	1.138	1.163	1.191	1.225	1.264	1.311	1.368	1.439	1.531
0.325	1.006	1.019	1.027	1.036	1.046	1.071	1.105	1.125	1.149	1.176	1.209	1.246	1.292	1.347	1.416	1.505	1.628
0.35	1.006	1.020	1.029	1.038	1.049	1.077	1.113	1.136	1.162	1.193	1.229	1.273	1.326	1.393	1.480	1.599	1.778
0.375	1.006	1.021	1.031	1.041	1.053	1.082	1.123	1.148	1.177	1.212	1.255	1.306	1.371	1.455	1.571	1.745	2.053
0.4	1.007	1.023	1.033	1.044	1.057	1.089	1.134	1.162	1.196	1.237	1.286	1.349	1.431	1.543	1.712	2.012	2.867
0.425	1.007	1.024	1.036	1.048	1.062	1.098	1.147	1.180	1.219	1.267	1.327	1.406	1.515	1.680	1.972	2.806	
0.45	1.008	1.026	1.039	1.052	1.067	1.107	1.164	1.201	1.248	1.306	1.383	1.488	1.648	1.932	2.745		
0.475	1.009	1.029	1.042	1.057	1.074	1.119	1.184	1.229	1.285	1.359	1.461	1.616	1.893	2.685			
0.5	1.009	1.031	1.047	1.062	1.082	1.133	1.210	1.264	1.335	1.434	1.584	1.853	2.624				
0.55	1.011	1.038	1.057	1.078	1.103	1.172	1.288	1.381	1.521	1.774	2.503						
0.6	1.014	1.048	1.074	1.101	1.136	1.241	1.457	1.694	2.379								
0.65	1.018	1.064	1.099	1.140	1.194	1.392	2.252										
0.7	1.025	1.091	1.147	1.216	1.325	2.118											

Figure 7-11: Interaction β -factor Table (Effect of Crack B on $\Delta K(A)$)

SHEET	7-19	NO.	4-087051-20
TOTAL	7-28		
ISSUE DATE	12/22/04		

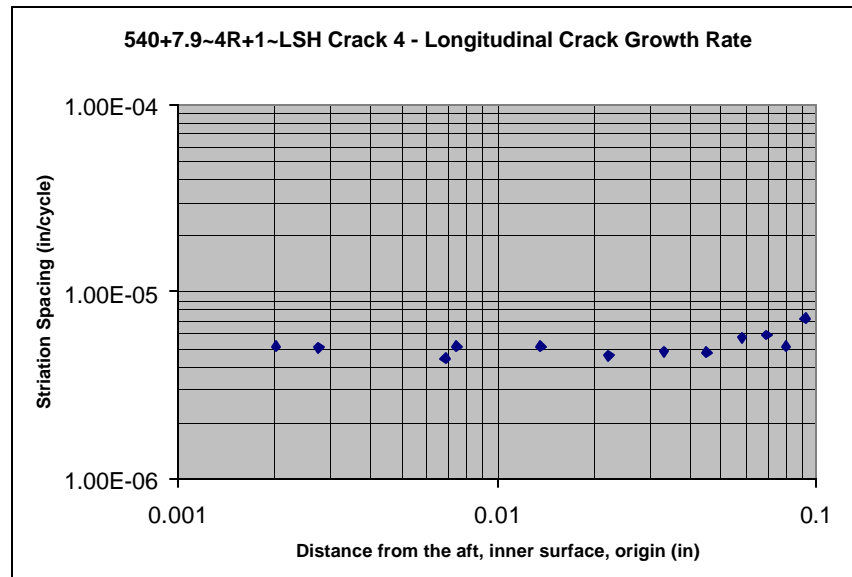


Figure 7-12: Typical Crack Growth Rate Data from Fracture Surface Striation Count

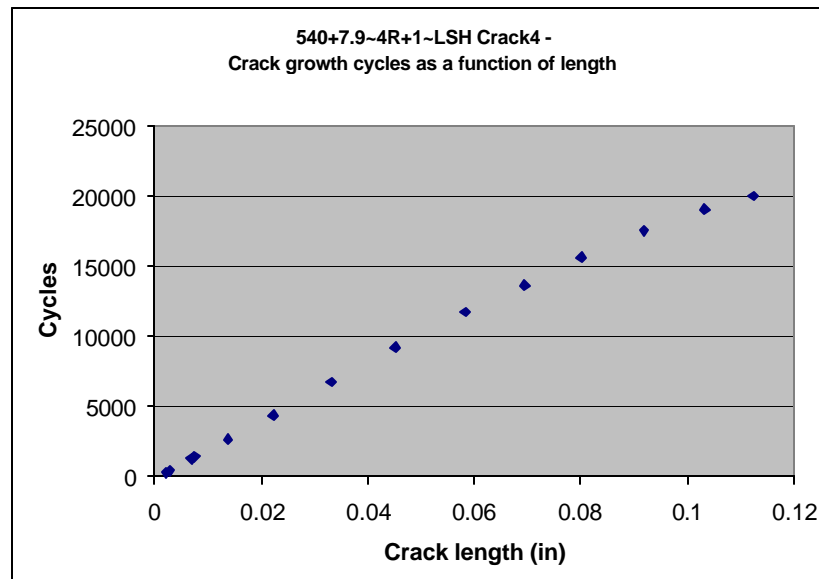
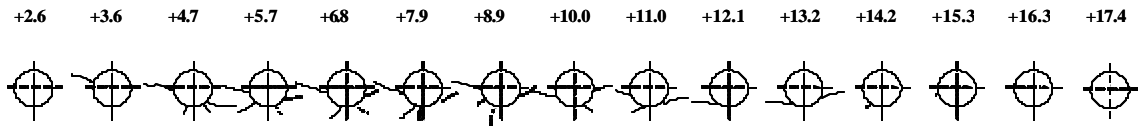


Figure 7-13: Typical Crack Length vs Cycles Data, Integrated from Striation Count

SHEET	7-20	NO.	4-087051-20
TOTAL	7-28		
ISSUE DATE	12/22/04		



Modeled as

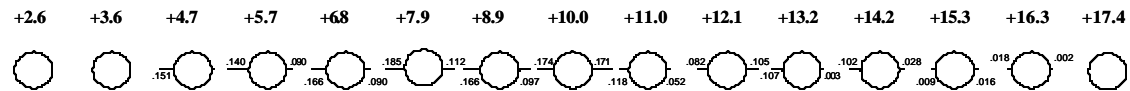


Figure 7-14: Simplified Model of Multiple Cracks within Simulation

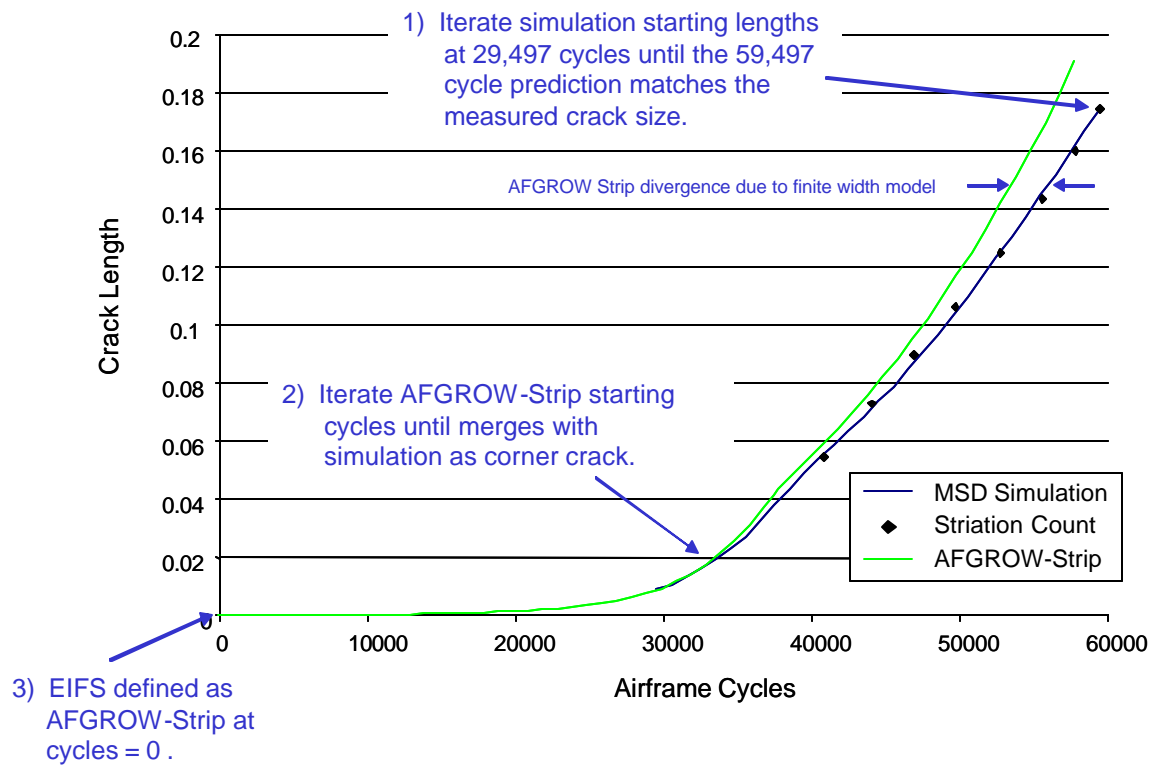


Figure 7-15: Procedure for Locating Data – Hole 540+10.0~4R+1~LSH

ENGINEERING DEPARTMENT

SHEET	7-21	NO.	4-087051-20
TOTAL	7-28		
ISSUE DATE	12/22/04		

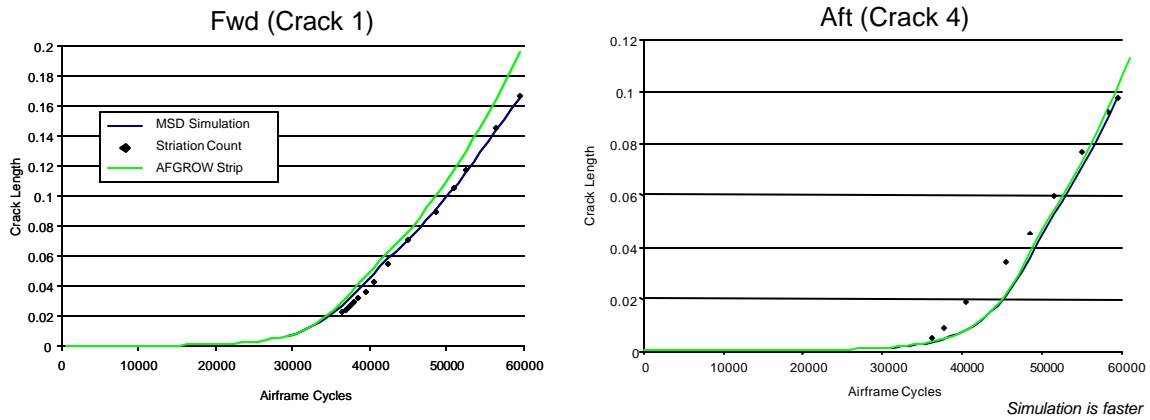


Figure 7-16: Hole 540+8.9~4R+1~LSH

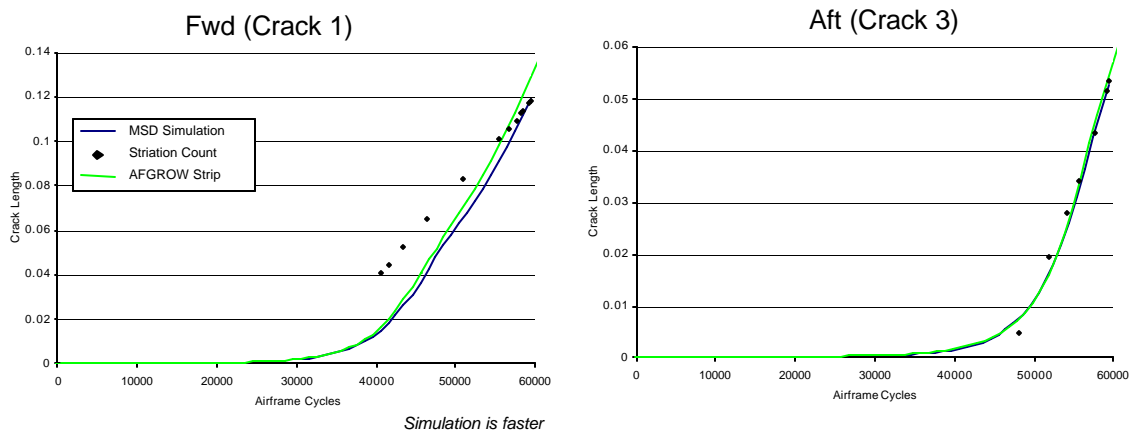


Figure 7-17: Hole 540+11.0~4R+1~LSH

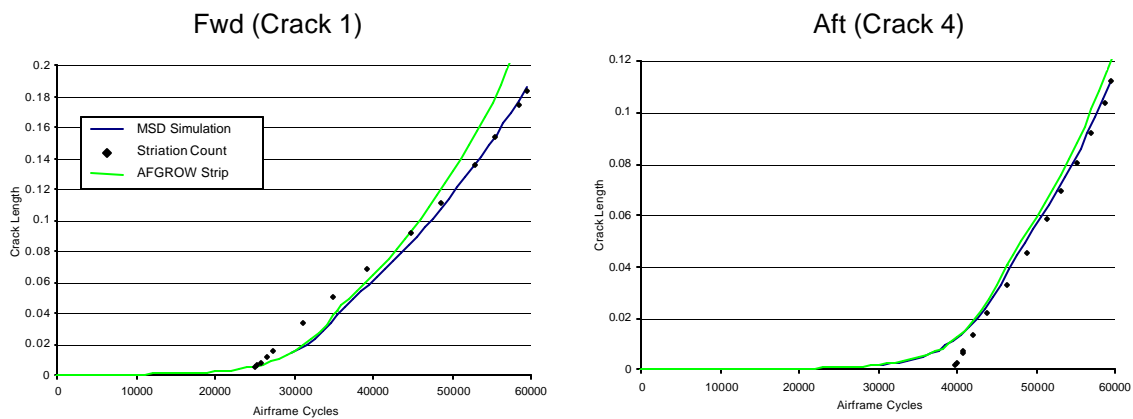


Figure 7-18: Hole 540+7.9~4R+1~LSH

ENGINEERING DEPARTMENT

SHEET	7-22	NO.	4-087051-20
TOTAL	7-28		
ISSUE DATE	12/22/04		

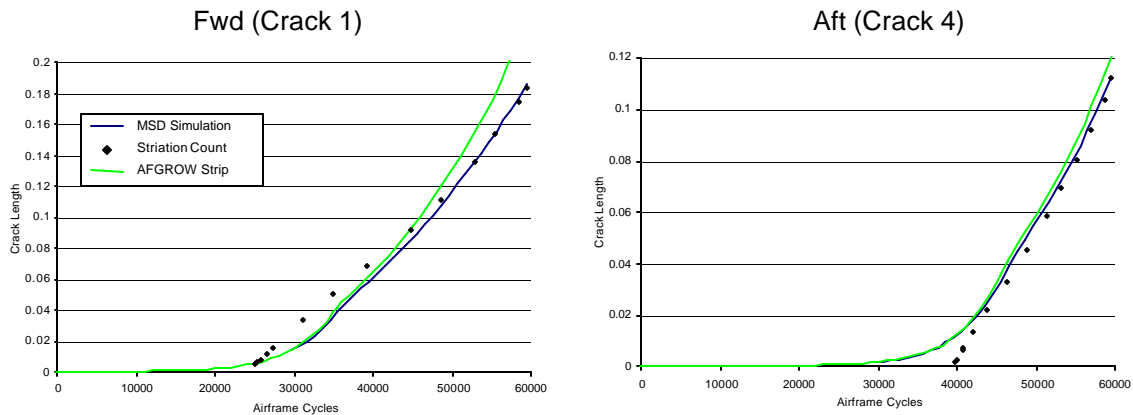


Figure 7-19: Hole 540+6.8~4R+1~LSH

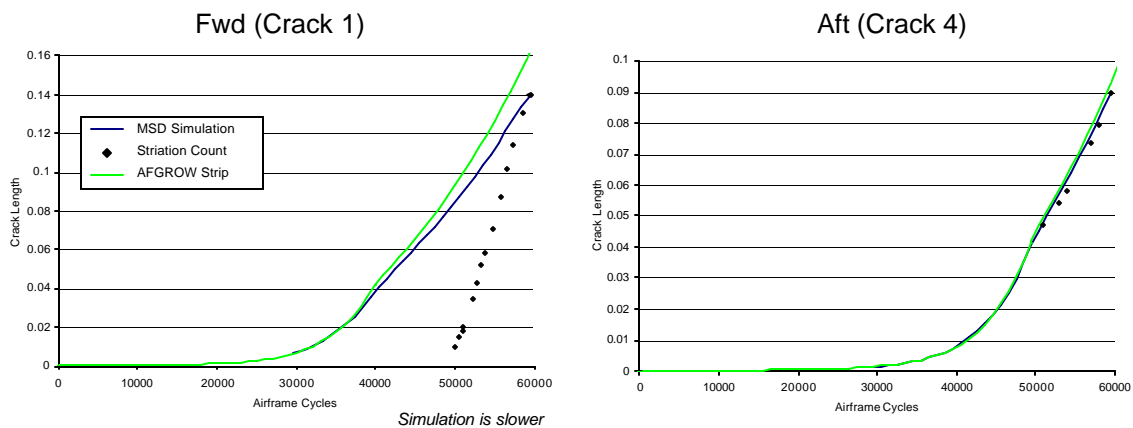


Figure 7-20: Hole 540+5.7~4R+1~LSH

Crack	Max size	Simulation is...
540+16.3~4R+1~LSH Crack4	0.019	Slow
540+14.2~4R+1~LSH Crack2	0.027	Slow
540+11.0~4R+1~LSH Crack3	0.053	Good
540+12.1~4R+1~LSH Crack1	0.083	Good
540+5.7~4R+1~LSH Crack4	0.090	Good
540+6.8~4R+1~LSH Crack4	0.090	Slow
540+8.9~4R+1~LSH Crack4	0.098	Fast
540+14.2~4R+1~LSH Crack1	0.103	Good
540+13.2~4R+1~LSH Crack4	0.108	Good
540+7.9~4R+1~LSH Crack4	0.113	Good
540+11.0~4R+1~LSH Crack1	0.118	Fast
540+5.7~4R+1~LSH Crack1	0.140	Slow
540+4.7~4R+1~LSH Crack4	0.151	Good
540+8.9~4R+1~LSH Crack1	0.166	Good
540+6.8~4R+1~LSH Crack1	0.167	Slow
540+10.0~4R+1~LSH Crack1	0.175	Good
540+7.9~4R+1~LSH Crack1	0.184	Good

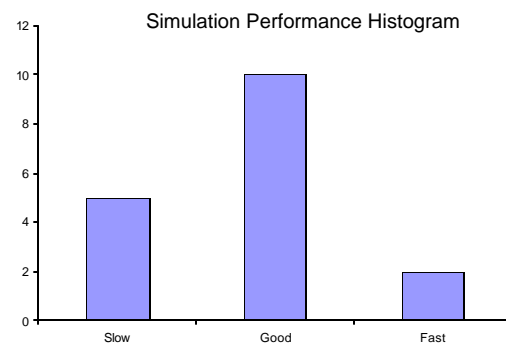


Figure 7-21: MSD Simulation Performance Assessment

SHEET	7-23	NO.	4-087051-20
TOTAL	7-28		
ISSUE DATE	12/22/04		

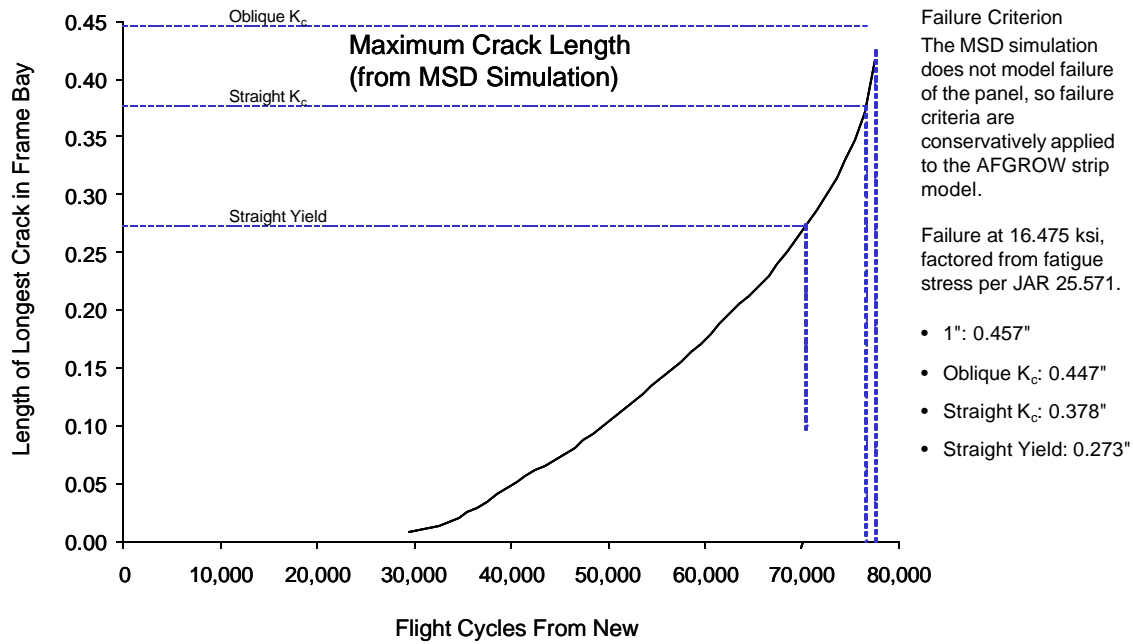


Figure 7-22: MSD Simulation Propagated Forward (Largest Crack)

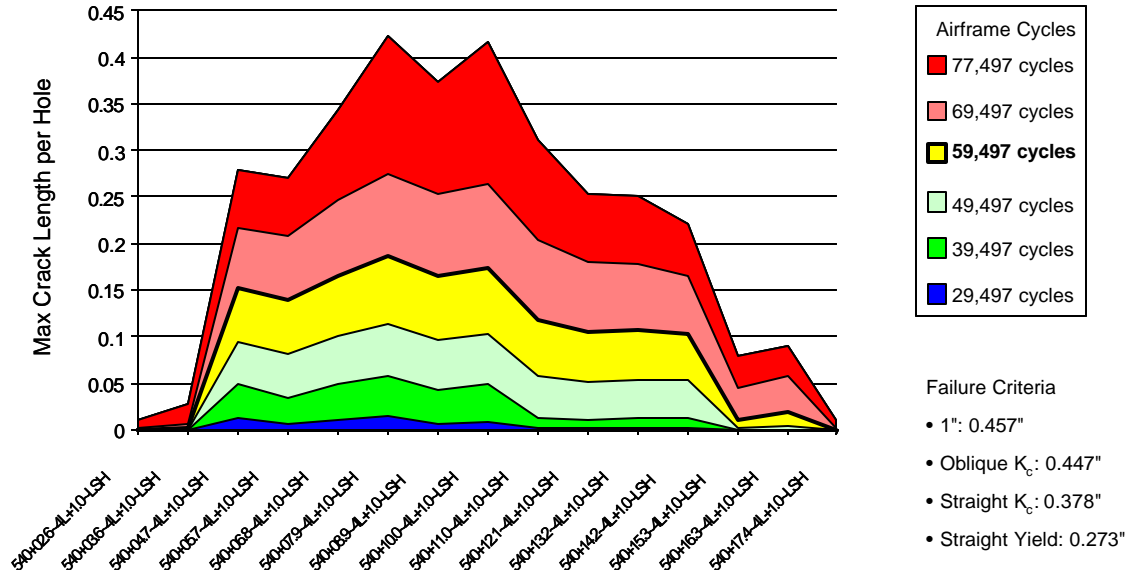


Figure 7-23: MSD Simulation Propagated Forward (Crack Array)

SHEET	7-24	NO.	4-087051-20
TOTAL	7-28		
ISSUE DATE	12/22/04		

Crack	EIFS (in)	EIFS (micron)
540+4.7~4R+1~LSH Crack4	0.000383	9.7
540+5.7~4R+1~LSH Crack1	0.000224	5.7
540+5.7~4R+1~LSH Crack1	0.000128	3.2
540+6.8~4R+1~LSH Crack1	0.000239	6.1
540+6.8~4R+1~LSH Crack4	0.000108	2.7
540+7.9~4R+1~LSH Crack1	0.000252	6.4
540+7.9~4R+1~LSH Crack4	0.000122	3.1
540+8.9~4R+1~LSH Crack1	0.000190	4.8
540+8.9~4R+1~LSH Crack4	0.000099	2.5
540+10.0~4R+1~LSH Crack1	0.000202	5.1
540+11.0~4R+1~LSH Crack1	0.000121	3.1
540+11.0~4R+1~LSH Crack3	0.000066	1.7
540+12.1~4R+1~LSH Crack1	0.000097	2.5
540+13.2~4R+1~LSH Crack4	0.000135	3.4
540+14.2~4R+1~LSH Crack1	0.000152	3.9
540+14.2~4R+1~LSH Crack2	0.000074	1.9
540+16.3~4R+1~LSH Crack4	0.000090	2.3

Figure 7-24: Equivalent Initial Flaw Size Table

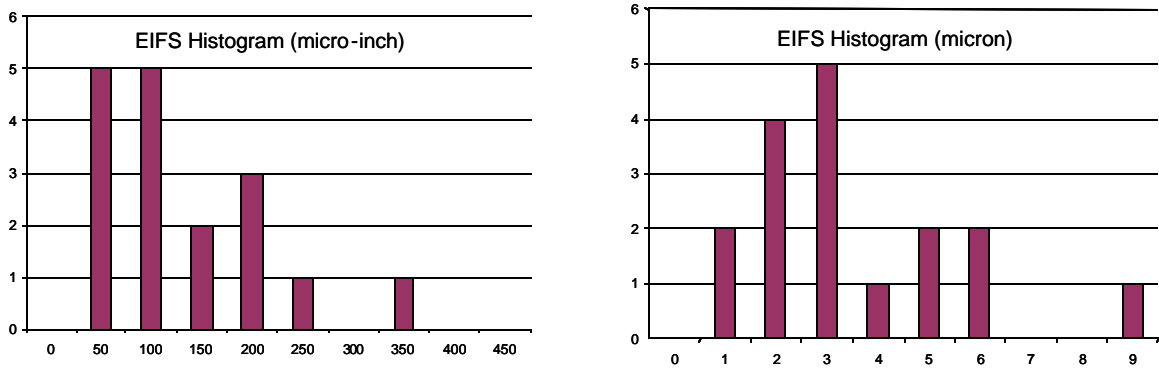


Figure 7-25: Equivalent Initial Flaw Size Histogram

SHEET	7-25	NO.	4-087051-20
TOTAL	7-28		
ISSUE DATE	12/22/04		

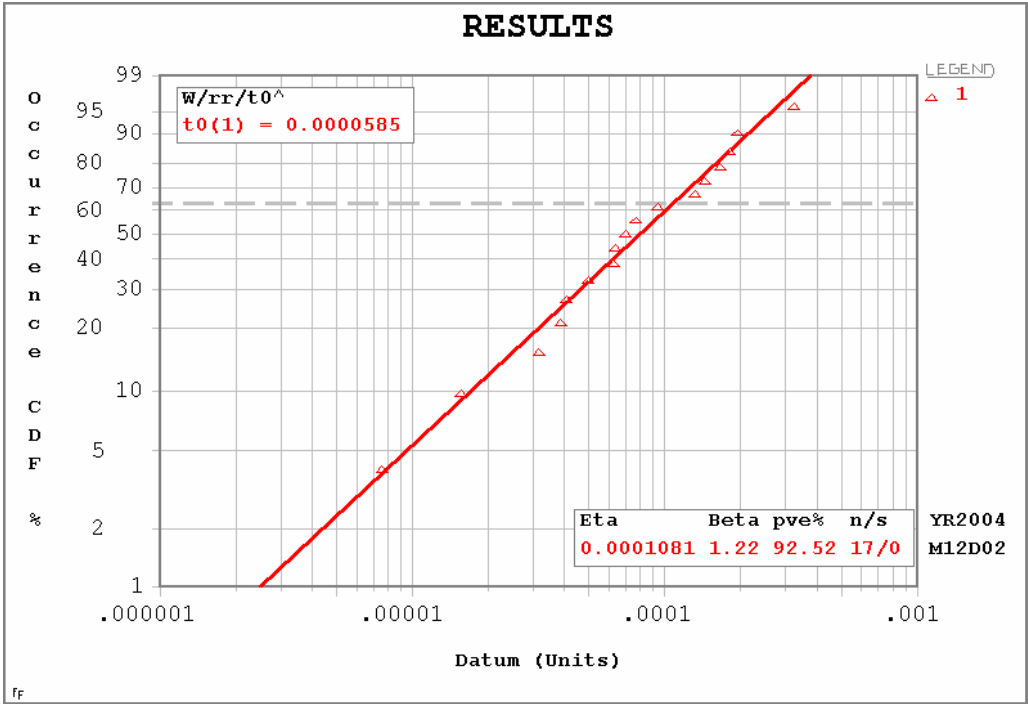


Figure 7- 26: Results from Rank Regression Weibull Analysis

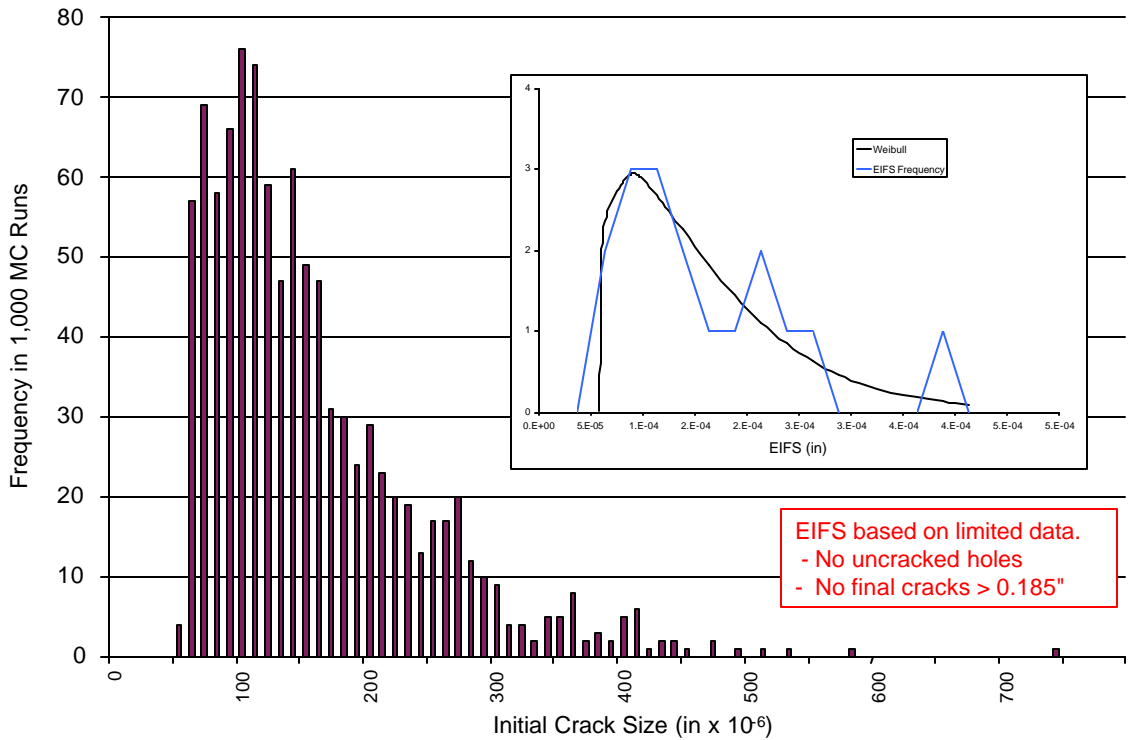


Figure 7- 27: Derived EIFS Distribution

SHEET	7-26	NO.	4-087051-20
TOTAL	7-28		
ISSUE DATE	12/22/04		

Mean	540+02.6~4L+1.0~LSH	540+03.6~4L+1.0~LSH	540+04.7~4L+1.0~LSH	540+05.7~4L+1.0~LSH	540+06.8~4L+1.0~LSH	540+07.9~4L+1.0~LSH	540+08.9~4L+1.0~LSH	540+10.0~4L+1.0~LSH
Standard Error	0.569118	0.576327	0.576327	0.576327	0.576327	0.576327	0.576327	0.576327
Median	0.001333	0.001463	0.001463	0.001463	0.001463	0.001463	0.001463	0.001463
Standard Deviation	0.568054	0.574116	0.574116	0.574116	0.574116	0.574116	0.574116	0.574116
Sample Variance	0.042138	0.046262	0.046262	0.046262	0.046262	0.046262	0.046262	0.046262
Kurtosis	0.001776	0.00214	0.00214	0.00214	0.00214	0.00214	0.00214	0.00214
Skewness	0.058087	1.021549	1.021549	1.021549	1.021549	1.021549	1.021549	1.021549
Range	0.291104	0.558427	0.558427	0.558427	0.558427	0.558427	0.558427	0.558427
Minimum	0.268081	0.334622	0.334622	0.334622	0.334622	0.334622	0.334622	0.334622
Maximum	0.464615	0.46431	0.46431	0.46431	0.46431	0.46431	0.46431	0.46431

Table 1: Statistical Data Analysis of Monte Carlo Results

SHEET	7-27	NO.	4-087051-20
TOTAL	7-28		
ISSUE DATE	12/22/04		

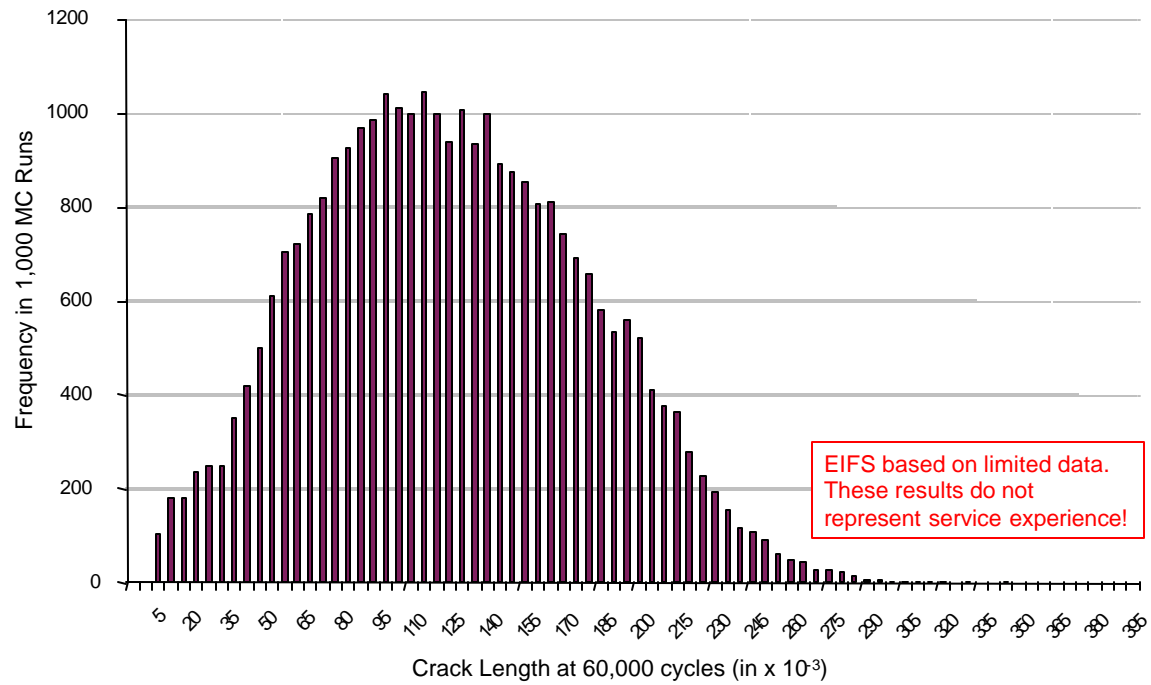


Figure 7- 28: Distribution of Crack Length

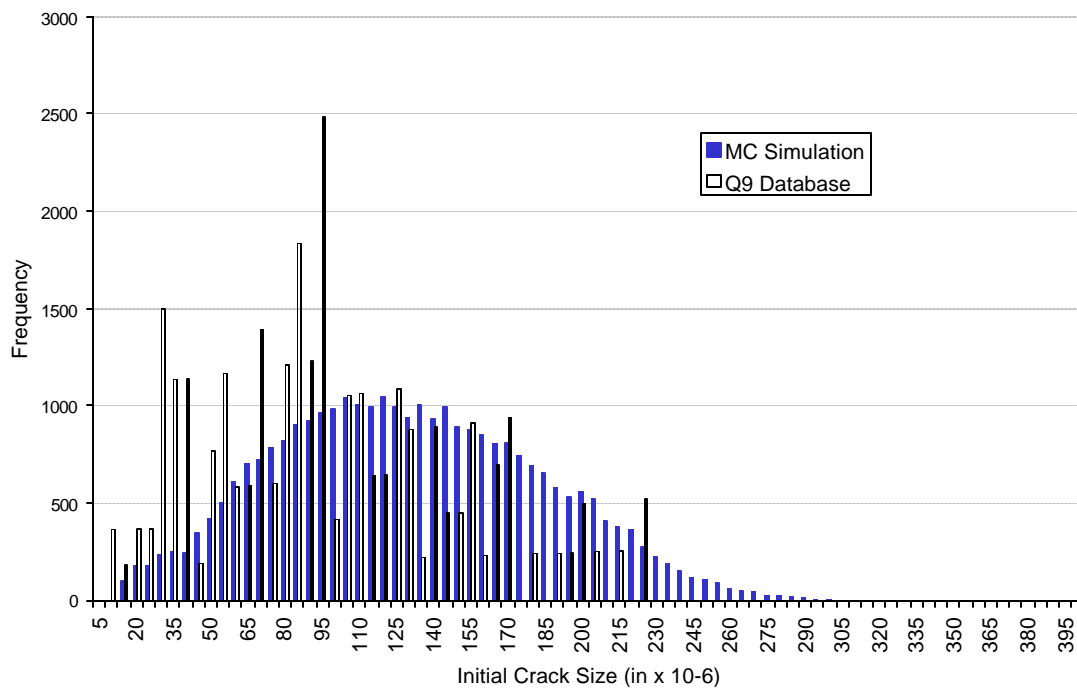


Figure 7- 29: Characterization Data Overlaid on Simulation Results

SHEET	7-28	NO.	4-087051-20
TOTAL	7-28		
ISSUE DATE	12/22/04		

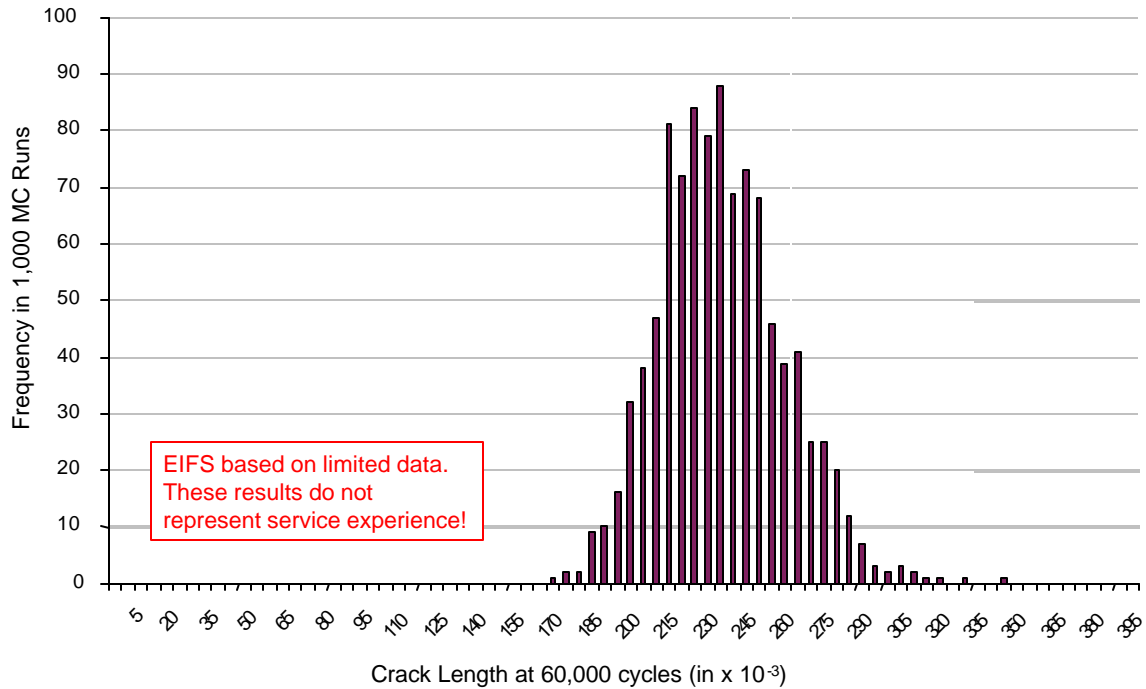


Figure 7- 30: Distribution of Maximum Crack Length in One Frame Bay (Hole-to-Tip)

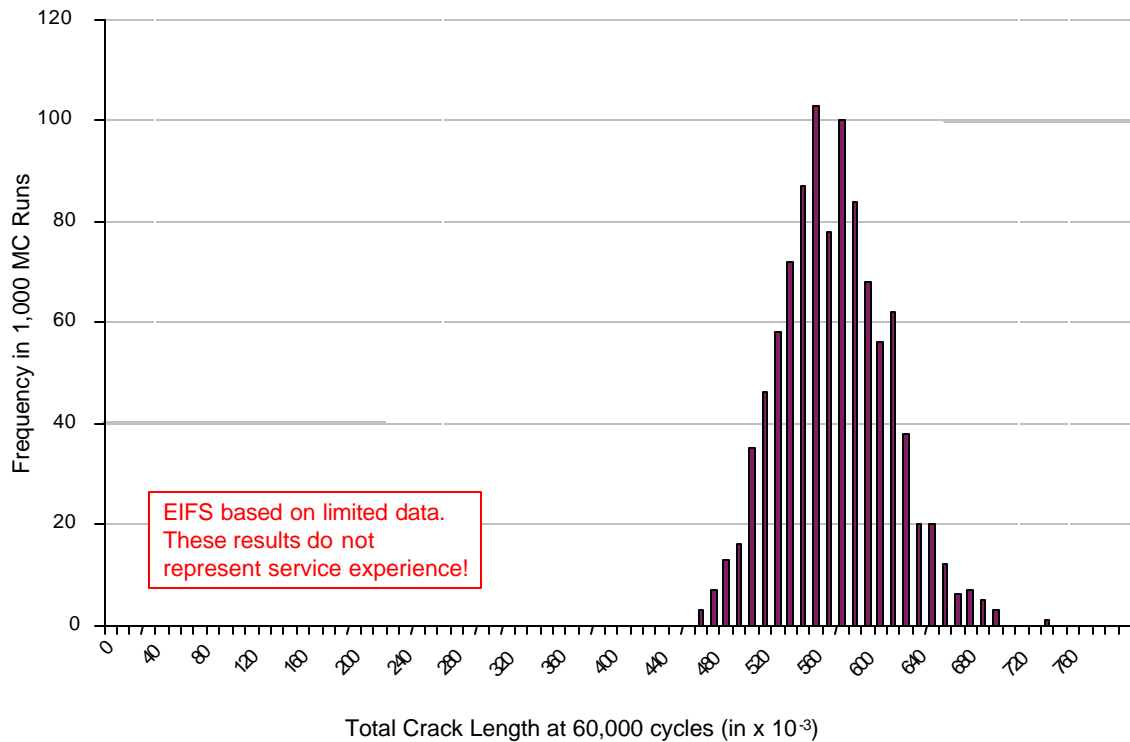


Figure 7- 31: Distribution of Maximum Crack Length in One Frame Bay (Tip-to-Tip)

SHEET	8-1	NO.	4-087051-20
TOTAL	8-18		
ISSUE DATE		12/22/04	

CHAPTER 8: INITIATION

Introduction

The analysis of crack initiation is an integral part of a WFD assessment. To investigate the relationships between the data gathered during a destructive evaluation and the outputs required of a WFD assessment, the conceptual schematic shown in Figure 8-1 was created. Along the left are some of the parameters gathered within the Damage Characterization. Along the right are the components of a program to preclude WFD in an aircraft fleets. Note that within the input parameters there is an overlap between factors influencing stress and those considered geometric. This overlap is present because most causes of crack initiation produce a local increase in stress, either by adding additional load or by creating local stress concentrations. Therefore, the boundary between stress and geometry effects is somewhat arbitrary.

The conceptual MSD/MED analysis is given further detail in Figure 8-2. Lines from the inputs lead to intermediate analysis boxes, then on to the results expected of the analysis. Many of the intermediate analyses in the top half of the figure have a strong history of successful deterministic analysis, such as the widely accepted formulae for linear stress concentrations, stress intensity, and crack growth rate (Ref [8-1]). The analyses in the lower half of the block are less applicable to deterministic analysis, both due to the complexity of the physics and to the probabilistic nature of the inputs. The focus of this chapter is the probabilistic modeling of those areas, where the input stress and geometry inputs are modeled to output crack shapes and features, and the cycles to crack initiation.

SHEET	8-2	NO.	4-087051-20
TOTAL	8-18		
ISSUE DATE	12/22/04		

Neural Network Algorithms

Data from analysis of crack initiation is typical of complex engineering data sets that exhibit large scatter resulting from the contribution of multiple random variables. Nondeterministic modeling approaches have to be applied to fully capture the physical processes. The simulation tools must have good generalization capabilities for problems with large noise and ill-posed conditions.

Also, the data sets are often sparse due to prohibitive costs associated with collecting large amount of data in a multi-dimensional parameter space. Models that require a minimum amount of measurements for an accurate simulation of the process are needed.

Neural networks are well suited for such tasks. Multi-layer perception networks enable accurate approximation of any continuous response [8-2]. If the network parameters are defined as random variables, the response probability distributions can be obtained as functions of the input through Bayesian learning. Bayesian learning also enables filtering noise, allows for the model complexity independence on the amount of training data, and results in the network convergence that is similar to the convergence of a closed-form series-type solution.

Multi-layer perception networks are nonlinear multi-parameter models. An example of such a network that takes an input vector $\mathbf{x} = \{x_1, \dots, x_n\}$ and from them computes an output vector

$\mathbf{f} = \{f_1(\mathbf{x}), \dots, f_p(\mathbf{x})\}$ using one or more layers of hidden units $h_j(\mathbf{x})$, is

$$\begin{aligned} f_k(\mathbf{x}) &= b_k + \sum_j v_{jk} h_j(\mathbf{x}) \\ h_j(\mathbf{x}) &= \tanh(a_j + \sum_i u_{ij} x_i) \end{aligned} \quad (8-1)$$

The unknown parameters in eqns (8-1) are the weights u_{ij} and v_{jk} , and the biases a_j and b_k of the hidden units and the output units, respectively. These parameters are evaluated through a regression analysis using a set of input and target vectors $\{(\mathbf{x}^{(1)}, \mathbf{y}^{(1)}), \dots, (\mathbf{x}^{(m)}, \mathbf{y}^{(m)})\}$. A pair of the input and target vectors $(\mathbf{x}^{(k)}, \mathbf{y}^{(k)}) = (\{x_1, \dots, x_n\}^{(k)}, \{y_1, \dots, y_p\}^{(k)})$ represents a single point in the data set resulting from measurements.

SHEET	8-3	NO.	4-087051-20
TOTAL	8-18		
ISSUE DATE	12/22/04		

The process of evaluating the network parameters is called training, and the data used in this process are called the training data. The network output probability distributions can be obtained as continuous functions of the inputs if the network weights and biases are defined as random variables. Capturing the crack growth rate probability distribution as a function of the crack size from the striation count data is a key to the development of crack growth models that enhance the predictive capabilities of the models simulating only the average crack growth behavior.

If the network parameters are defined as random variables, Bayesian techniques can be applied to evaluate the corresponding probability distributions [8-2]. Bayes' theorem expresses the conditional probability density $P(\theta|D)$ of the network parameters vector θ given the data D (posterior probability density of the network parameters) in terms of the conditional probability density $P(D|\theta)$ of the data given the network parameters (likelihood function), and the network parameter probability density form $P(\theta)$ selected prior to the analysis, as

$$P(\theta|D) = \frac{P(D|\theta)P(\theta)}{P(D)} = \frac{P(D|\theta)P(\theta)}{\int P(D|\theta)P(\theta)d\theta} \quad (8-2)$$

The denominator $P(D)$ in eqn (8-2) represents a normalization factor which ensures that the integral of $P(\theta|D)$ over the network parameter space equals one.

The prior probability distribution for the network weights and biases must encompass a wide range of possible values. Normal distribution with unknown standard deviation is typically assumed [8-1]. The unknown standard deviation becomes a hyperparameter that is determined during the network training.

The likelihood function that results in the maximum likelihood expression equivalent to the least squares approximation is the Gaussian noise model [8-2]. For a single output variable model, the Gaussian noise is expressed as

$$P(D|\theta) = \prod_{k=1}^m \frac{1}{\sqrt{2\pi}\sigma_k} \exp\left(-[f_k(\mathbf{x}) - y_k]^2 / 2\sigma_k^2\right) \quad (8-3)$$

SHEET	8-4	NO.	4-087051-20
TOTAL	8-18		
ISSUE DATE	12/22/04		

The negative log of eqn (8-3) is proportional to the sum of the squared errors $\sum_{k=1}^m (f_k(\mathbf{x}) - y_k)^2$. The average network response represented by the mean values $f_k(\mathbf{x})$ in eqn (8-3), and the standard deviations \mathbf{S}_k are determined during the network training.

The Bayesian regularization technique [8-3] finds a network that maximizes the posterior probability density $P(\mathbf{?}|D)$ for the network weights and biases. The required network training includes the minimization of the following performance function of the network parameters

$$F(\mathbf{?}) = \mathbf{b} \sum_{k=1}^m (f_k(\mathbf{x}) - y_k)^2 + \mathbf{a} \sum_{i=1}^s \mathbf{q}_i^2 \quad (8-4)$$

The regularization coefficient \mathbf{a} is inversely proportional to the variance of the network parameter distribution, and the regularization coefficient \mathbf{b} is inversely proportional to the variance of the Gaussian noise model if a single variance normal distribution for the network parameters, and a single variance Gaussian noise are assumed. The regularization coefficients \mathbf{a} and \mathbf{b} can be expressed in terms of the network parameters and the training data, and determined in the process of minimization of the performance function (8-2) using an iterative procedure [8-3] that handles the presence of multiple local minima. The number of effective network parameters is automatically established such that a larger number of parameters in the network will not affect its output. Bayesian regularization predicts the network output normal distribution as a continuous function of the input [8-2].

The Bayesian regularization has been successfully applied to simulate a multiple element damage probability distribution from the field inspection data [8-4] when the standard two- and three-parameter probability distributions could not provide acceptable fit due to the lack of flexibility.

SHEET	8-5	NO.	4-087051-20
TOTAL	8-18		
ISSUE DATE	12/22/04		

Application to Teardown Data

Classification

In this section, the concepts introduced previously section are applied to preliminary teardown data. This analysis is preliminary, intended to illustrate the underlying concepts of a neural network classifier. An actual classifier for this problem would depend on more than the two variables shown. Also, due to the large demonstrated difference in initiation between S-4L and S-4R, the generalization of any classification algorithm is limited until S-4L teardown data is available and included.

The data shown in Figure 8-3 is the result of a parametric study of three bays of S-4R data. The left chart plots average rivet tail height versus the maximum crack length in each hole. Average tail height is related to the rivet installation, where under driven rivets have a higher tail height and a lower rivet interference. Maximum crack length is related to the time of crack initiation, assuming that the holes with the longest cracks initiated earliest. Although a trend is expected in this data, the data is scattered and a regression line has a low quality of fit ($R^2 = 0.1$).

The right chart in Figure 8-3 plots distance from the nearest frame versus the maximum crack length in each hole. As shown in the finite element analysis of the target areas (see Chapters 3-5), the hoop skin stress is lowest at the frame, and increases as the distance from the frame increases. A trend is expected in this data where the maximum crack length increases as the distance increases, but no such trend is evident in Figure 8-3.

This data demonstrates the difficulty in applying conventional regression techniques to data with a large amount of scatter. In Figure 8-4, the same data is plotted as a classification problem, with the data discriminated into two classes: those holes that have maximum crack lengths greater than 0.100", and those that do not. The decision boundary is used to classify new data: points with features below the decision boundary are classified as ">0.100", while data points with features above the boundary are classified as "<0.100". In a typical two-class classifier algorithm, the decision boundary is defined as those combinations of parameters \mathbf{x} where the output vector $\mathbf{f}(\mathbf{x})$ in equation (8-1) is equal to zero.

SHEET	8-6	NO.	4-087051-20
TOTAL	8-18		
ISSUE DATE	12/22/04		

The Figure 8-4 decision boundary is nearly optimal because it is set to minimize the probability of misclassifying any new data point. Based on the training data, the probability of correct classification is approximately 80%. This probability of correct classification is determined using Bayes' Theorem similar to equation (8-3); the posterior probability of correct classification of new data is determined from the conditional and prior probabilities from the known data (i.e. training data).

Concept Evaluation

During Q9, a probabilistic neural network architecture termed a Gaussian Radial Basis Network (GRBN) was explored. This network is a recasting of an older statistical analysis into a neural network framework (Ref 8-2), using the architecture shown in Figure 8- 5. The method identifies data clusters by placing a number of nodes into data domain that minimizes the sum of distances from each data point to its nearest node (see Figure 8- 6). The activation at the output node is the weighted sum of the basis functions plus a bias term:

$$\bar{y}_k(x) = \sum_{j=1}^M w_{kj} \phi_j(\bar{x}) + w_{k0}$$

where the basis function ϕ has a value 1 at the node, diminishing radially away from the node, as below:

$$\phi_j(x) = \exp\left(-\frac{\|\bar{x} - \mu_j\|^2}{2\sigma_j^2}\right),$$

where μ_j is the location of the j th node.

This architecture has two tunable parameters: the number of nodes, which is typically much smaller than the number of training data points, and σ . Small values of σ result in a smoother decision boundary that may not capture important features of training data, as shown in Figure 8- 8. Large values of σ may result in an overly complex (flexible) decision boundary that over-fit the training data but not generalize well, as shown in Figure 8- 9. Changes to the number of nodes has a similar effect.

During Q9, a prototype proof-of-concept network was developed to evaluate modeling concepts. The network is a simple single-input, single-output model as shown in Figure 8- 10. For this model, the input is crack length, and the output is probability of detection. These parameters were selected

SHEET	8-7	NO.	4-087051-20
TOTAL	8-18		
ISSUE DATE	12/22/04		

because the relationship between them is intuitive, and because accepted industry methods for modeling this relationship exist. Although this network could be useful as a POD model, it is primarily intended as a building block towards the multi-parameter initiation model facing similar data challenges.

A controlled set of data was created to evaluate the Gaussian Radial Basis Network (GRBN). The data was created and analyzed as follows:

- Probability of Initiation curves for two NDT inspection types were fabricated, as shown in Figure 8- 11. Inspection A represents a first-layer inspection, and Inspection B represents a second-layer inspection. Both inspections produce indications independent of crack length below 0.050", and both inspections have a maximum POI at 95%.
- For each inspection type, two sets of crack length vs. hit/miss data were created using Monte Carlo techniques. The first data set has crack lengths distributed evenly throughout the 0 – 0.500" domain. The second data set uses the actual crack length distribution as of the Q8 Damage Characterization report. This second set represents the typical data distribution that the initiation model will be presented with. Both sets have 145 data points.
- Each of the four data sets was evaluated using both the prototype neural network and the industry standard log/logistic fit (see Inspection Capability Reports). The ideal method, given enough data points, will return a close approximation of the POI curve.

The results for Inspection A, Distributed Data are shown in Figure 8- 12, and demonstrate the fundamental shortcomings of both approaches. The 2-parameter log/logistic fit assumes a POD of 0% at 0" crack length, and 100% POD at some finite length. That assumption is not valid for these fabricated inspections, so the log/logistic misses the POD in those regions. Conversely, the GRBN is a non-parametric method that includes no assumptions of functional shape, so it can capture the POD floor and ceiling. However, the related disadvantage is that the three misses at crack lengths > 0.440" lead the GRBN to predict a POD reduction for large cracks that does not reflect the physics of the inspection.

SHEET	8-8	NO.	4-087051-20
TOTAL	8-18		
ISSUE DATE	12/22/04		

The results for Inspection A, Typical Data, and Inspection B, Distributed Data are shown in Figure 8-13 and Figure 8-14, respectively. For both cases, both methods are able to recapture the POI curve approximately, including the critical 90% POD point. Non-parametric methods do not extrapolate well, so the GRBN result is only shown within the source data.

The results for Inspection B, Typical Data are shown in Figure 8-15. This is an important case where the data set does not include lengths longer than 90% POD. The GRBN produces a close approximation to the inspection curve, but the log/logistic fit diverges significantly. This divergence is a well-known shortcoming of this standard approach, but is a critical shortcoming for an initiation model as the input data is expected to lie between 10% and 90% probability of initiation for many parameters. Based on this evaluation, a GRBN appears well-suited to this type of data.

In summary, the conclusions from the Proof-of-Concept GRBN evaluation are:

- Since a curve fit assumes a shape to the functional relationship, it performs best when:
 - The relationship between variables is understood and preferably monotonic, as with:
 - i) Probability of crack initiation vs. time in service
 - ii) Probability of detection vs. crack length
 - The output data is spread consistently across the complete range;
 - Non-linear effects and interactions are not significant.
- Due to its flexibility and lack of predetermined shape, a Probabilistic Neural Network model performs best when:
 - The relationship between variables are non-linear and not necessarily monotonic.
 - Relationships are a function of several interacting variables, such as:
 - i) Location of crack initiation vs. rivet tail geometry.
 - ii) Probability of detection vs. orientation and number of cracks.
- Data is clustered in areas of interest, but does not span a range

ENGINEERING DEPARTMENT

SHEET	8-9	NO.	4-087051-20
TOTAL	8-18		
ISSUE DATE		12/22/04	

- Extrapolation is not needed.

Based on the successful performance of the prototype network, future work will apply the GRBN to the multi-parameter initiation problem.

SHEET	8-10	NO.	4-087051-20
TOTAL	8-18		
ISSUE DATE		12/22/04	

References

- [8-1] S. Suresh, *Fatigue of Materials*, 2nd Edition, Cambridge University Press, 1998.
- [8-2] Bishop, C. M., *Neural Networks for Pattern Recognition*, Oxford University Press, 1995
- [8-3] Foresee, F. D., and Hagan, M. T., "Gauss-Newton Approximation to Bayesian Regularization," *Proceedings of the 1997 International Joint Conference on Neural Networks*, pp. 1930-1935, 1997.
- [8-4] Makeev, A., Carter, A., and Steadman, D., "Statistical Tools for the Analysis of Aircraft Widespread Fatigue Damage Based on Field Inspection Data," *Proceedings of the 7th Joint FAA/DOD/NASA Conference on Aging Aircraft*, New Orleans, LA, September 8-11, 2003.

SHEET	8-11	NO.	4-087051-20
TOTAL	8-18		
ISSUE DATE	12/22/04		

Figures

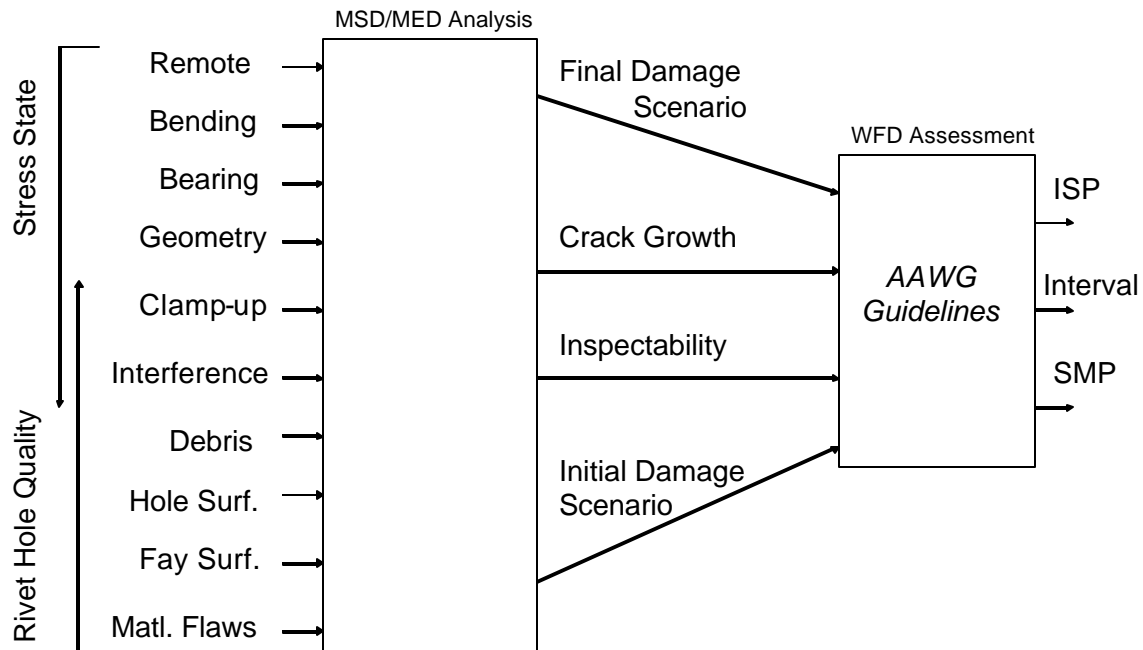


Figure 8-1: Conceptual Schematic of WFD Assessment

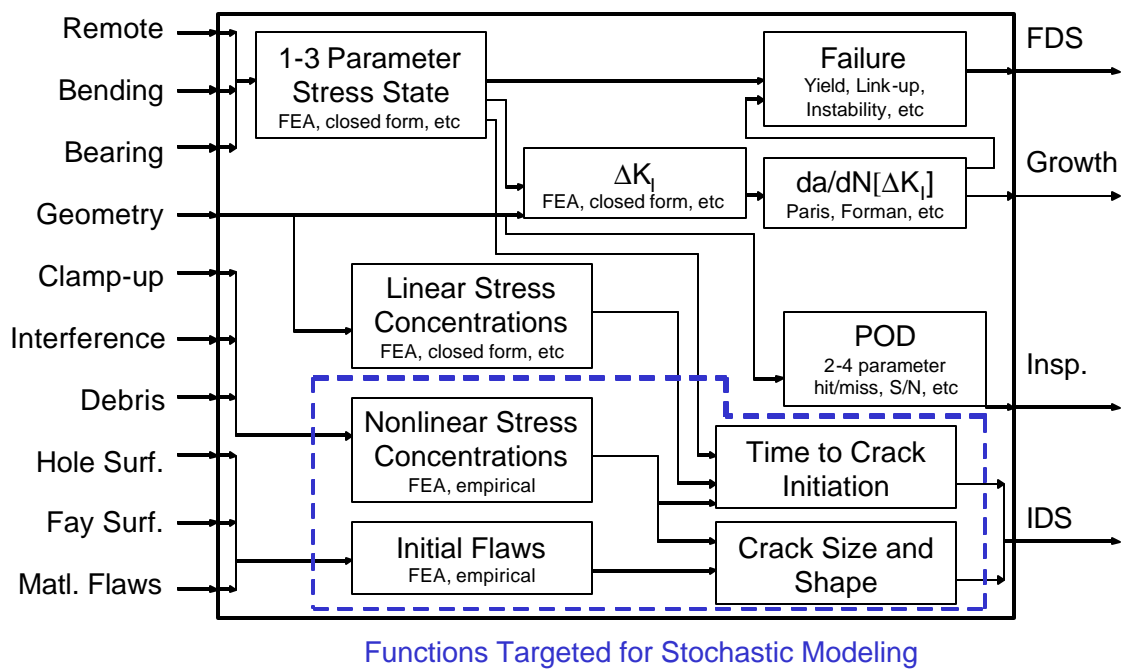


Figure 8-2: Conceptual Schematic of MSD/MED Analysis

SHEET	8-12	NO.	4-087051-20
TOTAL	8-18		
ISSUE DATE	12/22/04		

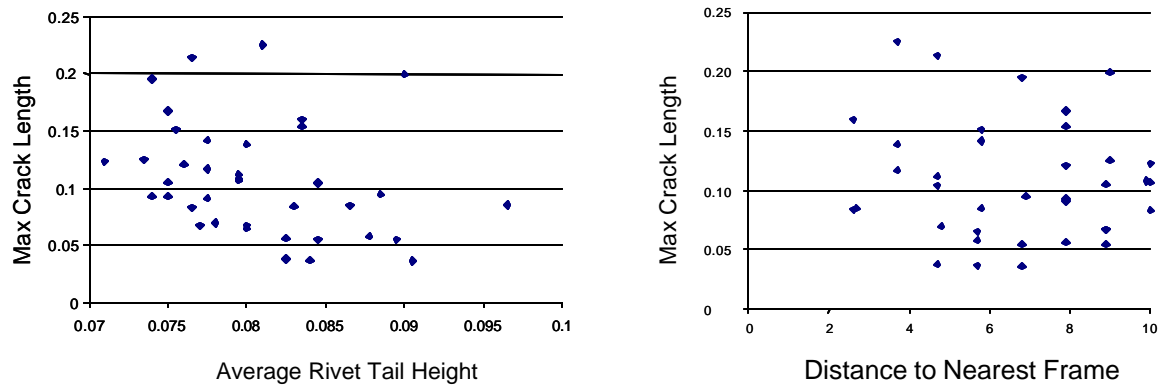


Figure 8-3: Scatter Plots from Parametric Study

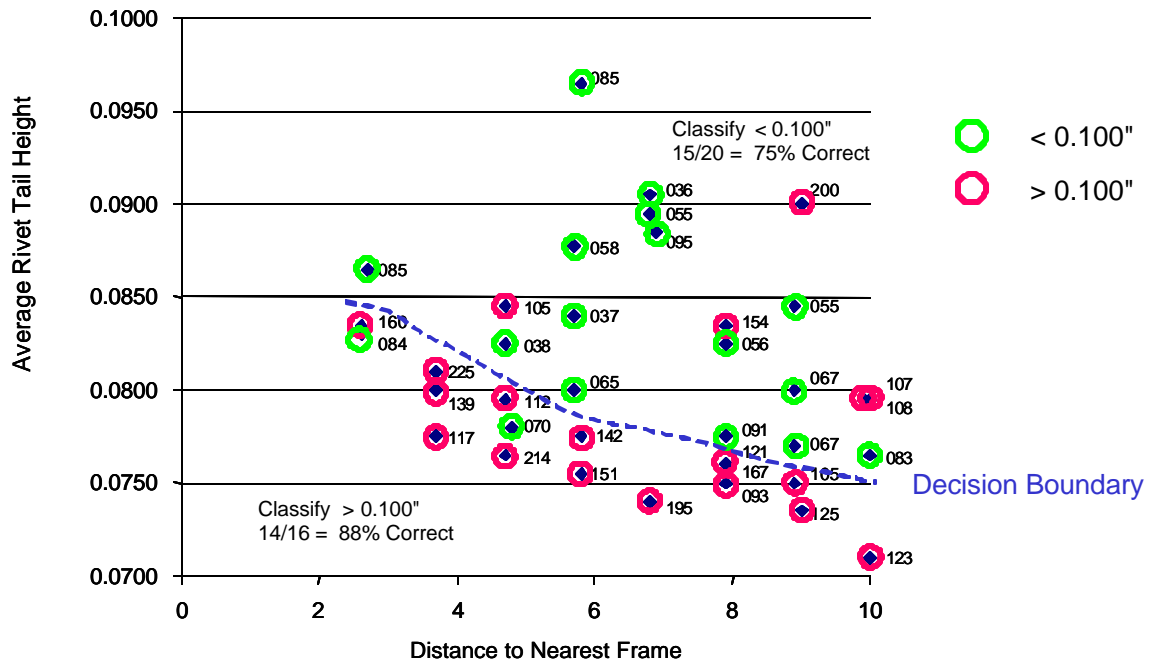


Figure 8-4: Classification with Optimal Decision Boundary

SHEET	8-13	NO.	4-087051-20
TOTAL	8-18		
ISSUE DATE	12/22/04		

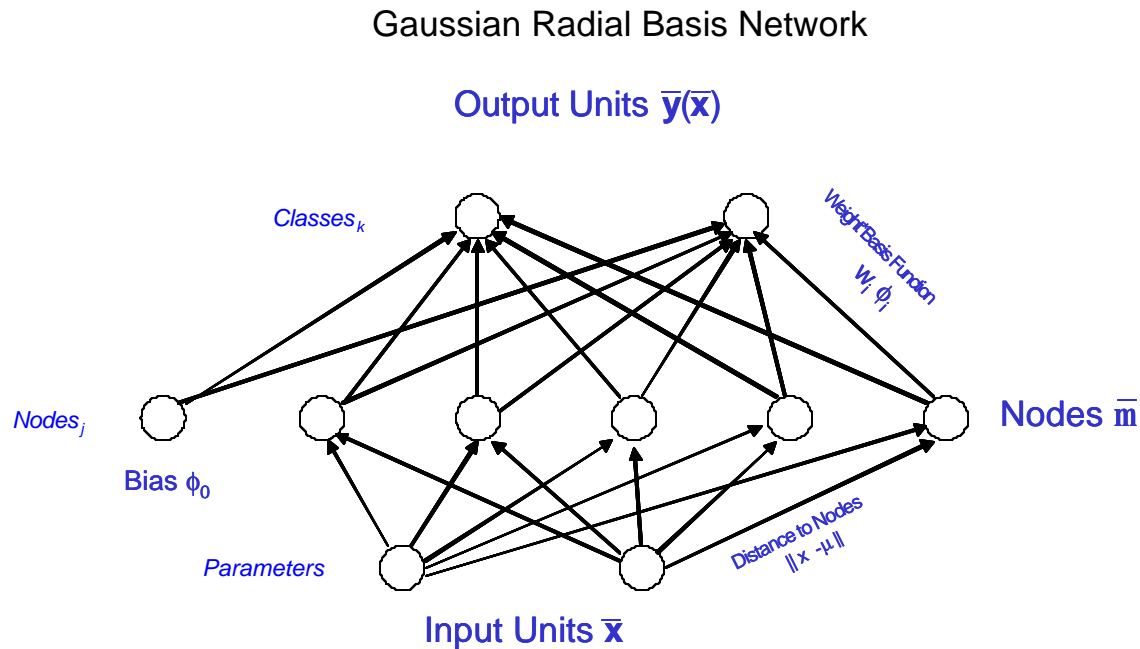


Figure 8- 5: Neural Model of Gaussian Radial Basis Network

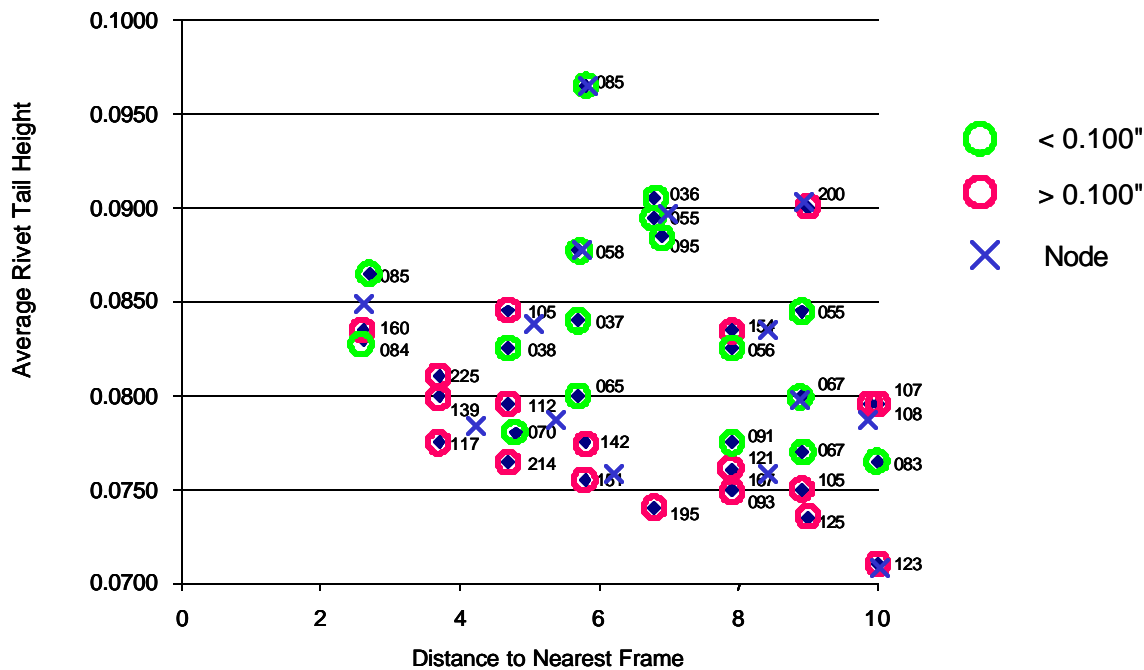


Figure 8- 6: Schematic – Node Placement within Data Domain

SHEET	8-14	NO.	4-087051-20
TOTAL	8-18		
ISSUE DATE	12/22/04		

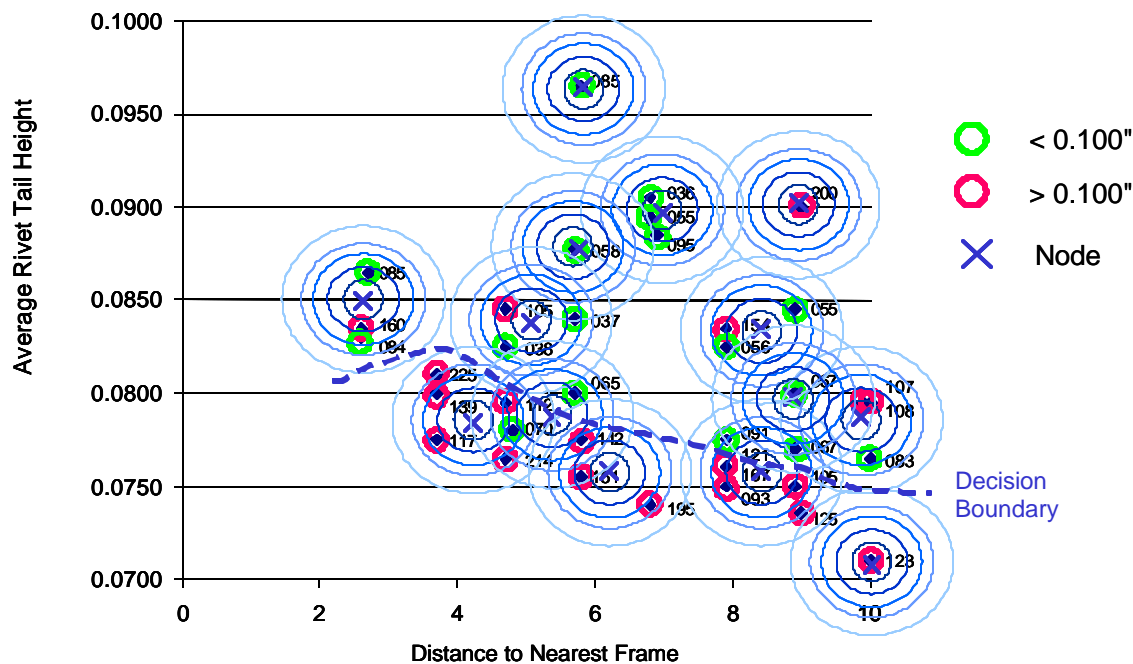


Figure 8- 7: Schematic-Decision Boundary and Node Interactions

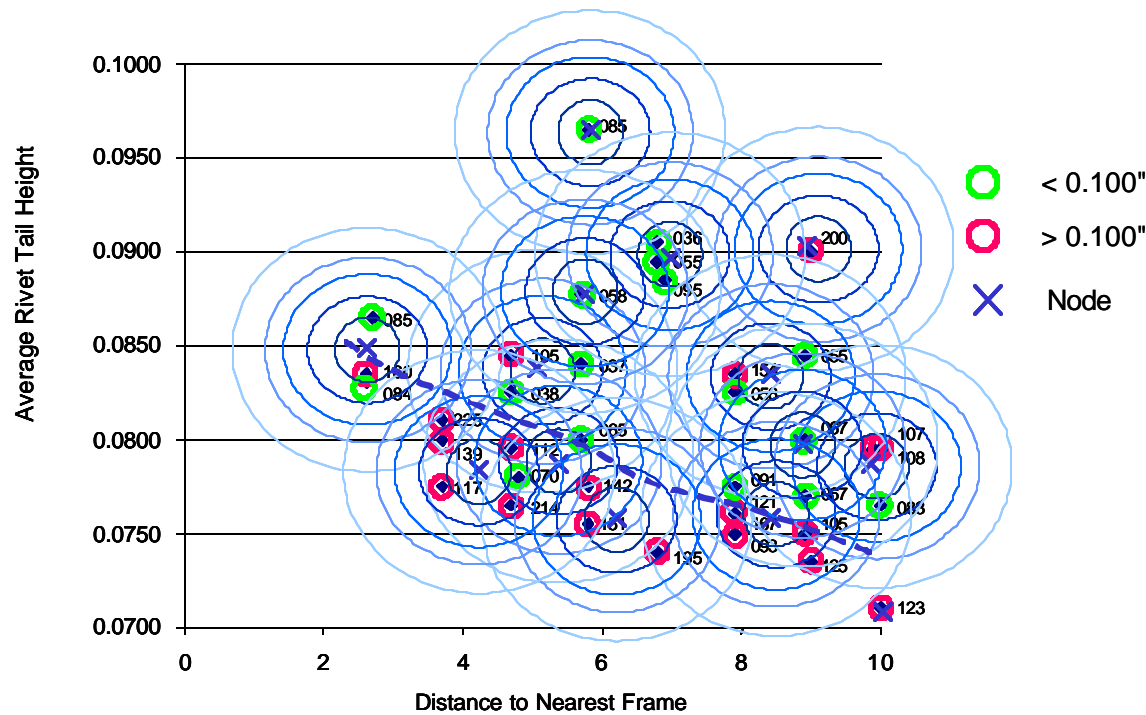


Figure 8- 8: Schematic - Decision Boundary Too Stiff, Does Not Capture Effects

SHEET	8-15	NO.	4-087051-20
TOTAL	8-18		
ISSUE DATE	12/22/04		

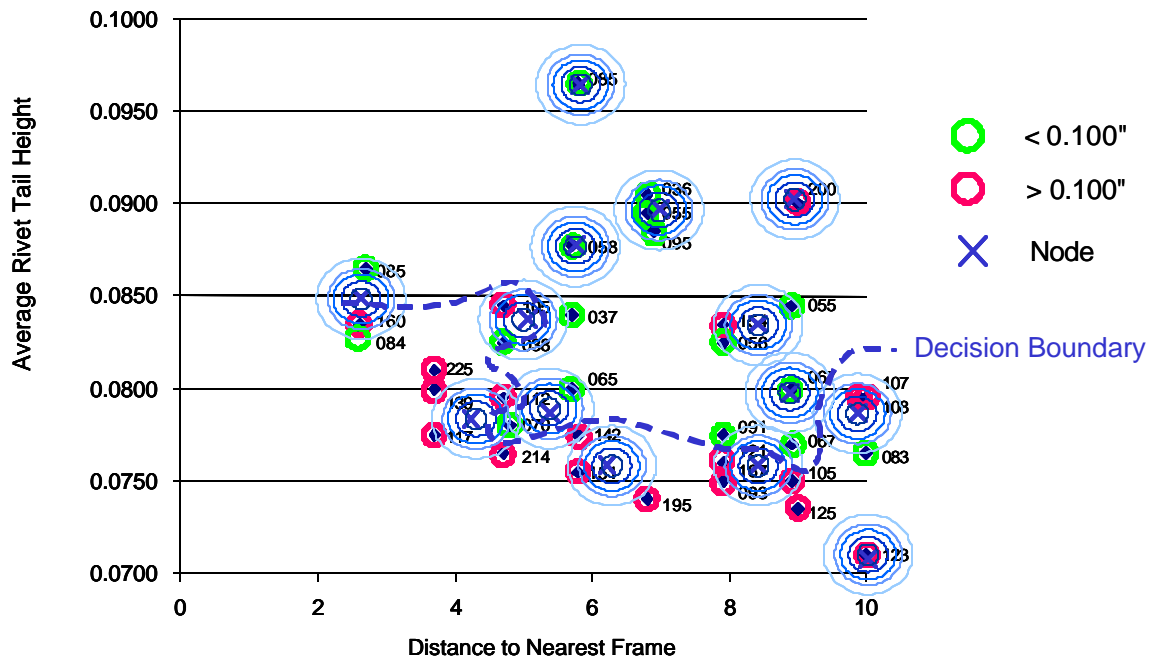
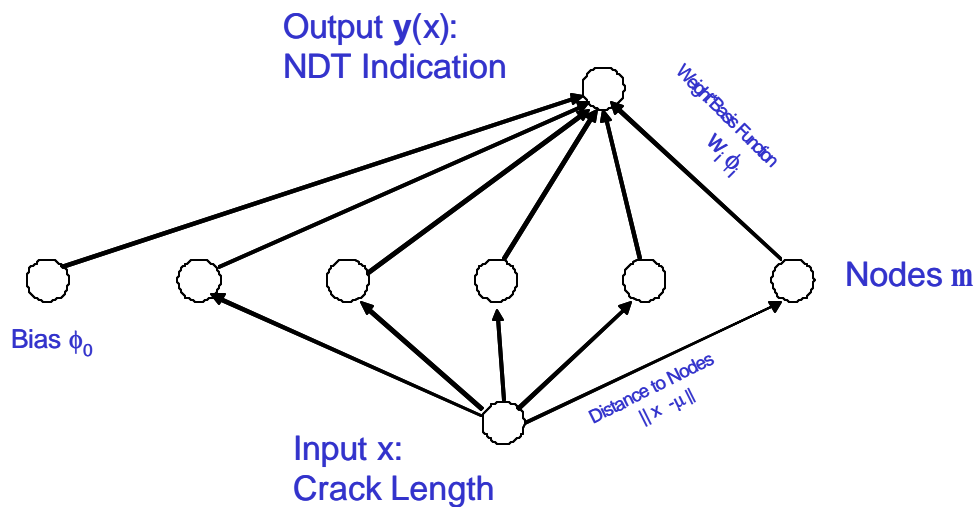


Figure 8- 9: Schematic-Decision Boundary Too Flexible, Does Not Generalize



First Layer Basis Function

$$\phi_j(x) = \exp\left(\frac{\|x - \mu_j\|^2}{-2\sigma_j^2}\right)$$

Second Layer Mapping Function

$$y(x) = \sum_{j=1}^M w_j \phi_j(x) + w_0$$

Figure 8- 10: Proof of Concept Network

SHEET	8-16	NO.	4-087051-20
TOTAL	8-18		
ISSUE DATE	12/22/04		

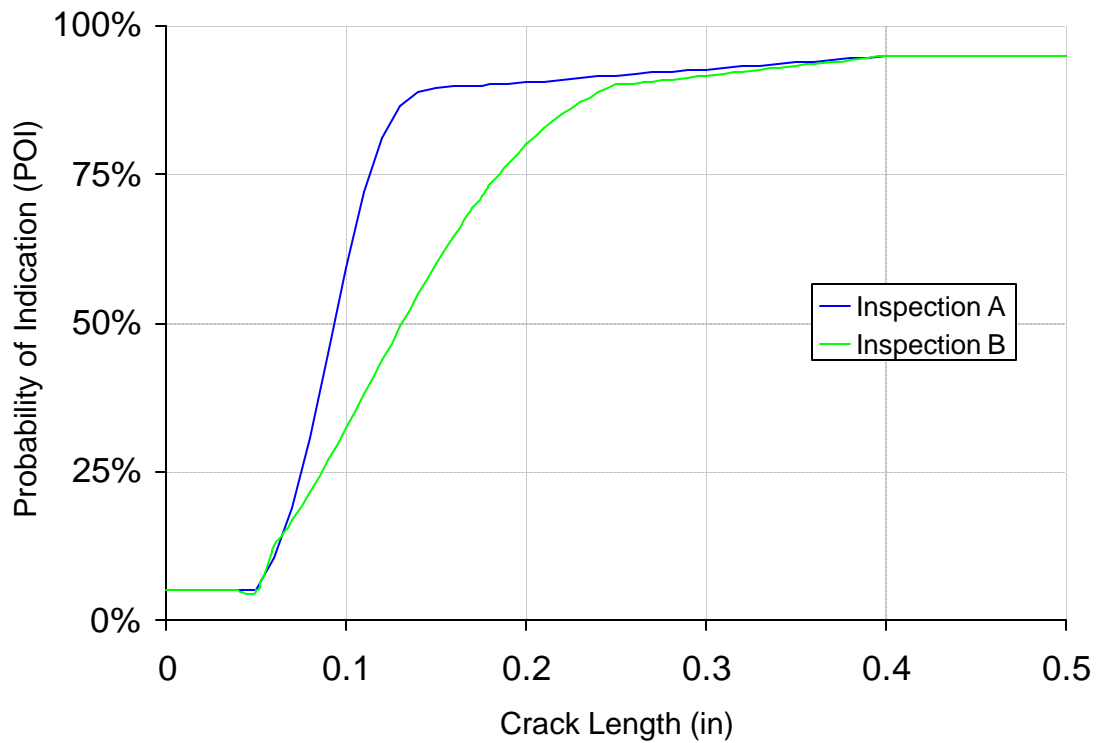


Figure 8- 11: Inspection POI Curves

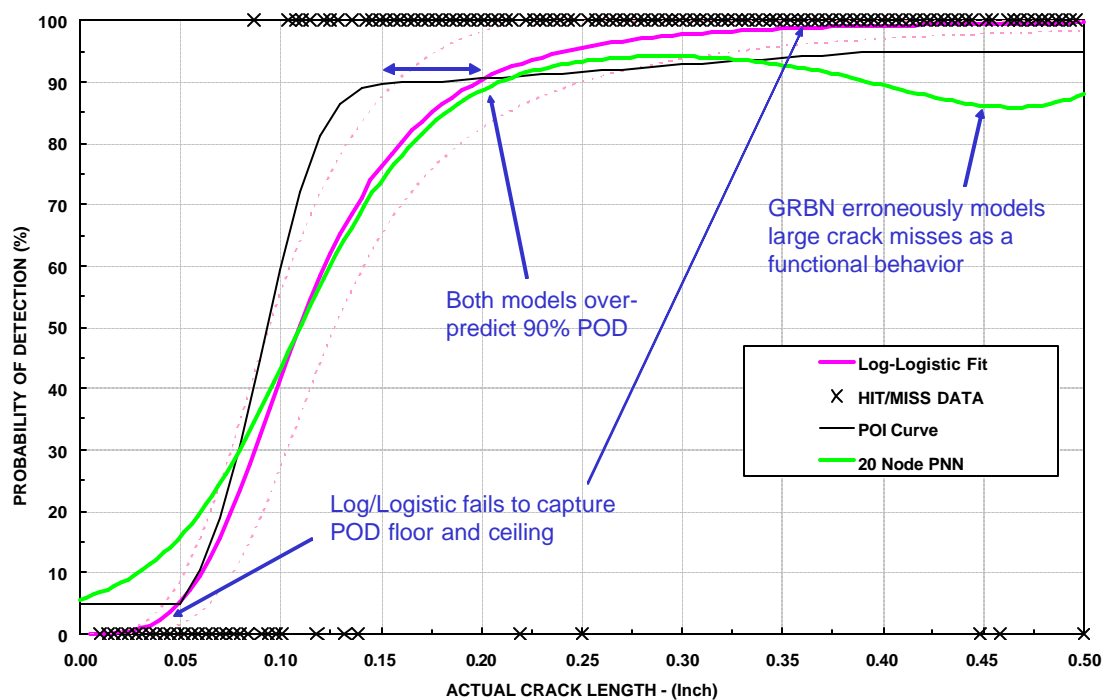


Figure 8- 12: Results for Inspection A, Distributed Data

SHEET	8-17	NO.	4-087051-20
TOTAL	8-18		
ISSUE DATE	12/22/04		

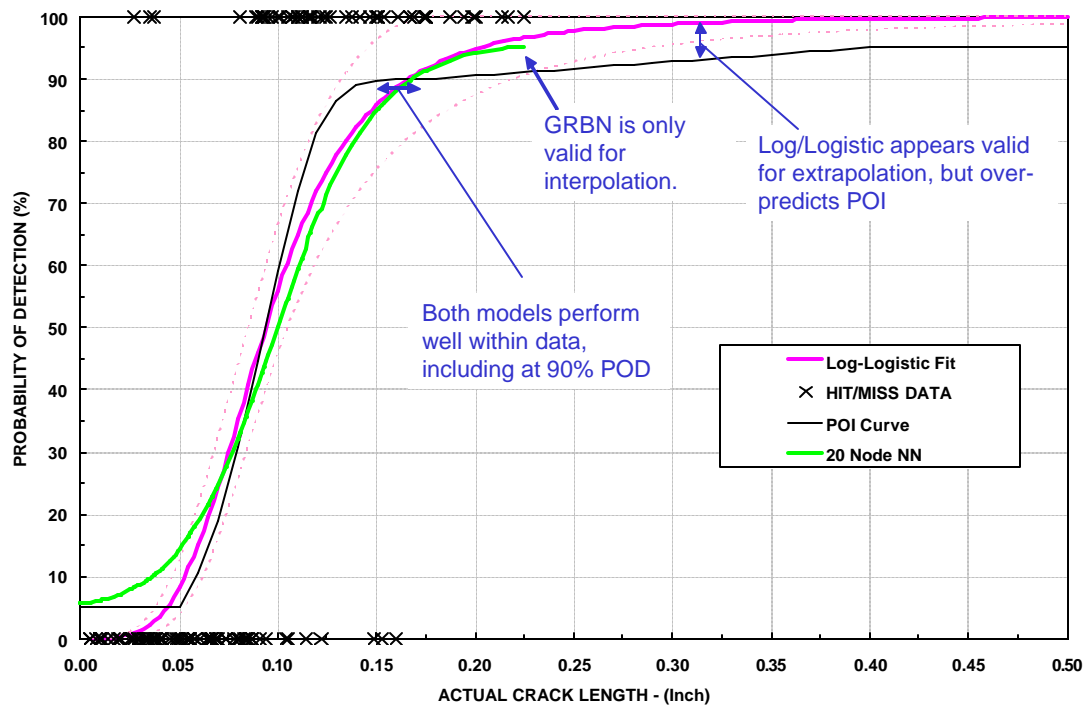


Figure 8- 13: Results for Inspection A, Typical Data

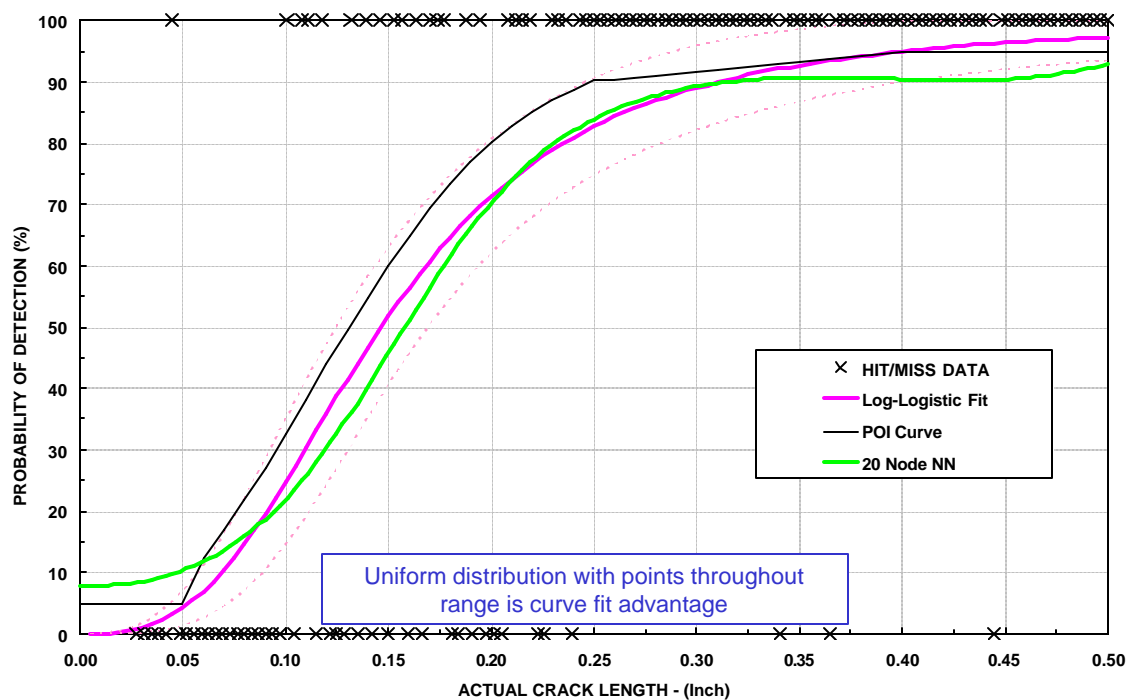


Figure 8- 14: Results for Inspection B, Distributed Data

SHEET	8-18	NO.	4-087051-20
TOTAL	8-18		
ISSUE DATE	12/22/04		

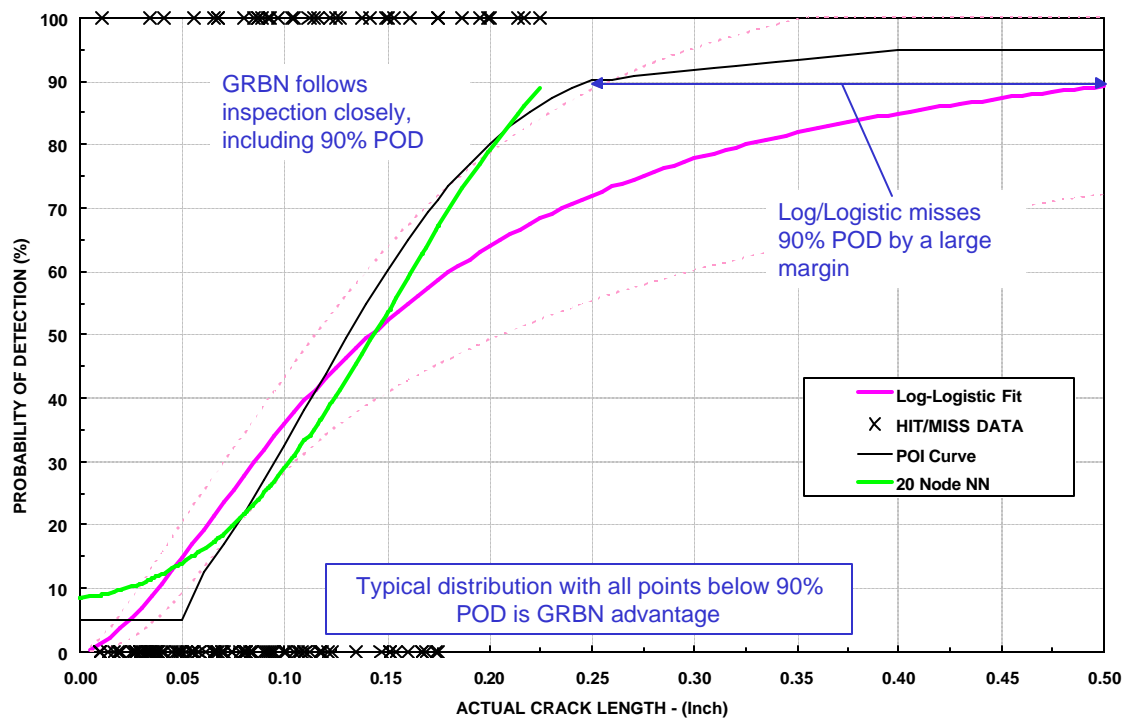


Figure 8- 15: Results for Inspection B, Typical Data

SHEET	9-1	NO.	4-087051-20
TOTAL	9-35		
ISSUE DATE	12/22/04		

CHAPTER 9: ANALYSIS SUPPORTING PANEL TESTING

Introduction

This chapter contains analysis conducted during the FASTER testing. This chapter includes results of the FT2 pre-test strain survey conducted in advance of any fatigue testing. In addition, it includes an evaluation of FASTER's feedback load control system. Finally, it includes discussions and analysis regarding stringer clip and skin cracking discovered during the FT2 test.

FT2 Strain Surveys

The Final Test Plans for each of the four panels includes a strain survey at the fatigue condition prior to the start of the extended fatigue testing. The objectives of the strain surveys are:

- Create a high-fidelity strain map of the test panel at Design Service Goal, before additional damage has initiated. This map will be the baseline for comparison with later strain measurements as MSD develops.
- Validate the FEA models used to develop the test plans, and ensure that the panel is behaving as expected.
- Optimize the FEA models as necessary to improve correlation with the strain measurements. The FEA models' boundary conditions are particularly important to this correlation.

Evolution of the FEA models based on the strain surveys are discussed in the Chapters 3 and 4. The focus of this chapter is the comparison between FASTER measurements and FEA results.

Test Plan for Strain Surveys

As FT2 was the first panel to be tested, the strain gage surveys in advance of fatigue testing were particularly exhaustive. The initial surveys were conducted at 5 psi internal pressure to ensure that all internal loads were relatively low. In addition, a 5 psi condition is more difficult to model or accomplish consistently, since fluctuations due to fixture friction, panel weight, and actuator load tolerances are

SHEET	9-2	NO.	4-087051-20
TOTAL	9-35		
ISSUE DATE	12/22/04		

more evident at low pressures. These effects are expected to reduce at the higher loads specified for the fatigue test. Although other tests were conducted, the primary strain surveys are as follows:

- Nominal 5 psi Cylindrical: 5 psi internal pressure, with hoop skin and frame loads determined from the symmetric FT2 model. The ratio of combined frame load to total hoop load was 12.04%, as specified in the FT2 Final Test Plan. The total applied hoop load was 42,540 lbs. The 2590 lbs applied at each longitudinal actuator corresponds to cylindrical internal pressure only.
- 5 psi F/S Ratio Sensitivity: 5 psi internal pressure, with hoop skin and frame loads variable. Total load was held constant at 42,540 lbs, while the ratio of frame load to total hoop load was varied from 10% to 14%. Tabular results are not yet available, but observation showed little change in strain during this test.
- 5 psi Total Hoop Sensitivity: 5 psi internal pressure, with hoop skin and frame loads variable. The ratio of frame load to total hoop load was held constant at 12.04%. The total load was varied $\pm 5\%$ of nominal, varying from 40,413 lbs to 44,667 lbs.
- 8.9 psi cylindrical: 8.9 psi internal pressure, with hoop skin and frame loads as specified in the FT2 Test Plan. The longitudinal load corresponds to cylindrical internal pressure only. This test may be accomplished in three subtests: hoop and pressure only, longitudinal load only, and then complete load condition. As of 3/24/04, this test was planned but not yet accomplished.
- Test Phase 1 Condition (8.9 psi pressure plus 1.25 g flight load), with hoop and longitudinal actuators per the FT2 Test Plan. Test may be accomplished in three subtests: hoop and pressure only, longitudinal load only, and then complete load condition. As of 3/24/04, this test was planned but not yet accomplished.

FT2 Focus Strain Gages

There are 66 strain gages called out in the FT2 test plan. In addition, the FAA installed several additional strain gages in discretionary locations for data collection during the strain survey. A map of all locations is shown in Figure 9-1. However, analysis comparing the strain measurements to FEA

SHEET	9-3	NO.	4-087051-20
TOTAL	9-35		
ISSUE DATE	12/22/04		

focuses on the gages listed below. Numbers identify the strain gages per the FT2 Test Plan, while the nomenclature from Figure 9-1 is shown in parenthesis:

FS 660, below S-6L

- 19 (S19) - Outer Surface Skin (Hoop)
- 20 (F20A) - Frame Outer Chord (Hoop)
- 21 (F21B) - Frame Inner Chord (Hoop)

FS 640, below S-4L

- 4 (S4B) - Inner Surface Tearstrap (Hoop)
- 5 (F5A) - Frame Outer Chord (Hoop)
- 6 (S6) - Outer Surface Skin (Hoop)
- 7 (F7B) - Frame Inner Chord (Hoop)

Between FS 640 and FS 660, below S-4L

- 1 (S1L) - Outer Surface Skin (Longitudinal)
- 28 (S28, S28L, S28-45) - Outer Surface Skin (Rosette)
- 31 (S31B, S31L, S31-45) - Inner Surface Skin (Rosette)
- 46 (S46) - Outer Surface Skin (Hoop)
- 47 (S47B) - Inner Surface Skin (Hoop)

Between FS 640 and FS 660, below S-5L

- (S90, S90L, S90-45) - Outer Surface Midbay Skin (Rosette)

FS 660, below S-4L

- 8 (S8B) - Inner Surface Tearstrap (Hoop)
- 9 (F9A) - Frame Outer Chord (Hoop)
- 10 (S10) - Outer Surface Skin (Hoop)
- 11 (F11B) - Frame Inner Chord (Hoop)

Between FS 640 and FS 660, below S-5L

- 3 (S3L) - Outer Surface Skin (Longitudinal)

Between FS 640 and FS 660, above S-4L

- 16 (S16) - Outer Surface Skin (Hoop)
- 58 (S58B) - Inner Surface Skin (Hoop)

SHEET	9-4	NO.	4-087051-20
TOTAL	9-35		
ISSUE DATE	12/22/04		

Frame radial links at FS 640 and FS 660

FT2 Strain Survey Results and Conclusions

Three separate strain surveys were accomplished for each load case. For each survey, the applied load was stepped to the load case in 10% increments. The table in Figure 9- 2 contains the measured strain results of the 5 psi Nominal and Total Load Sensitivity Surveys. Strain values have been corrected by the FAA to ensure that zero strain corresponds to zero applied load. For each gage, “ ϵ_x ” is the average the three measurements, and “Var.” is a measure of variability in the three measurements.

$$\text{Var.} = | (\text{Max} - \text{Min}) / \text{Average} |$$

A table comparing results of this survey is shown in Figure 9-3. The bold border locations are those gages on the lower skin just below the S-4 joint that are most critical for the behavior of lap joint MSD.

The two FEA data sets refer to two similar FEA models with different boundary conditions to represent the frame and skin loaders. “FEA 1” refers to the FEA panel model with simplified constraints defined in the global coordinate system. “FEA 2” refers to the modified panel model with more complex restraints defined in local coordinate systems. See Chapter 3 for a detailed discussion. “?” is a measure of the difference between the average measured strain and the respective FEA prediction:

$$? = | \text{FEA} - \text{FASTER} | / \text{Average (FEA, FASTER)}$$

Plots of these results are contained in Figure 9-4 through Figure 9-13.

The following conclusions can be made from the 5 psi data:

- There is good correlation between the predicted and measured strains in the panel skin. In the skin below S-4, prediction and measured values are typically within 6-8 %. This correlation improves as the hoop load is increased, so correlation is expected to improve at 8.9 psi.
- Both the predicted and measured hoop strains in the panel skin are relatively insensitive to the total hoop load. Apparently, internal pressure is the dominant factor in the skin hoop strain in the critical locations, since variations in frame/skin ratio and total hoop load have little effect.

SHEET	9-5	NO.	4-087051-20
TOTAL	9-35		
ISSUE DATE	12/22/04		

- Conversely, the predicted and measured strains in the frame chords are quite sensitive to actuator loads and to boundary conditions. Sensitivity to applied load is shown by the steep slopes in the sensitivity plots for gages 5, 7, 9, and 11. Sensitivity to boundary conditions is shown by the difference among the two FEA models, and the significant variability among FASTER measurements at the same condition. This sensitivity is particularly evident near the panel center, where the frame bending inherent to D-box testing is the greatest.
- Due to this sensitivity, correlation and repeatability in the frames are less than in the skin. However, this is not considered consequential for fatigue propagation of lap joint MSD. Cracking in the frames or in the frame-to-stringer attachments will likely initiate and propagate differently during FASTER testing than in service. The arrest of linked lap joint MSD at the frames and tearstraps may also be affected.
- The correlation to strain measurements is strongly related to the fidelity of the structure's FEA model. The models used here were designed to predict the stress state in the fuselage skin at S-4 and have proved acceptable for that objective. The frames and frame attachments in these models are relatively coarse to maximize model performance during non-linear solution. A model optimized for frame analysis would be needed to provide better correlation with the frame strain measurements.

SHEET	9-6	NO.	4-087051-20
TOTAL	9-35		
ISSUE DATE	12/22/04		

FT2 Load Transducer Survey

FASTER is a load-controlled test machine, meaning that the loads at the skin edges and frames are applied rather than reactive. These loads are controlled through operation of 40 electro/ pneumatic valves, using a full proportional integral derivative (PID), closed-loop feedback error control process (Ref 9-1). The only significant reaction forces are at the frame radial links. Therefore, the performance of this feedback control system is critical to the correct application of test loads.

This performance was evaluated by examining time-domain data from FASTER's circular buffer at approximately 7,500 cycles. This time domain data is not necessarily the worst case, but rather is considered representative of typical performance. Figure 9- 14 shows time value traces for the feedback loads from internal pressure, 2 frames, and 3 hoop skin loaders. The load magnitudes are plotted versus percentage of target load to allow comparison on the same axis. Values for target load are the maximum loads from the FT2 Test Plan, and shown in the first row of Table 9-1. The time value on the x-axis is in seconds, with $t = 0$ defined at an arbitrary start point not related to the test.

Figure 9- 15 shows one complete load cycle from the same data. This figure shows that the pressure response is extremely good, with a smooth sinusoidal response from 10% to 100% command. The skin response is also good, though the skin load leads the pressure slightly during loading and unloading, and overshoots the target maximum by a few percentage points. The frame response shown deviates further from command, and there is a significant overshoot after the pressure reaches maximum. The effect of this asynchrony between the skin, frame, and pressure loads is evaluated using finite element analysis in a subsequent section.

Figure 9- 16 shows the measured response at all load transducers at the time slice corresponding to "Max Pressure" in Figure 9- 15. Table 9-1 tabulates the variation in measured load between the load transducers. Note that Figure 9- 16 also shows differences in load between transducers on opposite ends of the same frame. This situation indicates an increased load in the stringer clips as that load is redistributed.

ENGINEERING DEPARTMENT

SHEET	9-7	NO. 4-087051-20
TOTAL	9-35	
ISSUE DATE		12/22/04

Table 9-1

	Targets	Max/Min vs. Target	Max vs. Min
Internal Pressure	8.9 psi	0.4 psi (0.4%)	---
Hoop Skin	9,510 lbs	530 lb (5.6%)	8.4%
Frames	1,530 lbs	182 lb (12%)	17%
Long. Skin	16,220 lbs.	562 lb (3.5%)	4.4%

SHEET	9-8	NO.	4-087051-20
TOTAL	9-35		
ISSUE DATE	12/22/04		

FT2 Stringer Clip Analysis

Starting at 7,500 test cycles, cracks were found in a large number of FT2 stringer clips. Figure 9- 17 is a schematic showing the locations where clips were found between 7,500 and 15,000 cycles.

Detailed discussion of the fractography and analysis of the stringer clip cracks is contained in the Q7 Damage Characterization progress report. The conclusions from that analysis considered here are:

- Cracks initiated at multiple surface origins, often on both sides of opposing surfaces.
- Fracture surfaces indicate 1,800 - 2,800 cycles of fatigue crack growth in reverse bending.
- Stress corrosion is not a significant factor.

SHEET	9-9	NO.	4-087051-20
TOTAL	9-35		
ISSUE DATE	12/22/04		

History of Stringer Clip Cracking

There are no Boeing Service Bulletins applicable to stringer clip cracking in the 727 fuselage crown.

There are service bulletin inspections of clips at the floor cusp because un-heat treated clips were inadvertently installed, and there are service bulletin inspections for cracking in stringers and frames at locations where stringers were attached directly to the frames.

Figure 9- 18 shows the results of Service Discrepancy Report (SDR) search of FedEx 727 "Tie Clip" reports between S-10L and S-10R, from 1995 to present. This figure demonstrates that stringer clip cracking does occur in service at locations within the FASTER test panels. Note that SDR reports of structural repairs are only required if the repair is considered major, whereas a stringer clip replacement is a relatively simple procedure. Therefore, it is expected that many more 727 crown stringer clips have been replaced in service than are contained in the SDR database.

Stringer clips in the 737 fuselage crown are similar to the 727, and Boeing Service Bulletins have been issued to address 737 clip cracking. SB 737-53-1085 inspects for similar cracks due to sonic fatigue in the crown from BS 540 to BS 727A, 6L - 6R. The FAA-AANC testbed 737 (737-222 with 46,358 cycles) has 24 "tie-clips" with visually detectable cracks within the SB inspection area (Ref 9-2). Figure 9- 19 shows a photograph taken of the 737 clip next to a photograph of one of the cracked replacement FT2 clips, demonstrating that the crack location and morphology are virtually identical.

Note that the Service Bulletin modification addressing this damage is to replace the clip with a laminated 0.016"+0.016" 7075-T6 clip. Per the service bulletin, clips with cracks less than 0.50" with no adjacent cracked clips were allowed to stay service with 2,000 cycle inspections.

SHEET	9-10	NO.	4-087051-20
TOTAL	9-35		
ISSUE DATE		12/22/04	

Finite Element Analysis

As shown in Figure 9- 17, stringer clips have been discovered cracked all over the panel but particularly along stringer 3. Although such cracks have been observed during regular operations, it is unusual for stringer clips at certain locations to be more severely loaded than others. Therefore, the FT2 loading conditions and the fixtures had to be carefully studied.

The objectives of this analysis are as follows:

- To study the observed stringer clip cracking during the FT2 testing.
- To investigate the effect of the frame and the stringer deformation on the clip.
- To assess the FASTER test load input perturbations.

Approach

The analysis was carried out in 3 steps as shown.

- The global FT2 model (See Figure 9- 20) displacement results, with the test plan loads, were mapped on to the local stringer clip models at stations 620 and 640 at stringer locations 3 and 6. Stringer 3 locations had the most severe cracking and Stringer 6 locations were arbitrarily chosen for comparison.
- The measured actuator loads from the FASTER test at 2 different time instances were applied to the global FT2 model and the displacements mapped on to the local clip model at the above mentioned 4 locations to evaluate asynchrony effects during the test.
- The stringer clip at station 620/ stringer 3 was assumed completely failed, to determine the effect on the skin at the lap joint location.

Description of the Model

The global FT2 model has a detailed representation of the radial links and fixtures and a fairly accurate representation of the skin, stringers and the frames. The model has approximately 105,000 degrees of freedom and the displacements on the skin, stringers and frames converged for the original test plan load

SHEET	9-11	NO.	4-087051-20
TOTAL	9-35		
ISSUE DATE	12/22/04		

of 8.9 psi skin pressure, 9510 lbf / actuator hoop load, 16220 lbf/actuator axial load and 1530 lbf of frame hoop load. These displacements were mapped on to the boundaries of the local model which has approximately 60,000 degrees of freedom (See Figure 9- 21).

Results

The model based on test plan loads showed a high maximum principal stress of 15 ksi at the crack location on Frame 620/ Stringer 3 (See Figure 9- 22) compared to only around 3.3 ksi near the crack location on the stringer 6 clip. Similar observation can be made on Frame 640 (See Figure 9- 23). Therefore it can be concluded that the loads on clips on stringer 3 are more severe compared to the loads on clips on stringer 6. The clip at station 620/ stringer 3 was the worst among the 4 locations picked for comparison.

Actuator loads were measured at time slices (Max P-) and (Max P +) shown in Figure 9- 15, and these loads were applied to the global model. The response was mapped on to the local clip models at stringers 3 and 6 at stations 620 and 640 to determine the effects of the phase lag in load application. Both models (test plan loads and measured actuator loads) show high stress levels at the crack location on clips at Stringer 3 for stations 620 and 640. The maximum principal stress at the crack location at STA 620 is severe at 15 ksi for the model based on test plan loads (8.9 psi, 16220 lbs longitudinal, 9510 lbs hoop), predominantly due to the torsion in Frame 620 (See Figure 9- 24). The maximum principal stress at the crack location at STA 620 is more severe at 18 ksi for the model based on measured actuator loads, at Max P- (See Figure 9- 25). The maximum principal stress at the crack location at STA 620 is around 17 ksi for the model based on measured actuator loads at Max P+ (See Figure 9- 26).

An additional run was made with STA 620, stringer 3 clip removed in the global model and displacements mapped to the local models on STA 640 at stringer 3 and 6. This was done to see the effect of the load path change assuming that the STA 620, stringer 3 clip had failed. The results were compared at the skin on the Lap joint location. Figure 9- 27 and Figure 9- 28 show that the skin stress

SHEET	9-12	NO.	4-087051-20
TOTAL	9-35		
ISSUE DATE	12/22/04		

at the lap joint location did not change substantially due to the failure of the clip at frame 620 and stringer 3.

In summary, the conclusions from the FEA analysis are:

- Cracking occurs at the critical location of the clip
- Asynchrony in applied load increases the stress in the critical area
- Failure of a stringer clip does not cause significant load redistribution to either the adjacent clips or the lap splice skin.

SHEET	9-13	NO.	4-087051-20
TOTAL	9-35		
ISSUE DATE	12/22/04		

Corrective Actions Considered

A number of options were considered to improve test performance and potentially reduce clip cracking for the remainder of FT2 testing. These options were:

1) Continue test unchanged

- Proposal: Continue test per current procedures, and monitor clip for crack growth at a practical interval.
- Advantages: Test Plan is already as close as practical to service 727, and undetected cracked clips are a service problem on 727 and 737 aircraft. The effect to lap splice MSD is minimal for inbd/outbd cracks.
- Disadvantages: It is possible that all clips will be cracked eventually, with resulting impact to schedule. With less than 3,000 cycles of crack growth, cracks in replaced clips can reoccur within test. Each clip replacement risks damage to underlying stringer and frame

2) Improve FASTER load control performance to improve tracking between commanded and measured loads.

- Proposal: Evaluate performance for effects of continuous operation. Retune PID controller and/or recalibrate load sensors to improve control performance, or change command signal profile for a better match.
- Advantages: Improved performance will also benefit lap joint MSD without the risk of future complications.
- Disadvantages: The control system has already been tuned extensively, so the potential for improvement may be limited. This reductions will reduce loads on clips, but so low that clip cracking will be eliminated.
- Conclusion: Load tracking should be improved if possible.

3) Increase hoop loads as necessary to reduce bending in the panel frames.

SHEET	9-14	NO.	4-087051-20
TOTAL	9-35		
ISSUE DATE	12/22/04		

Proposal: Use FEA to determine new total hoop load to reduce frame bending to acceptable level, then validate results with strain survey.

- Advantages: The frame bending is higher than expected for the service condition. As demonstrated by the strain surveys of the skin (see Figure 9-9) and frame chords (see Figure 9-7 and Figure 9-8), increased hoop loads may correct this condition with only moderate increase in skin stress.
- Disadvantages: Based on extrapolation of the 5 psi strain survey, up to a 20% hoop load increase would be required. The resulting increase in skin stress at S-4 lower row is counter to test objectives. In addition, any significant change to the load profile mid-test may cause complications in interpreting fracture surfaces and the test results. Also, this option has a major impact to the testing schedule to accomplish the required analysis and validating strain survey.
- Conclusion: The disadvantages of increased load outweigh the potential benefits, so this option is not recommended.

4) Replace cracked/failed clips with an improved design.

- Advantages: Improved durability would result in less downtime for clip replacement, and less risk of tooling damage to frames and stringers during clip replacement.
- Disadvantages: The replacement clips must be similar in compliance to original equipment, or else the load distribution within test panel will change, and the crack problem may move to an adjacent structure that is more critical and more difficult to repair.
- Conclusion: Replacement clips will have similar compliance, but improved durability.

Discussion and Recommendations

In summary, the conclusion from this analysis is that the stringer clip cracking is similar to that seen in service, though the stress in the clip are be elevated due to FASTER's boundary conditions and asymmetry in applied loads. Changes to the Test Plan were considered but not recommended. The recommendations for the remainder of the test are:

SHEET	9-15	NO.	4-087051-20
TOTAL	9-35		
ISSUE DATE	12/22/04		

- Continue with target loads per Test Plan
- Improve command/response tracking performance as much as practical
 - Ensure PID controller is tuned appropriately for the separate actuators
 - Evaluate if long hours of continuous operation affect performance
 - Reduce frequency if tracking is improved
- Replace clips by attrition after Replace after failure or at a convenient time just before failure
 - Cracked clips should be monitored every 500 cycles, preferably with remote camera
 - Replacement clips should have similar compliance with improved durability

Note that all of these changes are relatively minor. The FASTER panel test is still considered representative of the service environment for lap splice MSD.

SHEET	9-16	NO.	4-087051-20
TOTAL	9-35		
ISSUE DATE	12/22/04		

FT2 Skin Cracking Analysis

Starting at 17,235 cycles, a series of circumferential skin cracks have been discovered in FT2 near the edge reinforcement doublers. Specifically, cracks have been found:

- In the skin just inboard of the end tear straps (see Figure 9-29) caused by higher stresses applied to knife edged fastener countersinks due to panel loading redistribution.
- At the stringer run outs (stringer and skin cracking, see Figure 9- 30) caused by high fastener pin loads due to stringer load redistribution at the ends of the panel.
- In the skin at the edge of the end reinforcement doublers (see Figure 9- 31) caused by bond failure and the resulting increased pin loads.

Repairs have been designed to address these issues, and instructions will be issued via ER/A to be accomplished by FAA technicians. See ER/A attachments to the FT2 Test Plan.

Modifications to FT1

Because of the similarity of the test panels, the durability of FT1 was evaluated at the locations where skin cracks have developed in FT2 . This assessment was based on a comparison of FEA analysis of FT2 (see Figure 9- 32) and FT1 (see Figure 9- 33) at these critical crack locations. Most of the stress reduction results from FT1 's location from the forward fuselage, so the longitudinal loads experienced in service and applied in the test plan are significantly lower than FT2. In addition, the internal loads in the global FEA model were reduced at Q9 (see Chapters 3 and 4). Comparison of the two FEA models leads to the following conclusions:

- The stress level just inboard of the end tear straps at the knife edged fastener countersinks decreases by approximately 32% over the FT2 panel.
- The fatigue threshold for cracking at the edge of the end reinforcement doublers with a bond failure is greater than twice that of the FT2 panel design.
- The stress level at the stringer run out decreases by 40% over the FT 2 panel.

SHEET	9-17	NO.	4-087051-20
TOTAL	9-35		
ISSUE DATE	12/22/04		

Based on these results, FT1 is considered less critical for circumferential skin cracking than FT2.

However, to reduce the likelihood of skin cracking occurring early in the test, the following modifications will be performed to FT1 prior to testing:

- Zero time and remove countersinks from all the fastener holes shown below replacing the existing 5/32 inch diameter fasteners with 1/4 inch diameter fasteners per Engineering Authorization 093215-14 (see Figure 9- 34).
- Taper the end of all the stringers at the run out as shown below per Engineering Authorization 093215-14, Revision A. This will reduce the pin loads at the end of the stringers (see Figure 9-35).
- Proactively replace the stringer clips at the FS 580 frames with a more durable design.

Instructions for these modifications have been issued via ER/A to be accomplished by FAA technicians. See ER/A attachments to the FT1 Test Plan.

References

- 9-1 "Full-Scale Testing and Analysis of Fuselage Structure Containing Multiple Cracks," DOT/FAA/AR-01/46, 2002.
- 9-2 "Visual Inspection Research Project Report on Benchmark Inspections", DOT/FAA/AR-96/65, 1996

SHEET	9-18	NO.	4-087051-20
TOTAL	9-35		
ISSUE DATE	12/22/04		

Figures

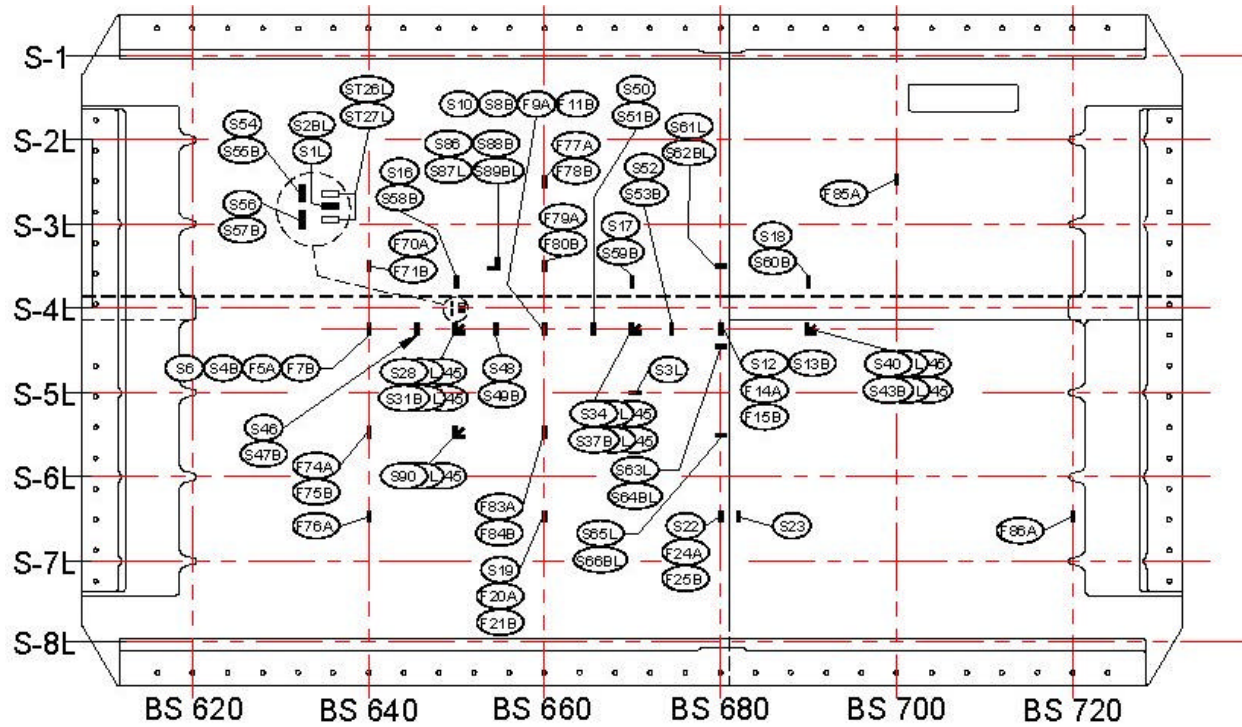


Figure 9-1: FT2 Strain Gage Locations

ENGINEERING DEPARTMENT

SHEET	9-19	NO.	4-087051-20
TOTAL	9-35		
ISSUE DATE	12/22/04		

			Gage Value			ϵ_x	Var.
Average			1	2	3		
View A:	3 - Outer Surface Skin (Long)		101	94	92	9.657E-05	9%
View B:	16 - Outer Surface Skin (Hoop)		733	734	745	7.373E-04	2%
	58 - Inner Surface Skin (Hoop)		685	686	696	6.857E-04	0%
View C:	19 - Outer Surface Skin (Hoop)		473	461	472	4.653E-04	5%
	20 - Frame Outer Chord (Hoop)		193	222	194	2.030E-04	14%
	21 - Frame Inner Chord (Hoop)		274	284	287	2.817E-04	5%
View E:	4 - Inner Surface Tearstrap (Hoop)		297	305	330	3.107E-04	11%
	5 - Frame Outer Chord (Hoop)		570	574	535	5.597E-04	7%
	6 - Outer Surface Skin (Hoop)		459	454	446	4.530E-04	3%
	7 - Frame Inner Chord (Hoop)		-133	-64	-103	-1.000E-04	69%
	8 - Inner Surface Tearstrap (Hoop)		257	270	287	2.713E-04	11%
	9 - Frame Outer Chord (Hoop)		689	678	678	6.817E-04	2%
	10 - Outer Surface Skin (Hoop)		506	501	493	5.000E-04	3%
	11 - Frame Inner Chord (Hoop)		-125	-73	-65	-8.767E-05	68%
View F:	1 - Outer Surface Skin (Long)		145	128	129	1.340E-04	13%
	28 - Outer Surface Skin (Rosette)		687	686	682	6.850E-04	1%
	31 - Inner Surface Skin (Rosette)		687	686	700	6.910E-04	2%
	46 - Outer Surface Skin (Hoop)		683	679	676	6.793E-04	1%
	47 - Inner Surface Skin (Hoop)		631	630	653	6.380E-04	4%
	90 - Center Bay		854	839	850	8.477E-04	2%
Maximum			Gage Value			ϵ_x	Var.
View A:	3 - Outer Surface Skin (Long)		62	67	67	6.200E-05	16%
View B:	16 - Outer Surface Skin (Hoop)		756	771	768	7.650E-04	2%
	58 - Inner Surface Skin (Hoop)		728	726	727	7.270E-04	0%
View C:	19 - Outer Surface Skin (Hoop)		456	482	472	4.700E-04	6%
	20 - Frame Outer Chord (Hoop)		68	109	95	9.057E-05	45%
	21 - Frame Inner Chord (Hoop)		425	340	616	4.600E-04	60%
View E:	4 - Inner Surface Tearstrap (Hoop)		337	353	364	3.513E-04	8%
	5 - Frame Outer Chord (Hoop)		384	467	451	4.340E-04	19%
	6 - Outer Surface Skin (Hoop)		464	460	456	4.597E-04	2%
	7 - Frame Inner Chord (Hoop)		59	-52	10	5.657E-06	1958%
	8 - Inner Surface Tearstrap (Hoop)		302	314	321	3.123E-04	6%
	9 - Frame Outer Chord (Hoop)		494	587	552	5.443E-04	17%
	10 - Outer Surface Skin (Hoop)		509	506	499	5.047E-04	2%
	11 - Frame Inner Chord (Hoop)		68	-27	6	1.667E-06	576%
View F:	1 - Outer Surface Skin (Long)		94	104	99	9.900E-05	10%
	28 - Outer Surface Skin (Rosette)		707	706	704	7.057E-04	0%
	31 - Inner Surface Skin (Rosette)		717	727	729	7.243E-04	2%
	46 - Outer Surface Skin (Hoop)		698	670	697	6.893E-04	4%
	47 - Inner Surface Skin (Hoop)		661	677	677	6.717E-04	2%
	90 - Center Bay		856	872	864	8.640E-04	2%
Minimum			Gage Value			ϵ_x	Var.
View A:	3 - Outer Surface Skin (Long)		121	118	115	1.180E-04	5%
View B:	16 - Outer Surface Skin (Hoop)		703	717	716	7.120E-04	2%
	58 - Inner Surface Skin (Hoop)		657	655	655	6.557E-04	0%
View C:	19 - Outer Surface Skin (Hoop)		450	465	469	4.613E-04	4%
	20 - Frame Outer Chord (Hoop)		398	369	425	3.973E-04	14%
	21 - Frame Inner Chord (Hoop)		141	162	196	1.663E-04	33%
View E:	4 - Inner Surface Tearstrap (Hoop)		270	297	295	2.873E-04	9%
	5 - Frame Outer Chord (Hoop)		705	686	716	7.023E-04	4%
	6 - Outer Surface Skin (Hoop)		439	427	432	4.327E-04	3%
	7 - Frame Inner Chord (Hoop)		-251	-243	-239	-2.443E-04	5%
	8 - Inner Surface Tearstrap (Hoop)		230	263	242	2.417E-04	10%
	9 - Frame Outer Chord (Hoop)		655	641	696	6.640E-04	6%
	10 - Outer Surface Skin (Hoop)		485	475	477	4.790E-04	2%
	11 - Frame Inner Chord (Hoop)		-246	-214	-194	-2.177E-04	23%
View F:	1 - Outer Surface Skin (Long)		154	155	157	1.553E-04	2%
	28 - Outer Surface Skin (Rosette)		659	653	656	6.550E-04	1%
	31 - Inner Surface Skin (Rosette)		645	660	658	6.543E-04	2%
	46 - Outer Surface Skin (Hoop)		654	651	656	6.533E-04	1%
	47 - Inner Surface Skin (Hoop)		601	615	613	6.097E-04	2%
	90 - Center Bay		816	829	830	8.250E-04	2%

Figure 9- 2: 5 psi FASTER Strain Results (Corrected)

SHEET	9-20	NO.	4-087051-20
TOTAL	9-35		
ISSUE DATE	12/22/04		

View	FEA 1	FEA 2	FASTER	Var.	A.1	A.2	+5%		-5%	Var.	A.1	A.2
							FEA 1	FEA 2				
View A	3 - Outer Surface Skin (Long)	111	90	96	9%	16%	63	64	161	101	118	5%
View B	16 - Outer Surface Skin (Short)	635	642	737	2%	16%	647	656	622	628	712	2%
	68 - Inner Surface Skin (Short)	674	677	686	0%	3%	685	684	683	670	656	0%
View C	19 - Outer Surface Skin (Short)	475	474	465	5%	2%	475	471	474	479	461	4%
	20 - Frame Outer Chord (Short)	309	279	303	14%	52%	305	328	312	290	307	14%
	21 - Frame Inner Chord (Short)	121	343	282	6%	139%	227	424	5	264	166	33%
View E	4 - Inner Surface Teardrop (Short)	434	436	311	11%	40%	440	442	429	430	287	9%
	5 - Frame Outer Chord (Short)	361	325	560	7%	52%	390	201	373	360	702	4%
	6 - Outer Surface Skin (Short)	435	410	463	2%	4%	435	434	443	416	433	2%
	7 - Frame Inner Chord (Short)	29	343	100	69%	-27%	180	536	-218	48	244	52%
	8 - Inner Surface Teardrop (Short)	426	431	271	11%	59%	435	439	420	425	242	10%
	9 - Frame Outer Chord (Short)	380	330	662	2%	69%	342	284	320	337	864	6%
	10 - Outer Surface Skin (Short)	424	400	520	3%	16%	414	394	424	406	479	2%
	11 - Frame Inner Chord (Short)	58	300	48	68%	-34%	178	632	-256	37	218	23%
View F	1 - Outer Surface Skin (Long)	100	79	134	13%	34%	52	74	160	95	100	2%
	28 - Outer Surface Skin (Forward)	648	647	655	1%	6%	656	653	639	641	656	1%
	31 - Inner Surface Skin (Forward)	665	664	661	0%	6%	660	664	640	663	664	2%
	46 - Outer Surface Skin (Short)	640	636	679	1%	7%	647	641	632	631	653	1%
	47 - Inner Surface Skin (Short)	645	652	638	4%	1%	659	663	630	642	610	2%
	50 - Outer Surface Skin Midway	695	700	848	0%	21%	710	708	691	708	835	2%
Nominal 5 psi												
Skin	1 - Outer Surface Skin (Long)	100	79	134	13%	34%	52	74	150	95	155	2%
	3 - Outer Surface Skin (Long)	111	90	96	9%	16%	63	64	161	101	118	5%
	6 - Outer Surface Skin (Short)	435	410	463	2%	4%	435	434	443	416	433	2%
	10 - Outer Surface Skin (Short)	424	400	520	3%	16%	414	394	424	406	479	2%
	16 - Outer Surface Skin (Short)	635	642	737	2%	16%	647	656	622	628	712	2%
	18 - Outer Surface Skin (Short)	475	474	465	5%	2%	475	471	474	479	461	4%
	28 - Outer Surface Skin (Forward)	648	647	655	1%	6%	656	653	639	641	656	1%
	31 - Inner Surface Skin (Forward)	665	664	661	0%	6%	660	664	640	663	664	2%
	46 - Outer Surface Skin (Short)	640	636	679	1%	7%	647	641	632	631	653	1%
	47 - Inner Surface Skin (Short)	645	652	638	4%	1%	659	663	630	642	610	2%
	50 - Outer Surface Skin Midway	695	700	848	0%	21%	710	708	691	708	835	2%
Nominal 5 psi												
Teardrop	4 - Inner Surface Teardrop (Short)	434	436	311	11%	40%	440	442	429	430	287	9%
	6 - Inner Surface Teardrop (Short)	426	431	271	11%	59%	435	439	420	425	242	10%
Frame OC												
	5 - Frame Outer Chord (Short)	361	325	560	7%	52%	390	201	373	360	702	4%
	9 - Frame Outer Chord (Short)	380	330	662	2%	69%	342	284	320	337	864	6%
	20 - Frame Outer Chord (Short)	309	279	303	14%	52%	305	328	312	290	307	14%
Frame IC												
	7 - Frame Inner Chord (Short)	29	343	100	69%	-27%	180	536	-218	48	244	52%
	11 - Frame Inner Chord (Short)	460	461	459	0%	0%	460	461	459	461	459	0%
	21 - Frame Inner Chord (Short)	121	343	282	6%	139%	227	424	5	264	166	33%

Figure 9-3: FT2 FASTER and FEA Results (5 psi Nominal and +/- 5% Total Hoop Sensitivity)

ENGINEERING DEPARTMENT

SHEET	9-21	NO.	4-087051-20
TOTAL	9-35		
ISSUE DATE	12/22/04		

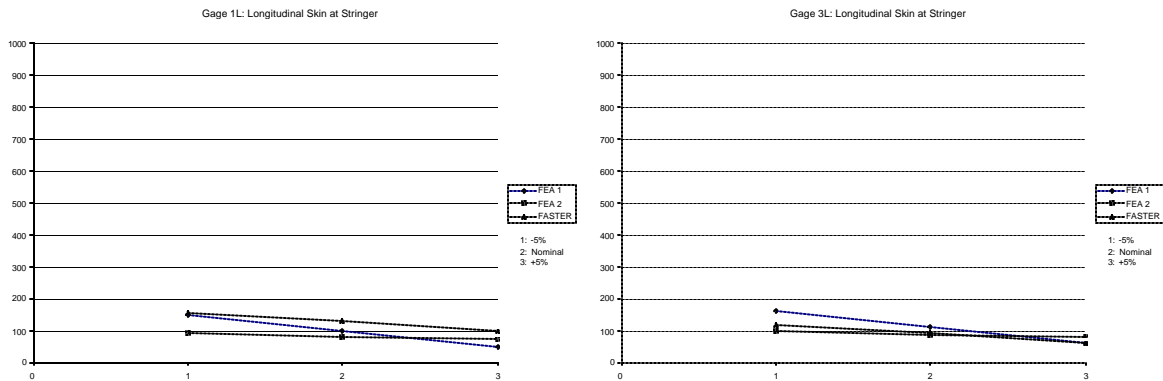


Figure 9-4: Longitudinal Skin Gages 1 and 3

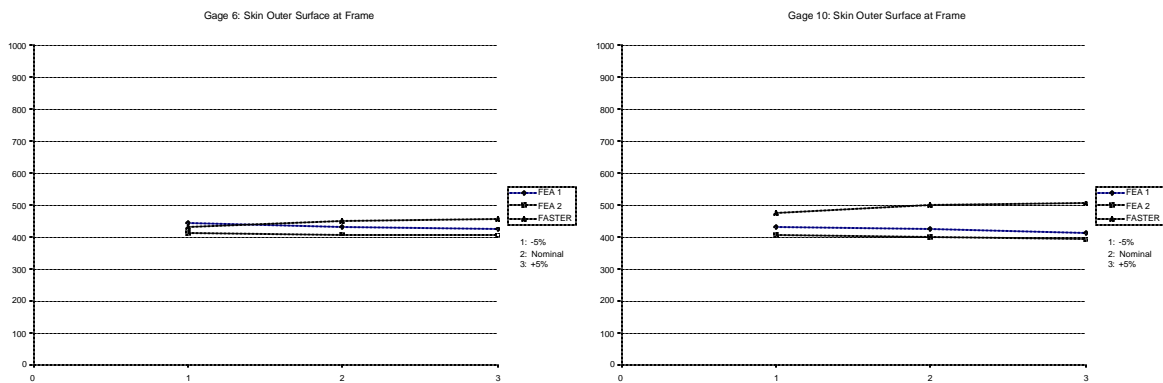


Figure 9-5: Hoop Outer Skin Gages at Frames Below S-4, Gages 6 and 10

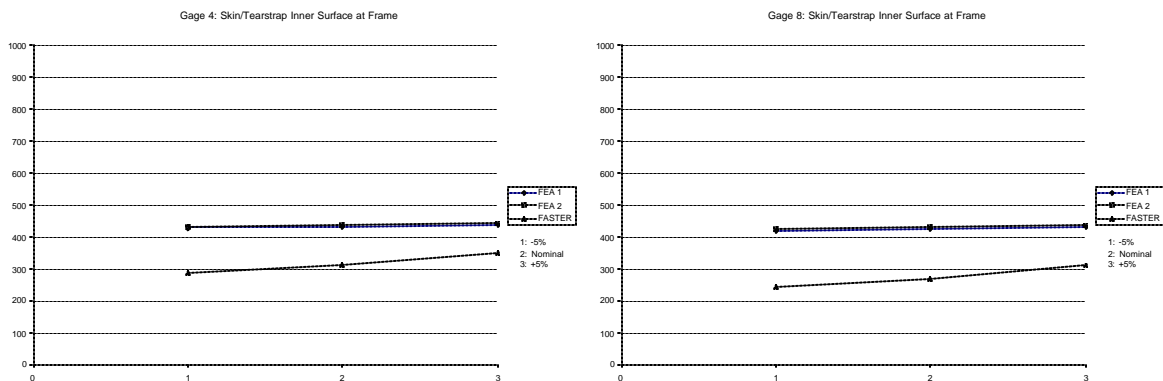


Figure 9- 6: Hoop Inner Tearstrap Gages at Frames Below S-4, Gages 4 and 8

ENGINEERING DEPARTMENT

SHEET	9-22	NO.	4-087051-20
TOTAL	9-35		
ISSUE DATE	12/22/04		

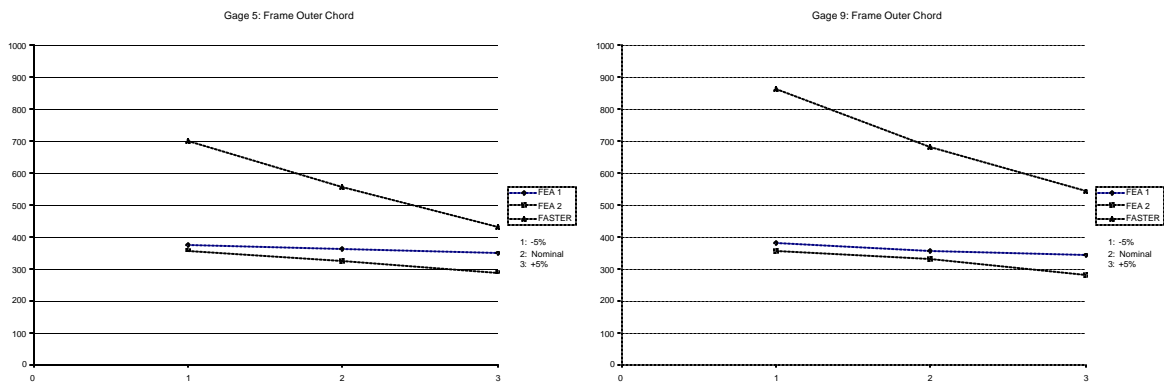


Figure 9-7: Frame Outer Chord Gages Below S-4, Gages 5 and 9

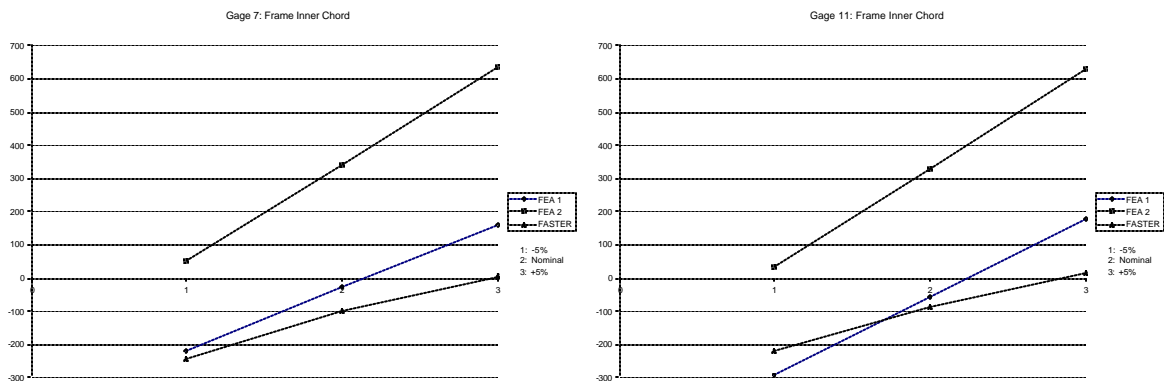


Figure 9-8: Frame Inner Chord Gages Below S-4, Gages 7 and 11

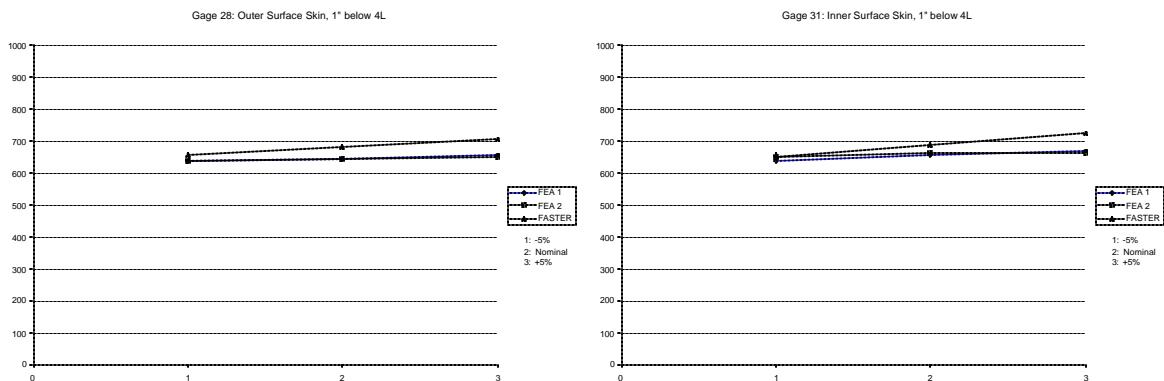


Figure 9-9: Mid-bay Outer and Inner Skin Gages Below S-4, Gages 28 and 31

ENGINEERING DEPARTMENT

SHEET	9-23	NO.	4-087051-20
TOTAL	9-35		
ISSUE DATE	12/22/04		

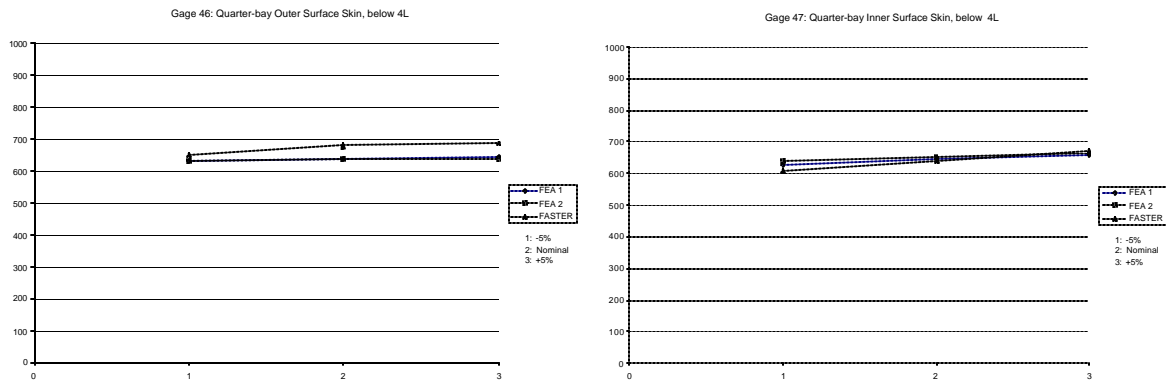


Figure 9-10: Quarter-bay Outer and Inner Skin Gages Below S-4, Gages 46 and 47

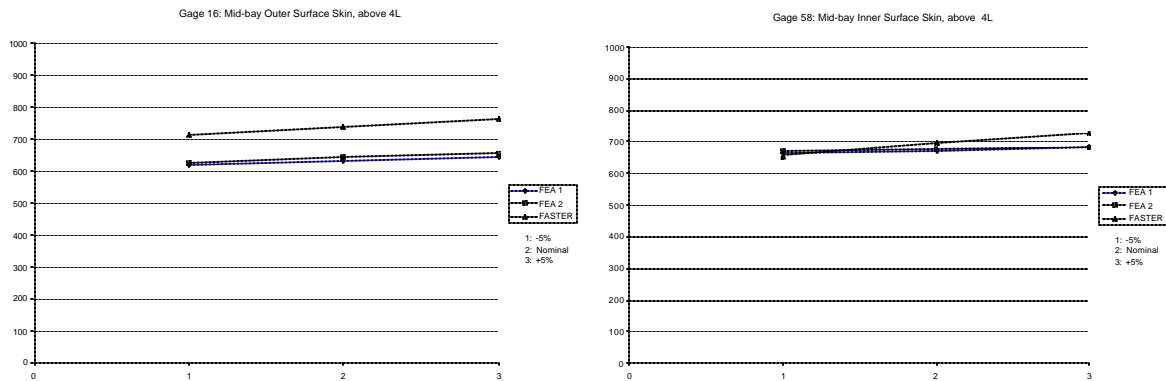


Figure 9-11: Outer and Inner Skin Gages Above S-4, Gages 16 and 58

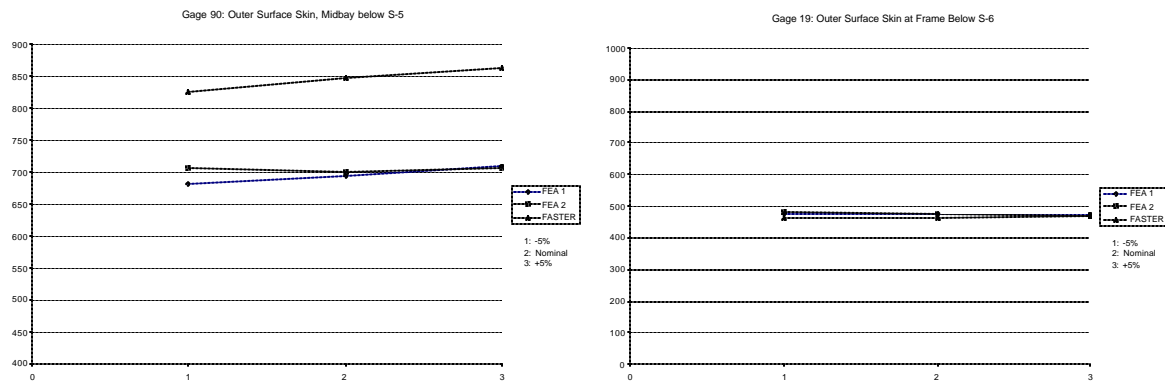


Figure 9-12: Outer Skin Gages away from S-4, Gages 90 and 19

ENGINEERING DEPARTMENT

SHEET	9-24	NO.	4-087051-20
TOTAL	9-35		
ISSUE DATE	12/22/04		

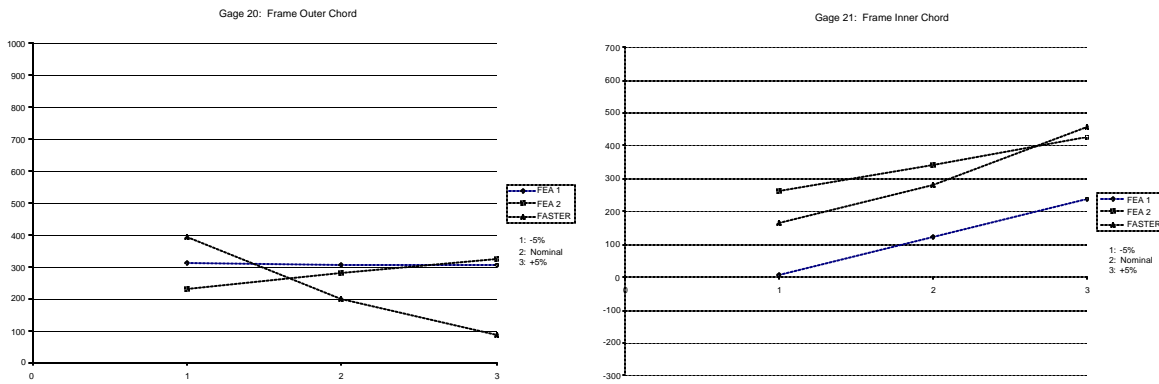


Figure 9-13: Outer and Inner Frame Chord Gages away from S-4, Gages 20 and 21

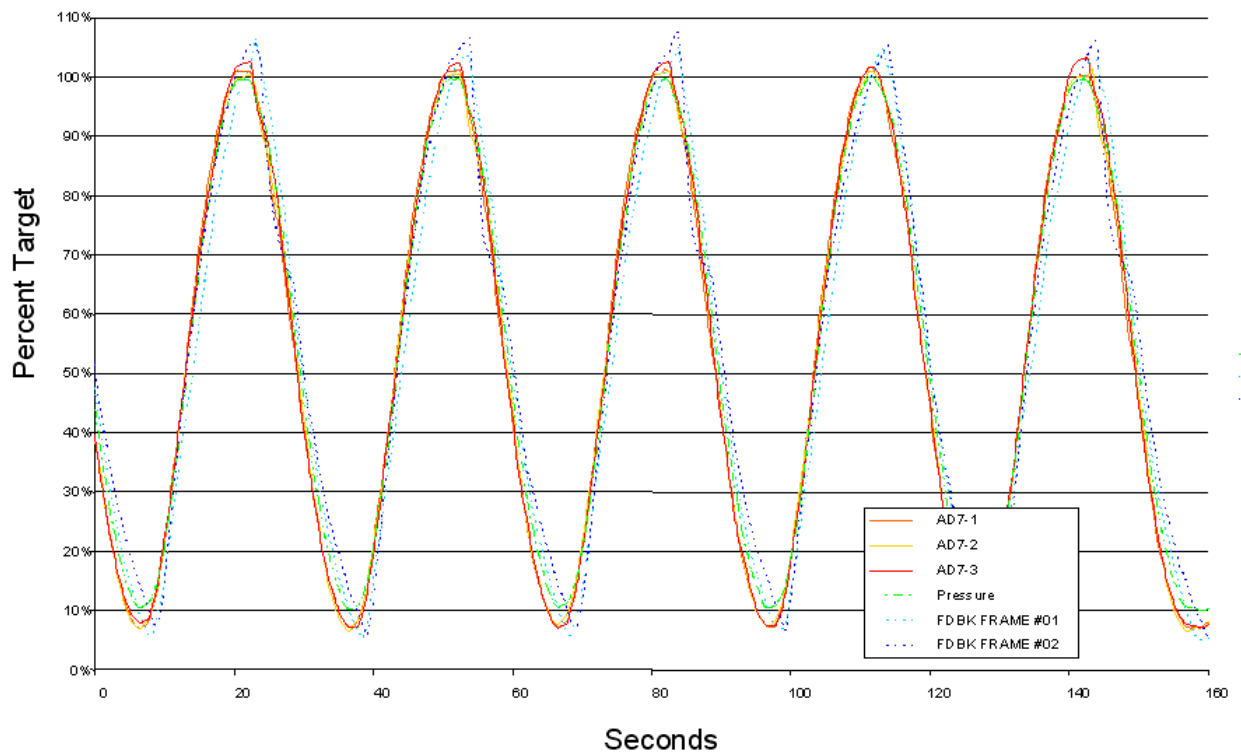


Figure 9- 14: Time-Domain Data from FASTER Circular Buffer

ENGINEERING DEPARTMENT

SHEET	9-25	NO.	4-087051-20
TOTAL	9-35		
ISSUE DATE	12/22/04		

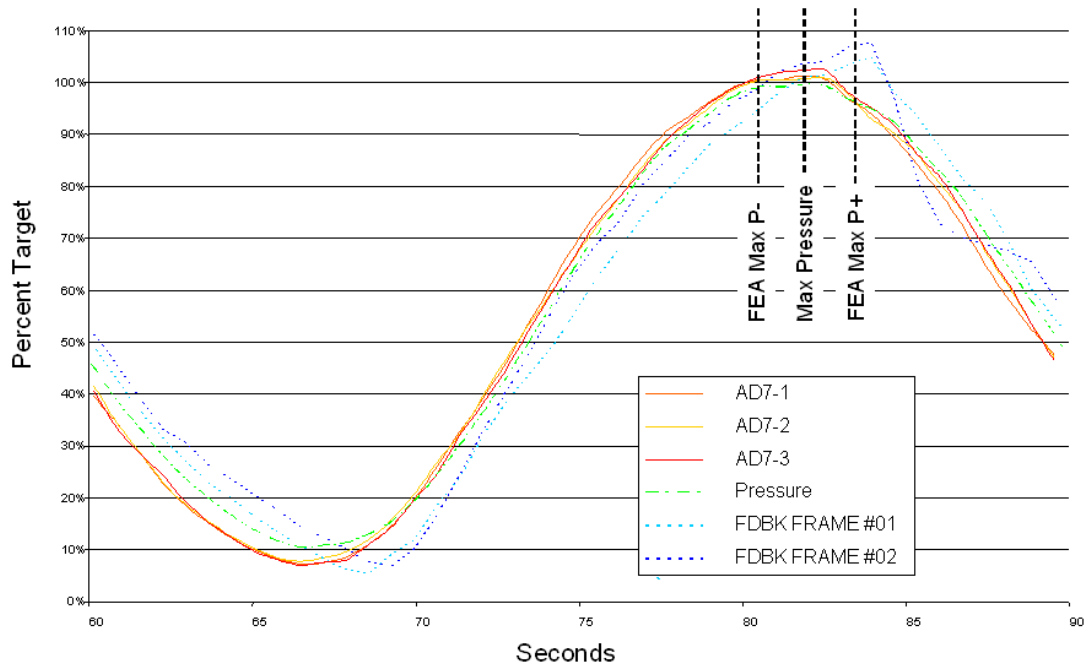


Figure 9- 15: Single Load Cycle from FASTER Circular Buffer

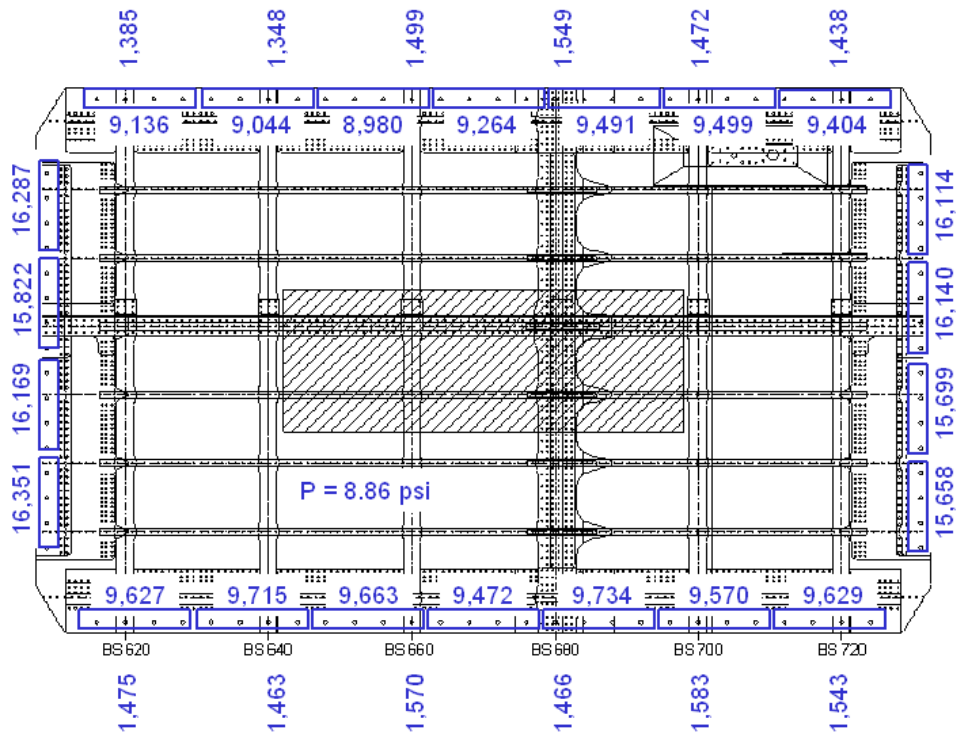


Figure 9- 16: Load Transducer Measurements at Max Pressure

SHEET	9-26	NO.	4-087051-20
TOTAL	9-35		
ISSUE DATE	12/22/04		

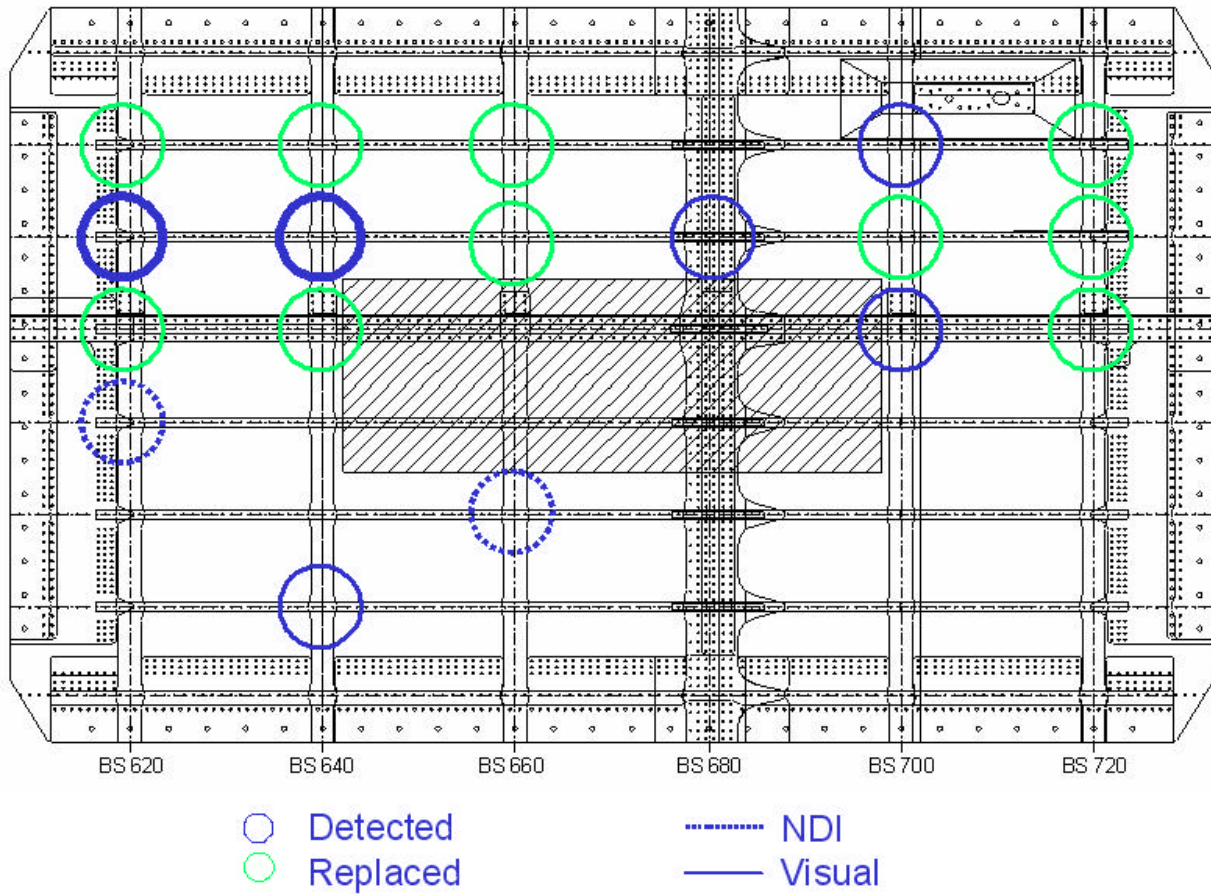


Figure 9- 17: Stringer Clip Cracking at 15,000 cycles

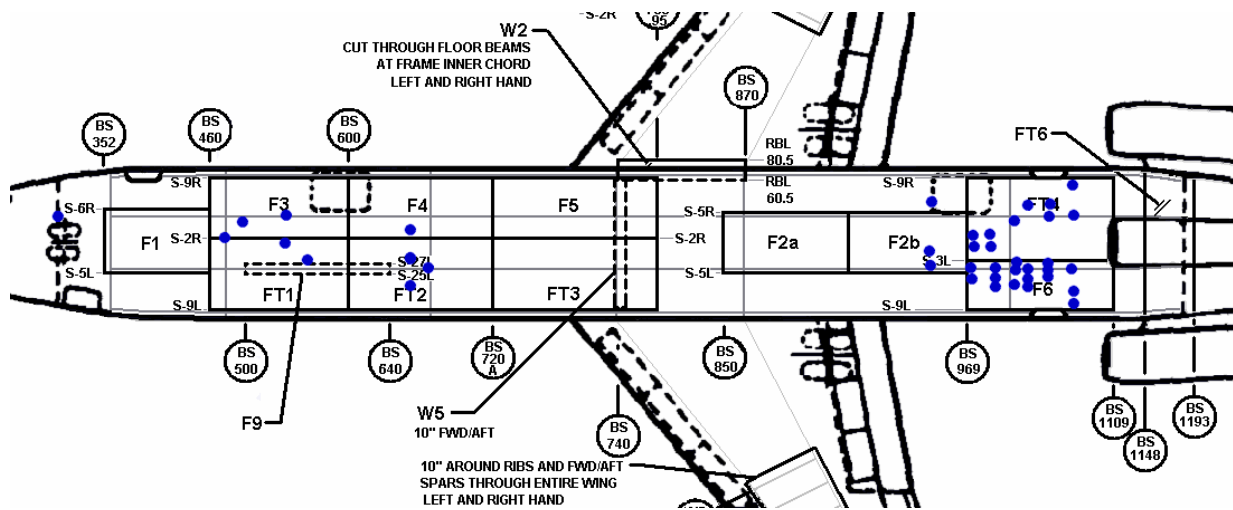


Figure 9- 18: Stringer Clip Cracks from SDR search

SHEET	9-27	NO.	4-087051-20
TOTAL	9-35		
ISSUE DATE	12/22/04		

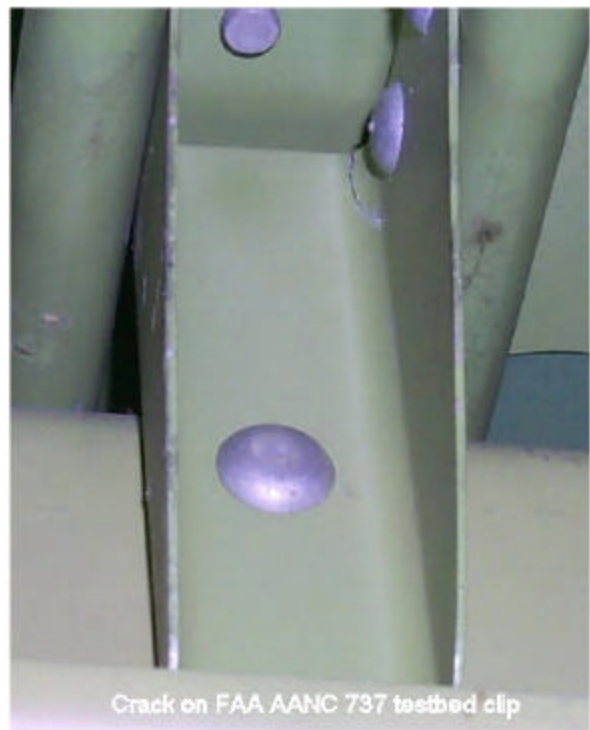


Figure 9- 19: Comparison, FASTER clips to 737

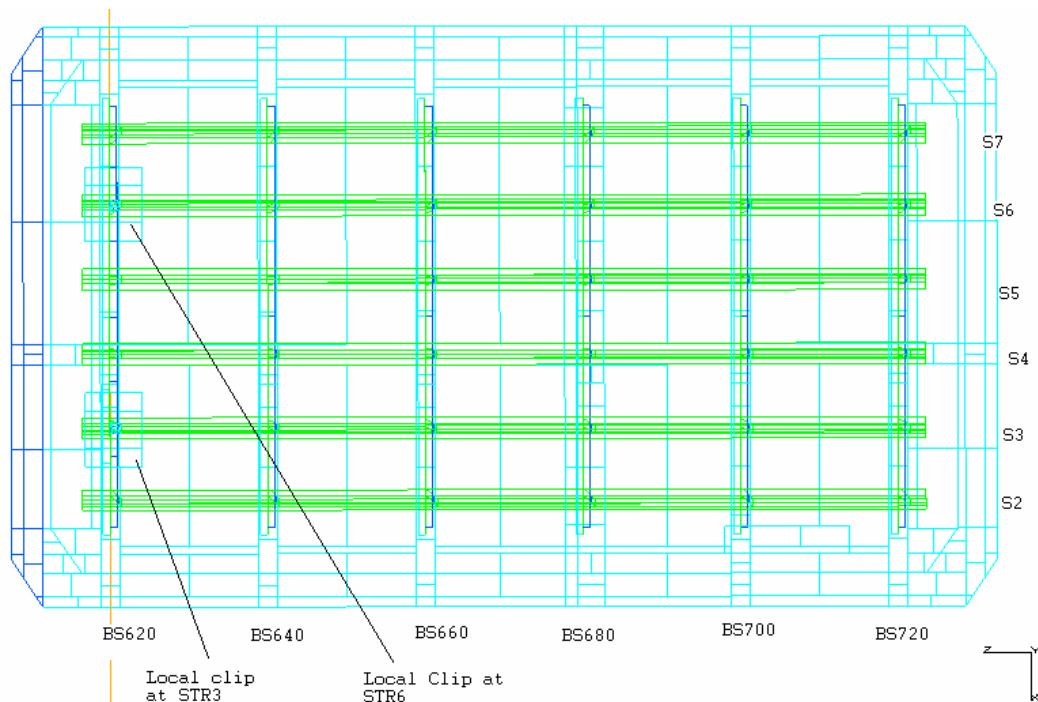


Figure 9- 20: Global FT2 model

SHEET	9-28	NO.	4-087051-20
TOTAL	9-35		
ISSUE DATE	12/22/04		

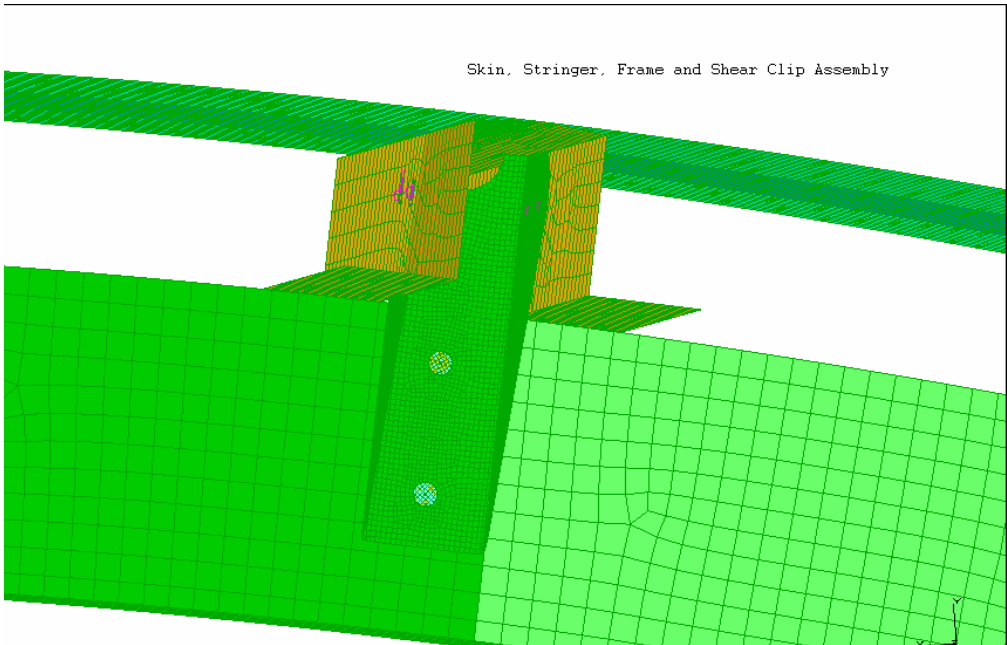


Figure 9- 21: Local Clip Model (Location on the global model can be varied)

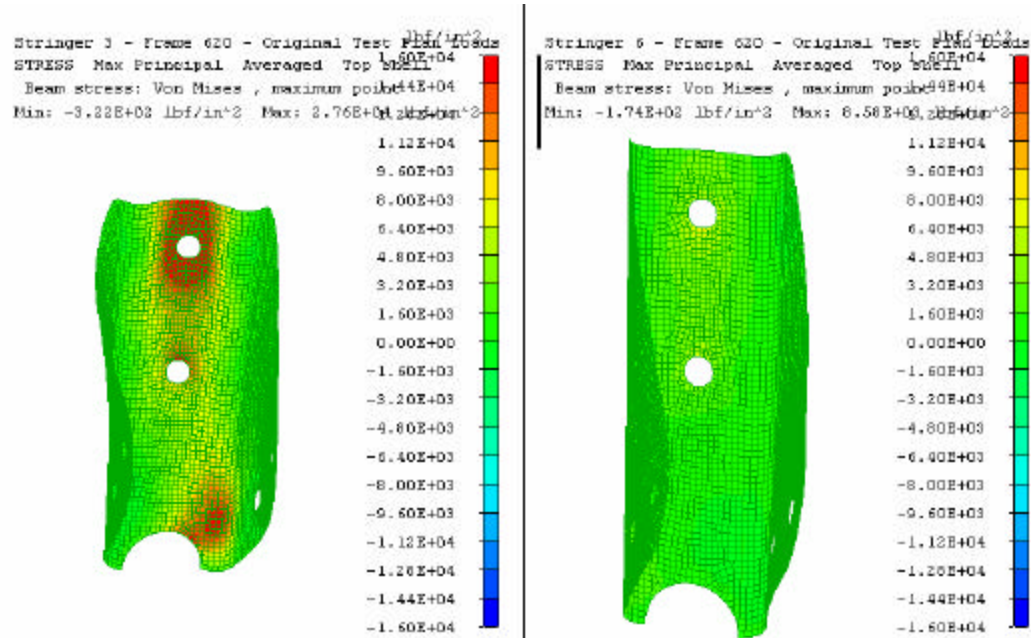


Figure 9- 22: Frame 620 (Original Test Plan Loads), Maximum Principal Stress

SHEET	9-29	NO.	4-087051-20
TOTAL	9-35		
ISSUE DATE	12/22/04		

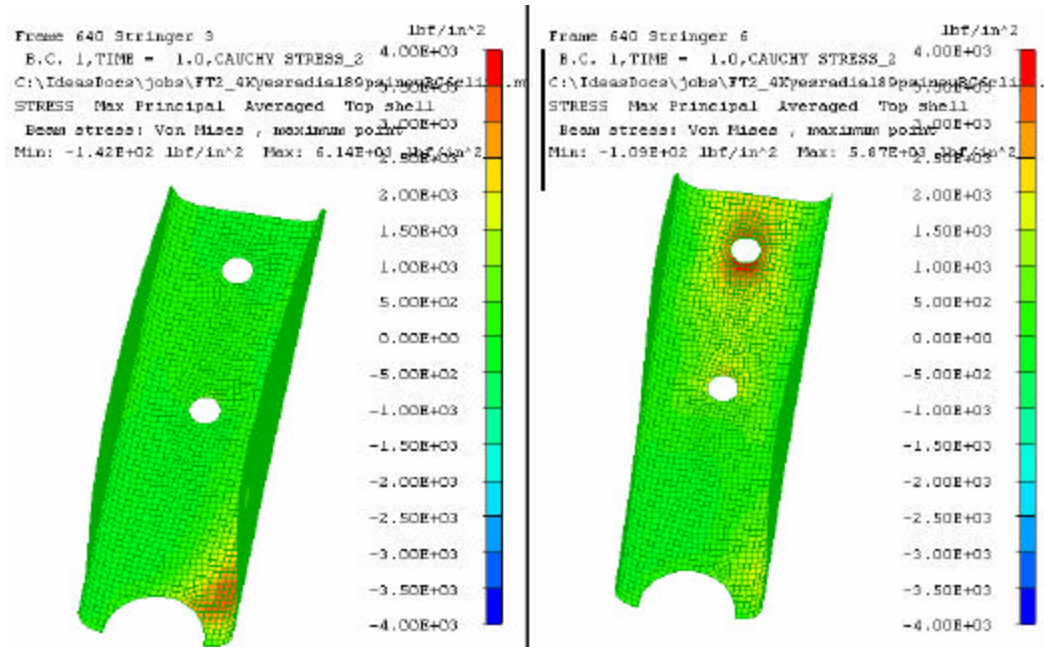


Figure 9- 23: Frame 640 (Original Test Plan Loads), Maximum Principal Stress

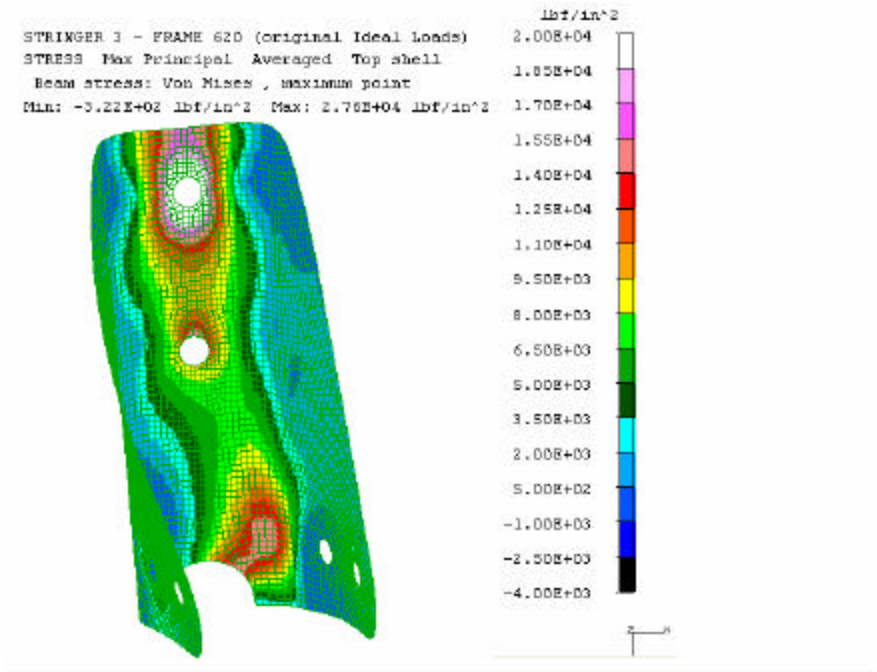


Figure 9- 24: Maximum principal Stress at Worst Location (STA 620/STR 3) - Original Test Plan Loads

SHEET	9-30	NO.	4-087051-20
TOTAL	9-35		
ISSUE DATE	12/22/04		

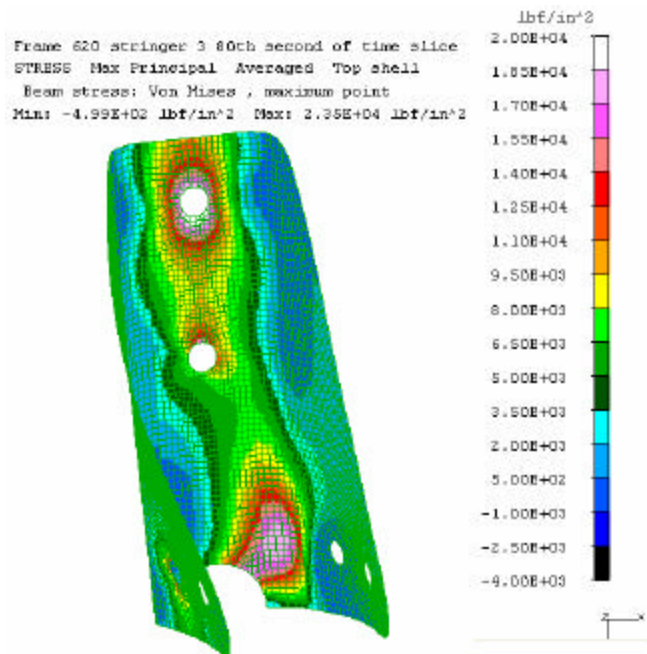


Figure 9- 25: Maximum Principal Stress at Worst Location (STA 620/STR 3) at time Max P-

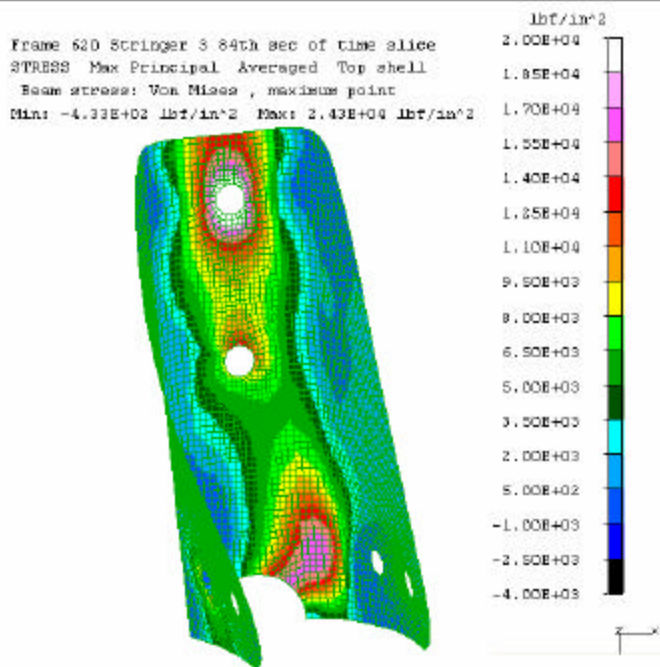
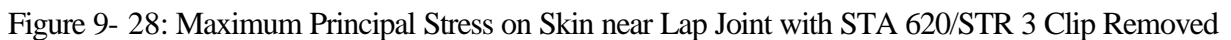
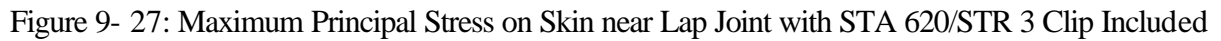


Figure 9- 26: Maximum Principal Stress at Worst Location (STA 620/STR 3) at time Max P+



SHEET	9-32	NO.	4-087051-20
TOTAL	9-35		
ISSUE DATE	12/22/04		

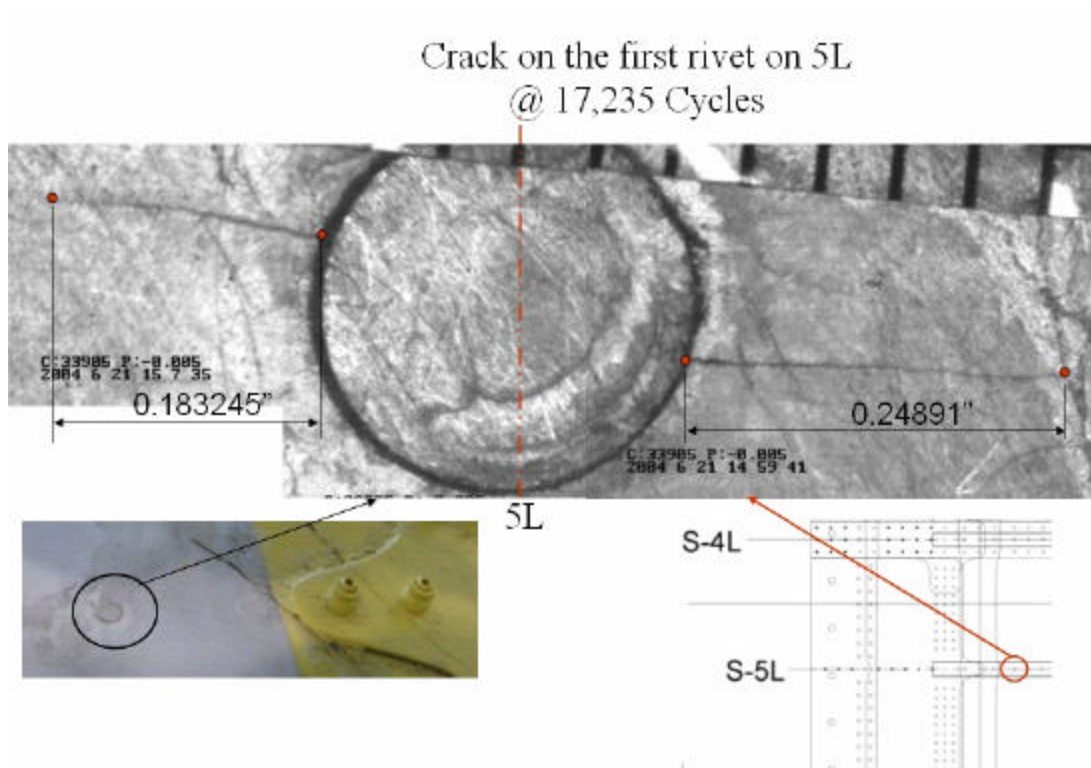


Figure 9-29: FT2 Crack at Stringer 5L and BS 622.6

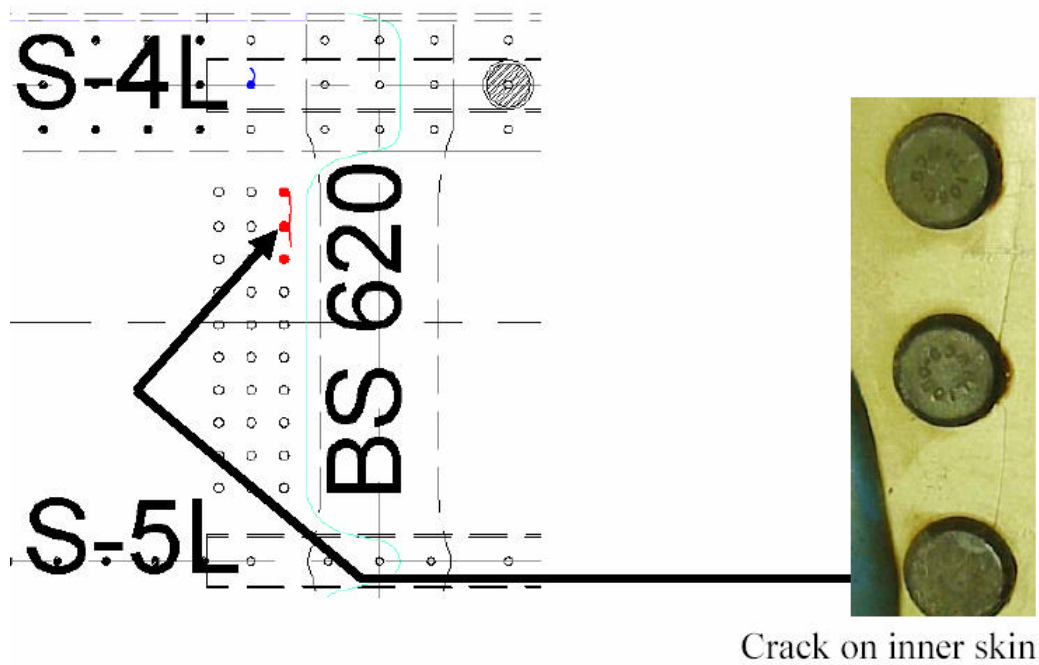


Figure 9- 30: FT2 Cracking at Doubler Edge

SHEET	9-33	NO.	4-087051-20
TOTAL	9-35		
ISSUE DATE	12/22/04		

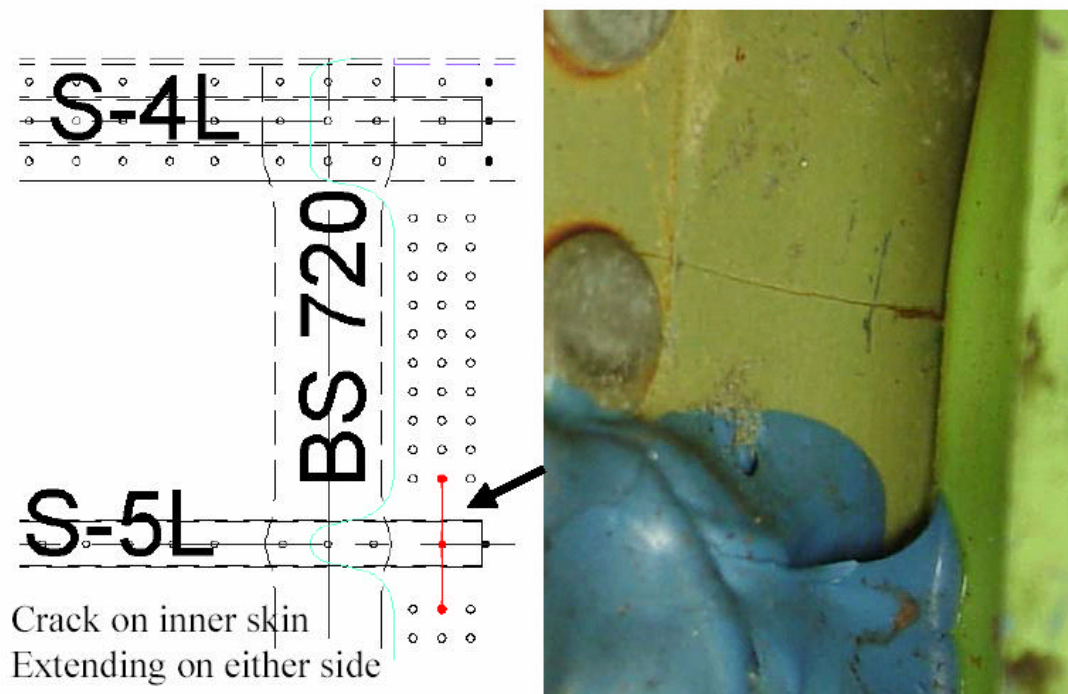


Figure 9- 31: FT2 Cracking at Stringer Run Out

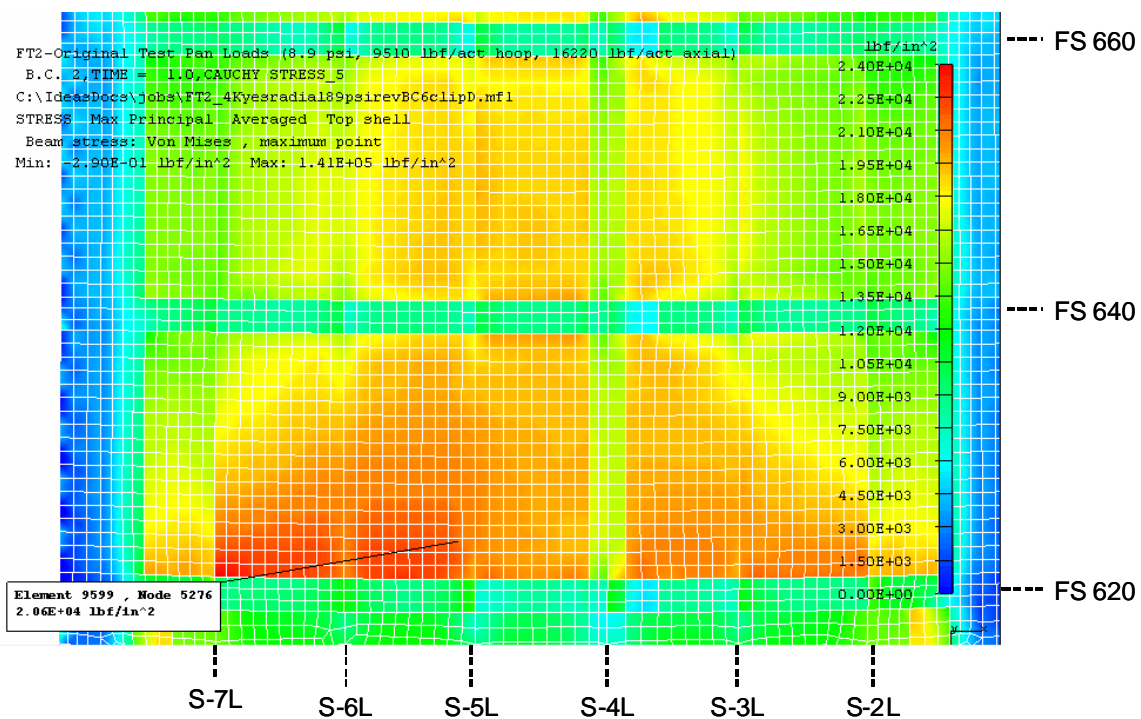


Figure 9- 32: FEA Results at FT2 Crack Finding

SHEET	9-34	NO.	4-087051-20
TOTAL	9-35		
ISSUE DATE	12/22/04		

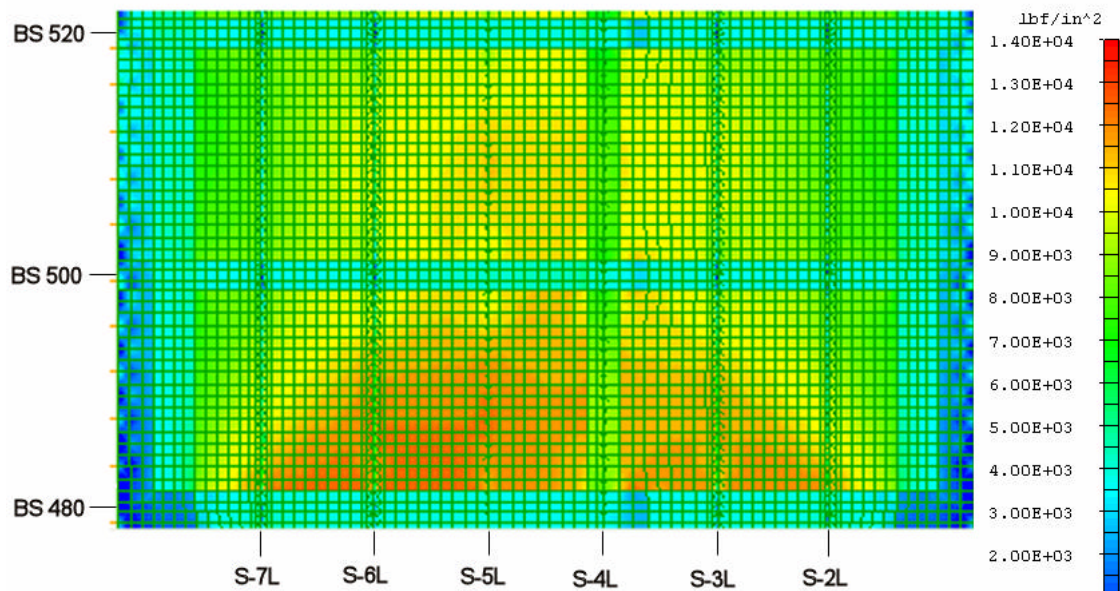


Figure 9- 33: FT 1 FEA Results at FT2 Crack Findings

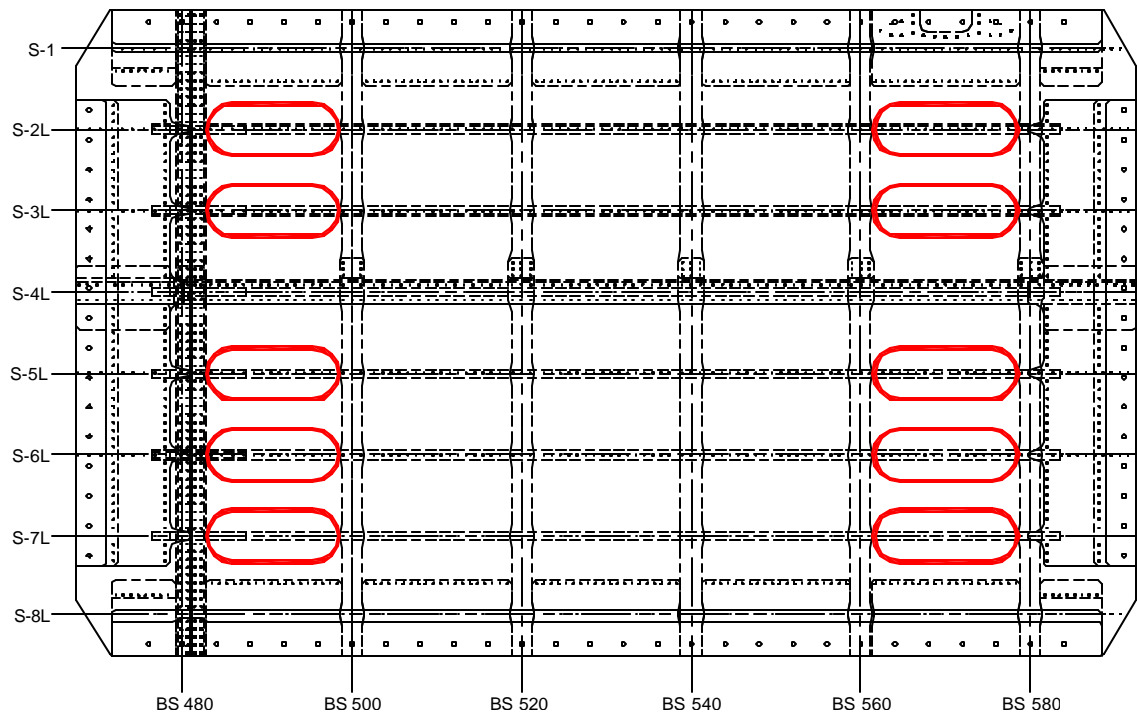


Figure 9- 34: Fastener Hole Rework Locations to Prevent Skin Cracking

SHEET	9-35	NO.	4-087051-20
TOTAL	9-35		
ISSUE DATE	12/22/04		

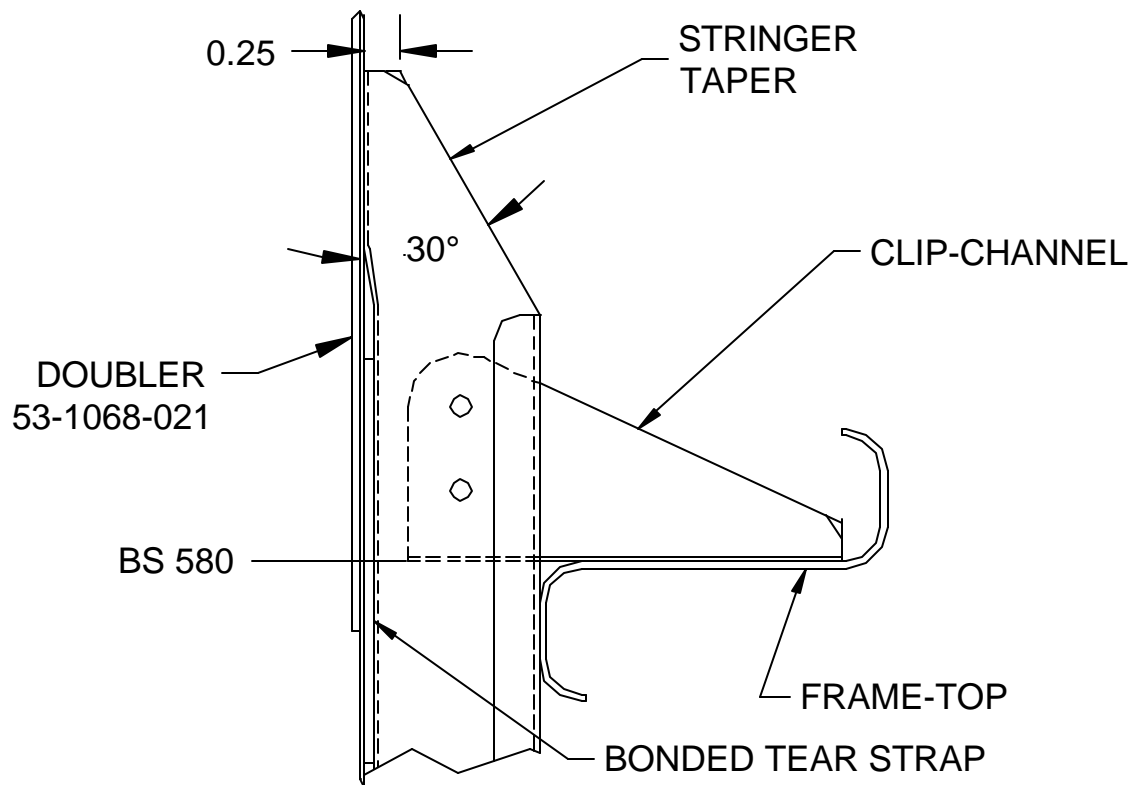


Figure 9- 35: Stringer Rework to Prevent Skin Cracking

SHEET	A-1	NO.	4-087051-20
TOTAL	A-23		
ISSUE DATE		10/08/04	

APPENDIX A: INITIATION MODELS LITERATURE REVIEW

A Review of Published Literature on Initial Damage Scenariios And Initiation

Equivalent Initial Flaw Size	1
Improved Stochastic Approach.....	13
Eijkhout's Model.....	14
R.P. Wei's Corrosion Fatigue Model	19

EQUIVALENT INITIAL FLAW SIZE

Aircraft structure components have flaw or crack like defects from inherent material differences and from processes. Table 1 shows the possible flaws induced by different processing. The crack-initiating flaws may be either extrinsic or intrinsic. Extrinsic flaws can be machining marks, surface scratches, nicks, etc., and intrinsic flaws are microstructural inhomogeneities such as inclusions, slip bands, incomplete fusion, heat affected zone, microporosity, and grain boundaries. Thus, the initial flaw quality of an aircraft alloy is very important to the fatigue life of the structural components. Initial flaws of a high quality structure are not detectable. The flaws can promote crack initiation sites. However, not all flaws are propagated from an initial defect. For these reasons, the Equivalent Initial Flaw Size (EIFS) concept was introduced 30 years ago.^{1,2,3,4,5,6} It is being developed as an analytical method to account for the initial quality of structural details in the durability analysis. Since the 70's Air Force has investigated EIFS approach.⁷ Boeing also has conducted EIFS project.⁸ From October 1997 to June 2000 the Federal Aviation Administration's (FAA) Widespread Fatigue Damage (WFD) Evaluation program⁹ had conducted an EIFS Testing and Analysis program at the Air Force Research Laboratory, Air Vehicles Directorate, Structures Division, Analytical Structural Mechanics Brach. FAA William J. Hughes Technical Center has been investigating EIFS approach to the curved panel configuration [11]

SHEET	A-2	NO.	4-087051-20
TOTAL	A-23		
ISSUE DATE	10/08/04		

Table 1: Processing induced flaws.

Processes	Flaw Type
Casting or forging	inclusions, porosity
Welding	incomplete fusion, heat affected zone
Machining quality	surface finish, stress concentrators
Heat treatment	quench rate, temper embrittlement, decarburizing
Stress relief	straightening, residual stress
Machining after heat treatment	hole drilling, grinding, untempered martensite
Plating	hydrogen embrittlement, poor adhesion, coating flaws
Assembly	residual stresses, eccentric loads, interference fasteners, fretting

The EIFS characterizes the initial fatigue quality of a durability of a critical component. Generally there are two concepts for making life predictions for aircraft structural reliability problems. There are (1) the distribution of time-to-crack initiation (TTCI) and (2) the EIFS distribution (Johnson, 1977). The period of crack initiation or the time to crack initiation (TTCI) is defined as the time in cycles or flights or flight hours it takes for a non detectable crack from the beginning of fatigue loading to grow to a reference crack size. The crack initiation distribution is physically observable and can be derived from the results obtained using coupon experimental data, full-scale experimental data, teardown data, and aircraft in-service data. In some instances, the TTCI period makes up a large proportion of the crack growth life of a structural component and this is especially the case for jet engine discs components. The reference-crack size is commonly selected on the basis of a detectable crack by the NDI. The Equivalent Initial Flaw Size is computerized from the terminal crack size by conducting the crack growth analysis backwards. The terminal crack size can be determined from coupon experimental data (such as fractographic data or S-N data), full-scale experimental data, tear-down data, and aircraft in-service data. In a similar way, the time of growth to minimum inspection size from time zero can also be determined.

The assumption for this model is that crack growth follows the power law:

$$da/dN = C(\Delta K)^n \quad (1)$$

where da/dN is the crack growth per cycle. C and n are material constants. ΔK is the stress intensity range.

Integrating the above equation yield:

SHEET	A-3	NO.	4-087051-20
TOTAL	A-23		
ISSUE DATE	10/08/04		

$$a = \left[c^* (1 - n^*) (t - t_i) + a_i^{(1-n^*)} \right]^{\frac{1}{1-n^*}} \quad (2)$$

Where t_i is the time to crack initiation and a_i is the crack length at crack initiation equal to minimum inspection size, C^* and n^* are material constants.

Johnson et al applied Weibull distributions to fit the times to crack initiation and to initial flaw sizes.

$$F_{t_i}(x) = 1 - \exp \left[- \left(\frac{x - x_0}{b - x_0} \right)^a \right] \quad (3)$$

$$F_{t_i}(x) = 0 \quad \text{for } x < 0 \quad (4a)$$

$$F_{t_i}(x) = 1 - \exp \left[- \left(\frac{-x_0}{b - x_0} \right)^a \right] \quad \text{for } x = 0 \quad (4b)$$

$$F_{t_i}(x) = 1 - \exp \left[- \left(\frac{x - x_0}{b - x_0} \right)^a \right] \quad \text{for } x > 0 \quad (4c)$$

$$f_{t_i}(x) = \frac{h}{\sqrt{2p}} \frac{l}{(x - e)(l - x + e)} \exp \left\{ - \frac{1}{2} \left[g + h \ln \left(\frac{x - e}{l - x + e} \right) \right]^2 \right\} \quad (5)$$

$$h = \frac{Z_{1-a} - Z_a}{\ln \left[\frac{(x_{1-a} - e)(e + l - x_a)}{(x_a - e)(e + l - x_{1-a})} \right]} \quad (6)$$

$$g = Z_{1-a} - h \ln \left(\frac{x_{1-a} - e}{e + b - x_{1-a}} \right) \quad (7)$$

Where γ and η are shape parameters, ε is scale parameter, λ is scale parameter, Z_a is the standard normal variate for a 100th percentile and Z_{1-a} is the standard normal variate for (1-a)100th percentile, x_a is the a percentile of data and x_{1-a} is the (1-a) percentile of data. $A=1\%$ to 2% was used in most cases. The distribution is bounded by ε and $\varepsilon + \lambda$. Once ε , λ , γ , and η is calculated for each set of data, the Johnson distribution function can be find by integrating the density function, equation(3).

The probability failure is

SHEET	A-4	NO.	4-087051-20
TOTAL	A-23		
ISSUE DATE	10/08/04		

$$F_T(t) = \int_0^{\infty} \left[1 - e^{-\left(\frac{y-x_0 l}{bl - x_0 l} \right)^a} \right] \frac{(lt)^y e^{-lt}}{\Gamma(y+1)} dy \quad (8)$$

where $y=\lambda x$, $dy=\lambda dx$, $\Gamma(\bullet)$ is the gamma function.

The relation between the TTCI distribution and EIFS distribution is shown in Figure 1. Yang et al has demonstrated this existence of compatibility between the TTCI distribution function and EIFS distribution function for the Weibull and the lognormal distributions. The power crack growth law, refer to equation (1), transforms the TTCI distribution function back to the y-axis at zero time to produce a compatible EIFS distribution.

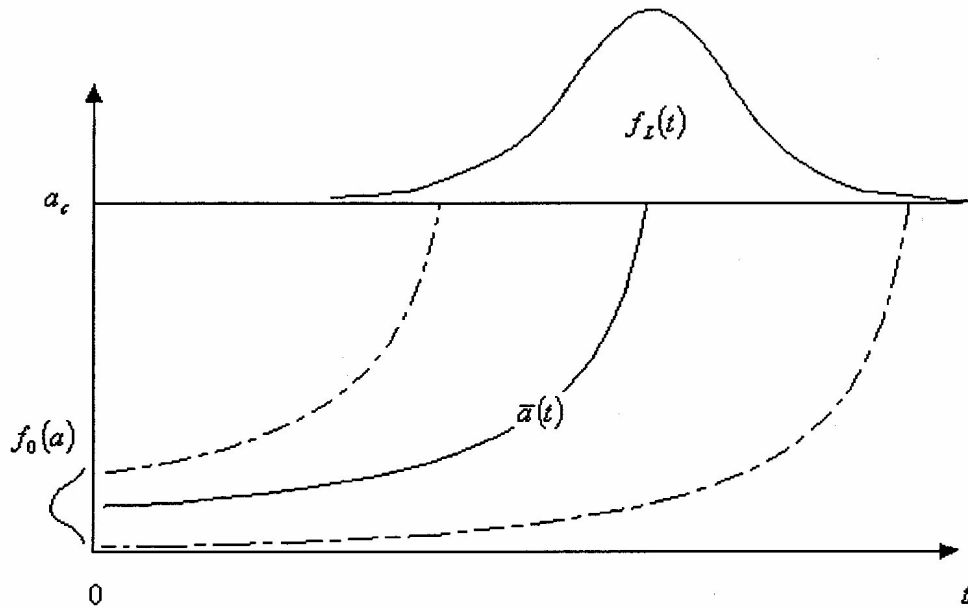


Figure 1: The relationship between TTCI and EIFS distribution.

The advantage of the TTCI is that test data can be obtained using coupon specimen and full-scale component. Also, TTCI values are physically observable for given crack sizes. But crack initiation time is a function of many variables, such as, stress level, loading spectra, and manufacturing processes, etc.

The EIFS distribution back-calculated from fatigue life has been shown to correlate well with actual flaw size measurements. The benefit of this approach is that the fatigue life data, which are test dependent,

SHEET	A-5	NO.	4-087051-20
TOTAL	A-23		
ISSUE DATE		10/08/04	

are transposed to an EIFS which is independent of specimen size, stress level and spectrum. This, however, still need to be proven. In addition, the EIFS calculations are prone to compounding errors in the crack growth analysis due to the changing stress intensity factor solutions and stress fields as the crack gets longer (Fawaz). Aircraft tear down project will provide an effective approach to verify the EIFS concept and the distribution in a physically meaningful manner. Many study indicated that Weibull distribution fitted particular well to the tail of the large crack size data found in teardown inspections and maintenance inspections.

Numerous investigators have studied and measured EIFS for aircraft materials. The available EIFS values are summarized in Table 2.

SHEET	A-6	NO.	4-087051-20
TOTAL	A-23		
ISSUE DATE	10/08/04		

Table 2. EIFS values from different investigators.

Sample	EIFS (inch)	References
2024-T3 non-corroded	$>1 \times 10^{-6}$ and $<1 \times 10^{-4}$	Liao and Xiong
2024-T3 corroded	1×10^{-4}	Liao and Xiong
Alcoa 7050-T7451	5.7×10^{-3}	Magnusen, Hinkle, Kaiser, Bucci, and Rolf ¹⁰
2024-T3	2.4×10^{-4}	Newman, Philips, Swain ¹¹ , Newman [¹²]
7075-T6	2.4×10^{-4}	Newman, Philips, Swain
2024-T3	$(5.0 \pm 0.9) \times 10^{-4}$ $(8.3 \pm 4.3) \times 10^{-4}$	S.A. Fawaz
2024-T3	3.3×10^{-4}	Falugi, Tuegel, Brooks, ¹³
2024-T3	2.6×10^{-3}	Brooks, Prost-Domasky, Honeycutt ¹⁴
7075-T6	2.6×10^{-3}	Brooks, Prost-Domasky, Honeycutt
7075?	4.3×10^{-3}	Johnson, Heller, and Yang
7075?	5.0×10^{-3}	Johnson, Heller, and Yang
2024-T3 clad	2.0×10^{-3}	Harris, Piascik, Newman [26]

Lincoln¹⁵ fitted the crack size distribution from the B-707 tear down inspection data using a Weibull distribution. Only the large cracks are used to fit the Weibull distribution. Because large cracks contribute more to the failure. Similar work was performed again by Lincoln in a structural risk assessment on USAF trainer aircraft. Inspection data were fitted by both the lognormal and Weibull distributions. Results show that Weibull distribution fit data better than the lognormal distribution.

Yang et al have proposed a mechanistic-based analysis methodology for determining the EIFS distribution for any given critical location, based on limited experimental test results, such as S-N data. This methodology take into account the size (volume) effect so that the EIFS distribution for different critical locations can be established from test results using different specimen sizes and geometries. High stress regions (determined by high stress gradient) have a significant effect on EIFS. The stress gradient effect has been accounted for in the analysis methodology so that test results from smooth specimens can be used to determine the EIFS distributions at notches. This technique is extremely useful for EIFS distribution estimation when detail experimental data are not available.

Newman, Philips, and Swain et al pointed out that small crack growth is controlled by metallurgical features. Small cracks nucleated at inclusion particles or voids, in regions of intense slip, or at weak

SHEET	A-7	NO.	4-087051-20
TOTAL	A-23		
ISSUE DATE		10/08/04	

interfaces and grains. Local grain orientation can influence crack growth too. In their study, aluminum alloy 2024-T3 and 7075-T6's initial flaw size is assumed to be 2.4×10^{-4} inch with an area equal to the average inclusion-particle sizes. In another report, Harris, Piascik, and Newman selected the normal thickness of the clad as the EIFS size, 2.0×10^{-3} inch. Because they found that the majority of fatigue cracks initiated by a fretting damage located in the faying surface clad from the results of the detailed destructive examination. They also noticed that an EIFS of 3.90×10^{-3} inch reasonably predicts the life of the lap joint that exhibited much greater fretting damage and cracks that initiated earlier in life. The 2.4×10^{-4} -inch EIFS results in a prediction that substantially over predicts the total fatigue life of the fuselage lap joint. According to Harris, small crack initiation and growth is a three-dimensional process with cracks growing in the depth and length directions interacting with the grain boundaries at different times in their cyclic history. Whereas a crack growing in the length direction may have decelerated at or near a grain boundary, the crack depth may still be growing. As the crack grows in the depth direction, the rise in the crack-driving force contributes to the crack penetrating that barrier. As the cracks become longer, the influence of the grain boundaries become less as the crack front begins to average behavior over more grains.

M. Falugi, E. Tuegel, C. Brooks, R. Bee and D. Shelton proposed an interesting methodology that is known as Discontinuity State Evolution Process (DSEP). DSEP use an Initial Discontinuity State concept to characterize the as-produced or as-manufactured condition of the material in order to establish the initial analysis condition. An ECLIPSE lap splice model was established to account for the interactions of all of the effects and considers actual physical changes in the lap splice. An Initial Discontinuity State distribution grows (including short crack considerations) under the effects of cyclic mechanisms and time-dependent mechanisms such as thickness loss, pillowling, pitting, roughness or topography, and multisite damage. The holistic analysis used by ECLIPSE predicts the elapsed time and elapsed cycles (based on a specified aircraft utilization frequency) from the as-manufactured pristine condition until a time when the component can no longer acceptably remain in service.

Kurth et al applied EIFS approach to the curved panel configuration to predict the initiation, growth, first link-up and residual strength of the curved panel test. It was found that similar configuration flat panel EIFS behavior was different from test to test. It was explained by the differences in the 3-

SHEET	A-8	NO.	4-087051-20
TOTAL	A-23		
ISSUE DATE		10/08/04	

dimensional growth behavior of the cracks depending on where they initiated. It was also pointed out that it will work better with either the assumption that EIFS does not appear until some life has been used or the assumption that a new fatigue law or new material constants control the initiation stage.

Various computer software¹⁶ have been developed for fatigue life estimation using EIFS methodologies, refer to Table 3.

SHEET	A-9	NO.	4-087051-20
TOTAL	A-23		
ISSUE DATE	10/08/04		

Table 3: Available EIFS software.

Software	Organization	References
PROF	U.S. Air Force	Berens, West, and Trego ¹⁷
NERF	Defense Science and Technology Organization	Graham, Mallinson, and Tong ¹⁸
FEBREL	The Boeing Company	Torng and Edwards ¹⁹
PROMISS	Martec	Orisamolu, Lou and Lichodziejewski ²⁰
NESSUS	Southwest Research Institute	Southwest Research Institute ²¹
PRISM	Bombardier Aerospace, Inc., contract from National Research Council of Canada	Forges ²²
FASTRAN III	NASA Langley Research Center	Fawaz, Harris ²³ , Newman ²⁴
AFGROW	Air Force Research Laboratory	Fawaz
ECLIPSE	Air Force, APES, Lockheed	Falugi, Tuegel, Brooks, Bell and Shelton

Test Methodology: Data from aircraft full-scale fatigue test and teardown can be applied for model validation. For coupon samples any increasing ΔK fatigue test can be applied for testing. Air Force Research Laboratory use flat wide panel for EIFS measurement. The testing panels are based on fuselage splice joint designs that have been used in commercial aircraft for many years. The four types of configuration chosen are:

- two longitudinal lap-splice joints
- one longitudinal butt splice joint
- one circumferential butt splice joint

The strain gage wires can be connected to the data collection system. The rotating self-nulling eddy current probe system can be applied for crack detection and measurement. Traveling optical microscope can measure through-thickness cracks. A linear voltage displacement transducer can be applied for the quantities measurement in the specimen width direction such as crack length. Optical microscope and scanning electron microscope (SEM) can be applied for fractography examination. Details refer to the report by Fawaz.

SHEET	A-10	NO.	4-087051-20
TOTAL	A-23		
ISSUE DATE	10/08/04		

Matrix of EIFS options

The methodology to determine EIFS can be classified by a collection of analysis options:

1) Data Points Per Crack

- a) Single Length Point, typically from service inspection results. A single EFIS value is calculated from back-counting, so many cracks are needed to determine distribution.
- b) Multiple Length Points, either from marker bands on the fracture surface or measurement during testing. Allows for regression on EFIS to fit data.
- c) Multiple Rate Points, typically from striation count measurements on the fracture surface.

2) Integration Method (for Multiple Rate Points only)

- a) Point to Point
- b) Linear Fit (Paris)
- c) Bi-Linear Fit (Small and Long Crack Paris)
- d) $\beta(a)$ – LEFM function of length and/or stress state
- e) Non-parametric curve fit that is not based on fracture mechanics

3) Applied Loads

- a) Known loads, either constant or variable amplitude, applied during testing
- b) Unknown loads from service, modeled as constant amplitude.
- c) Unknown loads from service, modeled as variable amplitude,

4) Assumed Stress State

- a) 1 Parameter, typically far field stress (σ)
- b) 2-3 Parameters, such as far field stress plus bearing (σ_{brg}) and/or bending stress (σ_{bend})
- c) Higher Parameter Load Cases, including shear, tearing, clamp-up (out-of-plane preload), interference (in-plane pre-load)

5) Geometric β -factors and Crack Parameters

- a) Constant
- b) Function of crack length (1 Parameter) or length and depth (2 Parameter) and stress state

Table 4 contains this classification for a selection of published EIFS methodologies.

SHEET	A-11	NO.	4-087051-20
TOTAL	A-23		
ISSUE DATE	10/08/04		

Table 4: Matrix of EIFS Options

	Data Points per Crack	Applied Load Amplitudes	Stress State Parameters	Geometry and Crack Parameters
Johnson, Heller, and Yang, 1977 ¹	1 Length Inspections in service	Unknown, Modeled Constant	1 σ	Constant geometry factor, 1 Thru
Rudd, 1977 ⁶	1 Length Measurements after test	Known Variable	2 σ, σ_{brg}	Shape and retardation constants for each crack 1 Thru
	Multiple Rate Paris Integration	Known Variable	2 σ, σ_{brg}	1 Thru
Piasecik and Willard, 1998 ²⁵	Multiple Length Marker bands in testing	Known Constant	2 σ, σ_{bend}	$\beta(a)$, 1-2-1 Cir. Corner/Corner/Thru
Harris, Piasecik, and Newman, 1999 ²⁶	Multiple Length Marker bands in testing	Known Constant	3 $\sigma, \sigma_{bend}, \sigma_{brg}$	$\beta(a)$, 1-2-1 Cir. Corner/Corner/Thru
Fawaz, 2000 ⁹	Multiple Length Marker bands in testing	Known Constant	3 $\sigma, \sigma_{bend}, \sigma_{brg}$	$\beta(a)$, 1-2 Cir. Corner/Oblique Thru

SHEET	A-12	NO.	4-087051-20
TOTAL	A-23		
ISSUE DATE		10/08/04	

Lessons learned: The crack initiation generated from Air Force Research Laboratory and other investigators may not represent the real situation for the crack initiation of aircraft structures. Because the fatigue testing spectrum designed is clipped and truncated and may not represent the in-service aircraft loading conditions. The EIFS calculations are prone to compounding errors in the crack growth analysis due to the changing stress intensity factor solutions and stress fields as the crack gets longer.

Equivalent Initial Flaw Size is the most promising approach to determine the crack initiation. An EIFS database can be established based on the full-scale fatigue testing. Eijkhout model, corrosion fatigue model, and Monte Carlo method are also useful for crack initiation study. The published initial fatigue crack initiation size for Al 2024-T3 ranges from 1×10^{-6} to 2.6×10^{-3} inch. The available (in the open literature) initial crack size for Al 7075-T6 ranges from 2.4×10^{-4} to 5×10^{-3} inch.

SHEET	A-13	NO.	4-087051-20
TOTAL	A-23		
ISSUE DATE		10/08/04	

IMPROVED STOCHASTIC APPROACH

This approach²⁷ is similar to EIFS. It proceeds a backward calculation from a failure distribution function till a reference crack length. The reference crack length is determined by the inspection method used or a value which is regarded as sufficiently small without reducing the strength and safe operation of the component. From the resulting distribution function at this reference crack size, which is a function of time, the initial inspection time is derived based on a certain percentage of time, since cracks of these sizes are present in the structure. In this way the crack initiation phase is accounted for in a natural way.

SHEET	A-14	NO.	4-087051-20
TOTAL	A-23		
ISSUE DATE	10/08/04		

EIJKHOUT'S MODEL

Eijkhout^{28,47} established an empirical model to estimate early MSD fatigue behavior from lap splice fractography examination. A schematic of the model is shown in Figure 2 and Figure 3.

This model was based on the following observations:

- MSD fatigue cracks tend to initiate at several sites near or at rivet hole corners, and grow in directions varying gradually from transverse (through-thickness) to longitudinal.
- The transverse crack growth rates are nearly constant
- The transverse and longitudinal crack growth rates are similar for cracks smaller than twice the sheet thickness.

The assumptions for this model are:

- Constant crack growth rate in the transverse direction, in general equal to the initial crack growth rate in the longitudinal direction

$$dc/dN = A e^{B a_i} \quad (9)$$

where c is the crack length in the transverse direction, N is cycle, a_i is the initiation length.

- Crack depth $c=0$ at a_i , the “initiation length.”
- Quarter-circular crack fronts in the transition from transverse to longitudinal crack growth, and growth rate is

$$da/dN = A e^{B a} \quad (10)$$

where a is the crack length in the longitudinal direction.

Integrating both side of Equation (10)

$$\int_{N_i}^{N_f} dN = \int_{a_i}^{a_f} \frac{1}{A} e^{-B a} da \quad (11)$$

$$N_f - N_i = \frac{1}{AB} (e^{-B a_i} - e^{-B a_f}) \quad (12)$$

SHEET	A-15	NO.	4-087051-20
TOTAL	A-23		
ISSUE DATE	10/08/04		

$$a_i = -\frac{1}{B} \ln \left[e^{-Ba_f} + AB(N_f - N_i) \right] \quad (13)$$

$$a_{\text{int}} = -\frac{1}{B} \ln \left[e^{-Ba_i} - AB(N_{\text{int}} - N_i) \right] \quad (14)$$

$$c_{\text{int}} = (N_{\text{int}} - N_i) A e^{Ba_i} \quad (15)$$

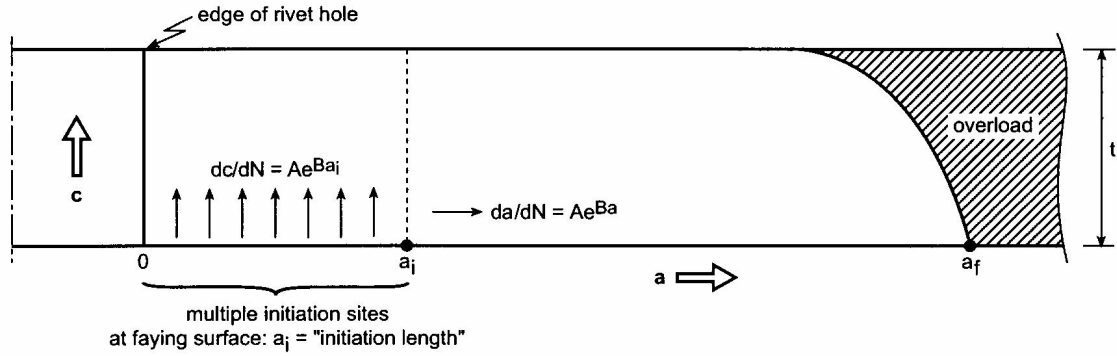
where N_f and N_i are, respectively, the length of fatigue initial and the length of final failure, a_{int} and c_{int} are, respectively, the intermediate crack size in the longitudinal direction and in the transverse direction.

Since the model estimates the fatigue initiation lives and the through-thickness life, it is useful for making in-service NDT inspection program. The model can be made compatible with marker bands on the fatigue fracture surfaces of full-scale test articles. When determining the striation-based crack growth rate equations, $da/dN = Ae^{Ba}$, for individual cracks one can check the equations' compatibility with the distances between marker bands, adjusting the equations if necessary.

Lessons learned: Since the model is empirical, the parameters in the model have to be determined for each type of lap splice geometry, each type of surface treatment, and each type of aircraft, and also- possibly - for fuselage areas where the design stress levels are significantly different, e.g. varying by more than 10% from the average. In case dc/dN is not constant and crack initiated at rivet hole corners, one has to be careful about the application of this model.

SHEET	A-16	NO.	4-087051-20
TOTAL	A-23		
ISSUE DATE	10/08/04		

From fractographic observations and striation spacings:



- a_i , a_f and N_f are known. Calculate N_i from: $N_f - N_i = \frac{1}{AB} (e^{-Ba_i} - e^{-Ba_f})$
- Calculate intermediate values of a for given values of n : $a_{int} = -\frac{1}{B} \ln [e^{-Ba_i} - AB(N_{int} - N_i)]$
- For each a_{int} calculate c_{int} from: $c_{int} = (N_{int} - N_i) Ae^{Ba_i}$
- Construct crack fronts as follows:

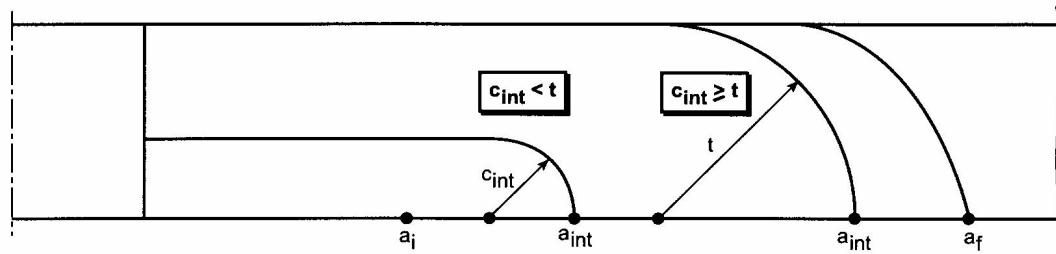


Figure 2: Eijkhout's empirical model illustrated for a non-countersunk sheet and multiple fatigue initiation sites.

SHEET	A-17	NO.	4-087051-20
TOTAL	A-23		
ISSUE DATE	10/08/04		

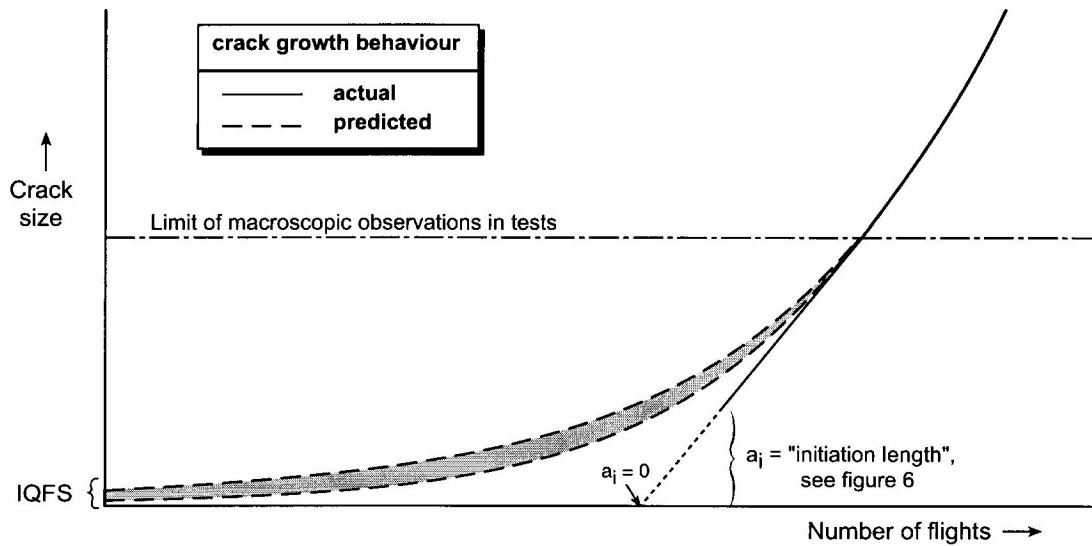


Figure 3: Schematic of differences between actual and predicted early crack growth behavior in transport aircraft fuselage longitudinal lap splices: the predictions are fitted to the macroscopic observations and the IQFS values are obtained from actual manufacturing flaws or by back-extrapolation using a macroscopic crack growth model.

SHEET	A-18	NO.	4-087051-20
TOTAL	A-23		
ISSUE DATE		10/08/04	

PITTING CORROSION MODELS

According to Lincoln²⁹, hidden corrosion is a major concern for continuing structural integrity. Hidden corrosion is the undetected corrosion after inspection. The amount of hidden corrosion is dependent of the NDT equipment and NDT personnel skills. Pitting corrosion may accelerate the onset of widespread fatigue damage. Experiments with specimens exhibiting pitting corrosion show that cracks appear much faster than otherwise expected. R.Wei et al. developed a predictive model for pitting corrosion.

Fatigue cracks will initiate earlier and grow faster in moist and other corrosive environment. Moisture promote pitting and intergranular corrosion, thereby creating stress concentrations. Faying surfaces and rivet/hole interfaces promote this type of attack through the mechanisms of crevice corrosion. Darvish³⁰ et al studied fatigue crack growth in the environments of high and low humidity. The material studied is 7075 alloy. It was found that cyclic condensation caused the formation of periodic beach marks on the fracture surface at low and medium stress intensities in the high strength 7075 alloys. The increase in the humidity can affect the crack growth rate and may also cause a local change in crack growth direction.

Since the early 1970s, corrosion has been recognized as one of the dominant factors in the inspection and maintenance activities of airline operations. Extensive resources have been devoted to the development of corrosion prevention and control by Boeing, Air Force, etc.

SHEET	A-19	NO.	4-087051-20
TOTAL	A-23		
ISSUE DATE		10/08/04	

R.P. WEI'S CORROSION FATIGUE MODEL

It is reported that constituent particles in the alloys contributed to pitting corrosion.^{31, 32} There are two types of particles: one containing Al, Cu and Mg, and the other, Al, Cu, Mn and Fe. The Al-Cu-Mg-Fe-containing particles acted as cathodes and the Al-Cu-Mg-containing particles acted as anodes. The interactions between the particles, and between the particles and the matrix, result in the nucleation of pits. The growth and coalescence of pits, in depth and in breadth, led to the formation of large corrosion pits, from which corrosion fatigue cracks nucleate. The transition from pit to corrosion fatigue crack growth is determined not only by the need to overcome the threshold K value for fatigue crack growth, but also by the competition between pit and fatigue crack growth rates.

A simplified mechanically based probability model³³ was used for estimating the probability of occurrence of damage in aircraft materials subjected to localized (pitting) corrosion and corrosion fatigue crack growth. Probability of occurrence as a function of pit size was measured in this study. Fatigue cracks are most likely nucleated at sites of localized corrosion (pits), and grow in competition with (crevice) corrosion. Pits are assumed to be hemispherical throughout and grow at a constant volumetric rate. The pit depth a , up to the transition size a_r at which a crack initiates, is given by

$$a = \left[\left(\frac{3MI_{p_0}}{2\rho nF} \right) \exp\left(-\frac{\Delta H}{RT}\right)t + a_0^3 \right]^{1/3}; a \leq a_r \quad (16)$$

where M is the molecular weight of the material; n is the valence; F is Faraday's constant; ρ is the density; ΔH is the activation enthalpy; R is the universal gas constant; T is the absolute temperature of the ambient temperature; I_{p_0} is the pre-exponential term in the Arrhenius relationship for the pitting current; a_0 is the initial pit radius; and t is the time required for a pit to develop to a depth of a . a_0 and I_{p_0} are assumed to be random variables. For aluminum, the different parameters are:

SHEET	A-20	NO.	4-087051-20
TOTAL	A-23		
ISSUE DATE	10/08/04		

Table 5. Parameters for Wei's Model.⁹⁹

Parameter	Aluminum
Density, ρ (g/m ³)	2.7×10^6
Molecular weight, M	27
Valence, n	3
Activation Energy, ΔH (kJ/mol)	40
Temperature, T (K)	293
Crack growth exponent, nc	3.55
Effective stress, $\Delta \sigma$ (MPa)	100
Stress concentration factor, K_t	2.8
Frequency, f (cycle/day)	10
Radius of hole, r_0 (mm)	3

Statistical variability is modeled³⁴ through I_{po} , a_0 , C_c , and ΔK_{th} , which are chosen to be mechanistically and statistically independent of time. a_0 reflects material and manufacturing quality. Variability associated with the influences of material properties and environmental factors on the resistance to fatigue crack growth is reflected in C_c , and ΔK_{th} . I_{po} , the pitting current generated from electrochemical reactions for pit growth. The three-parameter Weibull cumulative distribution function is used to characterize random variables.

$$F(x) = 1 - \exp \left\{ - \left[\frac{x - g}{b} \right]^a \right\}, \quad x \geq \gamma \quad (17)$$

where x is the test value, γ is the location parameter, β is the scale parameter, and α is the shape parameter.

The statistical estimation for I_{po} was based primarily on laboratory data obtained from pitting corrosion experiments conducted for 384 h.³⁵ The mean and coefficient of variation (cv) for the three-parameter Weibull cdf for 2024-T3 aluminum alloy are reported to be:¹⁰³

SHEET	A-21	NO.	4-087051-20
TOTAL	A-23		
ISSUE DATE	10/08/04		

Table 6. Random variables published by Wei et al.³⁶

Random variable	The Mean	cv (%)
Initial pit radius a_0 (m)	4.8×10^{-6}	100
Fatigue coefficient C_c (m/cyc)/(MPa \sqrt{m})	6.2×10^{-11}	32
Pitting current constant I_{po} (A)	9.5×10^{-3}	220
Threshold driving force ΔK_{th} (MPa \sqrt{m})	2.3	50

ρ , M , n , ΔH , T (K), I_{po} , and a_0 are known parameters based on Table 13 and Table 14,. Thus Equation (16) becomes:

$$a^3 = 9.2 \times 10^{-11} t[in^3][day^{-1}] + 6.7 \times 10^{-12} [in^3] \quad (17)$$

It is evident that Wei's model can be calibrated and validated if corrosion fatigue cracks are identified and the cracking history is known.

Lessons Learned: I_{po} , the pitting current generated from electrochemical reactions for pit growth, has the most uncertainty because of the complexity of the process, the difficulty in measurements, and the lack of the actual environmental history.

SHEET	A-22	NO.	4-087051-20
TOTAL	A-23		
ISSUE DATE	10/08/04		

REFERENCES

- ¹ W.S. Johnson, R.A. Heller, and J.N. Yang, "Flight Inspection Data and Crack Initiation Times," Proceedings 1977 Annual Reliability and Maintainability Symposium, 1977.
- ² J. Rudd and T. Gray, "Equivalent Initial Quality Method," AFFDL-TM-76-83-FBE, 1976.
- ³ D.W. Hoepfner, and W.E. Krupp, "Prediction of Component Life by Application of Fatigue Crack Growth Knowledge," Engineering Fracture Mechanics, 1974, P.47-70.
- ⁴ J.N. Yang and W.J. Trapp, "Joint Aircraft Loading/Structures Response Statistics of Time to Service Crack Initiation," J. Aircraft, AIAA, Vol. 13, No.4, 1976, pp. 270-278.
- ⁵ H.A. Wood, R.M. Engle, J. Gallagher, and J.M. Potter, "Current Practice on Estimating Crack Growth Damage Accumulation with Specific Application to Structural Safety, Durability and Reliability," Air Force Flight Dynamic Lab., AFDL-TR-75-32, WPAFB, 1976.
- ⁶ J.L. Rudd, "Applications of Equivalent Initial Quality Method," AFFDL-TM-77-58-FBE, July 1977.
- ⁷ J. Rudd and T. Gray, "Equivalent Initial Quality Method," AFFDL-TM-76-83-FBE, 1976.
- ⁸ J. Yu, "Equivalent Initial Flaw Size Study Test Plan," The Boeing Company, USA, 1997.
- ⁹ S.A. Fawaz, "Equivalent Initial Flaw Size Testing and Analysis," AFRL-VA-WP-TR-2000-3024, 2001
- ¹⁰ P.E. Magnusen, A.J. Hinkle, W.T. Kaiser, R.J. Bucci, and R.L. Rolf, "Durability assessment based on initial material quality," Journal of Testing and Evaluation, 18, No.6, (1990) 439-445.
- ¹¹ J.C. Newman Jr., E.P. Philips, M.H. Swain, "Fatigue-life prediction methodology using small-crack theory," International Journal of Fatigue 21 (1999)109-119
- ¹² J.C. Newman, Jr., "Advances in Fatigue and Fracture Mechanics Analyses for Metallic Aircraft Structures," NASA/TM-2000-210084.
- ¹³ M. Falugi, E. Tuegel, C. Brooks, R. Bee and D. Shelton, " A comparison of the corrosion/fatigue effects on sealed and unsealed longitudinal fuselage splices" *Proceedings of the 5 th Joint DoD/FAA/NASA Conference on Aging Aircraft, 2001.*
- ¹⁴ C. Brooks, S. Prost-Domasky, and K. Honeycutt, " Determining the initial quality state for materials," ASIP 1998.
- ¹⁵ J.W. Lincoln, "Aging Aircraft-USAF Experiences and Action," Proceedings of the 19th Symposium of the International Committee on Aeronautical Fatigue, Edinburgh Scotland, June 1997.
- ¹⁶ M.Liao and Y. Xiong, "Risk Analysis of Fuselage Splices Containing Multisite Damage and Corrosion," Journal of Aircraft, 38, No.1, 2001, P.181-187.
- ¹⁷ A.P. Berens, J.D. West, and A. Trego, " Risk Assessment of Fatigue in Corroded Lap Joints," Fatigue in the Presence of Corrosion, Proceedings of the Research and Technology Organization of North Atlantic Treaty Organization Meeting Proceedings 18, Neuilly-Sur-Seine Cedex, France, 1998, pp.21-1-21-10.
- ¹⁸ D. Graham, G.D. Mallinson, and C. Tong, "NERF-A Tool for Aircraft Structural Risk Analysis," Proceedings of the International Conference on Application of Statistics and Probability, Dec.1999, pp.1175-1190.
- ¹⁹ T.Y. Torng and R.M. Edwards, "Comparing B-1B Wing Carry Through Inspection Requirements as Defined by Deterministic and Probabilistic Approaches," Proceedings of 1998 USAF Aircraft Structural Integrity Program Conference, 1998.

SHEET	A-23	NO.	4-087051-20
TOTAL	A-23		
ISSUE DATE		10/08/04	

²⁰ I.R. Orisamolu, X. Lou, and M. Lichodziejewski, "Development of Probabilistic Optimal Strategies for Inspection/Monitoring/Maintenance/Repair and Life Extension," Martec, Ltd. Halifax, Canada, TR SRV-6-00251, 1999.

²¹ "Probabilistic Analysis and Design," 9th Annual Short Course Notes, Southwest Research Institute, San Antonio, TX, 1998.

²² S.A. Forges, "PRISM User's Guide," Report RAZ-DSD-101, Bombardier Aerospace, Inc., Montreal, Canada. Defense Services, 1997.

²³ C. E. Harris, "Recent Fracture Mechanics Results from NASA Research Related to the Aging Commercial Transport Fleet," AGARD (Advisory Group For Aerospace Research & Development) - CP-506, Fatigue Management, Bath, United Kingdom 29th April to 3rd of May 1991.

²⁴ J.C. Newman, Jr. "FASTRAN-II - A Fatigue Crack Growth Structural Analysis Program, NASA TM-104159," February 1999.

²⁵ R.S. Piascik and S.A. Willard, "The Growth of Multi-Site Fatigue Damage in Fuselage Lap Joints," Proceedings of the 2nd NASA/FAA/DoD Conference on Aging Aircraft, 1998.

²⁶ C.E. Harris, R.S. Piascik, and J.C. Newman, "A Practical Engineering Approach to Predicting Fatigue Crack Growth in Riveted Lap Joints", International Conference on Aeronautical Fatigue (ICAF), 1999.

²⁷ F.P. Grooteman, H.H. Ottens, and H.J. ten Hoeve, "Stochastic fatigue analysis of an F-16 forward engine mount support fitting," NLR-TP-2001-275

²⁸ M.T. Eijkhout, "Fractographic analysis of longitudinal fuselage lap joint at stringer 4 of Fokker 100 full scale test article TA15 after 126250 simulated flights," Fokker Report RT2160, Amsterdam: Fokker Aircraft Ltd., 1994.

²⁹ J.W. Lincoln, "Corrosion and Fatigue: Safety Issue or Economic Issue," Fatigue in the Presence of Corrosion Research and Technology Organization Meeting Proceedings 18, Corfu, Greece, 7-9 October 1998

³⁰ M. Darvish and S. Johansson, "Cyclic Change in Humidity of the Environment during Fatigue Crack Propagation and Its Effect on Fracture Surface Appearance," Scandinavian Journal of Metallurgy 21, p68-77, 1992.

³¹ G.S. Chen, M.Gao, D.G. Harlow and R.P. Wei, "Corrosion and Corrosion Fatigue of Airframe Aluminum Alloys," C.E. Harris editor. FAA/NASA International Symposium on Advanced Structural Integrity Methods for Airframe Durability and Damage Tolerance. P.157-173, 1994.

³² C. Liao, G.S. Chen, and R.P. Wei, "A technique for studying the 3-dimensional shape of corrosion pits," Scripta Materialia, 35, No.11, pp.1341-1346, 1996.

³³ D.G. Harlow and R.P. Wei, "Probabilities of occurrence and detection of damage in airframe materials," Fatigue Fract Engng Mater Struct 22, 427-436, 1999.

³⁴ D.G. Harlow and R.P. Wei, "Materials Ageing and Structural Reliability," Int. J. Materials & Product Technology, 14, No.4/5, 2001, P.304-316

³⁵ E.J. Dolley, B. Lee and R.P. Wei, "The effect of pitting on fatigue life," Fatigue Fracture Engineering Materials Structure 23, 555-560, 2000.

³⁶ D.G. Harlow and R.P. Wei, "Probability modeling and statistical analysis of damage in the lower wing skins of two retired B-707 aircraft," Fatigue Fract Engng Mater Struct 24, 523-535, 2001.

SHEET	B-1	NO.	4-087051-20
TOTAL	B-18		
ISSUE DATE		10/08/04	

APPENDIX B: STRESS INTENSITY FACTOR LITERATURE REVIEW

A Review of Published Literature on Stress Intensity Factors and Crack Propagation.

Introduction.....	1
Stage 1: Multiple Small Cracks	1
Stage 2: Irregular Crack Shape	5
Stage 3: Regular Crack Shape	7
Stage 4: Starburst Crack Shape	9
Stage 5: Periodic MSD without Interaction.....	9
Stage 6: Asymmetric MSD with Interaction.....	11
References.....	13

INTRODUCTION

The purpose of this review is to collect the published literature that have particular relevance to the analysis of MSD/MED propagation in a fuselage lap joint. Damage Characterization of the cracks from N474DA has led to identification of six stages of crack growth, as shown in Figure 1. These stages provide the organization for this review.

Stage 1: Multiple Small Cracks

In this stage, the cracks are small compared to the plastic zone size at the crack tip, and of similar or smaller scale to the surrounding micro-structure. For Al 2024-T3, the local grain microstructure is on the order of $20\mu\text{m} - 40\mu\text{m}$ ($\sim 0.001'' - 0.002''$). Cracks less than $100\mu\text{m}$ ($\sim 0.004''$) are considered "physically small". This regime is classic small crack regime as discussed by Lankford[1], Miller[2], and Suresh and Ritchie[3], and is noted for:

- Crack shape and local microstructure are influential in growth or arrest
- Crack growth can be faster than predicted by long-crack models
- Growth threshold low to non-existent (compared to long crack threshold)

SHEET	B-2	NO.	4-087051-20
TOTAL	B-18		
ISSUE DATE		10/08/04	

- Consistent use of continuum mechanics to long crack growth is difficult. However, Newman et al. [4] have reported success with long crack equations in this regime provided that an effective stress intensity value (ΔK_{eff}) accounting for crack closure is used.

Lukáš and Kunz [5] provide a contemporary overview of the current state of the art in small crack nucleation and growth. According to the authors, despite the development of a large number of crack initiation models over the past fifty years, there are no quantitative descriptions of the interaction behavior between flaws just at the point of nucleation. In fact, the authors conclude that even the qualitative prediction of whether a given interaction is shielding or amplifying has not been developed for a general case. However, as microcracks propagate to the point where they are no longer micro-structurally small, analysis based on linear or elastic-plastic fracture mechanics quickly becomes applicable even for mechanically small cracks.

Murakami and Endo [6] discuss effect of small flaws on fatigue resistance. This work built upon the earlier work by Murakami [16] and the use of $\sqrt{\text{area}}$ as a geometric parameter for complex crack shapes (see discussion in following section). For 3D cracks or flaws, *area* is defined as the area of the fracture surface projected onto a plane normal to the maximum principal stress. Based on experimental results, Murakami and Endo derive the relationship for the threshold stress intensity for surface defects:

$$\Delta K_{\text{th}} = 3.3 \times 10^{-3} (H_v + 120) (\sqrt{\text{area}})^{2/3},$$

where H_v is the Vickers hardness of the material. Cracks with stress intensities below ΔK_{th} will remain non-propagating flaws.

TerMaath [7] determined the stress field on a plane containing multiple complex, interacting cracks through simultaneous solution of superimposed traction-free conditions. For metals, this solution is particularly applicable to a surface with a large number of micro-cracks in the earliest stages of crack initiation.

SHEET	B-3	NO.	4-087051-20
TOTAL	B-18		
ISSUE DATE		10/08/04	

Brezensek and Hancock [8] address the re-characterization of multiple complex flaws as a simple idealization. The authors perform FEA to determine SIF and T stress values along the crack front of two coalesced surface cracks, and conclude that the SIF in reentrant area is significantly elevated. Several possible geometries of coalescence are examined: co-planar cracks, non-coplanar with a distinct shear step, and overlapping non-coplanar cracks which coalesce away from the free surface. For these cases, the authors conclude that the current re-characterization guidelines in use in pipe and pressure vessel industry (see Refs [9] and [10]) are conservative for fatigue growth and ductile tearing calculations. Analytically, the presence of a shear step between cracks significantly decreased the Mode I (opening) SIF while increasing the Mode 3 (tearing) SIF, but experiments showed not significant effect to the crack growth rate of the re-entrant crack section. Based on experiments and analysis, the authors conclude that interaction effects are only significant when the crack tip spacing between two adjacent cracks is less than one half the depth of the deepest defect. Continuing their analysis into Ref [11], the authors conclude that while the current re-characterization guidelines are conservative for fatigue growth and ductile tearing, they may be unconservative in some cases for cleavage failure.

Newman et. al [4] used a simple interaction criteria for small crack growth. In their work, the objective was to discard experimental growth rate data from cracks under an interacting influence. Therefore, data was discarded from cracks during interaction as defined by the criteria in Figure 3. This procedure discards data from the time of first interaction to the time when the final coalesced crack has become stable.

Carpinteri et al. [12] conducted a parametric numerical study to investigate the interaction between two adjacent surface flaws of equal size in a finite width plate. Consistent with lap joint results [44], the authors conclude that there is no appreciable crack interaction if the distance between crack fronts is twice the total crack length. Interaction at a given spacing is highest for deeper cracks, and the influence of the aspect ratio on the interaction increases as the relative crack depth increases.

ENGINEERING DEPARTMENT

SHEET	B-4	NO.	4-087051-20
TOTAL	B-18		
ISSUE DATE		10/08/04	

SHEET	B-5	NO.	4-087051-20
TOTAL	B-18		
ISSUE DATE		10/08/04	

Stage 2: Irregular Crack Shape

Mastrojannis et. al [13] use numerical solution of an integral equation formulation to determine the stress field associated with square and triangular embedded cracks. These numerical solutions were used subsequently as a baseline for comparison with approximate solutions in Ref's [16] and [18].

Gao and Rice [14] investigate the stability of perturbations from an almost elliptical embedded crack. Stability is defined such that a stable crack will grow back into its original configuration after some perturbation, such as crack front “trapping” from a micro-level heterogeneity analyzed by the same authors[15]. Gao and Rice develop a critical wavelength below which perturbations will decrease, and show that, for circular cracks, any possible first-order perturbation is below that wavelength. Therefore, any circular crack under tensile loading will tend to return to a circular shape even as it transits micro-scale obstacles. While this work was oriented towards stable quasi-static fracture, the conclusions are valid for fatigue crack growth as well. It is generally accepted [3] that the physics of a crack’s interaction with impeding obstacles such as grain boundaries is an important driver in small crack behavior.

Murakami and Nemat-Nassar [16] develop a stress intensity solution for an arbitrary crack shape by discretizing the crack into triangular sub-regions. The stress intensity for the entire crack is found through numerical integration over each of the triangular sub-regions. Murakami uses this approach to model the coalescence of two adjacent elliptical flaws to evaluate the stability of the coalesced crack. In addition, he models a number of arbitrary shapes to find an approximate solution valid for all of them. The conclusion is that the maximum stress intensity of a surface crack can be approximated with reasonable accuracy by

$$K_{\text{Imax}} \cong 0.629 \sigma_0 \sqrt{\pi \sqrt{\text{area}}}$$

where "area" is the effective area of the fracture surface. Murakami considers this approximation valid for any convex crack shape with a aspect ratio less than 5. Noda [17]

SHEET	B-6	NO.	4-087051-20
TOTAL	B-18		
ISSUE DATE		10/08/04	

used an integral equation method to extend this approximation to shear and tearing modes (note that π is absent from Noda's published equation):

$$K_{II \max} \cong 0.55 \tau_{yz} \sqrt{\sqrt{\text{area}}}$$

$$K_{III \max} \cong 0.45 \tau_{yz} \sqrt{\sqrt{\text{area}}}$$

Cox and Morris[18] develop an approximate solution for the stress intensity anywhere along the crack front of an arbitrarily shaped 2D crack. The approximation was developed to be used in Monte Carlo analysis, and therefore trades reduced accuracy for the computational efficiency needed to perform a large number of calculations.

Hwang and Ingraffea [19] describe the current state of the art in numerical analysis of crack growth. Software exists to model the propagation of an arbitrary-shaped flaw within a complex 3-dimensional solid (e.g., FRANC3D combined with FEA[20]). The resolution of the analysis is primarily limited by computational resources. For example, the fracture simulation shown in Figure 4 produced a detailed model of crack propagation in a complex 3-dimensional body that correlated well with service findings. However, the simulation required approximately 200 computation hours on a 2.4 GHz, 128 processor PC cluster, a very large computational expense.

SHEET	B-7	NO.	4-087051-20
TOTAL	B-18		
ISSUE DATE		10/08/04	

Stage 3: Regular Crack Shape

The stress intensity solutions such as Newman and Raju [21] are the baseline equations for fracture mechanics analysis in industry. These semi-empirical fits to numerical analysis were the core of the early fracture mechanics codes for personal computers such as NASA FLAGRO [22] and USAF MODGRO (to become AFGROW [26]). These codes were reasonably small and written in FORTRAN or BASIC, so a compact equation that could be solved within a subroutine was necessary. As computational abilities of personal computers improved, interpolation of a stress intensity value from a very large table such as in Fawaz [25] also became acceptable.

Gosz and Moran [23] determined K_I for small cracks growing from an open countersunk hole under remote tension. After a baseline comparison to simple elliptical cracks for which FEA solutions were available, a series of analysis was accomplished using the domain integral method. All analysis was conducted for one non-dimensional countersink geometry, in that h/t , R/t , and d/t remain constant (see Figure 5). Analyses were conducted for a series of crack lengths, beginning with a small elliptical crack at the knee of the countersink, and ending with a through crack beyond the countersunk region. The results of this report are a collection of tabulated Boundary Correction Factors for cracks of varying length and aspect ratio.

In a typical lap joint, Fawaz [24] applies a Virtual Crack Closure Technique (VCCT) FEAM to find stress intensity formula for through cracks with elliptical crack fronts. Because of the relatively large magnitude of secondary bending in a lap joint, corner crack propagation typically leads to elliptical through cracks which are significantly longer on the faying surface than on the exposed skin surface. Fawaz models these oblique crack fronts as an elliptical front with a minor axis (crack depth) longer than the skin thickness. Using a series of VCCT-FEAM analyses, Fawaz [25] tabulates the stress intensity along the elliptical crack front at several a/c ratios for remote tension, bi-axial tension, remote bending, and point, cosine and cosine² pin loads. These stress intensity tables were subsequently incorporated into the AFGROW analysis software [26] and were used in Fawaz's study of Equivalent Initial Flaw Sizes [27].

SHEET	B-8	NO.	4-087051-20
TOTAL	B-18		
ISSUE DATE		10/08/04	

Later, Fawaz and Andersson [28] conducted a hp-method FEA analysis to generate a large series of asymmetric double corner crack solutions. The hp-method increases both the element resolution and the numerical order of the FEA model; combined with a mathematical splitting scheme, this computationally efficient algorithm allowed a large number of crack geometry problems to be solved to an arbitrary precision. Fawaz and Andersson note that their result is the solution to the Bakuckas round robin problem [31], with other finite and boundary element methods correlating within 2%. Solutions by other methods were lower, and K_I per the baseline Newman and Raju solution were up to 26% lower for some geometries, particularly where the crack front intersects a free surface. Tabular solutions based on this work were also incorporated into AFGROW [26]. The solutions for symmetric and asymmetric corner cracks under remote stress were verified against experiments with Al 7075-T651 by Fawaz, Anderson, and Newman [29].

Rahman et al [30] used a global-intermediate-local FEA approach to tabulate K_I for five crack shapes in a open countersunk hole under tension, bending, and bearing loading. The depth of the countersink (h/t in Figure 5) was varied, but other non-dimensional parameters of the countersunk hole remained constant. The results of this report are a collection of tables and graphs for Boundary Correction Factors for each of the five crack lengths under each stress type and h/t ratio.

Bakuckas [31] conducted a round robin comparison of Boundary Correction Factors for a single straight shank hole geometry determined using a collection of 3D methods: FEA, domain integral, FEA alternating, boundary element, weight functions, and the semi-empirical equations from Newman and Raju [21]. All results were within a narrow, 3% band, supporting the conclusion that any of these methods are acceptable provided that good analysis practices (e.g., convergence studies) are followed.

SHEET	B-9	NO.	4-087051-20
TOTAL	B-18		
ISSUE DATE		10/08/04	

Stage 4: Starburst Crack Shape

Fastener hole starburst cracking was present in the teardown work of Piascik and Willard [32], but analysis of this type of cracking is not extensively discussed in the literature. This lack is due in part to the large number of variables, and the complex interrelationships between crack lengths, initiation locations, propagation angles, and local stress state. However, this configuration is particularly suitable for numerical analysis, such as

- VCCT (Virtual Crack Closure Technique) for 2D/3D FEA models, discussed by Krueger [33];
- FADD (Fracture Analysis by Distributed Dislocations) analysis code using 2D BEM models, partially incorporated into NASBEM/NASGRO [34] and FADD;
- Other 3D adaptive methods of Computational Fracture Mechanics (including FRANC2D, FRANC2D/L and FRANC3D) as discussed by Ingrassia [35].

Stage 5: Periodic MSD without Interaction

Harris, Piascik, and Newman [36] present an “engineering approach” to predict MSD growth in fuselage lap joints. The approach draws from the teardown of fastener holes from a fuselage lap joint with the equivalent of three DSG of pressure cycles. The authors’ approach has 5 basic components:

- 1) Global and local stress analysis, typically with a finite element model hierarchy;
- 2) Local (detail) analysis at the hole to determine the components of remote, bearing, and bending stresses. The authors report good results for bending stresses using the Hartman-Schijve equations [37], which have been extended to a three row lap joint by Fawaz[38]. The authors note that the rivets installed in the subject test article were neat fit, so a complex analysis of the potential effects of rivet interference was not required.
- 3) Stress intensity factor determination to represent the expected crack configuration. In this study, the authors’ note that the final results for a corner crack initiating at a

SHEET	B-10	NO.	4-087051-20
TOTAL	B-18		
ISSUE DATE		10/08/04	

countersink were not overly sensitive to the choice of initial crack geometry (corner or straight) or hole geometry (countersunk or straight shank). In keeping with an “engineering approach”, the authors use a simplified geometry representing a corner crack from a neat-fit straight hole in their analysis, with good results.

- 4) Fatigue analysis, including the choice of starting flaw size and crack growth rate. The authors recommend using a crack growth model incorporating crack closure (e.g., FASTRAN [39]), which allows use of an effective stress intensity throughout the analysis, even for very small cracks.
- 5) Residual strength analysis to determine the critical end state of the analysis. The authors conclude that non-linear fracture mechanics is required to satisfactorily complete this step. This requirement is in contrast with current industry recommendations [40] that suggest that the crack growth analysis can be stopped at an earlier sub-critical condition where linear mechanics is still applicable (e.g. first crack link-up at limit load) without greatly reducing the predicted total crack growth time.

SHEET	B-11	NO.	4-087051-20
TOTAL	B-18		
ISSUE DATE		10/08/04	

Stage 6: Asymmetric MSD with Interaction

Dawicke and Newman [41] developed a stress intensity solution for interfering MSD cracks of unequal length under uniaxial tension. The stress intensity factor is calculated by superpositioning a hole correction factor onto the results of an iterative solution for the interacting cracks. Stress intensity results were validated through comparison to an FEA solution, and life prediction results were validated through comparison to a series of fatigue tests.

Stefanescu [42] conducted a series of constant $\sqrt{K_I}$ experiments with asymmetric cracks within a finite width plate to determine empirical correction factors from the diametrically opposed case. The author's results are consistent with previously published [43] analytical results showing that the stress intensity at each crack tip is more than for the same length single-crack case, with the greatest increase at the longer crack. His correction factor for the primary (longest) crack is

$$F_{ecc}^p = e^{0.4298ecc},$$

where the normalized eccentricity ecc is defined as a function of the hole radius and the long (a_p) and short (a_s) crack lengths

$$ecc \equiv \frac{a_p - a_s}{r + a_p + a_s}.$$

De Rijck and Fawaz [44] use a 3D VCCT analysis similar to [24] to quantify the point where interaction between adjacent oblique (elliptical) through cracks in a fastener joint becomes significant. The authors conclude that for oblique cracks that are almost straight (i.e., $a/c \gg 1$), interaction occurs when the distance between crack tips is 50% of the fastener spacing. This conclusion is consistent with previously published [43,45] conclusions for the interaction between adjacent through cracks. However, for more shallow cracks which are typical in a bending-influenced lap joint, interaction does not occur until the distance between crack tips is as low as 20% of the fastener spacing.

SHEET	B-12	NO.	4-087051-20
TOTAL	B-18		
ISSUE DATE		10/08/04	

For an infinite series of equal length MSD, Swift [46] states that failure will occur when the net section stress between cracks exceeds the flow stress, approximately $(F_{tu} + F_{ty})/2$. For other crack arrays, the premise for Swift's model is that MSD link-up occurs when the plastic zones leading each crack tip touch. This criterion is applicable both to the initial link-up between two adjacent MSD cracks with little surrounding damage, and to a lead crack propagating through existing MSD. Swift uses the Irwin model for plastic zone size, in which the plastic zone radius varies linearly with the square root of K_I / normal stress. Collins and Cartwright [47] built upon previous work by Dugdale[48], Tada[49], and Theocaris[50] to determine the plastic zone sizes at all tips of asymmetric, interacting cracks as a non-linear function of the normal stress/yield stress. As with Swift, crack link-up occurs when the two inner plastic zones coalesce.

More complex criteria for MSD crack link-up have also been proposed. Broek [51] proposed an empirical equation for the link-up stress as a function of the crack geometry and material collapse stress based on the Foster-Miller [52] testing of 20 inch panels with MSD. Based on the same test data plus additional STAGS analysis, Ingram et al [53] proposed an updated engineering approach resulting in a transition factor response surface fit from a least squares minimization. Smith et al. [54] revised the Broek criteria such that it is a function of yield stress values available from accepted industry sources (e.g., Mil-Hdbk-5, MMPDS)

SHEET	B-13	NO.	4-087051-20
TOTAL	B-18		
ISSUE DATE	10/08/04		

REFERENCES

- 1 J. Lankford, "The Growth Of Small Fatigue Cracks In 7075-T6 Aluminum", Fatigue Of Engineering Materials And Structures, Vol. 5, No 3, pp 233-248, 1982.
- 2 K. J. Miller, "The Short Crack Problem", Fatigue Of Engineering Materials And Structures, Vol. 5, No 3, pp 223-232, 1982.
- 3 S. Suresh And R. O. Ritchie, "Propagation of Short Fatigue Cracks," International Metals Review, Vol. 29, No. 6, pp 445 – 475, 1984.
- 4 J. C. Newman, Jr., X. R. Wu, S. L. Venneri, and C. G. Li, "Small-Crack Effects In High-Strength Aluminum Alloys", NASA Reference Publication 1309, May 1994.
- 5 P. Lukáš and L. Kunz, "Small Cracks—Nucleation, Growth And Implication To Fatigue Life", International Journal of Fatigue Volume 25, Issues 9-11 , September-November 2003, Pages 855-862.
- 6 Y. Murakami and M. Endo, "The $\sqrt{\text{area}}$ Parameter Model For Small Defects And Nonmetallic Inclusions In Fatigue Strength: Experimental Evidences And Applications," Theoretical Concepts And Numerical Analysis Of Fatigue, Editors: A. F. Blom and C. J. Beevers, 1992.
- 7 S. TerMaath, "An Analytical Technique For Determining Multiple Site Damage propagation", presented at the 7th Joint DoD/FAA/NASA Conference on Aging Aircraft, 2003.
- 8 B. Bezensek, and J. W. Hancock, "The Re-Characterisation Of Complex Defects - Part I: Fatigue And Ductile Tearing "Engineering Fracture Mechanics Volume 71, Issues 7-8 , May 2004, Pages 981-1000.
- 9 BS 7910 "Guidelines On Methods For Assessing The Acceptability Of Flaws In Metallic Structures", British Standard Institution, Chpt 7, London, 1999.
- 10 R6, "Assessment Of The Integrity Of Structures Containing Defects", Revision 4, Chpts I and II.3, British Energy Generation, Ltd, Gloucester, 2001.
- 11 B. Bezensek, , 1 and J. W. Hancock , "The Re-Characterisation Of Complex Defects - Part II: Cleavage", Engineering Fracture Mechanics Volume 71, Issues 7-8 , May 2004, Pages 1001-1019.
- 12 A. Carpinteri, R. Brighenti and S. Vantadori, "A Numerical Analysis On The Interaction Of Twin Coplanar Flaws", Engineering Fracture Mechanics Volume 71, Issues 4-6 , March-April 2004, Pages 485-499.
- 13 E. N. Mastrojannis, L. M. Keer, and T. Mura, "Stress intensity factor for a plane crack under normal pressure", International Journal of Fracture, Vol 15, pp 247-258, 1979.

SHEET	B-14	NO.	4-087051-20
TOTAL	B-18		
ISSUE DATE	10/08/04		

- 14 H. Gao And J. Rice, "Somewhat Circular Tensile Cracks", International Journal Of Fracture, Vol. 33, pp. 155-174, 1987.
- 15 H. Gao And J. Rice, "A First-Order Perturbation Analysis Of Crack Trapping By Arrays Of Obstacles", Journal Of Applied Mechanics, Vol. 56, pp 828-835, December 1989.
- 16 Y. Murakami and S. Nemat-Nasser, "Growth And Stability Of Surface Flaws Of An Arbitrary Shape", Engineering Fracture Mechanics, Vol. 17 Issue 3 pp 193-210, 1983 .
- 17 N. Noda, "Stress Intensity Formulas For Three-Dimensional Crack Inhomogeneous And Bonded Dissimilar Metals", Engineering Fracture Mechanics, Vol 71, Issue 1, pp 1-15, 2004.
- 18 B. N. Cox and W. L. Morris, "Monte Carlo Simulations Of The Growth Of Small Fatigue Cracks", Engineering Fracture Mechanics Vol 31, no 4, pp 591-610, 1988.
- 19 C. G. Hwang and A. R. Ingraffea, "Shape Prediction And Stability Of Mode-I Planer Cracks", Engineering Fracture Mechanics, Vol. 71, pp 1751-1777, 2004.
- 20 T. Ingraffea, "Computational Fracture Mechanics for Aerospace Applications", presented at Lockheed Martin MAC04, March 2004
- 21 J. C. Newman, Jr., and I. S. Raju, "Stress-Intensity Factor Equations For Cracks In Three-Dimensional Bodies Subjected To Tension And Bending Loads," Computational Methods In The Mechanics Of Fracture, S. N. Atluri, Editor, Elsevier Science Publishers, 1986, pp 311-334.
- 22 Fatigue Crack Growth Computer Program "NASA/FLAGRO" Version 2.0, Revision A, 1994.
- 23 M. Gosz and B. Moran, "Stress-Intensity Factors for Elliptical Cracks Emanating From Countersunk Rivet Holes", Final Report DOT/FAA/AR-95/111, April 1998.
- 24 S. A. Fawaz, "Application Of The Virtual Crack Closure Technique To Calculate Stress Intensity Factors For Through Cracks With An Elliptical Front", Engineering Fracture Mechanics, Vol. 59, No. 3, pp. 327-342, 1998.
- 25 S. A. Fawaz, "Stress Intensity Factor Solutions For Part-Elliptical Through Cracks," Engineering Fracture Mechanics vol 63, pp 209-226, 1999.
- 26 J. A. Harter, AFGROW Users Guide And Technical Manual, AFRL-VA-WP-TR-2004-XXXX, Final Report For The Period 4/2/87-6/07/04, June 2004.
- 27 S. A. Fawaz, Equivalent Initial Flaw Size Testing And Analysis, AFRL-VA-WP-TR-2000-3024, Final Report for 10/01/97-6/15/2000, June 2000.

SHEET	B-15	NO.	4-087051-20
TOTAL	B-18		
ISSUE DATE	10/08/04		

- 28 S. A. Fawaz, and B. Andersson, "Accurate Stress Intensity Factor Solutions For Corner Cracks At A Hole ", Engineering Fracture Mechanics Volume 71, Issues 9-10 , June-July 2004, Pages 1235-1254.
- 29 S. A. Fawaz, B. Andersson, and J. C. Newman Jr., "Experimental Verification Of Stress Intensity Factor Solutions For Corner Cracks At A Hole Subject To General Loading", Presented at the International Conference On Aeronautical Fatigue (ICAF), 2003.
- 30 A. Rahman, J Bakuckas , C. Bigelow, and P Tan, "Boundary Correction Factors for Elliptic Surface Cracks Emanating From Countersunk Rivet Holes Under Tension, Bending, and Wedge Loading Conditions", Final Report DOT/FAA/AR-98/37, March 1999.
- 31 J. Bakuckas, "Comparison Of Boundary Correction Factor Solutions For Two Symmetric Cracks In A Straight Shank Hole," Final Report DOT/FAA/AR-98/36, April 1999.
- 32 R. S. Piascik and S. A. Willard, "The Characterization Of Fatigue Damage In The Fuselage Riveted Lap Joint", NASA/TP-97-206257, Nov. 1997.
- 33 R. Krueger, "The Virtual Crack Closure Technique: History, Approach and Applications", NASA/CR-2002-211628, ICASE Report No. 2002-10, April 2002.
- 34 Fatigue Crack Growth Computer Program "NASGRO" Version 3.0 Reference Manual (JSC-22267B), Engineering Directorate, Lyndon B. Johnson Space Center, National Aeronautics and Space Administration, December 2000.
- 35 R. Ingraffea, "Introduction to FRANC2D, FRANC2D/L and FRANC3D", ASTM Workshop on Computational Fracture Mechanics for Composites Salt Lake City March 22-23, 2004.
- 36 C. E. Harris, R. S. Piascik, and J. C. Newman, Jr., "A Practical Engineering Approach To Predicting Fatigue Crack Growth In Riveted Lap Joints", Presented at the International Conference On Aeronautical Fatigue (ICAF), 1999.
- 37 A. Hartman and J. Schijve, "The Effect Of Secondary Bending On Fatigue Strength Of 2024-T3 Alclad Riveted Joints", NLR TR 69116 U, 1969.
- 38 J. J. M de Rijck and S. Fawaz, "A Simplified Approach For Stress Analysis Of Mechanically Fastened Joints", Fourth Joint DOD/FAA/NASA Conference on Aging Aircraft, May 2000.
- 39 J. C. Newman, Jr, "FASTRAN-II – A Fatigue Crack Growth Structural Analysis Program", NASA Technical Memorandum 104159, February 1992.
- 40 K. Gopinath and A. Carter, "WFD Training Syllabus", A Final Report of the Airworthiness Assurance Working Group (Widespread Fatigue Damage Bridging Task), Aviation Rulemaking Advisory Committee, July 2003.

SHEET	B-16	NO.	4-087051-20
TOTAL	B-18		
ISSUE DATE		10/08/04	

- 41 D. S. Dawicke; J. C. Newman Jr, "Analysis and Prediction of Multiple-Site Damage (MSD) Fatigue Crack Growth", NASA TP-3231 , August 1992.
- 42 D. Stefanescu, L. Edwards and M. E. Fitzpatrick, "Stress Intensity Factor Correction For Asymmetric Through-Thickness Fatigue Cracks At Holes", International Journal of Fatigue Volume 25, Issue 7 , July 2003, Pages 569-576.
- 43 Y. Murakami, editor, Stress Intensity Factors Handbook, Pergamon Press, New York, 1990.
- 44 J. J. M. de Rijck, and S. A. Fawaz, "Stress Intensity Factors And Crack Interaction In Adjacent Holes", Engineering Fracture Mechanics Volume 68, Issue 7 , May 2001, Pages 963-969.
- 45 O. Pártl and J. Schijve, "Multiple Site Damage In 2024-T3 Alloy Sheet", Report LR-660, Faculty Of Aerospace Engineering, Delft University Of Technology, 1992.
- 46 T. Swift, "Damage Tolerance Capability", presented at the Specialist's Conference on Fatigue of Aircraft Materials, Delft – the Netherlands, Oct. 1992.
- 47 R. A. Collins, and D. J. Cartwright, "An Analytical Solution For Two Equal-Length Collinear Strip Yield Cracks", Engineering Fracture Mechanics Volume 68, Issue 7 , May 2001, Pages 915-924.
- 48 D.S. Dugdale, "Yielding Of Steel Sheets Containing Slits", J. Mech Phys Solids 1960;8:100-4.
- 49 H. Tada, P.C. Paris, and G. R. Irwin, The Stress Analysis of Cracks Handbook, Del Research Company, 1973.
- 50 P.S. Theocaris, "Dugdale Models For Two Collinear Unequal Cracks", Engng Frac Mech 1983;18(3):545-59,
- 51 D. Broek, "The Effects Of Multi-Site Damage On The Arrest Capability Of Aircraft Fuselage Structures," FractuResearch TR 9302, June 1993.
- 52 D. Thompson, D. Hoadley, And J. McHatton, "Load Tests Of Flat And Curved Panels With Multiple Cracks," Foster-Miller, Inc. (Prepared For FAA), September 1993.
- 53 J. E. Ingram, Y. S. Kwon, K. J. Duffié, And W. D. Irby, "Residual Strength Analysis Of Skin Splices With Multiple Site Damage", Proceedings Of The Second Joint NASA/FAA/DoD Conference On Aging Aircraft, 1999
- 54 B. L. Smith, A. L. Hijazi, A. K. M. Haque, And R. Y. Myose, "Modified Linkup Models For Determining The Strength Of Stiffened Panels With Multiple Site Damage," Presented At The Third Joint NASA/FAA/DoD Conference On Aging Aircraft, 1999.

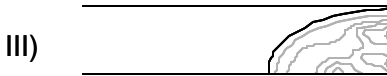
SHEET	B-17	NO.	4-087051-20
TOTAL	B-18		
ISSUE DATE	10/08/04		

FIGURES

Multiple Initiations along rivet hole and joint faying surfaces



Interactions to form irregular crack shape



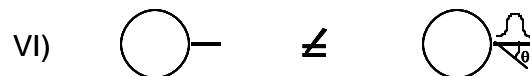
Crack tip becomes more regular, with shapes that may be represented as polynomial functions



"Starburst" crack state develops around fastener hole



Similar MSD crack states at adjacent fasteners with some cracks becoming dominant



Simulation of crack states with distributions of equivalent initial flaw sizes

Figure 1: Six Stages of Crack Growth

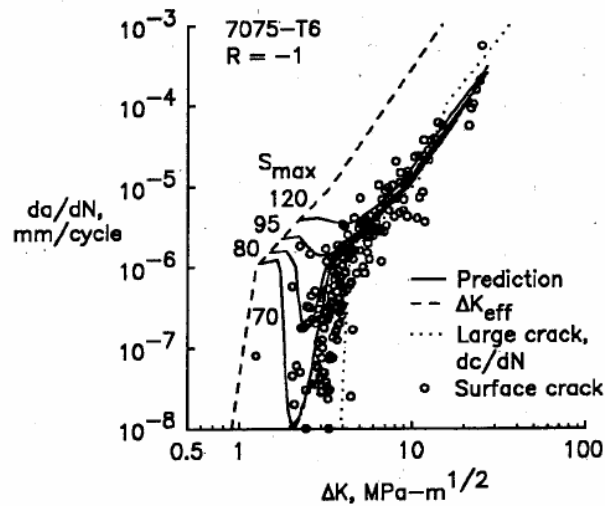


Figure 2: Small Crack Measurements and Prediction from Newman et al. [4]

SHEET	B-18	NO.	4-087051-20
TOTAL	B-18		
ISSUE DATE	10/08/04		

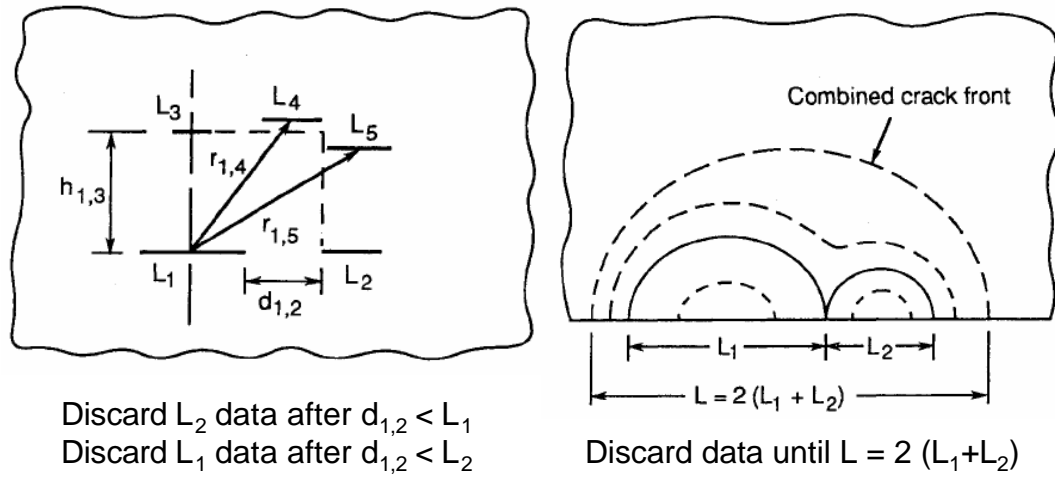


Figure 3: Interaction Criteria from Newman et al.[4]

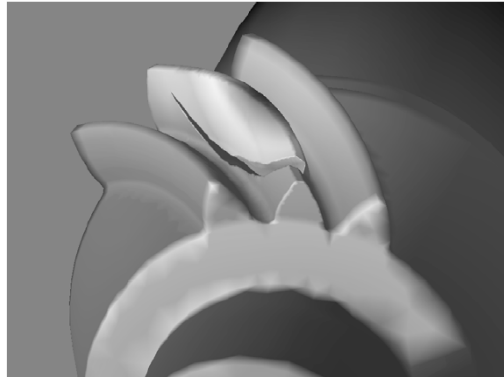


Figure 4: Model of crack growth in spiral bevel transmission gear described by Ingraffea [20]

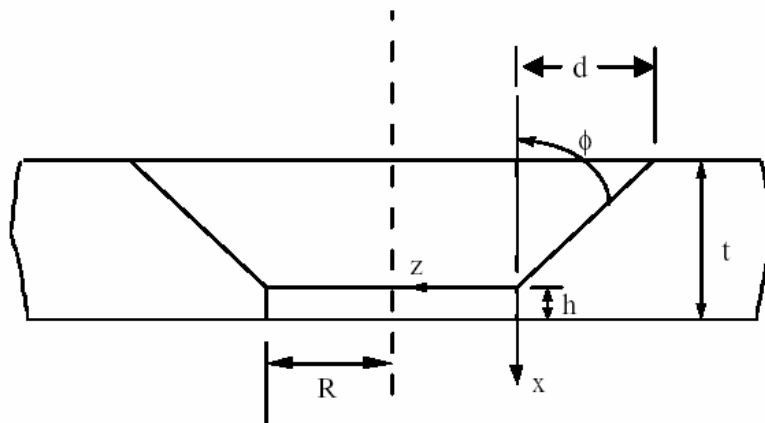


Figure 5: Notation for Countersunk Holes (from Gosz [23])